

# Semianual Technical Report

## Interface Properties of Wide Bandgap Semiconductor Structures

Supported under Grant #N00014-92-J-1477  
Office of the Chief of Naval Research  
Report for the period 1/1/95-6/30/95



R. F. Davis, S. Bedair,\* J. Bernholc,\*\*  
J. T. Glass and R. J. Nemanich\*\*  
c/o Materials Science and Engineering Department  
\*Electrical and Computer Engineering Department  
and \*\*Department of Physics  
North Carolina State University  
Campus Box 7907  
Raleigh, NC 27695-7907

DTIC QUALITY INSPECTED 5

June, 1995

19950721 021

DISTRIBUTION STATEMENT A

Approved for public release;  
Distribution Unlimited

# REPORT DOCUMENTATION PAGE

Form Approved  
OMB No. 0704-0188

Public reporting burden for this collection of information is estimated to average 1 hour per response, including the time for reviewing instructions, searching existing data sources, gathering and maintaining the data needed, and completing and reviewing the collection of information. Send comments regarding this burden estimate or any other aspect of this collection of information, including suggestions for reducing this burden to Washington Headquarters Services, Directorate for Information Operations and Reports, 1215 Jefferson Davis Highway, Suite 1204, Arlington, VA 22202-4302, and to the Office of Management and Budget Paperwork Reduction Project (0704-0188), Washington, DC 20503.

1. AGENCY USE ONLY (Leave blank)			2. REPORT DATE		3. REPORT TYPE AND DATES COVERED		
			June, 1995		Semiannual Technical 1/1/95-6/30/95		
4. TITLE AND SUBTITLE			Interface Properties of Wide Bandgap Semiconductor Structures				
6. AUTHOR(S)			Robert F. Davis and R. J. Nemanich				
7. PERFORMING ORGANIZATION NAME(S) AND ADDRESS(ES)			North Carolina State University Hillsborough Street Raleigh, NC 27695				
9. SPONSORING/MONITORING AGENCY NAMES(S) AND ADDRESS(ES)			Sponsoring: ONR, 800 N. Quincy, Arlington, VA 22217-5660 Monitoring: Administrative Contracting Officer, Office of Naval Research Regional Office Atlanta, 101 Marietta Tower, Suite 2805 101 Marietta Street Atlanta, GA 30323-6145				
11. SUPPLEMENTARY NOTES			By _____ Distribution / _____				
12a. DISTRIBUTION/AVAILABILITY STATEMENT			Approved for Public Release; Distribution Unlimited				
13. ABSTRACT (Maximum 200 words)			Page 1 of 2 <p>Oriented (100) and (111) diamond films were grown at 900°C on Ni<sub>4</sub>C precipitated from cooled Ni-C-H molten surface layers. Studies of interface interactions of diamond with Si, Ni and Ni<sub>3</sub>Si substrates revealed that the (100)-diamond/(100)-Si interface adopts a 3:2 match arrangement, as predicted by extended Hückel tight-binding (EHTB) calculations. Growth on polycrystalline Ni<sub>3</sub>Si resulted in oriented diamond particle; largely graphite was formed on the nickel substrate. <i>Ab initio</i> molecular dynamics showed that a Cl-based ALE cycle on diamond(111) is not advantageous due to strong steric hindrances. New ALE processes have been proposed which exploit the cyclic use of H and F. All clean surfaces of 6H-SiC(0001) except those terminated by H exhibited surfaces states. H termination unpinned the surface Fermi level. Monocrystalline β(3C)-SiC films were grown on α(6H)-SiC(0001) substrates using gas-source MBE, silane and ethylene precursors between 1050 and 1450°C. Cubic (3C)-SiC was achieved at all T&lt;1400°C; 6H-SiC films achieved at T&gt;1400°C when H<sub>2</sub> diluent was present. As-deposited NiAl contacts were rectifying on p-type 6H-SiC (0001) substrates with very low leakage current densities (~1×10<sup>-8</sup> A/cm<sup>2</sup> at 10 V), ideality factors between 1.4 and 2.4, and a Schottky barrier height (SBH) of approximately 1.37 eV. As-deposited Ni and Au contacts on p-type 6H-SiC displayed similar characteristics with calculated SBH's of 1.31 and 1.27 eV, respectively. The former became ohmic on p<sup>+</sup> (1×10<sup>19</sup> cm<sup>-3</sup>) 6H-SiC (0001) after annealing for 10-80 s at 1000 °C in a N<sub>2</sub> ambient. The estimated specific contact resistivity from a non-mesa etched TLM pattern was (2-3)×10<sup>-2</sup> Ω·cm<sup>2</sup>. An AES depth profile obtained by a film annealed for 80 s showed the formation of Al oxide at the surface. The Ni/NiAl contacts deposited on p-type SiC with lower carrier concentrations (1-5×10<sup>18</sup> cm<sup>-3</sup>) were not ohmic after annealing at 1000 °C for 10-60 s but became nearly ohmic after annealing for 80 s. MIS diodes (Al/AlN/α-SiC(0001)) have been fabricated with various thicknesses of AlN deposited using gas-source MBE. High frequency C-V measurements between 10 kHz and 1 MHz showed that thin layers (&lt;1000 Å) of AlN exhibited moderate leakage currents; thicker layers reduced this problem. The diodes could be accumulated</p>				
14. SUBJECT TERMS			diamond, nucleation, nickel substrates, atomic hydrogen, Ni <sub>4</sub> C, molecular dynamics, atomic layer epitaxy, SiC, surface cleaning, surface states, surface resonance, Fermi level, H-termination, β-SiC, 6H-SiC, AlN, gas source molecular beam epitaxy, ohmic contacts, rectifying contacts, Ni/Al alloys, leakage current, Schottky barrier height, MIS diodes, GaN, gallium nitride powder, gallium nitride, GaN, aluminum nitride,				
15. NUMBER OF PAGES			229				
16. PRICE CODE							
17. SECURITY CLASSIFICATION OF REPORT		18. SECURITY CLASSIFICATION OF THIS PAGE		19. SECURITY CLASSIFICATION OF ABSTRACT		20. LIMITATION OF ABSTRACT	
UNCLAS		UNCLAS		UNCLAS		SAR	

## Table of Contents

I.	Introduction	1
<b>Carbon-based Materials</b>		
II.	Nucleation and Growth of Oriented Diamond Films on Ni Substrates <i>P. C. Yang, D. A. Tucker, F. R. Sivazlian, S. P. Bozeman, J. T. Glass and R. F. Davis</i>	3
III.	Comparison of Silicon, Nickel and Nickel Silicide (Ni <sub>3</sub> Si) as Substrates for Epitaxial Diamond Growth <i>D. A. Tucker, F. R. Sivazlian, S. P. Bozeman, A. T. Sowers, R. J. Nemanich and J. T. Glass</i>	7
IV.	Flourine-based Mechanisms for ALE Growth on Diamond (110) <i>M. G. Wensell, Z. Zhang and J. Bernholc</i>	35
V.	Growth and Characterization of Homoepitaxial Diamond Negative Electron Affinity Surfaces <i>A. T. Sowers, D. T. Mathes and R. J. Nemanich</i>	45
VI.	Negative Electron Affinity Effects and Schottky Barrier Height Measurements of Cobalt on Diamond (100) Surfaces <i>P. K. Baumann and R. J. Nemanich</i>	49
VII.	Diamond Negative Electron Affinity Surfaces, Structures and Devices <i>P. K. Baumann, J. van der Weide and R. J. Nemanich</i>	54
VIII.	Characterization of Electron Emission from Cold Cathode Emitters <i>B. Ward and R. J. Nemanich</i>	63
IX.	Angular Resolved UPS (ARUPS) Investigation of 6H SiC Electronic Surface Structure <i>M. C. Benjamin, S. W. King, J. P. Barnak, R. S. Kern, R. F. Davis and R. J. Nemanich</i>	68
X.	Homoepitaxial Growth of Silicon Carbide Polytypes by Gas-Source Molecular Beam Epitaxy <i>S. Kern and R. F. Davis</i>	75
XI.	Rectifying and Ohmic Contacts for P-Type Alpha (6H) Silicon Carbide <i>L. Porter and R. F. Davis</i>	79
XII.	Fabrication and Characterization of MIS Diodes of Al/AlN/SiC by Gas-Source Molecular Beam Epitaxy <i>S. Kern, O. Aboelfotoh and R. F. Davis</i>	87
<b>Nitrogen-based Materials</b>		
XIII.	Synthesis and Characterization of High Purity, Single Phase GaN Powder <i>C. M. Balkas, C. Basceri and R. F. Davis</i>	92

XIV.	Undoped and Doped GaN and $\text{Al}_x\text{Ga}_{1-x}\text{N}$ Thin Films Deposited on High-Temperature Monocrystalline AlN Buffer Layers on Vicinal and On-axis $\alpha$ (6H)-SiC(0001) Substrates via Organometallic Vapor Phase Epitaxy <i>M. D. Bremser, T. W. Weeks, Jr. and R. F. Davis</i>	98
XV.	Novel Computer-controlled CVD System for the Deposition and Doping of III-V Nitride Thin Films <i>D. Hanser and R. F. Davis</i>	121
XVI.	New Buffer Layers for GaN on Sapphire by Atomic Layer and Molecular Stream Epitaxy <i>E. L. Piner, Y. W. He, N. A. El-Masry, K. S. Boutros, F. G. McIntosh, J. C. Roberts and S. M. Bedair</i>	125
XVII.	Low Temperature Atomic Layer Epitaxy of GaN and InGaN <i>K. S. Boutros, F. G. McIntosh, J. C. Roberts, S. M. Bedair, E. L. Piner and N. El-Masry</i>	131
XVIII.	Growth of AlN and GaN Thin Films via Gas Source Molecular Beam Epitaxy <i>K. Linthicum and R. F. Davis</i>	142
XIX.	Electron Cyclotron Resonance Growth of AlN, GaN and InN <i>J. Christman, R. J. Nemanich and R. F. Davis</i>	148
XX.	Native Defects in Gallium Nitride <i>P. Boguslawski, E. L. Briggs and J. Bernholc</i>	152
XXI.	Towards the Identification of the Dominant Donor in GaN <i>J. Bernholc</i>	166
XXII.	Luminescence Studies of GaN, AlN, InN and Their Solid Solutions <i>W. Perry and R. F. Davis</i>	179
XXIII.	UV Photoemission Study of Heteroepitaxial AlGaN Films Grown on 6H-SiC <i>M. C. Benjamin, M. D. Bremser, T. W. Weeks, Jr., S. W. King, R. F. Davis and R. J. Nemanich</i>	193
XXIV.	Reactive Ion Etching of GaN and AlN <i>K. Gruss and R. F. Davis</i>	201
XXV.	Surface Cleaning and Contact Formation on GaN <i>L. Smith and R. F. Davis</i>	213
XXVI.	Distribution List	229

## I. Introduction

Heteroepitaxy is the growth of a crystal (or a film) on a foreign crystalline substrate that determines its orientation. Such oriented growth requires that lattice planes in both materials have similar structure. In general, an epitaxial relationship is probable whenever the orientation of the substrate and overgrowth produces an interface with a highly coincident atomic structure having low interfacial energy relative to a random arrangement.

During the past decade, nonequilibrium techniques have been developed for the growth of epitaxial semiconductors, superconductors, insulators and metals which have led to new classes of artificially structured materials. In many cases, the films were deposited on substrates having a different chemistry from that of the film, and heteroepitaxy was achieved. Moreover, layered structures with a periodicity of a few atomic layers have also been produced by the sequential heteroepitaxial deposition of a film of one type on another. Metastable structures can be generated which possess important properties not present in equilibrium systems. A consideration of the materials under consideration for next generation electronic and optoelectronic devices, e.g., the III-V nitrides show that only a few of them can currently be grown in bulk, single crystal form having a cross-sectional area of  $>3\text{cm}^2$ . Thus other, commercially available substrates must be used. This introduces a new set of challenges for the successful growth of device quality films which are not present in homoepitaxial growth and which must be surmounted if these materials are to be utilized in device structures.

In addition to providing structures which do not exist in nature, applications of advanced heteroepitaxial techniques permit the growth of extremely high quality heterostructures involving semiconductors, metals, and insulators. These heterostructures offer the opportunity to study relationships between the atomic structure and the electrical properties of both the film itself and the interface between the two dissimilar materials. They also allow the study of epitaxial growth between materials exhibiting very different types (ionic, covalent, or metallic) of bonding.

While the potential of heteroepitaxial deposition has been demonstrated, significant advances in theoretical understanding, experimental growth and control of this growth, and characterization are required to exploit the capabilities of this process route. It is particularly important to understand and control the principal processes which control heteroepitaxy at the atomic level. It is this type of research, as well as the chemistry of dry etching via laser and plasma processing, which forms the basis of the research in this grant.

The materials of concern in this report are classified as wide bandgap semiconductors and include diamond, SiC and the III-V nitrides of Al, Ga, and In and their alloys. The extremes in electronic and thermal properties of diamond and SiC allow the types and numbers of current and conceivable applications of these materials to be substantial. However, a principal driving force for the interest in the III-V nitrides is their potential for solid-state optoelectronic devices

for light emission and detection from the visible through the far ultraviolet range of the spectrum.

The principal objectives of the research program are the determination of (1) the fundamental physical and chemical processes ongoing at the substrate surface and substrate/film interface during the heteroepitaxial deposition of both monocrystalline films of the materials noted above, as well as metal contacts on these materials, (2) the mode of nucleation and growth of the materials noted in (1) on selected substrates and on each other in the fabrication of multilayer heterostructures, (3) the resulting properties of the individual films and the layered structures and the effect of interfacial defects on these properties, (4) the development and use of theoretical concepts relevant to the research in objectives (1-3) to assist in the fabrication of improved films and structures and (5) the determination of process chemistry which leads to the laser assisted and plasma etching of these wide bandgap compound semiconductors.

This is the sixth bi-annual report since the initiation of the project. The following sections introduce each topic, detail the experimental approaches, report the latest results and provide a discussion and conclusion for each subject. Each major section is self-contained with its own figures, tables and references.

# Carbon-based Materials

## II. Nucleation and Growth of Oriented Diamond Films on Ni Substrates

P.C. Yang<sup>1</sup>, T.J. Kistenmacher<sup>2</sup>, D.A. Tucker<sup>1</sup>, W. Liu<sup>1</sup>, F.R. Sivazlian<sup>1</sup>  
S.P. Bozeman<sup>1</sup>, B.R. Stoner<sup>3</sup>, J.T. Prater<sup>4</sup>, J.T. Glass<sup>3</sup> and R.F. Davis<sup>1</sup>

<sup>1</sup>Department of Materials Science and Engineering, North Carolina State University, Raleigh, North Carolina 27695-7919

<sup>2</sup>Milton S. Eisenhower Research Center, Applied Physics Laboratory, Johns Hopkins University, Laurel, Maryland 20723-6099

<sup>3</sup>Kobe Steel USA , Inc., Electronic Materials Center, RTP, NC 27709

<sup>4</sup>Army Research Office, Research Triangle Park, NC

Key words: oriented diamond, surface melting, X-ray diffraction, H, Ni, Co, Ni<sub>4</sub>C

### Abstract

Oriented (100) and (111) polycrystalline diamond has been achieved without graphite formation. Nucleation is believed to occur from a Ni-C-H molten surface layer on oriented, metastable, cubic Ni<sub>4</sub>C previously nucleated on similarly oriented single crystal Ni substrates. The incorporation of the atomic H lowers the eutectic melting point of the Ni-C system from 1325°C to the 900-1000°C range and also promotes the nucleation of the Ni<sub>4</sub>C. X-ray diffraction analysis revealed that the Ni<sub>4</sub>C occurs only between diamond particles and the Ni substrate.

### 1. Introduction

The growth of highly oriented heteroepitaxial diamond films represents an important step toward the goal of obtaining large area, device quality diamond. Nickel was chosen for investigation as a substrate material in this research initially because of its close lattice match (1.13%) and solvent-catalytic reactivity with diamond [1]. However, more complex, multi-step melt formation, precipitation and nucleation chemistries were discovered. The procedures, results and conclusions of this study are reported below.

### 2. Experimental

The nucleation and growth were conducted using the three-step sequential process shown in Fig.1. Step 1 involved deoxidization of the diamond seeded surface of [111] and [100] oriented Ni substrates in H<sub>2</sub> at 900°C for 10-30 minutes. In step 2 the Ni temperature was raised to 1100°C where the diamond seeds dissolved rapidly into the Ni. The annealing time varied depending on the degree of seeding and the surface temperature. This allowed sufficient reaction between the nickel, diamond seeds and atomic hydrogen (produced via a hot filament) to form a molten Ni-C-H intermediate layer. In-situ laser reflection interferometry (LRI) revealed large surface reflectivity changes during this multi-step process. This technique monitored the reflection of a He/Ne laser beam from the substrate surface. The intensity of this light depended on the reflection and scattering characteristics on the substrate surface. As shown in Fig. 2, the reflective light intensity during process step 1 was very low, due to the strong scattering by the carbon seeds. This intensity increased rapidly as the temperature was increased. At ≈1100°C a step increase in intensity was observed which was correlated with the formation of a molten surface layer. At this point, the temperature was lowered

to 900°C and the flow of CH<sub>4</sub> was initiated to begin diamond growth (step 3). X-ray diffraction (XRD) and scanning electron microscopy (SEM) were used to study the Ni/C/H interfacial reactions.

## Results and Discussion

Figure 3 shows an SEM micrograph of a [111] oriented diamond film; [100] oriented films were also achieved. The representative XRD pattern of the [111] film shown in Fig. 4 consists of a set of strong diffraction spots from the single crystal Ni and weaker diffraction lines from the diamond film. The latter are further divided into a set of closely spaced discrete spots corresponding to diamond crystallites having an average grain size of >5μm and a set of smooth lines corresponding to the normally metastable cubic (NaCl structure) Ni<sub>4</sub>C phase having an average grain size of <5μm. These results are summarized in Table I. Additional XRD and SEM studies on surfaces containing only a few diamond particles reveal that the Ni<sub>4</sub>C does not occur as a separate phase apart from its association with these particles.

Table I. X-ray diffraction data

d(Å) smooth lines	d(Å) grainy lines	Ni <sub>4</sub> C planes	diamond planes
2.03	2.03	{111} 2.04	{111} 2.06
1.75		{200} 1.75	
1.24	1.25	{022} 1.26	{022} 1.26

Based on the above results, a model is proposed to explain the mechanism of oriented diamond nucleation. Specifically, atomic H is incorporated into and lowers the eutectic melting point of the Ni-C system from 1326°C to the 900 - 1000°C range (step 2 in Fig. 1). The reduction in temperature to 900°C (step 3) in tandem with the atomic H in the melt causes the metastable Ni<sub>4</sub>C phase to solidify from the melt with the same orientation as the solid Ni on which it nucleates and grows. This carbide phase also solidifies from molten Ni in HPHT diamond processes. The incorporation of atomic H in the Ni-C solution of the present research is believed to play a role analogous to high pressure high temperature in favoring the formation of Ni<sub>4</sub>C. It is not known if H is incorporated into the Ni<sub>4</sub>C lattice. The Ni<sub>4</sub>C provides the sites and template for the subsequent nucleation of the diamond particles as a result of the close lattice matching of the lattice vectors of both phases (see Table I). It is important to note the essential role of atomic H. Neither Ni<sub>4</sub>C nor diamond precipitates are produced in an inert ambient at 1 atm. The occurrence of the Ni<sub>4</sub>C also contrasts with the formation of an initial graphite layer on solid [100] or [111] oriented Ni prior to the nucleation of diamond in the more common methods of deposition [3].

## Conclusions

A multi-step process has been developed to nucleate and grow [111] and [100] oriented diamond films, without graphite deposition, from a molten layer formed via the incorporation of C and atomic H on a solid Ni surface. In-situ LRI was used to study the seeding and multi-step process as a function of temperature. A model involving the initial precipitation on the solid Ni of an oriented metastable cubic Ni<sub>4</sub>C phase and the subsequent nucleation of diamond with the same orientation on this essentially lattice matched carbide has been proposed. Atomic H in the melt appears to be analogous to high pressure in the commercial diamond forming process routes.

## Acknowledgments

The financial support of BMDO-IST via ONR is acknowledged. Helpful discussions with Drs. R.J. Nemanich and W. Zhu are greatly appreciated.

## References

1. Y. Sato, H. Fujita, T. Ando, T. Tanaka, and M. Kamo, Philosophical Transactions of the Royal Society of London A **342** (1993) 225.
2. P.C. Yang, W. Zhu, and J.T. Glass, Journal of Materials Research **8** (1993) 1773.
3. D.N Belton and S.J. Schmieg, Journal of Applied Physics **66** (1989) 4223.

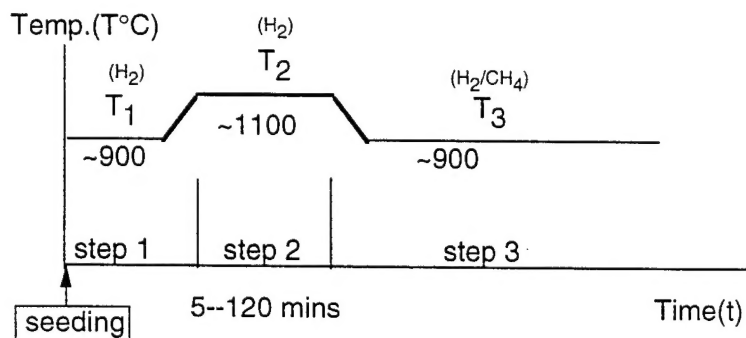


Fig. 1. The schematic diagram of the seeding and multi-step process.

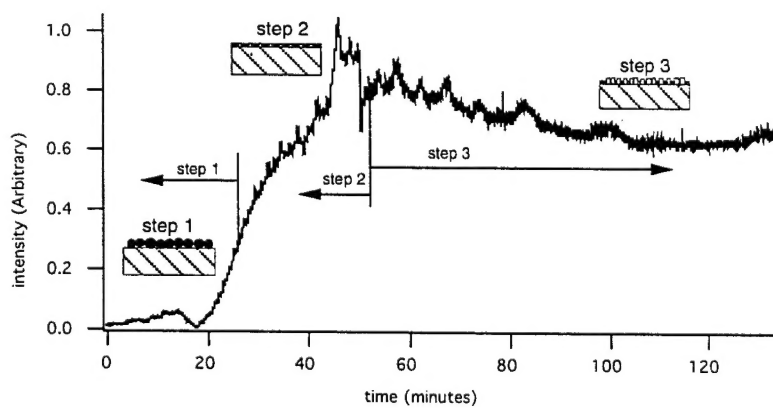


Fig. 2. Laser reflection interferometry spectrum of the seeding and multi-step process.

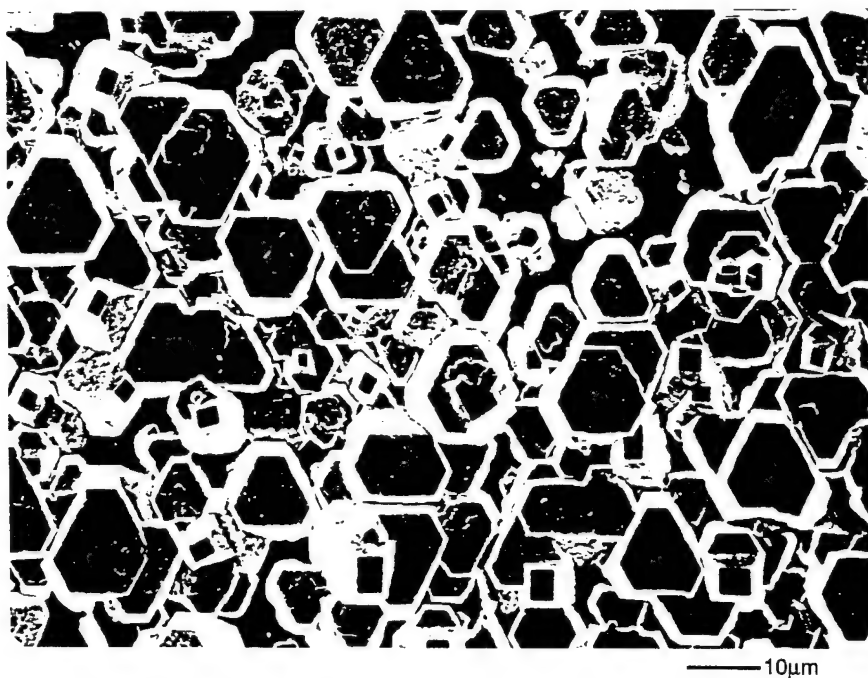


Fig. 3. SEM microstructure of a (111) oriented diamond film on a Ni(111) substrate grown out by microwave CVD.

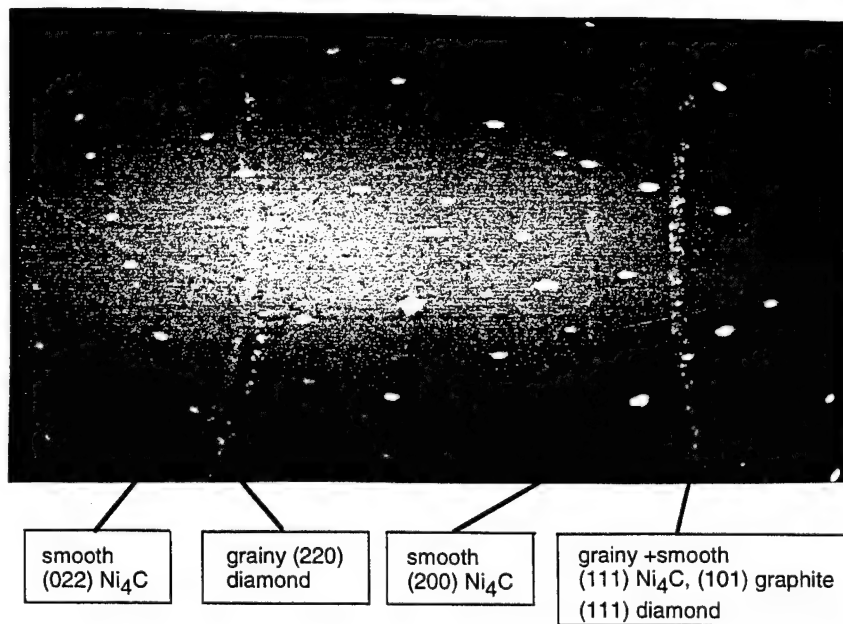


Fig. 4. X-ray diffraction pattern of the (111) oriented diamond film on the (111) single crystal Ni substrate.

### **III. Comparison of Silicon, Nickel and Nickel Silicide ( $Ni_3Si$ ) as Substrates for Epitaxial Diamond Growth**

D. A. Tucker <sup>(a)</sup>, D.-K. Seo <sup>(b)</sup>, M.-H. Whangbo <sup>(b)</sup>, F. R. Sivazlian <sup>(a)</sup>, B. R. Stoner <sup>(d)</sup>, S. P. Bozeman <sup>(a)</sup>, A. T. Sowers <sup>(c)</sup>, R. J. Nemanich <sup>(c)</sup>, and J. T. Glass <sup>(d)</sup>

- (a) Department of Materials Science and Engineering, North Carolina State University, North Carolina 27695-7919
- (b) Department of Chemistry, North Carolina State University, North Carolina 27695-8204
- (c) Department of Physics, North Carolina State University, North Carolina 27695-8202
- (d) Kobe Steel USA Inc., Electronic Materials Center, 79 T. W. Alexander Drive, PO Box 13608, Research Triangle Park, North Carolina 27709

#### **Abstract**

We carried out experimental and theoretical studies aimed at probing interface interactions of diamond with Si, Ni and  $Ni_3Si$  substrates. Oriented diamond films deposited on (100) silicon were characterized by polar Raman, polar XRD and cross-sectional HRTEM. These studies show that the (100)-diamond/(100)-Si interface does not adopt the 45°-rotation but the 3:2-match arrangement. Our extended Hückel tight-binding (EHTB) electronic structure calculations for a model system show that the interface interaction favors the 3:2-match arrangement. Growth on polycrystalline  $Ni_3Si$  resulted in oriented diamond particles while, under the same growth conditions, largely graphite was formed on the nickel substrate. Our EHTB electronic structure calculations for model systems show that the (111) and (100) surfaces of  $Ni_3Si$  have a strong preference for diamond-nucleation over graphite-nucleation, but this is not the case for the (111) and (100) surfaces of Ni.

## A. Introduction

Diamond has many excellent properties (e.g., large bandgap, high hole mobility, optical transparency, large thermal conductivity, chemical inertness, and high hardness) that are important for applications in high temperature electronic devices, tool coatings, heat sinks, and optical windows. For the microelectronics industry to capture the full utility of diamond's unique properties, however, it is necessary to attain heteroepitaxial diamond. Currently, thin film growth of single crystal diamond has not been achieved, and the chemistry involved in diamond nucleation on a substrate surface is poorly understood. Studies of diamond nucleation and interfaces can help improve adhesion, control morphology, and produce heteroepitaxy. All these aspects are important in applications of diamond thin-films for electronic purposes, wear and optical coatings.

At present, there is no completely lattice-matched substrate for heteroepitaxial diamond growth, but several have a relatively small lattice mismatch: cubic boron nitride (1.5 %), nickel (1.2 %), copper (1.2 %), and cobalt (0.6 %). Currently, oriented diamond particles have been deposited on cubic boron nitride (cBN) [1-4], silicon [5-7], silicon carbide [8-10], nickel [11-15], cobalt [16], beryllium oxide [17], and graphite [18,19] by different growth methods (e.g., DC plasma, microwave, and hot-filament), and novel processes utilizing these methods have been employed to produce these oriented diamond particles (e.g., the bias-enhanced nucleation process developed by Stoner *et al.* [5,20,21] and the seeding-annealing-growth process developed by Yang *et al.* [12-15]). However, all of these substrates possess some limitations: For example, cBN is attractive in terms of the small lattice mismatch and the expected interface chemical bonding (e.g., C-N and C-B bond formation), but it is very difficult to produce single crystals of cBN suitable in size for substrates. Stoner *et al.* [5,8,9] obtained oriented diamond particles on silicon and silicon carbide ( $\beta$ -SiC) by the bias-enhanced nucleation process, but the large lattice mismatch (34% for Si and 18% for  $\beta$ -SiC) leads to misorientation in the resulting diamond particles. In diamond growth on silicon, the percentage of oriented particles (with respect to the substrate lattice) after the bias-nucleation step can be as high as 50 %. From these particles, highly oriented films, in which nearly all of the grains are aligned to within about 6° of the substrate, can be grown [5,7] by a judicious use of the van der Drift evolutionary method [22]. Normal diamond growth conditions on nickel and cobalt substrates usually result in graphite or graphite interlayers [23,24]. However, oriented diamond particles can be grown on these substrates by using the process of Yang *et al.* [12-15], which consists of seeding the metal surface with carbon powders (either diamond or graphite), annealing the sprinkled powders in a high temperature step, and growing diamond particles on the annealed surface under typical diamond growth conditions. It is believed that the annealing step produces a supersaturated M-C-H (M = Ni or Co) phase on the substrate surface, and diamond nucleation starts from this phase upon assuming the typical diamond growth conditions. Nickel and cobalt

have a relatively close lattice match with diamond (1.2 and 0.6 % mismatch, respectively). However, it is difficult to obtain complete diamond films probably because the carbon continues to dissolve into the substrate during growth, as evidenced by lack of stable carbide formation. In the search for a suitable substrate for improved heteroepitaxial diamond growth, therefore, the lattice-matching and strong directional bond formation in the diamond/substrate interface appear to be essential.

Several theoretical studies examined interface interactions in (100)-diamond/(100)-Si, (100)-diamond/(100)-Ni, and (111)-diamond/(111)-Ni. On the basis of MNDO and PM3 semiempirical SCF-MO calculations, Verwoerd examined the (100)-diamond/(100)-Si interface [25-28]. To reduce the large lattice mismatch (34%), he first considered an arrangement in which one (100) surface is rotated by 45° with respect to the other (hereafter, referred to as the 45°-rotation arrangement) since it provides a much smaller lattice mismatch (7%) [25,26]. As an alternative arrangement for the (100)-diamond/(100)-Si interface, Verwoerd considered the possibility that the epitaxy arises from matching three diamond unit cells to two silicon unit cells without rotating the two surfaces (hereafter, referred to as the 3:2-match arrangement) [27,28]. The lattice constants of the Si/diamond (100) surfaces have a ratio very close to 3:2, and the lattice mismatch is only 1.5 % from this viewpoint. In Verwoerd's calculations, the positions of the surface and subsurface atoms are completely relaxed, and the atoms of one surface are allowed to penetrate into the lattice of the other surface. His calculations suggest that the 3:2-match arrangement becomes energetically favored over the 45°-rotated arrangement when the diamond overlayer is thick enough (greater than 3 atomic layers) [27,28]. Pickett and Erwin studied the (100)-diamond/(100)-Ni and (111)-diamond/(111)-Ni interfaces on the basis of ab initio electronic band structure calculations [29-35]. For each interface they considered two arrangements: one emphasized the "tetrahedral bonding" by placing the carbon atoms at the bridge positions of the (100) Ni surface and at the atop positions of the (111) Ni surface. The other arrangement maximized "metallic bonding" by placing the carbon atoms at the missing Ni positions above the Ni surface, which are 4-fold hollow sites of the (100) Ni surface and 2-fold hollow sites of the (111) Ni surface. For both (100)-diamond/(100)-Ni and (111)-diamond/(111)-Ni interfaces, the "tetrahedral bonding" arrangement was calculated to be more favorable [31].

In the present work, we carry out both experimental and theoretical studies aimed at probing interface interactions of diamond with Si, Ni and Ni<sub>3</sub>Si substrates. The nickel silicide Ni<sub>3</sub>Si has the Cu<sub>3</sub>Au-type structure, and its (100) surface (3.504 Å) has a small lattice mismatch with the (100) diamond surface (1.8 %). Silicon readily forms a stable carbide, whereas nickel carbide is metastable. As mentioned above, under normal diamond growth conditions, nucleation attempts on Ni usually results in graphite, while that on Si leads to diamond particles. Thus, for Ni<sub>3</sub>Si, one might expect that the Si atoms make interface bonds

with the diamond carbon atoms, and the small lattice mismatch reduces the misorientation of the diamond particles. To help explain our experimental observations of diamond and/or graphite growth on Si, Ni and Ni<sub>3</sub>Si substrates, we examine their associated interface interactions on the basis of extended Hückel tight-binding (EHTB) electronic band structure calculations [36].

## B. Experimental

*Growth on Silicon.* Diamond films were deposited on (100) silicon substrates utilizing a microwave plasma chemical vapor deposition (CVD) reactor (ASTeX™). A more detailed description is given elsewhere [21]. Silicon wafers were cleaned by dipping into a dilute hydrofluoric acid for one minute, rinsed with deionized water before loading into the chamber, and then subjected to a three-step growth process (i.e., carburization, nucleation and thin-film growth) similar to what has been described previously [6]. In the nucleation step, which lasts approximately 3–10 minutes, the substrate is biased at -250 V while immersed in the methane/hydrogen plasma. Finally, from the resulting oriented nuclei, typical deposition conditions are used to grow diamond films. The diamond films were characterized by Raman spectroscopy, scanning electron microscopy (SEM), X-ray diffraction (XRD), and high resolution transmission electron microscopy (HRTEM).

Most of these techniques have been frequently used in characterization of diamond films. Polar XRD is especially effective at determining texture, orientation and crystallographic quality of films [37-39]. Although polarization sensitive Raman spectroscopy (PSR) is not as popular, it can be successfully used to give crystallographic information [3,4,40].

Raman spectroscopy has established itself as a key technique for determining the quality of diamond thin films. The basic application of Raman scattering is to evaluate the sp<sup>2</sup>/sp<sup>3</sup> bonding ratio and strain present in the films. However, due to anisotropy in the Raman scattering tensor for the diamond crystal structure [41], Raman spectroscopy can also be used to characterize the crystallographic orientation of highly oriented or single crystal diamond samples. In these polar Raman measurements the observed Raman scattering intensity is function of the incident laser beam polarization, the sample orientation, and the polarization of the observed scattered light.

For the crystallographic measurements the routine Raman scattering apparatus is used with slight modifications. The incident laser beam is polarized vertically using a polarization rotator/linear polarizer combination. The sample is mounted on a rotary stage and the axis of rotation is normal to the sample surface. The Raman scattered light is collected and passed through another linear polarizer with its transmission axis vertically oriented before entering the monochromator.

With the scattering apparatus in this configuration, the sample stage is rotated through  $360^\circ$  in  $10^\circ$  increments. At each increment Raman spectra of the silicon and diamond peaks ( $520\text{ cm}^{-1}$  and  $1332\text{ cm}^{-1}$ , respectively) are taken. The polar response for both silicon and diamond is then obtained by plotting the scattering intensity of each peak versus the sample rotation angle.

*Growth on  $\text{Ni}_3\text{Si}$  and Ni.* The deposits on  $\text{Ni}_3\text{Si}$  and Ni substrates were both grown and analyzed in the in-vacuo CVD and surface analysis apparatus (Fig. 1), which consists of a hot-filament CVD (HFCVD) system connected to two analytical chambers via a transfer station. Once the substrates are introduced into the apparatus, however, the samples can be transferred into the analysis chamber without exposure to atmosphere. The HFCVD chamber is a modified six-way cross processed by a dual-stage rotary pump during diamond deposition. Filaments utilized in diamond growth were spiral tungsten filaments powered by a Sorensen DC power supply. One chamber is equipped with an X-ray source (dual anode VG XR3E2) for X-ray photoelectron spectroscopy (XPS), an electron gun (VG LEG62) for Auger electron spectroscopy (AES), and a hemispherical electron energy analyzer (VG CLAM II). Another chamber is outfitted with an ion gun used to clean the substrates. The two chambers are

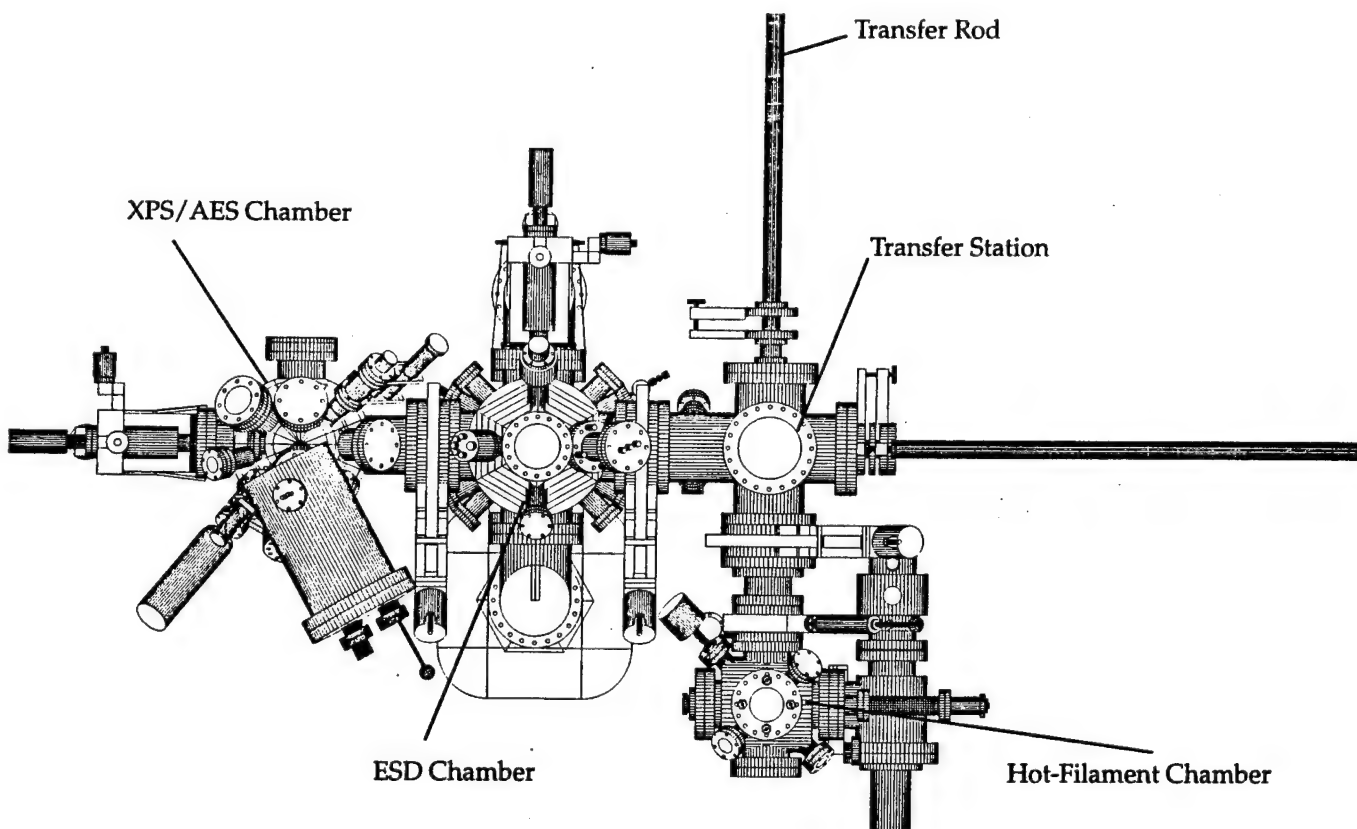


Figure 1. Schematic diagram of growth and surface-characterization systems. ESD refers to electron stimulated desorption.

pumped by an ion pump (Perkin Elmer 400 l/s) and a water-cooled titanium sublimation pump. A base pressure for the two chambers (typically  $3 \times 10^{-10}$  Torr) was monitored by an ionization gauge. XPS and AES spectra, both collected in pulse-counting mode, were acquired with a software package (VGX900). In addition, the AES spectra were differentiated with this software.

$\text{Ni}_3\text{Si}$  was produced by an arc melting and drop casting technique from a stoichiometric mixture of Ni and Si (by Dr. C. T. Liu and coworkers, Metals and Ceramics Division, Oak Ridge National Laboratory). The resulting silicide was characterized by metallography, XRD (both diffractometer and Debye-Scherrer), XPS, and AES. Diamond films were deposited on  $\text{Ni}_3\text{Si}$  in the HFCVD chamber described earlier. The same conditions were used in depositing on polycrystalline Ni for the purpose of comparisons. Both the  $\text{Ni}_3\text{Si}$  and Si substrates were polished (down to 0.01  $\mu\text{m}$  alumina) before deposition. Typical experimental conditions were: a filament temperature of over  $2200^\circ\text{C}$ , substrate temperature of approximately  $850^\circ\text{C}$ , pressure of 20 Torr, and methane concentration of 1 % in hydrogen. The films deposited on the  $\text{Ni}_3\text{Si}$  and Ni substrates were characterized by SEM, Raman spectroscopy, XPS and AES.

### C. Experimental Results

*Growth on Silicon.* The diamond films grown on (100) silicon were both highly oriented and textured to within  $10^\circ$  of the (100) Si. The SEM micrograph of a typical diamond film is shown in Fig. 2. Figure 3 displays a progression of the SEM micrographs, polarization sensitive Raman spectra (PSR), and polar XRD spectra as a function of the thickness of the grown diamond layer. In the Raman spectra, the solid and open circles refer to the silicon and diamond responses, respectively (both have been normalized). The improvement of texturing, visually detected from the SEM micrographs (Fig. 3a), is verified in the polar XRD patterns (Fig. 3c): the {220} twin spots disappear at higher thicknesses, and the area of the {220} spots decreases progressively. The {220} spots for the thicker film are asymmetric with a FWHM of  $10^\circ$  and  $8^\circ$  in the radial and transversal directions, respectively. The FWHM relates to a minor misorientation of the particles and corresponds to a tilt of the diamond out of the (100) surface plane and an azimuthal rotation of the diamond in the plane. The polarization sensitive Raman spectra (Fig. 3b) also confirm the improvement in orientation with texturing: with increasing thickness, the response of the diamond film becomes more similar to that of the cloverleaf pattern of the underlying silicon. This occurs because both diamond and silicon have the same crystal structure and thus have the same surface theoretical dependence on rotation. This phenomenon is described by the equation  $I \propto \sin^2(2\theta)$ , where  $I$  is the intensity of the Raman vibration and  $\theta$  is the rotation angle of the sample. These Raman spectra strongly suggest that the diamond is predominantly aligned with respect to the (001) Si planes and [110] directions, i.e., there is no evidence of a  $45^\circ$ -rotation of the diamond atop the silicon in the

(100)-diamond/(100)-Si interface. If this rotation were present, the "cloverleaf" pattern of the diamond response would be rotated from that of the silicon response by 45°.

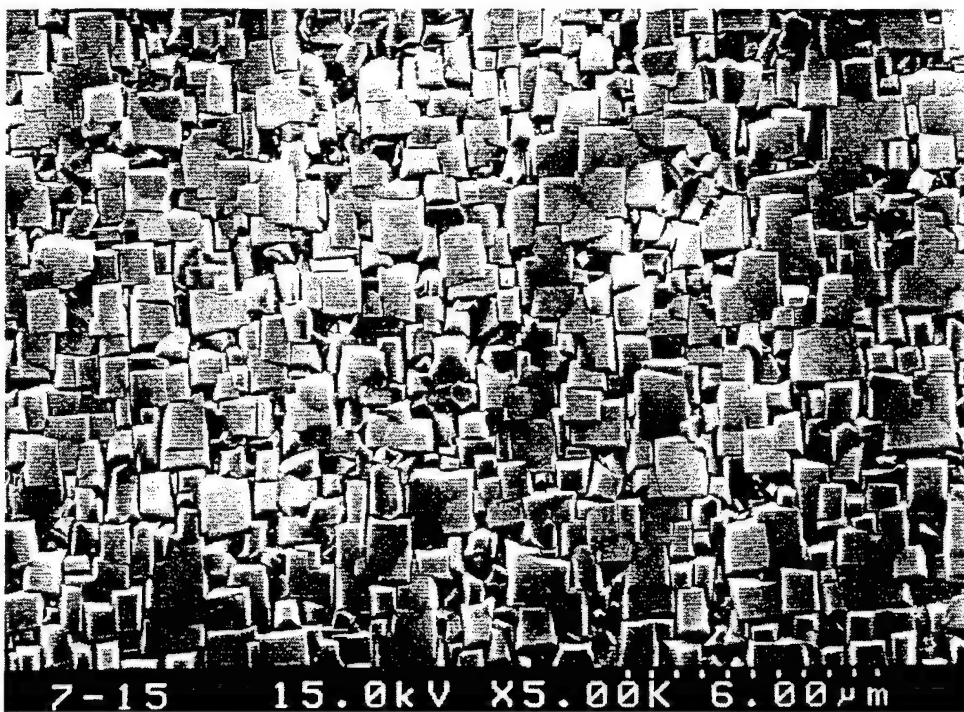


Figure 2. SEM micrograph of a textured diamond film grown on a (100) silicon substrate by the three-step process, which consists of the carburization, the bias-enhanced nucleation and the textured-growth steps.

The intent of the carburization step in the experimental procedure was to form a silicon carbide interlayer, because a HRTEM study has shown evidence for oriented diamond on  $\beta$ -SiC [10]. A cross-sectional HRTEM micrograph taken for a diamond particle grown on a (100) Si surface is presented in Fig. 4, where the parallel linear patterns originate from the atoms of the (111) planes of the diamond and silicon lattice. The HRTEM micrograph shows what appears to be an epitaxial interface in which diamond is oriented on the silicon without a visible silicon carbide interlayer. Also a selected area diffraction pattern of the interface exhibits no spots characteristic of silicon carbide. Thus, the formation of an observable  $\beta$ -SiC interlayer does not appear necessary in growing diamond on the (100) Si surface. (However, other areas of the same sample do show the presence of a silicon carbide interlayer.) As schematically depicted in Fig. 5, the HRTEM micrograph suggests that the ratio of the diamond (111) planes to the silicon (111) planes is close to 3:2, and there occurs an approximately 9° tilt of the (111) diamond planes out of the (100) surface. We note that a 9.5° tilting is needed for the diamond

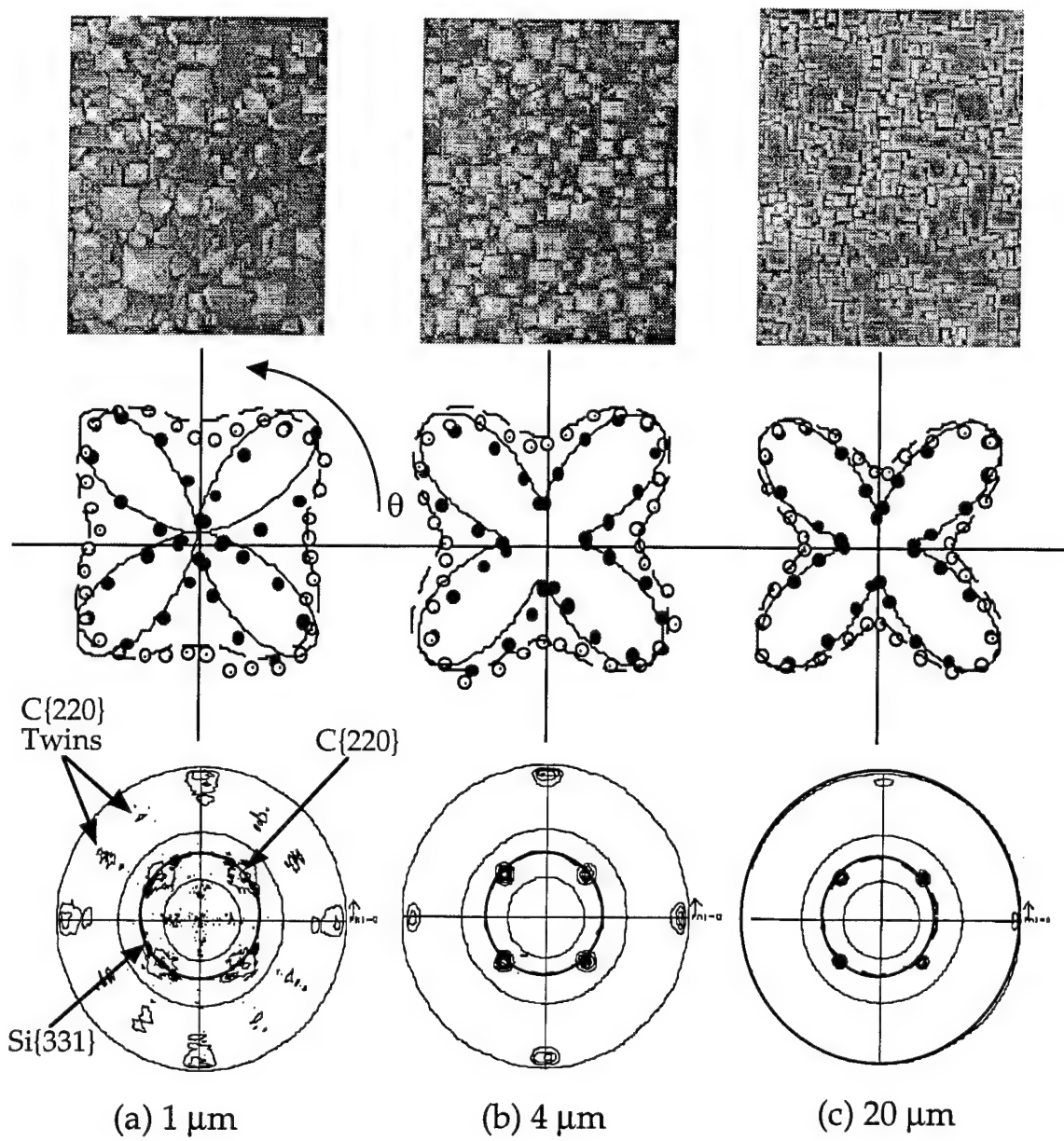


Figure 3. SEM micrographs (top), polar Raman spectra (middle) and polar XRD spectra (bottom) taken for the diamond growth on (100) Si for diamond-film thicknesses of (a) 1  $\mu\text{m}$ , (b) 4  $\mu\text{m}$  and (c) 20  $\mu\text{m}$ . The open and filled circles of the polar Raman spectra refer to the diamond film and the Si substrate, respectively. The {220} spots of the polar XRD spectrum in Figure 3c are asymmetric with a FWHM in the radial and transversal directions of 10° and 8°, respectively. This indicates that the texturing reduces the extent of tilting, but not that of azimuthal misorientation. This observation is consistent with the van der Drift method.

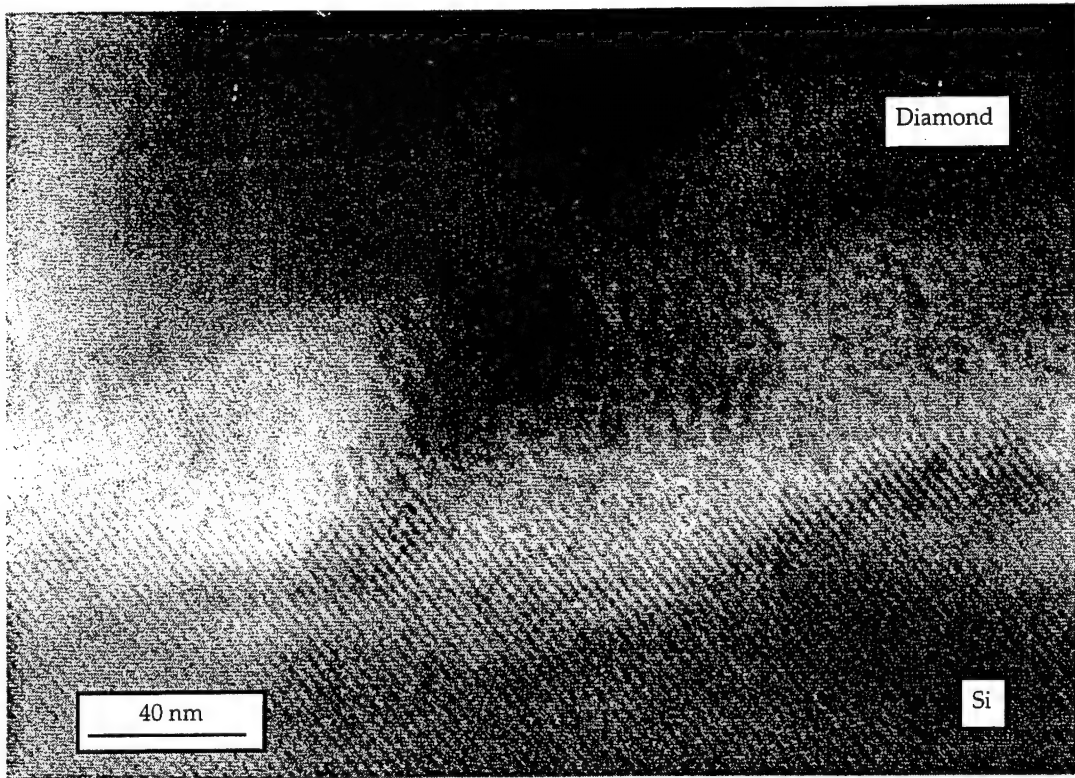


Figure 4. Cross-sectional HRTEM micrograph taken for an oriented diamond/silicon interface.

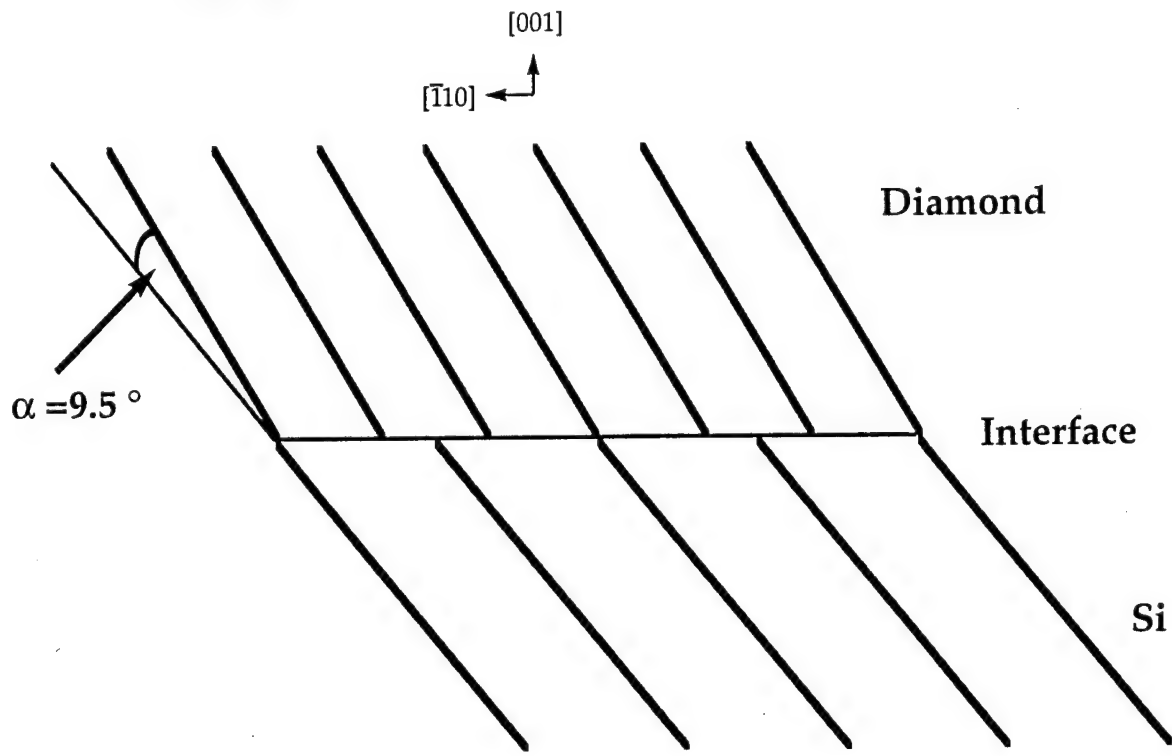


Figure 5. Schematic representation of the cross-sectional HRTEM micrograph predicted for the (100)-diamond/(100)-Si interface under the assumption that the interface adopts the 3:2-match arrangement, and the 1.5 % mismatch results in a tilt of the (111) diamond planes by  $\alpha = 9.5^\circ$ .  $\alpha = \arccos(3a_{\text{diamond}}/2a_{\text{Si}})$ , where  $a_{\text{diamond}}$  and  $a_{\text{Si}}$  are the lattice constants for diamond and Si, respectively.

and silicon lattices to match perfectly with a 3:2 registry of the planes. In addition, the HRTEM micrographs observed in this study do not reveal evidence of a 45°-rotation of the diamond atop the silicon surface in the (100)-diamond/(100)-Si interface. If this rotation were present, the HRTEM micrograph would not show the (111) planes of both diamond and silicon.

*Growth on Ni<sub>3</sub>Si and Ni*. Quantitative XPS and AES analyses of Ni<sub>3</sub>Si samples show that the Ni/Si composition ratio is close to 3, as expected. However, our XRD and optical microscopy measurements show that the Ni<sub>3</sub>Si samples contain more than one phase. An optical micrograph of the Ni<sub>3</sub>Si sample after a grain boundary etch is presented in Fig. 6. The Ni<sub>3</sub>Si sample is polycrystalline with an average grain size of approximately 20 μm in diameter and consists of two phases (labeled as 1 and 2 in Figure 6). Figure 7 compares the observed XRD diffraction pattern of Ni<sub>3</sub>Si (black lines) with the JCPDS (Joint Committee on Powder Diffraction Standards) pattern of cubic Ni<sub>3</sub>Si (gray lines). The observed peaks match well with the JCPDS pattern of cubic Ni<sub>3</sub>Si, except for the two peaks at  $2\Theta = 46.0^\circ$  and  $47.3^\circ$ , which are consistent with the high temperature monoclinic Ni<sub>3</sub>Si phase. This phase can be annealed out of the samples at high temperatures.

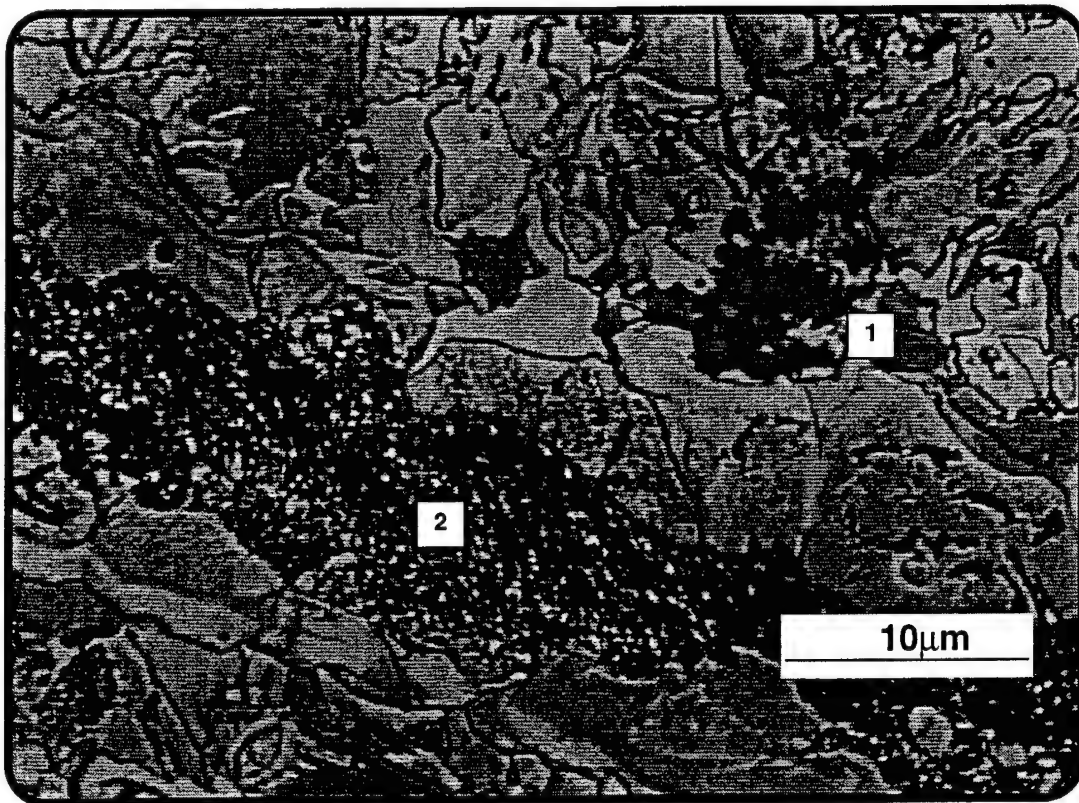


Figure 6. Optical micrograph of a bulk Ni<sub>3</sub>Si sample at 500X. The sample was polished down to 0.01 μm alumina and then subjected to a 10 min grain boundary etching.

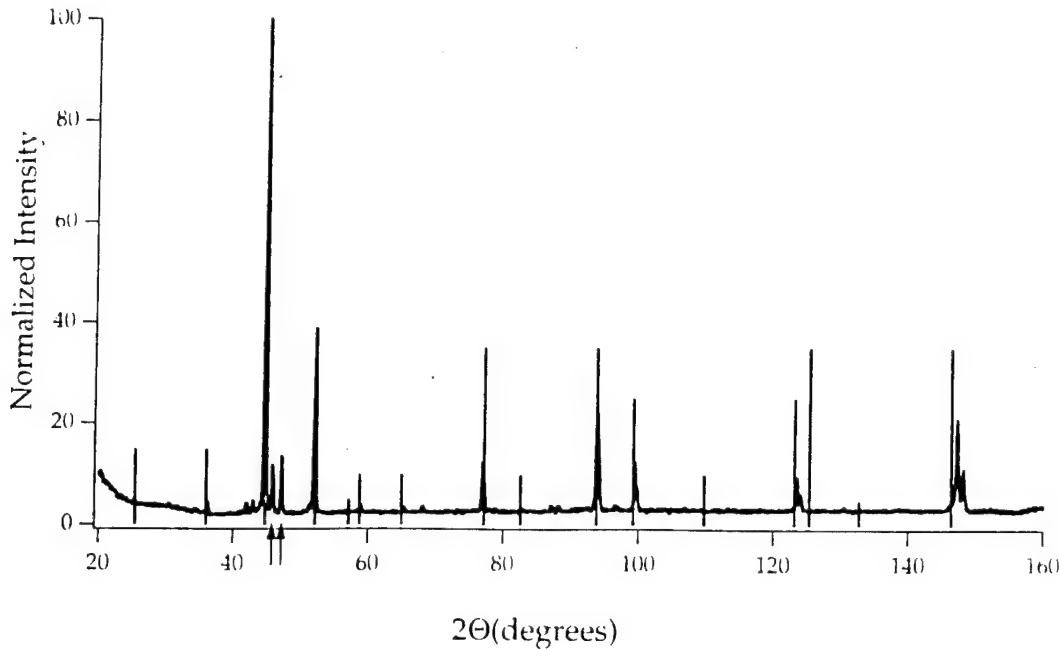


Figure 7. XRD pattern of the  $\text{Ni}_3\text{Si}$  sample in black, which was overlaid with the JCPDS pattern for cubic  $\text{Ni}_3\text{Si}$  in gray. The two peaks indicated by arrows are consistent with the high temperature, monoclinic  $\text{Ni}_3\text{Si}$  phase.

The diamond particles resulting from growth on cubic  $\text{Ni}_3\text{Si}$  are presented in the two SEM micrographs of Fig. 8, which show well-faceted, oriented diamond particles on  $\text{Ni}_3\text{Si}$ , presumably within a single grain. Shown in Fig. 9 are two SEM micrographs of the growth on Ni. The majority of the growth on Ni is graphitic (Fig. 9a), but poorly faceted particles are also found (Fig. 9b). The micro-Raman spectra for the growth on  $\text{Ni}_3\text{Si}$  and Ni are presented in Figs. 10a and 10b, respectively. For the growth on  $\text{Ni}_3\text{Si}$  the spectrum shows a sharp peak centered at  $1332 \text{ cm}^{-1}$  with a FWHM of  $3.6 \text{ cm}^{-1}$ , which signifies high quality diamond. For the growth on Ni, however, the spectrum exhibits a fairly weak/broad peak centered at approximately  $1350 \text{ cm}^{-1}$  and a large/broad peak at  $1580 \text{ cm}^{-1}$ . These findings show that the growth on Ni is a mixture of amorphous carbon and graphite [42], while well-faceted and possibly oriented diamond particles could be attained on  $\text{Ni}_3\text{Si}$ .

#### D. Estimation of Interface Interactions

*Growth on Si.* In general, the existence of a large lattice mismatch between a substrate and overgrowth prevents epitaxy, so it is surprising that oriented (100) diamond particles are grown on (100) silicon despite the large mismatch between diamond and silicon (34 %). The present TEM, PSR and polar XRD studies show that the  $45^\circ$ -rotation is absent in the (100)-diamond/(100)-Si interface. We now examine the interface interactions associated with the  $45^\circ$ -rotation and 3:2-match arrangements by performing EHTB electronic band structure calculations on suitable model systems. Verwoerd's calculations [27,28] showed that

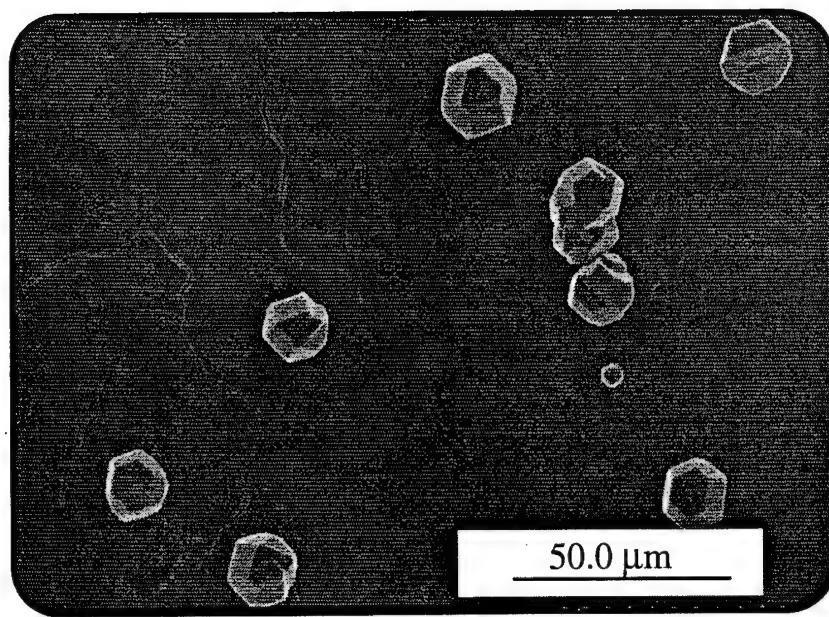
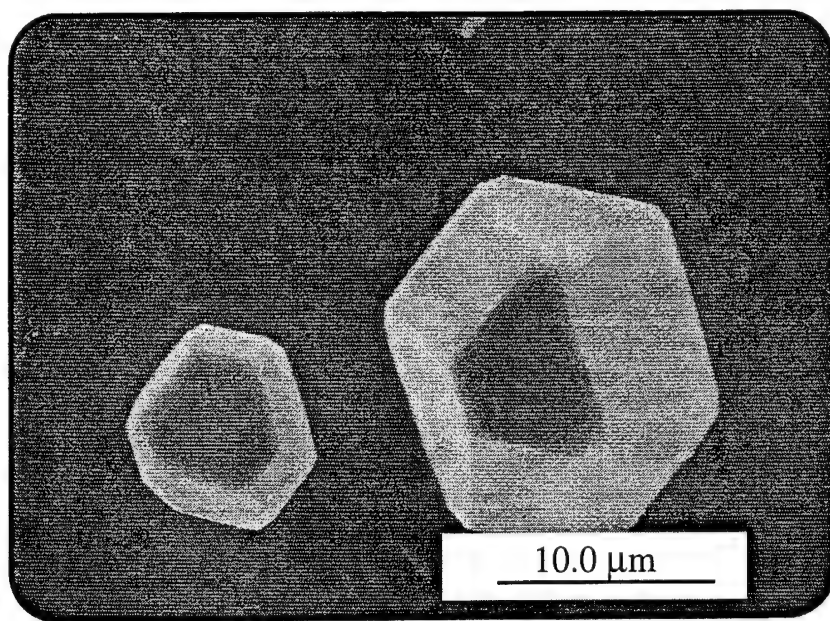
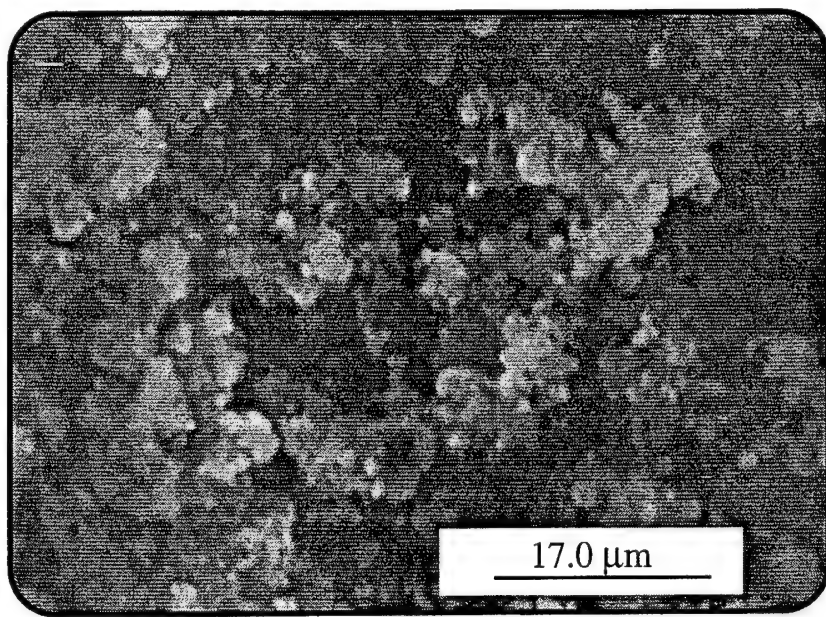
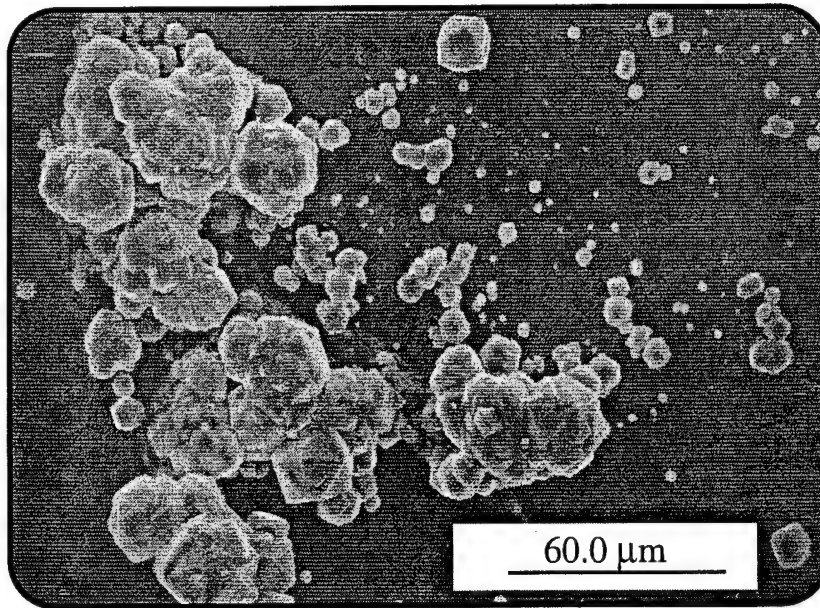


Figure 8. SEM micrographs of diamond particles deposited on Ni<sub>3</sub>Si after 16 hours growth under conditions of 1 % CH<sub>4</sub>/H<sub>2</sub> and substrate temperature of 850°C. Parallel lines on the micrographs mark particles that seem to be oriented.

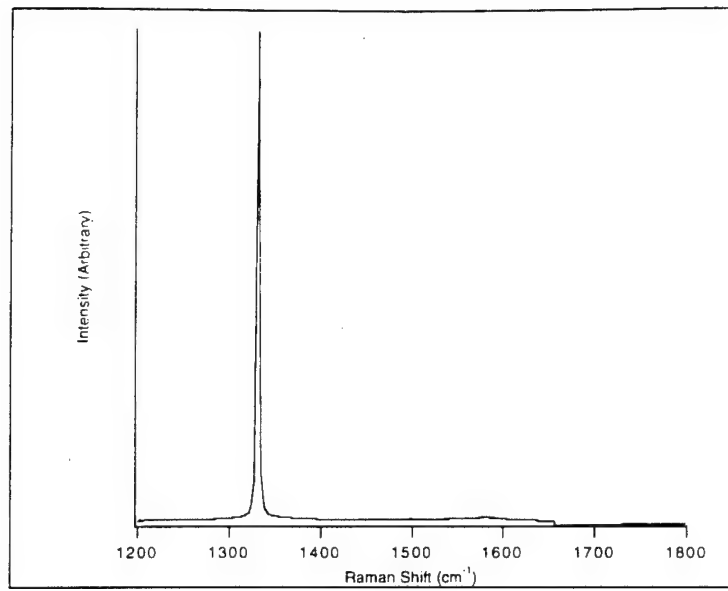


a

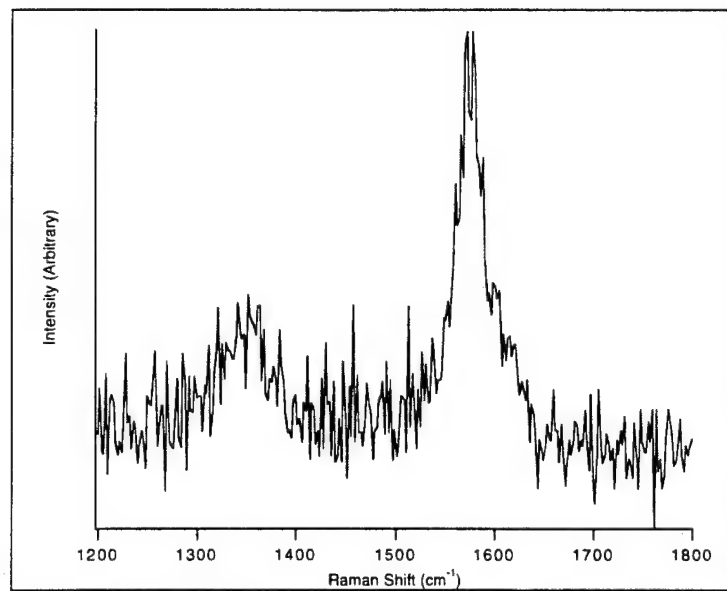


b

Figure 9. SEM micrographs of growths on Ni under the same conditions as used for the diamond growth on  $\text{Ni}_3\text{Si}$ . The majority of the substrate is covered by graphite in (a), and some of the substrate has poorly faceted diamond deposits in (b).



a



b

Figure 10. Micro-Raman spectra of (a) a diamond particle grown on  $\text{Ni}_3\text{Si}$  and (b) a graphite growth on Ni. The sharp peak at  $1332 \text{ cm}^{-1}$  (FWHM of  $3.6 \text{ cm}^{-1}$ ) of Fig. 11a signifies high quality diamond. The broad peaks at  $1350$  and  $1580 \text{ cm}^{-1}$  of Fig. 11b suggest that the growth is a mixture of graphite and amorphous carbon.

strain energy is a crucial part of the energetics in determining the interface interaction energies. To carry out realistic calculations of interface interaction energies, the positions of the surface and subsurface atoms are completely relaxed. Since the extended Hückel method is inadequate for bond length optimization, we ignore the elastic deformation in the heteroepitaxial layers in our EHTB calculations for the interface interaction energies associated with the 45°-rotation and 3:2-match arrangements.

The interface interactions are simulated by placing C<sub>7</sub> diamond clusters (Fig. 11) on a 3-layer silicon slab (Fig. 12). Except for two dangling bonds for each of the four carbon atoms at the bottom surface of the C<sub>7</sub> cluster, all dangling bonds of the C<sub>7</sub> cluster were capped with

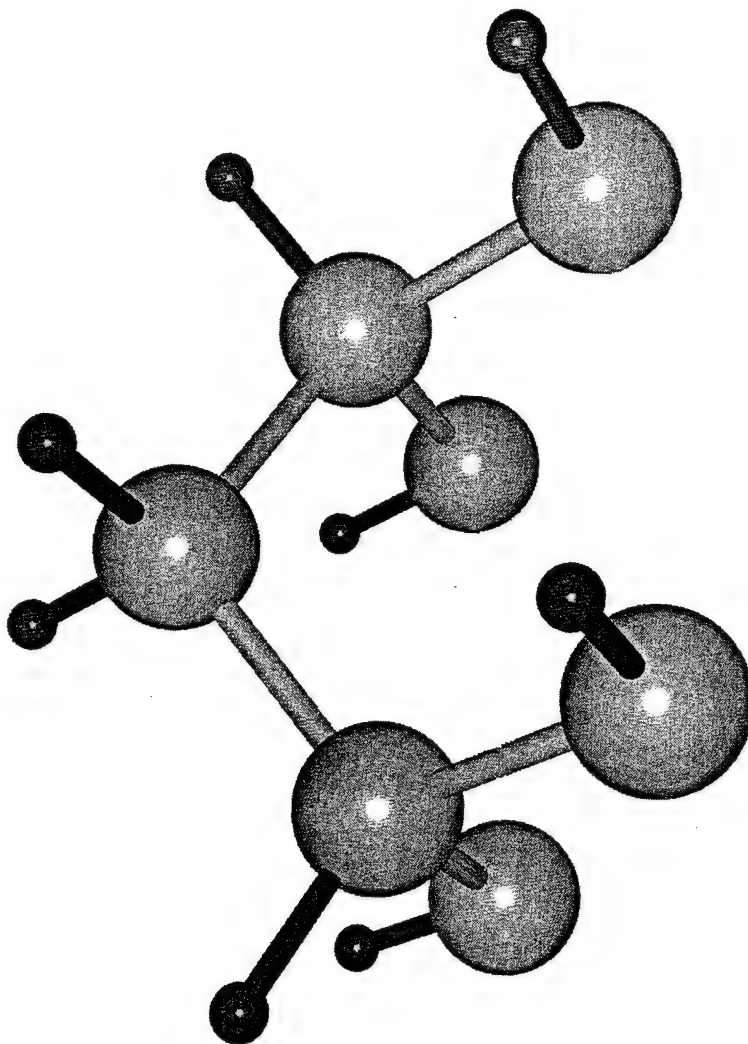
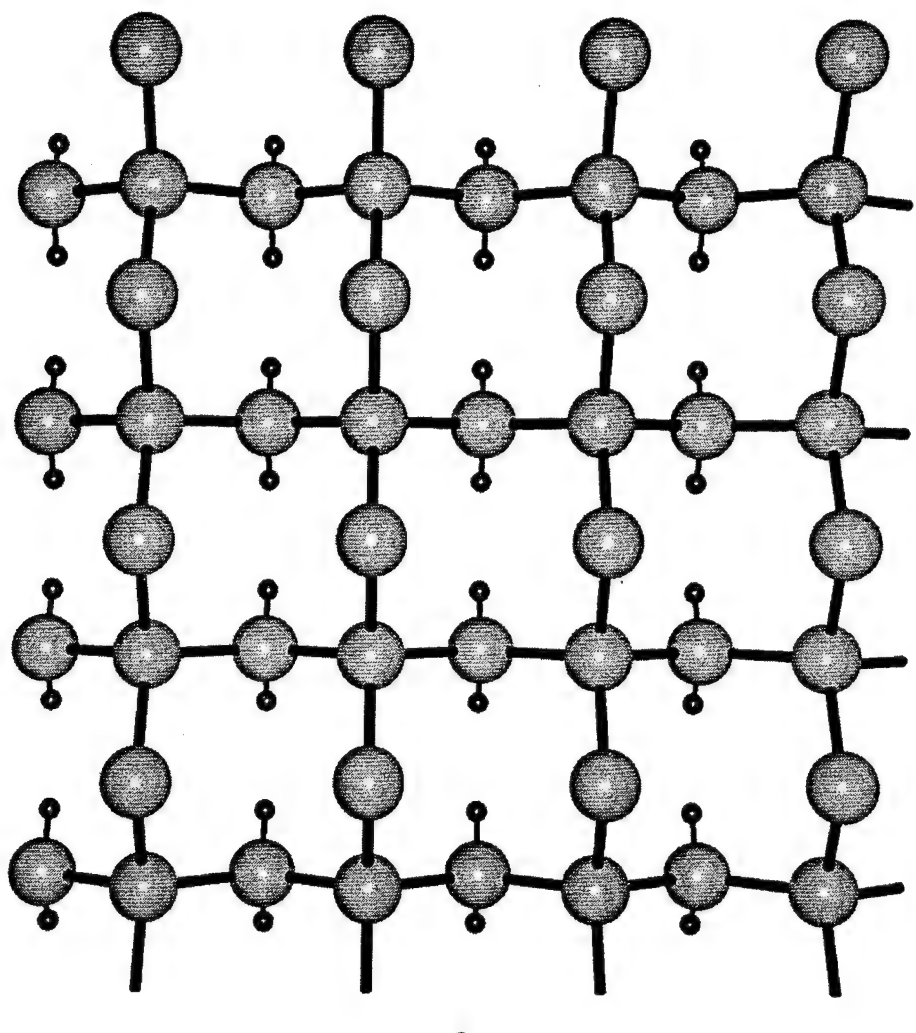
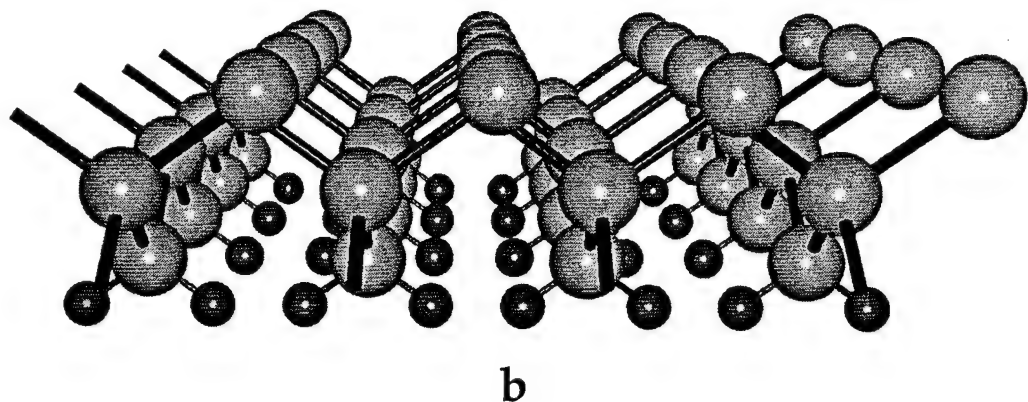


Figure 11. Perspective view of the C<sub>7</sub> diamond cluster employed for the study of the (100)-diamond/(100)-Si interface interaction.



a



b

Figure 12. Schematic representation of the 3-layer Si slab employed for the study of the (100)-diamond/(100)-Si interface interaction: (a) top view and (b) side view. The Si atoms of the bottom surface are capped with hydrogen atoms.

hydrogen atoms as in Fig. 12. For the 3-layer silicon slab, the bottom surface Si atoms are capped with hydrogen atoms [43], and the dangling bonds of the top surface Si atoms are exposed to engage in interface interactions.

To examine the preferred orientation of the C<sub>7</sub> diamond cluster with respect to the 3-layer silicon slab, we consider three arrangements: parallel, 45°-rotation and perpendicular. The (100) planes containing the two dangling bonds of the Si atoms make 0°, 45° and 90° with respect to those of the carbon atoms in the parallel, 45°-rotation and perpendicular arrangements, respectively. The parallel and perpendicular arrangements correspond to the 3:2-match structure. To determine the relative stabilities and the optimum structures of the three arrangements, we construct an overlayer of the C<sub>7</sub> diamond clusters on the 3-layer silicon slab with the repeat unit cell leading to a (4×4) surface unit cell. The latter is large enough to ensure negligible interactions between adjacent C<sub>7</sub> diamond clusters in the overlayer. On the basis of EHTB electronic band structure calculations, we then calculate the energies of the overlayer/Si-slab system for the parallel, 45°-rotation and perpendicular arrangements as a function of the interface separation and the position of the C<sub>7</sub> diamond cluster within the unit cell. In our calculations, the geometries of the interacting fragments (i.e., the C<sub>7</sub> diamond clusters and the 3-layer Si slab) were kept frozen [43].

For the parallel arrangement, Figure 13a shows mesh points of geometries used to find the optimum position of the C<sub>7</sub> diamond cluster (at an interface separation of 2 Å), Figure 13b the energy contour diagram associated with these mesh point calculations, and Figure 14a the optimum position determined from this search. Figures 14b and 14c show the optimum positions of the C<sub>7</sub> diamond cluster found for the 45°-rotation and perpendicular arrangements in a similar manner. Our calculations as a function of the interface separation show that the interface interaction has a very shallow minimum at an interface separation of around 2.3 Å for the parallel and perpendicular arrangements, but it is repulsive for the 45°-rotation arrangement. The parallel and perpendicular arrangements are similar in stability, and the small stability difference between the two (about 5 kcal/mol in favor of the perpendicular arrangement) is insignificant. However, the parallel and perpendicular arrangements are much more stable than the 45°-rotation arrangement (by about 50 kcal/mol). These results are consistent with the conclusions from our HRTEM, polar Raman and polar XRD studies.

It is of interest to analyze the essence of the interface interactions associated with the parallel, 45°-rotation, and perpendicular arrangements. From the viewpoint of the tetrahedral bonding of a carbon atom in bulk diamond and a silicon atom in bulk silicon, the (100) surface atoms of diamond and Si are considered to possess two sp<sup>3</sup> hybrid orbitals. In the molecular orbital picture these hybrid orbitals are linearly combined to form the n<sub>z</sub> and p<sub>π</sub> orbitals [44] (Fig. 15). The axes of the p<sub>π</sub> orbitals are contained in the (100) surface, and those of the n<sub>z</sub>

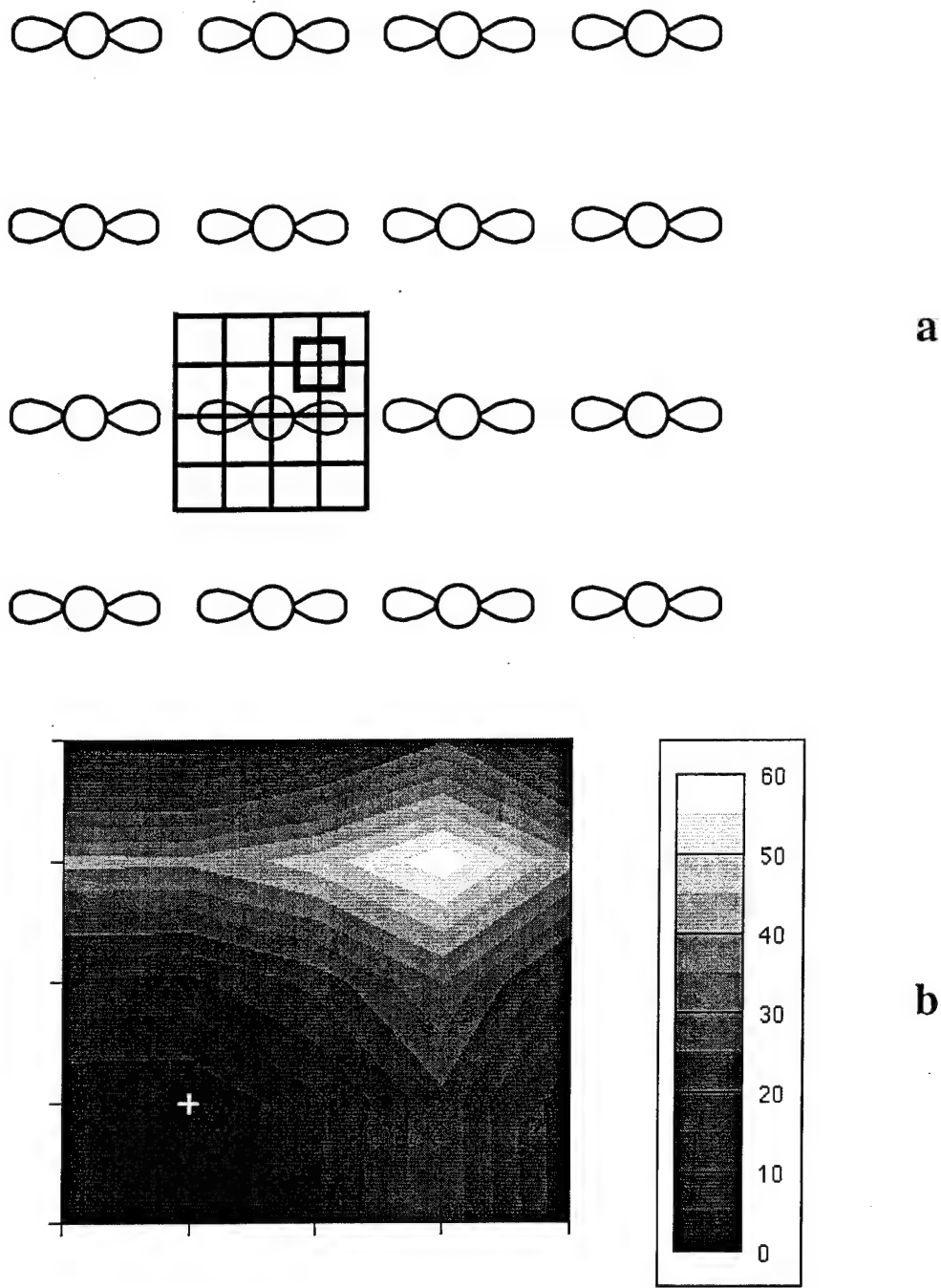
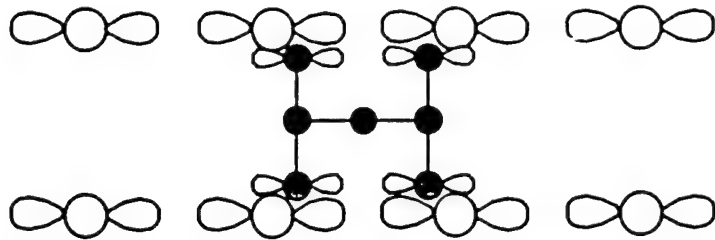
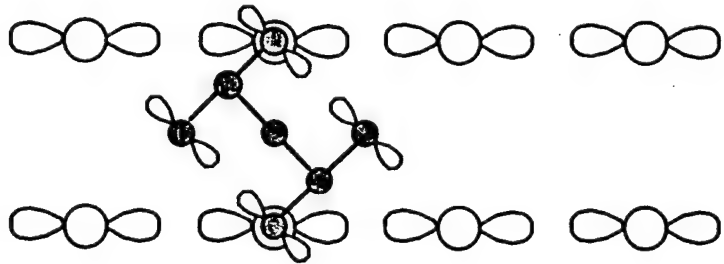


Figure 13. (a) Mesh points of the positions considered for the C<sub>7</sub> cluster above the (4×4) surface unit cell of the 3-layer Si slab in determining the optimum position of the C<sub>7</sub> cluster for the parallel arrangement. The circles represent the Si atoms, and the orbital lobes the dangling bonds. The small square inlaid at the upper right corner defines the fine-mesh points used for a more accurate geometry search. (b) Energy contour diagram associated with the fine-mesh points for the parallel arrangement, where the lowest energy point is indicated by a cross, and the values of the energy contours are given with respect to the minimum energy point.



a



b

Figure 14. Optimum positions of the C<sub>7</sub> cluster calculated for the (a) parallel, (b) 45°-rotation and (c) perpendicular arrangements. The large open and small filled circles represent the Si and C atoms, respectively, and the orbital lobes represent the dangling bonds.

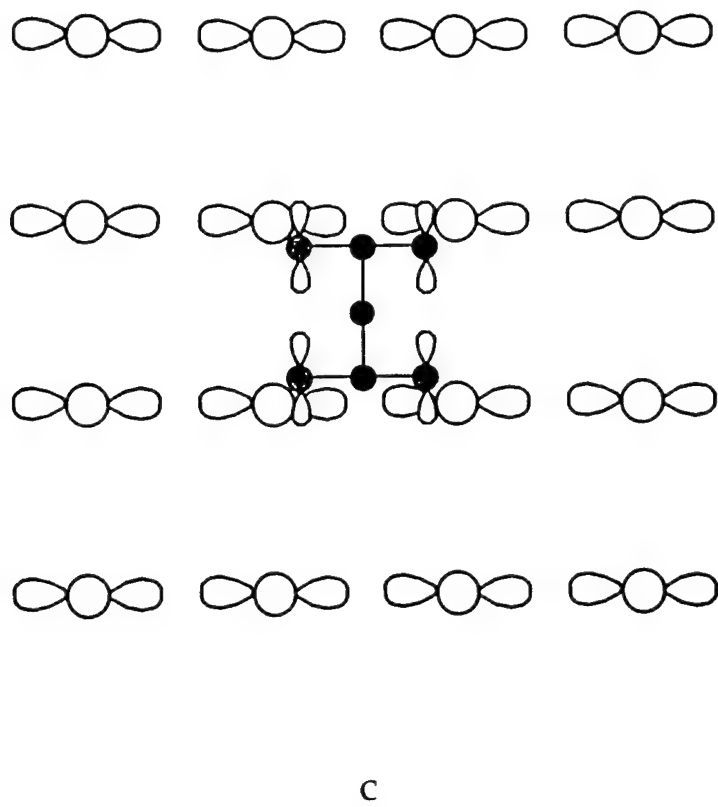


Figure 14. Con't.

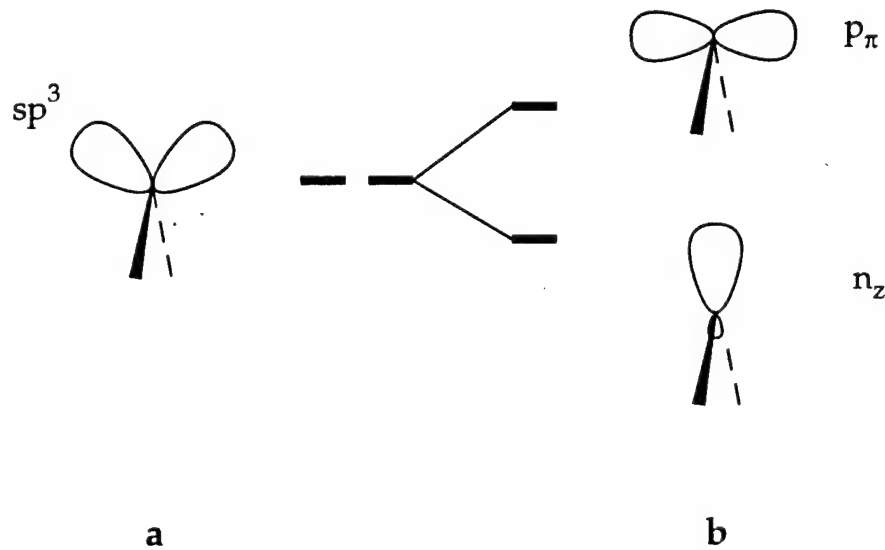


Figure 15. Dangling orbitals of an atom on the (100) surface of the diamond and Si lattices in the bond orbital and molecular orbital representations in (a) and (b), respectively. The  $p_{\pi}$  and  $n_z$  of the molecular orbital picture are given by the out-of-phase and in-phase combinations of the two  $sp^3$  hybrid orbitals of the bond orbital picture.

orbitals are normal to the surface. The main contributions of the  $n_z$  orbital are the  $p_z$  and s orbitals. [Here, we follow the convention that the z-axis is perpendicular to the (100) surface.] Figure 16a presents the projected density of states (PDOS) for the  $p_z$  and  $p_{\pi}$  orbitals of the four surface carbon atoms of the C<sub>7</sub> diamond cluster. What happens to these PDOS when the diamond cluster interacts with the 3-layer silicon slab is also shown in Fig. 16b for the parallel arrangement: the most significant change the interface interactions bring about lies in the PDOS peak of the  $p_z$  orbitals (around -11.5 eV), which becomes “split” into the lower and higher peaks (around -15.5 eV and -2.5 eV). The split results because the surface atom  $p_z$  orbitals of the diamond cluster establish bonding and antibonding interactions with the surface atom orbitals of the Si substrate. A similar analysis for the perpendicular arrangement reveals the

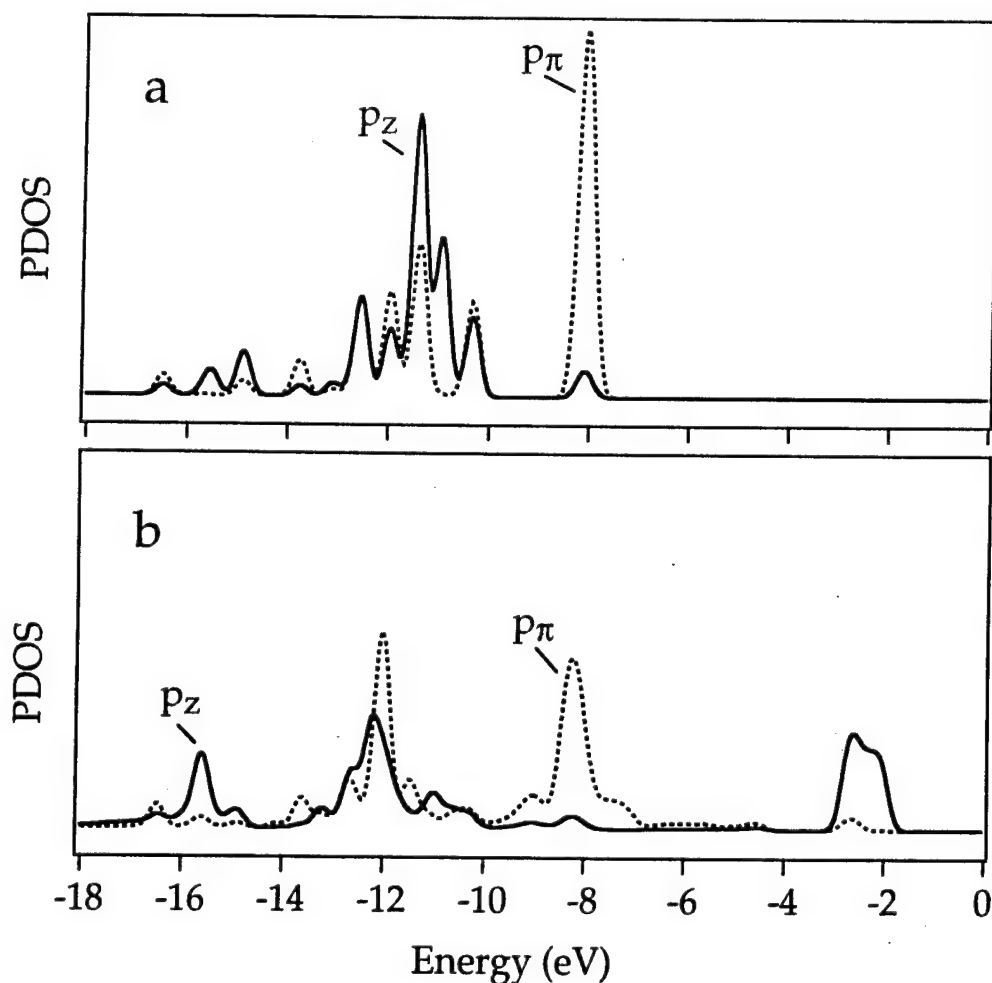


Figure 16. PDOS plots of the  $p_{\pi}$  (dotted) and  $p_z$  (solid) orbitals calculated for the four bottom surface carbon atoms of the C<sub>7</sub> cluster in the parallel arrangement: (a) before and (b) after interface interaction. The PDOS scales are the same in the two figures but are given in arbitrary units.

same trends. These results indicate that the  $n_z$  orbitals, being perpendicular to the surface, provide good overlap with the surface Si orbitals, so the carbon atom prefers to sit atop the silicon atom. The C<sub>7</sub> diamond cluster used in our model study has four carbon atoms to engage in the interface interactions. The 3:2-match arrangement (i.e., parallel or perpendicular one) can have more carbon atoms atop the silicon atoms than the 45°-rotation arrangement can (4 versus 2). Thus, the 3:2-match arrangement is energetically more favorable than the 45°-rotation arrangement. Use of a larger diamond cluster for our calculations of the interface interactions is unlikely to alter this conclusion, since the 45°-rotation arrangement has a much larger lattice mismatch than the 3:2-match arrangement (7 versus 1.5 %).

Our calculations do not include the elastic deformation of the heteroepitaxial layer, but the results are in qualitative agreement with experiment. It is interesting to note from Verwoerd's study [27,28] that the 3:2-match arrangement becomes energetically favored over the 45°-rotated arrangement when the diamond overlayer is greater than 3 atomic layers. (Since the experimental measurements deal with micrometer layer thicknesses, i.e., thousands of atomic layers, Verwoerd's conclusion is in agreement with experiment.) This implies that as the thickness of the diamond layer increases, the relaxation of the carbon atoms at the interface becomes weaker, probably because the C-C bond is stronger than the C-Si bond.

*Growth on Ni<sub>3</sub>Si and Ni.* The diamond growth on Ni<sub>3</sub>Si is remarkable in that very little graphite is observed. Under similar conditions, the growth on Ni substrates is largely graphitic. To gain insight into these differences, we examine the tendency of the Ni<sub>3</sub>Si and Ni substrates for diamond versus graphite nucleation on the basis of EHTB electronic band calculations. As structural models for the study of their (111) and (100) surfaces, we employ 3- and 4-layers thick substrate slabs, respectively. The (111) surface is especially interesting because both diamond and graphite can be epitaxially matched on this surface. To simulate the beginning stage of diamond and graphite nucleation, we place on these slabs one, two or three C<sub>2</sub> units (i.e., C<sub>2</sub>, C<sub>4</sub> or C<sub>6</sub> unit) in orientations that imitate the diamond and graphite structures. Figures 17a and 17b schematically show the (111) and (100) surface atoms in Ni and Ni<sub>3</sub>Si, respectively, where (1×2) unit cells are drawn in. We used a (1×2) surface unit cell to place one or two C<sub>2</sub> units, and a (1×3) surface unit cell to place three C<sub>2</sub> units. As depicted in Figs. 18a-18c, where the filled circles represent the atom, hollow, or bridge positions of the surface, the C<sub>2</sub> units of a unit cell were placed above the surface at a distance  $r$  from the "anchor" carbon of each C<sub>2</sub> (i.e., the one indicated by the dashed line). The anchor carbon atoms were lined up along the x-axis, so that the C<sub>2</sub> units form a carbon-carbon zigzag chain if a unit cell has more than one C<sub>2</sub> unit (e.g., C<sub>4</sub> and C<sub>6</sub> zigzag chains).

For the simulation of diamond nucleation, we fixed the C-C bond length of C<sub>2</sub> to 1.54 Å, and made the C-C bond non-parallel to the substrate surface. The angle  $\alpha$  of Figure 18a was

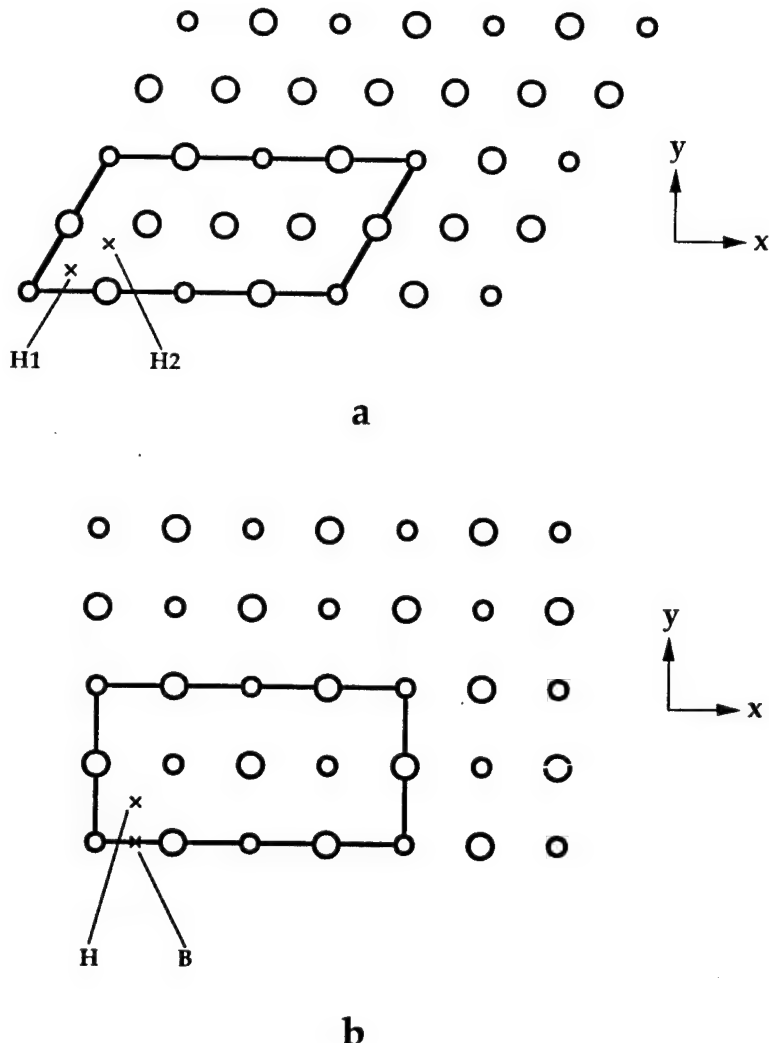
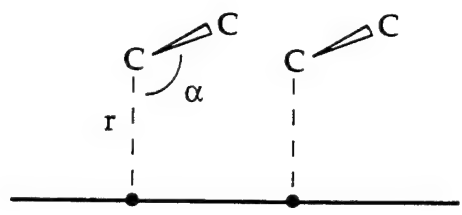
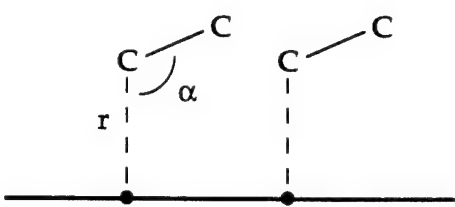


Figure 17. Schematic representation of the atom arrangements on the (111) and (100) surfaces of  $\text{Ni}_3\text{Si}$ : (a) (111) surface and (b) (100) surface. The small and large circles represent the Si and Ni atoms, respectively. These representations are also valid for Ni, for which all the surface atoms are equivalent. For convenience, (1x2) surface unit cells are indicated. The labels H, H1 and H2 refer to hollow sites, and the label B a bridge site.

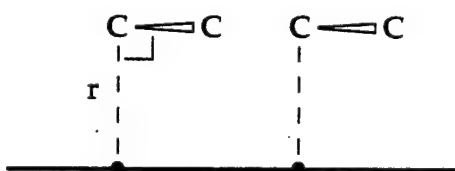
fixed at  $109.47^\circ$  and  $126^\circ$  for the (111) and (100) surfaces, respectively. With respect to the coordinate x-axis (Fig. 17a), the perpendicular plane containing a  $\text{C}_2$  unit was rotated by  $30^\circ$  for the (111) surface (Fig. 18a) and by  $0^\circ$  for the (100) surface (Fig. 18b). For the simulation of graphite nucleation, we fixed the C-C bond length of  $\text{C}_2$  to  $1.415 \text{ \AA}$ , and made the C-C bond parallel to the substrate surface (Fig. 18c). With respect to the coordinate x-axis of Fig. 17b, the perpendicular plane containing a  $\text{C}_2$  unit was rotated by  $30^\circ$  for the (111) and (100) surfaces.



a



b



c

Figure 18. Arrangements of  $C_2$  units on the (111) and (100) surfaces of  $Ni_3Si$  and Ni to simulate (a) diamond nucleation on the (111) surface, (b) diamond nucleation on the (100) surface, and (c) graphite nucleation on the (111) and (100) surfaces. A dashed line is shown from one carbon atom (i.e., "anchor" carbon) of each  $C_2$  to the surface. For simplicity, only two  $C_2$  units (to form a  $C_4$  zigzag chain) are shown. The filled circles on the horizontal line represent the atom, hollow, or bridge positions of the surface.

Results of our EHTB calculations for the  $C_n$ -overlayer/substrate ( $n = 2, 4, 6$ ) systems [34] are summarized in Table II. Both the (111) and (100) surfaces of  $Ni_3Si$  show a strong preference for diamond-nucleation over graphite-nucleation at all positions of the anchor carbon atoms. On the surfaces of Ni, diamond- and graphite-nucleations are equally probable or graphite nucleation is slightly favored, except for the atop positions of the (100) surface where diamond nucleation is slightly favored. These computational results are in general consistent with the experimental findings that the growth on Ni gives rise to a mixture of amorphous carbon and graphite, while that on  $Ni_3Si$  results in diamond particles.

---

Table I. Energy of the diamond-nucleation arrangement with respect to the graphite-nucleation arrangement on the (111) and (100) surfaces of  $Ni_3Si$  and Ni as calculated for the  $C_n$ -overlayer/substrate ( $n = 2, 4, 6$ ) systems (in kcal/mol per  $C_2$  unit).<sup>a,b</sup>

Overlayer	(111) surface		(100) surface		
	Atop	Hollow <sup>c</sup>	Atop	Hollow	Bridge
$C_2$ on $Ni_3Si$	-18 <sup>d</sup> (-13 <sup>e</sup> )	-18(-8.5)	-50 <sup>d</sup> (-38 <sup>e</sup> )	-38	-28
$C_4$ on $Ni_3Si$	-21	-11	-55	-27	-27
$C_6$ on $Ni_3Si$	-23	-13	-62	-25	-34
$C_2$ on Ni	1.8	4.7(4.7)	-6.1	23	6.9
$C_4$ on Ni	0.1	9.3	-21	28	5.8
$C_6$ on Ni	0.3	5.5	-21	26	4.2

---

<sup>a</sup> The negative numbers mean that diamond-nucleation is preferred over graphite-nucleation.

<sup>b</sup> The distance  $r$  from the anchor carbon atoms to the surface is chosen such that the bond lengths between the anchor carbon and the surface atoms are 2.0 Å. Thus,  $r = 2.0$  Å for the atop position of the (111) and (100) surfaces, 1.4 Å for the hollow position of the (111) surface, 0.95 Å for the hollow position of the (100) surface, and 1.6 Å for the bridge position of the (100) surface.

<sup>c</sup> The numbers in parentheses refer to the hollow sites H2, and all other numbers to the hollow sites H1.

<sup>d</sup> Atop Si. <sup>e</sup> Atop Ni.

## E. Concluding Remarks

Oriented diamond particles are deposited on (100) silicon and can be textured to provide nearly 100 % alignment with the substrate, although there exists a significant lattice mismatch (34 %). According to our polar Raman, polar XRD and cross-sectional HRTEM studies of the diamond grown on (100) Si surface, the (100)-diamond/(100)-Si interface does not have the 45°-rotation arrangement but the 3:2-match arrangement. In agreement with this finding, our EHTB electronic band structure calculations for a model system show that the interface interaction favors the 3:2-match arrangement (either the parallel or the perpendicular one) over

the 45°-rotation arrangement. In his semi-empirical SCF-MO study Verwoerd reached the same conclusion when the diamond overlayer of his model calculations was made thick enough [27,28].

As a new heteroepitaxial substrate for diamond, we examined diamond growth on Ni<sub>3</sub>Si, because it has a small lattice mismatch and contains silicon to form bonds with carbon. Our experiments with polycrystalline Ni<sub>3</sub>Si show the growth of oriented diamond particles and the lack of graphite formation. In contrast, under the same growth conditions as used for diamond growth on Ni<sub>3</sub>Si, largely graphite was formed on the nickel substrate. Our EHTB calculations for model systems show that both the (111) and (100) surfaces of Ni<sub>3</sub>Si have a strong preference of diamond-nucleation over graphite-nucleation, but this is not the case for the (111) and (100) surfaces of Ni. These computational results are consistent with the experimental findings.

#### F. Acknowledgments

This work was partially supported through the Ballistic Missile Defense Organization/Innovative Science and Technology and the University Research Initiative through the Office of Naval Research. The measurements of Raman spectra by A. Somashekhar are greatly appreciated. Also, we thank Dr. C. T. Liu for the silicide fabrication and Dr. R. C. Glass for polar XRD measurements. M.-H. W. thanks the financial support from the Office of Basic Energy Sciences, Division of Materials Sciences, U. S. Department of Energy, under Grant DE-FG05-86ER45259.

#### G. References

1. S. Koizumi, T. Murakami, T. Inuzuka, and K. Suzuki, *Appl. Phys. Lett.*, **57** (1990) 563.
2. H. Maeda, S. Masuda, K. Kusakabe, and S. Morooka, *Diamond and Related Materials*, **3** (1994) 398.
3. (a) M. Yoshikawa, H. Ishida, A. Ishitani, T. Murakami, S. Koizumi, and T. Inuzuka, *Appl. Phys. Lett.*, **57** (1990) 428.  
(b) M. Yoshikawa, H. Ishida, A. Ishitana, S. Koizumi, and T. Inuzuka, *Appl. Phys. Lett.*, **58** (1991) 1387.
4. A. Argoitia, J. C. Angus, J. S. Ma, L. Wang, P. Pirouz, W. R. L. Lambrecht, *J. Mater. Res.*, **9** (1994) 1849.
5. B. R. Stoner, S. Sahaida, J. P. Bade, P. Southworth, and P.J. Ellis, *J. Mater. Res.*, **8** (1993) 1334.
6. S. D. Wolter, B. R. Stoner, J. T. Glass, P. J. Ellis, D. S. Buhaenko, C. E. Jenkins, and P. Southworth, *Appl. Phys. Lett.*, **62** (1993) 1215.
7. X. Jiang, C.-P. Klages, R. Zachai, M. Hartweg, and H.-J. Füsser, *Appl. Phys. Lett.*, **63** (1993) 3438.
8. B. R. Stoner and J. T. Glass, *Appl. Phys. Lett.*, **60** (1992) 698.
9. B. R. Stoner, G. H. Ma, S. D. Wolter, W. Zhu, Y.-C. Wang, R. F. Davis, and J. T. Glass, *Diamond and Related Materials*, **2** (1993) 142.
10. W. Zhu, X. H. Wang, B. R. Stoner, G. H. M. Ma, H. S. Kong, M. W. H. Braun, and J. T. Glass, *Phys. Rev. B*, **47** (1993) 6529.

11. Y. Sato, H. Fujita, T. Ando, T. Tanaka, and M. Kamo, Phil. Trans. R. Soc. Lond. A, **342** (1993) 225.
12. P. C. Yang, W. Zhu, and J. T. Glass, J. Mater. Res., **8** (1993) 1773.
13. P. C. Yang, W. Zhu, and J. T. Glass, in Proc. Third International Symposium on Diamond Materials, Honolulu, Eds., J.P. Dismukes, K.V. Ravi, K.E. Spear, B. Lux, and N. Setaka (The Electrochemical Society, 1993) p. 435.
14. P. C. Yang, W. Zhu, and J. T. Glass, J. Mater. Res., **9** (1994) 1063.
15. W. Zhu, P. C. Yang, and J. T. Glass, Appl. Phys. Lett., **63** (1993) 1640.
16. W. Liu, D. A. Tucker, P. C. Yang, and J. T. Glass, to be published.
17. A. Argoitia, J. C. Angus, L. Wang, X. I. Ning, and P. Pirouz, J. Appl. Phys., **73** (1993) 4305.
18. (a) J. C. Angus, Z. Li, M. Sunkara, C. Lee, W. R. L. Lambrecht, and B. Segall, in Proc. The Third International Symposium on Diamond Materials, Honolulu, Eds., J. P. Dismukes, K.V. Ravi, K.E. Spear, B. Lux, and N. Setaka (The Electrochemical Society, 1993) p. 128.  
 (b) W.R.L. Lambrecht, C. H. Lee, B. Segall, J.C. Angus, Z. Li, and M. Sunkara, Nature, **364** (1993) 607.
19. K. Larsson, J.-O. Carlsson, and S. Lunell, Journal of Physical Chemistry, **98** (1994) 5019.
20. B. R. Stoner, B. E. Williams, S.D. Wolter, K. Nishimura, and J.T. Glass, J. Mater. Res., **7** (1992) 257.
21. B. R. Stoner, G.-H.M. Ma, S. D. Wolter, and J. T. Glass, Phys. Rev. B, **45** (1992) 11067.
22. A. van der Drift, Philips Res. Rep., **22** (1967) 267.
23. D. N. Belton and S. J. Schmieg, J. Appl. Phys., **66** (1989) 4223.
24. D. N. Belton and S. J. Schmieg, J. Vac. Sci. Technol. A, **8** (1990) 2353.
25. W. S. Verwoerd and K. Weimer, Surf. Coat. Technol., **47** (1991) 578.
26. W. S. Verwoerd, Diamond and Related Materials, **1** (1992) 195.
27. W. S. Verwoerd, Surface Sci., **304** (1994) 24.
28. W. S. Verwoerd, Diamond and Related Materials, **3** (1994) 457.
29. S. C. Erwin, M. R. Pederson, and W. E. Pickett, Phys. Rev. B, **41** (1990) 10437.
30. S. C. Erwin and W. E. Pickett, in Proc. Atomic scale calculations of structure in materials, San Francisco, Eds., M.A. Schluter and M.S. Daw (Materials Research Society, 1990) p. 59.
31. S. C. Erwin and W.E. Pickett, Surf. Coat. Technol., **47** (1991) 487.
32. W. E. Pickett and S. C. Erwin, Superlattices and Microstructures, **7** (1990) 335.
33. W. E. Pickett and S. C. Erwin, in Proc. Diamond, Silicon Carbide and Related Wide-Bandgap Semiconductors, Boston, Eds., J. T. Glass, R. F. Messier, and N. Fujimori (Materials Research Society, 1990) p. 35.
34. W. E. Pickett and S. C. Erwin, Phys. Rev. B, **41** (1990) 9756.
35. W. E. Pickett, M. R. Pederson, K. A. Jackson, and S. C. Erwin, in Proc. Wide Band Gap Semiconductors Symposium, Boston, Eds., T.D. Moustakas, J. I. Pankove, and Y. Hamakawa (Materials Research Society, 1992) p. 3.
36. M.-H. Whangbo and R. Hoffman, Journal of the American Chemical Society, **100** (1978) 6093.
37. R. Kohl, C. Wild, N. Herres, P. Koidl, B. R. Stoner, and J. T. Glass, Appl. Phys. Lett., **63** (1993) 1792.
38. C. Wild, N. Herres, and P. Koidl, J. App. Phys., **68** (1990) 973.
39. C. Wild, P. Koidl, N. Herres, W. Müller-Sebert, and T. Eckermann, in Proc. Diamond Materials, Pennington, Eds., A. J. Purdes, B. S. Meyerson, J.C. Angus, K. E. Spear, R. F. Davis, and M. Yoder (The Electrochemical Society, 1991) p. 224.
40. X. Jiang, R. Six, C.-P. Klages, R. Zachai, M. Hartweg, and H.-J. Füsser, in Proc. Third International Conference on the New Diamond Science and Technology, Heidelberg, Eds., P.K. Bachmann, A.T. Collins, and M. Seal (Elsevier, 1993) p. 407.
41. W. Hayes and R. Loudon, Scattering of Light by Crystals (Wiley, 1978).

42. D. S. Knight and W. B. White, J. Mater. Res., **4** (1989) 385.
43. The atomic parameters of C, Si, Ni and H employed in our EHTB calculations are as follows: the valence shell ionization potentials  $H_{\mu\mu}$  (eV) of the Slater type orbitals (STO's)  $\chi_\mu$  are -21.4 ( $C_{2s}$ ), -11.4 ( $C_{2p}$ ), -17.3 ( $Si_{3s}$ ), -9.2 ( $Si_{3p}$ ), -9.9 ( $Ni_{3d}$ ), -7.8 ( $Ni_{4s}$ ), -3.7 ( $Ni_{4p}$ ), -13.6 ( $H_{1s}$ , used to cap the C dangling bonds), and -20.0 ( $H_{1s}$ , used to cap Si dangling bonds). The exponents ( $\xi$  and  $\xi'$ ) and the mixing coefficients ( $c$  and  $c'$ ) of two STO's  $\chi_\mu$  and  $\chi_\mu'$  to form double a zeta orbital ( $c \chi_\mu + c' \chi_\mu'$ ) are:  $(\xi, c, \xi', c) = (1.831, 0.7931, 1.152, 0.2739)$  for  $C_{2s}$ ,  $(2.730, 0.2595, 1.257, 0.8026)$  for  $C_{2p}$ ,  $(2.059, 0.5843, 1.297, 0.5187)$  for  $Si_{3s}$ ,  $(1.819, 0.4216, 1.065, 0.6577)$  for  $Si_{3p}$ ,  $(5.75, 0.5683, 2.00, 0.6292)$  for  $Ni_{3d}$ . The single zeta STO's used are:  $\xi = 1.3$  for  $H_{1s}$  (for capping the C dangling bonds), 1.1 for  $H_{1s}$  (for capping the Si dangling bonds), 2.1 for  $Ni_{4s}$  and  $Ni_{4p}$ . For  $Ni_3Si$ , Si was represented by the single zeta STO's with  $\xi = 1.624$  for  $Si_{3s}$  and 1.428 for  $Si_{3p}$ .
44. T. A. Albright, J. K. Burdett, and M.-H. Whangbo, Orbital Interactions in Chemistry (Wiley, 1985).

## IV. Flourine-based Mechanisms for ALE Growth on Diamond (110)

M.G. Wensell, Z. Zhang and J. Bernholc

*Department of Physics, North Carolina State University, Raleigh, North Carolina 27695-8202*

(April 23, 1995)

### Abstract

Atomic layer epitaxy (ALE) processes for the growth of diamond are evaluated using *ab initio* molecular dynamics. It is shown that the Cl-based ALE cycle on diamond (111) is not advantageous, due to strong steric hindrances. New ALE processes are proposed and shown to be energetically favorable, self-limiting, and sterically unhindered. They exploit the large heat of formation and the small size of the HF molecule and are based on alternating exposure of the diamond (110) surface to hydro- and fluoro-carbons. Alternatively, H and F gases can be used in parts of the cycle.

PACS numbers: 81.1.-z, 68.55.-a

The discovery of methods to grow thin films of diamond on a variety of substrates with practical growth rates has been viewed as one of the most important technological breakthroughs of the past decade. However, growth of high quality single-crystal films has proven to be a substantial challenge. Even on diamond substrates, the quality of the resulting film is significantly lower than that of natural diamond. On non-diamond substrates, only oriented polycrystalline growth has been achieved to date [1]. These difficulties have largely prevented electronic applications of diamond technology, despite its substantial potential for high speed, high power and high temperature electronics [2]. The difficulties associated with the growth of diamond can mostly be traced to the competition between the diamond and graphite phases. At the low growth pressures used in thin film growth, graphite is the thermodynamically preferred bulk phase. Therefore, growth of a large area diamond film must be due to kinetic reasons. Growth in the presence of large amounts of hydrogen helps to maintain  $sp^3$  hybridization of C atoms and leads to the formation of diamond coatings and thin films, even on non-diamond substrates. However, the resulting diamond films are not of sufficient quality, due to both the presence of grain boundaries and small graphitic inclusions that do not anneal out despite relatively high growth temperatures.

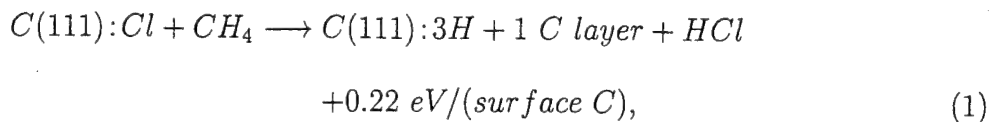
The quality of growth can be greatly improved if the film grows in a true layer-by-layer mode, in which each layer is fully completed before the next layer starts forming. Atomic Layer Epitaxy (ALE) is a "digital" growth method that results in a deposition of one or two atomic layers per each growth cycle. The simplest ALE cycle uses two reactant gases chosen in such a way that only a monolayer coverage of each gas is chemisorbed at the growth temperature. The self-limiting nature of ALE leads to uniform growth that does not depend on the geometry of the substrate nor is it sensitive to variations in the growth conditions [3,4]. ALE has been well-demonstrated for the growth of II-VI and III-V semiconductor thin films [5,6]. These processes take advantage of the difference in the electronegativity of the two constituents to achieve self-limiting growth. Alternative methods have been proposed for ALE growth of homopolar semiconductors that rely on sequential exposure of precursor gases to the substrate. This results in the alternation of the terminating adatoms

[7–12]. Our work has been stimulated by a preliminary report of ALE on the diamond (111) surface by Aleskovski and Drozd [8], based on the use of chloro- and hydro-carbons as precursors. However, to the best of our knowledge, their results have not been repeated by other groups. We have thus set out to investigate this method in mechanistic detail, using *ab initio* molecular dynamics. It was found that the proposed reactions have strong steric hindrances, making them unlikely to proceed at the required rates. However, this analysis has led us to propose a different set of ALE processes based on fluoro- and hydro-carbons. On the less crowded (110) surface, our *ab initio* calculations show that the proposed processes are energetically very favorable and sterically unhindered. They may thus lead to a practical ALE process for the growth of diamond films.

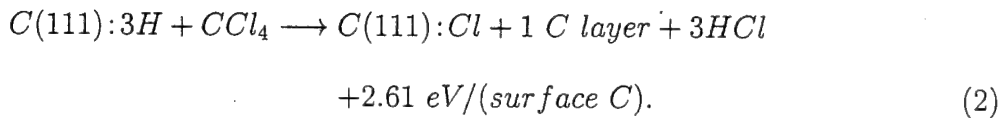
The ALE processes described below were investigated by large-scale *ab initio* calculations using the Car-Parrinello method [13], which combines density-functional theory with molecular dynamics. The electrons are described in the local density approximation with wavefunctions expanded in a plane-wave basis. The ions were described by norm-conserving pseudopotentials generated using either the Hamann procedure [14] (for C and Cl) or the soft-core optimization of Li and Rabii [15] (for H and F). The plane-wave cutoffs were 35 and 50 Ry, for the Cl- and F-based ALE mechanisms, respectively. The diamond surfaces were modeled as periodically repeated slabs containing 9–11 atomic layers and separated by about 10 Å of vacuum. The large separation was necessary to minimize interactions between slab surfaces. Each layer contained 8 atoms and the bottom layer atoms were held fixed at the perfect lattice positions while their dangling bonds were passivated with hydrogen. Due to the size of the unit cell, only the  $\Gamma$  point was used for k-space sampling. The total energies of the gas species employed in the growth mechanisms were calculated in cubic supercells with a 10 Å cube side.

The halogen-based mechanism proposed by Aleskovski and Drozd [8] involves the successive deposition of  $\text{CH}_4$  and  $\text{CCl}_4$  onto an initially chlorinated diamond (111) surface. The deposition would lead to evolution of  $\text{HCl}$  and an energy gain of 0.37 eV per each  $\text{HCl}$  molecule. However, our *ab initio* calculations show that both the Cl- and  $\text{CH}_3$ -terminated

surfaces are overcrowded, leading to a metallic behavior. The computed energetics is:



and

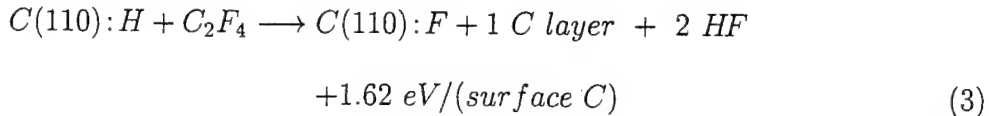


These results can be understood by noting that the covalent radius of Cl is 33% greater than C. Therefore, the density of coverage required to fully terminate the (111) surface leads to a substantial steric repulsion. The (111):3H surface is even more crowded. In order to minimize the steric repulsion we rotated every other methyl group by 60°. Nevertheless, one H atom on each group moved up by 0.5 Å, while the other two H atoms moved downward by 0.2 Å, resulting in a canted structure. We also performed a low-temperature molecular dynamics simulation of the surface and found that it readily becomes disordered. The inherent difficulties in stabilizing the growth surfaces make high quality ALE growth based on eqs. (1-2) unlikely.

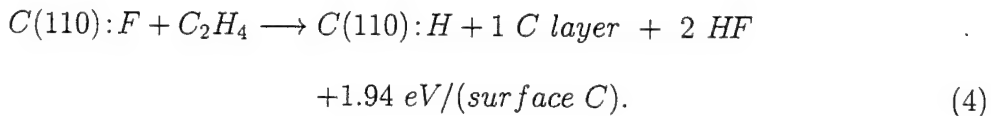
However, the above analysis had led us to devise a different class of ALE mechanisms, based on the use of fluorocarbons and utilizing the much more favorable geometry of the (110) surface. Fluorine has the advantage of having a smaller covalent radius than chlorine, which reduces the steric repulsion between halogen adatoms on a diamond surface. In halogenation studies of the diamond (100) and (111) surfaces, fluorine was found to both adsorb more readily and desorb at higher temperatures than chlorine [16]. The (110) surface was chosen because each surface plane in the (110) direction is the same and has only one dangling bond per surface atom. In contrast, in the (111) direction planes having one dangling bond alternate with those having three dangling bonds per atom. The (110) surface is thus both less crowded and results in simpler ALE growth mechanisms than the (111) surface. We propose to use  $C_2H_4$  and/or  $C_2F_4$  as precursor gases. The exposure of F- or H-terminated

(110) surfaces to the appropriate precursor gas would lead to the growth of a monolayer of diamond, a release of HF and a switching of the terminating adatoms from H to F or vice versa. Alternatively, exposure to atomic H, H<sub>2</sub> or F<sub>2</sub> could be used as part of the ALE sequence, resulting in a combination of a growth reaction and a switching reaction. We discuss these reactions in detail below.

The direct analog of reactions (1-2) would be an alternative exposure of the (110) surface to C<sub>2</sub>H<sub>4</sub> and C<sub>2</sub>F<sub>4</sub>. Starting from the hydrogenated surface, the reactions are:

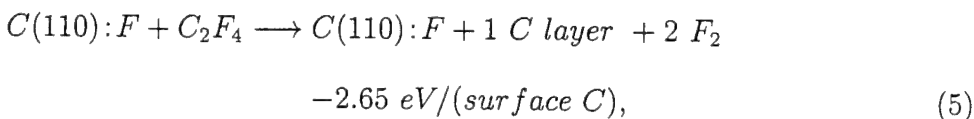


and



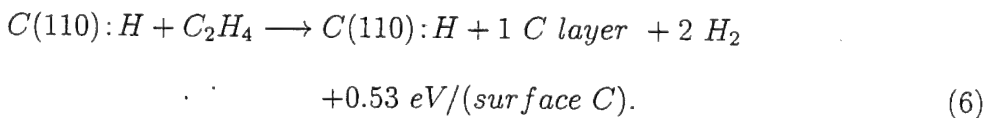
Note that the energies of these reactions were computed from total energies of the completely hydrogenated and fluorinated surfaces. Any steric repulsions between adatoms are thus taken into account. Both surfaces are semiconducting and the energy gains are quite large, which indicates the absence of substantial steric effects, although the 0.32 eV difference in the gain between the two reactions is due to the larger size of the F atom and thus the presence of some repulsion. One should also note that C<sub>2</sub>H<sub>4</sub> and C<sub>2</sub>F<sub>4</sub> are particularly suitable reactants for the (110) surface, since the existing C-C fragments can add parallel to the surface, see Fig. 1. The sizable energy gains are due to the large heat of formation of HF, which provides the driving force for the reactions (3-4). Due to its small size, HF formation and desorption should not be substantially hindered. Since ALE reactions proceed at high substrate temperatures, the reaction barriers are likely to be overcome and the reactions (3-4) are thus excellent candidates for ALE. These factors should further reduce the steric constraints.

The process based on reactions (3-4) would lead to the growth of two monolayers per cycle, but in order to corroborate its feasibility for ALE one needs to confirm the self-limiting aspect of the reactions. We thus examined the energetics of adding more than one layer during an exposure to a single reactant. Assume that the fluorinated surface, obtained as the result of reaction (3), continues to be exposed to  $C_2F_4$ . For continued growth on this surface one would need to desorb two  $F_2$  molecules per each  $C_2F_4$  adsorbed. However, we compute a substantial energetic loss for this reaction:



where the energy of the reaction was obtained in the limit of adding one full layer. The reaction (3) is thus clearly self-limiting, in the sense that a continued growth using  $C_2F_4$  is energetically very unfavorable.

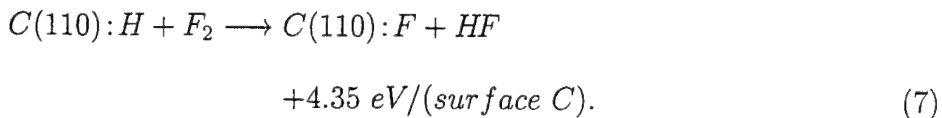
The self-limiting character of the second reaction was examined in a similar way. Continued growth of the completely hydrogenated surface using  $C_2H_4$  would require the desorption of two  $H_2$  molecules per each adsorbed  $C_2H_4$ . This reaction can be expressed as:



From reaction (6) it would appear that reaction (4) is not self-limiting, since there is an energy gain of 0.53 eV. However, in order to realize this gain, a two-center reaction must take place, so that the  $C=C$  bond breaks simultaneously with the formation of two  $H_2$  molecules. This is a very unlikely process. (In the reactions with the fluorinated surface, eq. (4), the high binding energy of HF provides the driving force for ethylene addition *without* the simultaneous breakage of the  $C=C$  bond.) The lack of reactivity of ethylene towards the diamond surface is also clear from experimental data, since growth of diamond from hydrocarbons requires either a plasma discharge or filament-induced decomposition of the

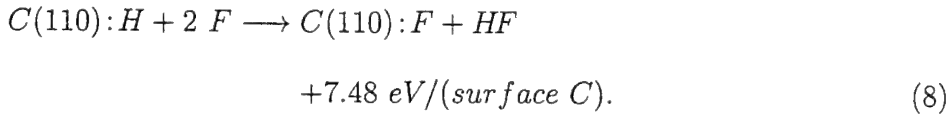
feed gas. Therefore, both growth reactions are most likely self-limiting with a single bilayer forming in each cycle. When used in an alternating fashion, ALE growth should result.

It is also possible to use alternative monolayer ALE cycles based on the main growth reactions (3-4). The reactions described below alternate between using one of the growth reactions together with a "switching" reaction that changes the termination of the surface. The first possibility is the reaction of  $F_2$  with a uniformly hydrogenated (110) surface:



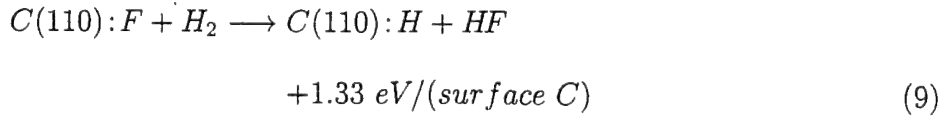
This reaction has a large energy gain, primarily due to the exchange of the weak  $F_2$  bond for the strong HF bond. The remaining fluorine atom replaces the hydrogen adatom as the terminating adatom.

One could also use a flux of atomic F to abstract H from the surface, which would be followed by flourine adsorption at the surface. For the (110) surface this gives

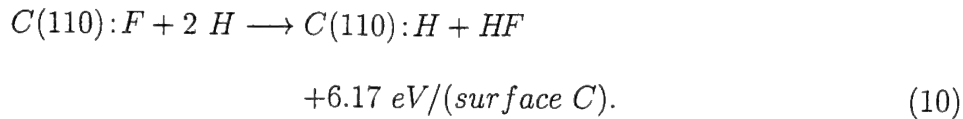


The difference between the energies of reactions (7) and (8) is due to the binding energy of  $F_2$ , which is well-known to be overestimated by the local density theory [18]. Nevertheless, it is obvious that the use of atomic F would increase the energy gain, and likely also reduce the initial energy barriers.

The equivalent reactions of diatomic and atomic hydrogen with fluorinated surfaces have also been studied. We obtain:



and



These reactions thus also exhibit large energy gains.

Any of the reactions (7–10) can be combined with the appropriate growth reaction (3 or 4) to obtain a monolayer per cycle ALE growth mechanism. Furthermore, the reactions (7–10) are obviously self-limiting. However, there exists a possibility of etching, in particular for the atomic species. Since atomic H is generated in large concentrations during plasma-assisted CVD growth of diamond, it is unlikely to etch diamond at a high enough rate to inhibit growth. In fact, it has been speculated that atomic H may be beneficial for the formation of diamond by preferentially etching graphitic precursors. Atomic F, although well-known to etch Si, does not etch diamond to a significant extent [16]. It has been suggested that this is due to the large radius of the F atom, which prevents its diffusion into subsurface layers. Such in-diffusion is necessary for etching silicon.

The most promising monolayer ALE mechanism would consist of reaction (3) together with either (9) or (10) to alternate the surface adatoms. This mechanism would be self-limiting and it exhibits substantial energy gains at each step of the cycle. In addition, it avoids the usage of the highly reactive atomic and diatomic fluorine.

In summary, we have identified several highly favorable reactions that have the potential of achieving a controlled layer-by-layer growth of diamond. All of the reactions should be self-limiting and can be appropriately combined into atomic layer epitaxy cycles with either monolayer or bilayer growth per cycle. Specifically, the reactions involve the exposure of gaseous hydro- and fluoro-species to a hydrogenated or fluorinated diamond (110) surface.  $C_2H_4$  and  $C_2F_4$  are used as growth precursors when exposed to an oppositely terminated surface. Atomic and diatomic hydrogen and fluorine react with the oppositely terminated surface and lead to switching of the surface-terminating adatoms. This can be used to achieve monolayer growth per cycle. All of the reactions are very favorable energetically. This is mainly due to the formation of strongly bonded HF molecules during each of the reactions.

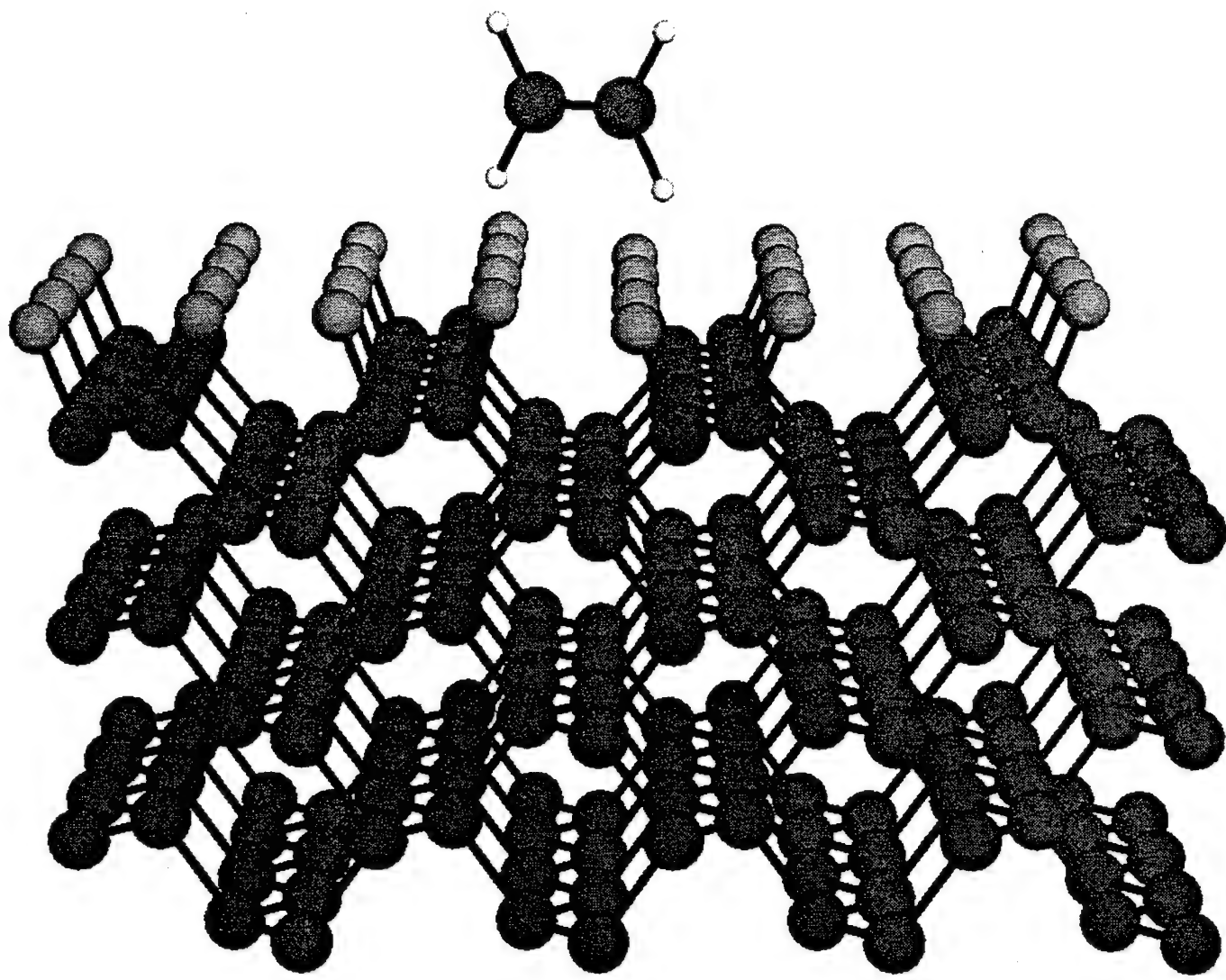


Fig. 1

## REFERENCES

- [1] W. Zhu, X. H. Wang, B. R. Stoner, G. H. M. Ma, H. S. Kong, M. W. H. Braun, and J. T. Glass, Phys. Rev. B **47**, 6529 (1993); S. D. Wolter, B. R. Stoner, J. T. Glass, P. J. Ellis, D. S. Buhaenko, C. E. Jenkins, and P. Southworth, Appl. Phys. Lett. **62**, 1215 (1993); R. Kohl, C. Wild, N. Herres, P. Koidl, B. R. Stoner, and J. T. Glass, Appl. Phys. Lett. **63**, 1792 (1993).
- [2] R. F. Davis, Physica B **185**, 1 (1993).
- [3] C. H. L. Goodman and M. V. Pessa, J. Appl. Phys. **60**, R65 (1986).
- [4] T. Suntola, Mat. Sci. Rep. **4**, 261 (1989).
- [5] M. L. Yu, Thin Solid Films **224**, 7 (1993).
- [6] J. R. Creighton and B. A. Bansenauer, Thin Solid Films **224**, 17 (1993).
- [7] J.-I. Nishizawa, K. Aoki, S. Suzuki, and K. Kikuchi, J. Cryst. Growth **99**, 502 (1990).
- [8] V. B. Aleskovski and V. E. Drozd, *Proc. First Inter. Symp. on Atomic Layer Epitaxy*, edited by L. Niinisto, Acta Polytechnica Scandinavica, Chem. Techn. and Metallurgy Ser. **195**, 156 (1990).
- [9] S. M. Cohen, T. I. Hukka, Y. L. Yang and M. P. D'Evelyn, Thin Solid Films **224**, 155 (1993).
- [10] T. L. Hukka, R. E. Rawles, and M. P. D'Evelyn, Mat. Res. Soc. Symp. Proc. **282**, 671 (1993).
- [11] S. Imai, T. Iizuka, O. Sugiura and M. Matsumura, Thin Solid Films **224**, 168 (1993).
- [12] D. D. Koleske, S. M. Gates and D. B. Beach, Thin Solid Films **224**, 173 (1993).
- [13] R. Car and M. Parrinello, Phys. Rev. Lett. **55**, 2471 (1985).
- [14] G. B. Bachelet, D. R. Hamann and M. Schlüter, Phys. Rev. B **26**, 4199 (1982).

## V. Growth and Characterization of Homoepitaxial Diamond Negative Electron Affinity Surfaces

### A. Introduction

Diamond has received much attention in the past due to its unique optical, mechanical, thermal, and electronic properties [1-4]. Advances in low pressure thin film diamond growth techniques have led to much emphasis being placed on electronic applications. However, at the present time electronic diamond devices are limited due to the inability to grow conductive n-type films.

There has recently been renewed interest in developing diamond cold cathode emitters using Negative Electron Affinity (NEA) emission. An NEA occurs when the vacuum level lies below the conduction band minimum at the surface. If an NEA is present, all electrons in the conduction band have enough energy to overcome the work function of the surface providing a highly efficient mechanism for electron emission. NEA has been observed for the (100), (110), and (111) surfaces of diamond using various *in situ* and *ex situ* surface preparations [5].

Due to the extreme mechanical and chemical properties of diamond, it is impossible to obtain atomically flat diamond surfaces, even with modern mechanical and electrochemical polish techniques. High resolution atomic force microscopy reveals residual polishing grooves on the polished surfaces [6]. Since NEA emission is inherently a surface process, it is important to understand the role of surface morphology on NEA electron emission. The objective of this research is to obtain atomically flat diamond surfaces by depositing thin high-quality homoepitaxial films. These films will then be characterized using several surface sensitive techniques (described below) to assess this role of surface morphology on NEA electron emission.

### B. Experimental Procedure

The diamond growth system used is shown in Fig. 1. It consists of a commercially available stainless steel ASTeX HPMS microwave plasma CVD chamber. The microwave generator is a 2.45 GHz ASTeX S-1500i rated up to 1500 W. The substrate heater is a graphite susceptor which is inductively heated using a dedicated ASTeX RF power supply. The temperature is measured using both an optical pyrometer and a standard type-K thermocouple located inside the graphite susceptor. The original ASTeX heater design was modified in order to use the standard molybdenum sample holder used in the integrated surface processing/characterization system. Pressure control is achieved downstream using a MKS Baratron and MKS Butterfly valve. The H<sub>2</sub>/CH<sub>4</sub> process gas mixture is controlled by MKS mass-flow controllers. The process pump is a Leybold D16BCS mechanical pump.

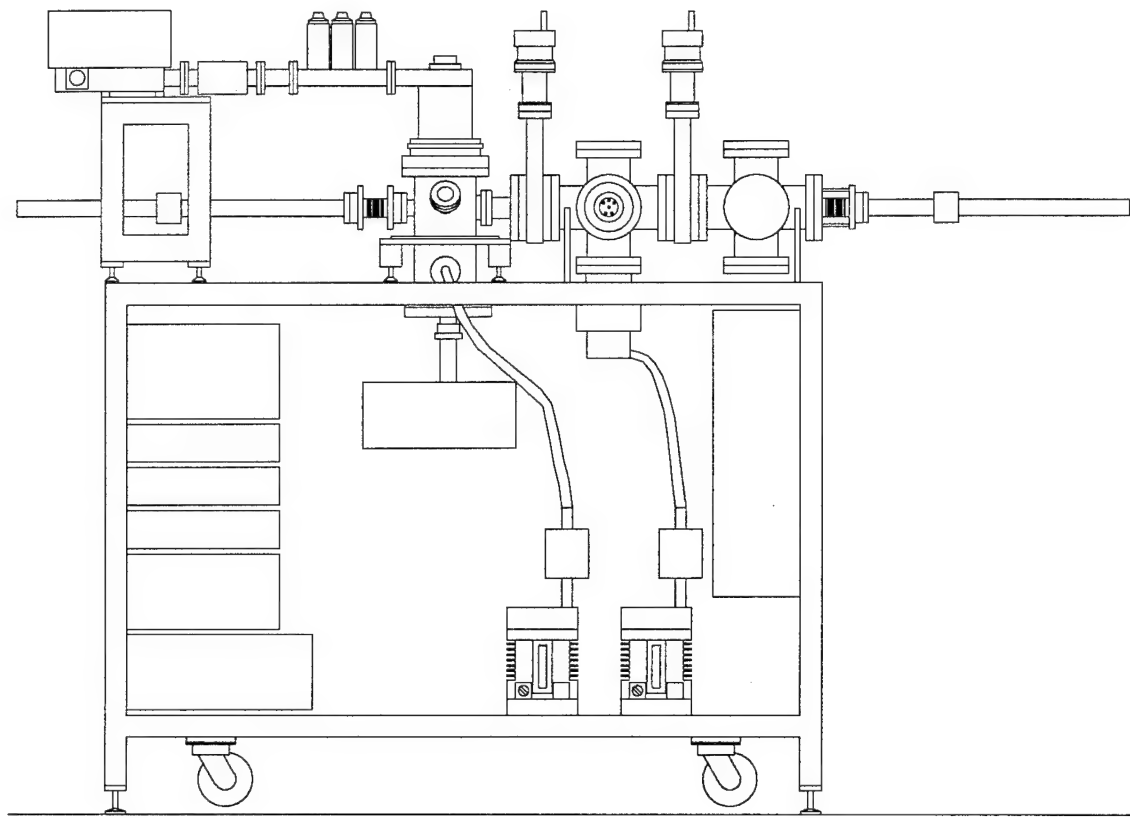


Figure 1. Schematic of the microwave plasma CVD diamond growth chamber.

A schematic of the integrated surface processing/characterization system is shown in Fig. 2. It consists of eight stations which are connected by a 35 ft UHV sample transfer system. These stations include a remote hydrogen plasma cleaning chamber, the HPMS growth chamber, Raman spectroscopy, Ultraviolet Photoemission Spectroscopy (UPS), Auger Electron Spectroscopy (AES), Low Energy Electron Diffraction (LEED), and X-ray Photoemission Spectroscopy (XPS). Raman spectroscopy is routinely used to determine the overall film quality of diamond films. Ultraviolet photoemission spectroscopy is used to observe whether a surface exhibits an NEA, while XPS and AES are used to determine the chemical composition of species on the surface. Since the diamond CVD chamber is simply mechanically pumped, it is necessary to have an intermediate chamber which is pumped by a Leybold 180 l/s turbomolecular pump to act as a pressure lock between the growth chamber and the UHV transfer system.

In addition to the *in situ* characterization tools available on the vacuum transfer system, other *ex situ* techniques are used to characterize the morphology and RMS roughness of the samples. These include Atomic Force Microscopy (AFM), Scanning Tunneling Microscopy (STM), and Scanning Electron Microscopy (SEM).

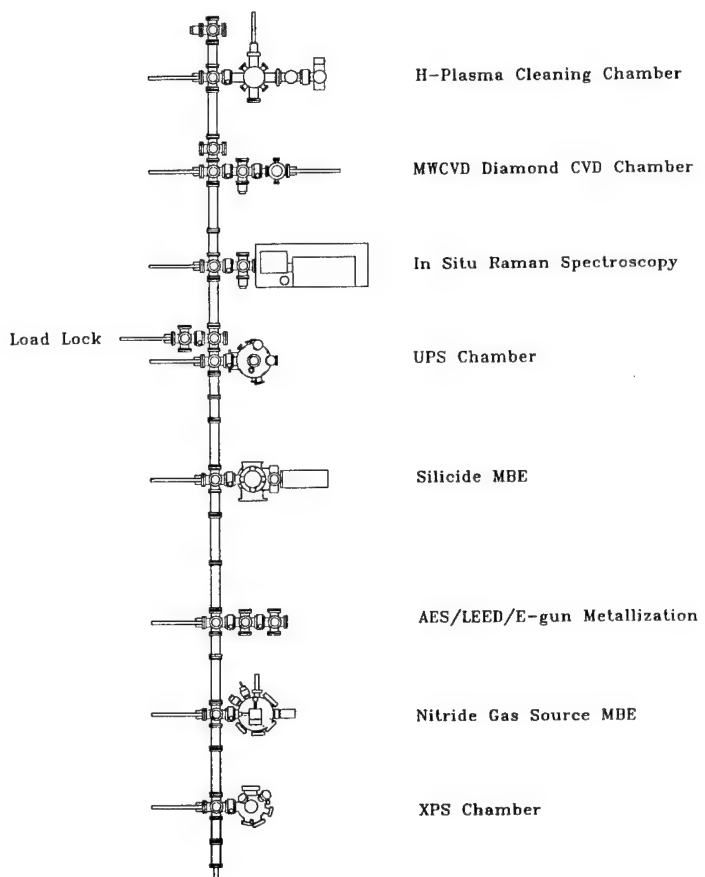


Figure 2. Schematic of the integrated surface processing/characterization system.

### C. Results and Discussion

Although diamond is considered to possess a highly-robust surface, it is imperative for these studies that samples be transferred from chamber to chamber without being exposed to the atmosphere. This way the surface can be examined and manipulated without possible ambient contaminants. Homoepitaxial films will be used to provide atomically flat diamond surfaces. Growth conditions, therefore, must be determined which will achieve uniform layer by layer growth. In addition, these films must be of extremely high quality in order to eliminate possible competition between the desired electron emission and unwanted recombination through defect centers.

The results to date involve the completion of the design of the ASTeX microwave plasma CVD chamber and its incorporation onto the UHV transfer system. Previous results with this chamber showed that deposition occurred on scratched (100) silicon wafers. However, during these initial tests of the chamber secondary or parasitic plasmas were formed around the corners of the sample holders. These parasitic plasmas greatly reduce the plasma energy

density in the vicinity of the substrate and can heat the sample holder to above 1100°C. With decreased plasma energy, growth rates well below 0.1 μm/h were observed. The recent focus of this research was to solve this problem by re-engineering the sample holder/heater design. With the new heater design, the top of the standard molybdenum sample holder is located flush with the top surface of the graphite susceptor. No parasitic plasmas are formed with the sample holder in this position and improvement in growth has been observed.

Optimum growth conditions for the growth on scratched (100) silicon substrates are currently being investigated using a statistical experiment design (SED). Silicon substrates are being used during this initial SED due to the scarcity and expense of natural diamond samples. In addition to determining the experimental parameters which produce high quality films, this SED should indicate which set of parameters are needed for (100) and (111) texturing. These optimum parameters for (100) and (111) growth will then be used as initial conditions when depositing homoepitaxial films.

#### D. Future Research Plans and Goals

Immediate plans include the continuation of this research as outlined above. Once high-quality deposition is achieved on (100) silicon, these parameters will be used as an initial starting point for the deposition on (100) and (111) diamond single crystal substrates. The next objective will be to obtain high-quality epitaxial films. Raman spectroscopy, SEM, AFM, and STM will be the key techniques in determining the optimum process conditions. Since C<sup>13</sup> is heavier than C<sup>12</sup>, C<sup>13</sup> labeled methane may be used in order to distinguish the deposited homoepitaxial CVD film from the underlying diamond substrate in the Raman analysis. When pristine films are obtained, the surface sensitive techniques outlined above will be used to examine the role of surface morphology on the NEA characteristics. Future plans also include the use of laser reflectance interferometry (LRI) as a real-time *in situ* characterization tool for the growth both on silicon and diamond substrates. For homoepitaxial growth the backside of the substrates will need to be metallized in order to achieve interference. The design of a hot filament source to be located in the same chamber is also being considered in order to compare microwave plasma and hot filament growth techniques. Modification of the gas manifold design to allow boron and nitrogen doping is also being planned.

#### E. References

1. C. A. Brookes and E. J. Brookes, Diam. Relat. Mat. **1**, 13 (1991).
2. L. Wei, P. K. Kuo, R. L. Thomas, edited by R. Messier, J. T. Glass, J. E. Butler, and R. Roy (Materials Research Society, 1990), p.875.
3. J. H. Edgar, J. Mater. Res. **7**, 235 (1992).
4. I. M. Buckley-Golder, R. Bullough, M. R. Hayns, J. R. Willis, R. C. Piller, N. G. Blamries, G. Gard, and J. Stephen, Diam. Relat. Mat. **1**, 43 (1991).
5. J. van der Weide, Personal Communication (1994).
6. S. E. Wagoner, Personal Communication (1994).

## **VI. Negative Electron Affinity Effects and Schottky Barrier Height Measurements of Cobalt on Diamond (100) Surfaces**

P. K. Baumann and R. J. Nemanich

Department of Physics, North Carolina State University, Raleigh, North Carolina 27695-8202  
USA

**Key words:** cold cathodes, metal contacts, negative electron affinity, Schottky barrier height

### **Abstract**

The effects of growing thin cobalt films on natural type IIb diamond (100) substrates were investigated by means of ultraviolet photoemission spectroscopy (UPS). Prior to deposition, the diamond samples were annealed to 1150°C in UHV resulting in a positive electron affinity surface. Upon deposition of 2Å of cobalt, a negative electron affinity (NEA) was observed and a Schottky barrier height of 0.35 eV was measured by means of UPS. The presence of a cobalt layer was confirmed employing *in-situ* Auger electron spectroscopy (AES). As evidenced by atomic force microscopy (AFM), uniform Co films were deposited replicating the underlying diamond substrates.

#### **A. Introduction**

The electron affinity of a semiconductor is defined as the energy difference between the vacuum level and the conduction band minimum. For most materials, the vacuum level lies above the conduction band minimum, thus corresponding to a positive electron affinity. Surfaces of wide bandgap semiconductors such as diamond have the potential for exhibiting a negative electron affinity (NEA) since the conduction band minimum lies near the vacuum level. Electrons present in the conduction band have sufficient energy to overcome the workfunction of a NEA surface and can be emitted into vacuum. Indeed, different surface preparation techniques can shift the position of the vacuum level and, therefore, induce a NEA or remove it [1-3]. Furthermore it has been demonstrated that metals like Ti, Ni and Cu can induce a NEA on diamond surfaces [4, 5, 1]. Photoemission spectroscopy is found to be a very sensitive method to determine whether a surface exhibits a NEA or not. Secondary electrons appear as a sharp peak at the low energy end of photoemission spectra for NEA surfaces [6, 7].

---

To appear in the Proceedings of the *3rd International Conference on the Applications of Diamond Films and Related Materials* at NIST Gaithersburg, MD (1995).

## B. Experimental Details

The UHV system used in this study consists of several interconnected chambers including systems used for annealing, metal deposition, UPS and AES. Natural type IIb single crystal diamond (100) substrates ( $3.0 \times 3.0 \times 0.25$  mm) were used in this study. First, the samples were electrochemically etched to remove non-diamond carbon and metal contaminants [8]. This etch included applying a DC bias of 350V between two Pt electrodes that were placed in deionized (DI) water as an electrolyte. The samples were suspended in water between the two electrodes. Following the electrochemical etch, a HF dip was employed to remove  $\text{SiO}_2$  from the surface [1]. Then the wafers were mounted on a Mo holder and transferred into the UHV system (base pressure  $\sim 1 \times 10^{-10}$  Torr). As an *in vacuo* cleaning step, the wafers were annealed to  $1150^\circ\text{C}$  for 10 minutes. This caused the pressure to rise to  $\sim 7 \times 10^{-9}$  Torr. Subsequent to annealing, thin Co films of 2 Å were deposited by means of a hot filament. The thickness of the Co layers was determined by means of a quartz crystal oscillator. During deposition, the pressure rose to  $\sim 2 \times 10^{-9}$  Torr. Following the annealing and the growth steps, UPS and AES were employed to analyze the surface properties. HeI (21.21 eV) radiation was used to facilitate the photoemission of electrons. The 50 mm hemispherical analyzer employed to measure the emitted electrons had an energy resolution of 0.15 eV. A bias of 1V was applied to the sample to overcome the workfunction of the analyzer and, thus, to detect the low energy electrons emitted from the NEA surface. The position of the sharp NEA peak at the low energy end of photoemission spectra corresponds to the energy position of the conduction band minimum,  $E_C$  (Fig. 1). Emission from  $E_C$  is positioned at  $E_V + E_G$  in the spectrum, where  $E_V$  is the energy of the valence band maximum and  $E_G$  that of the bandgap. Emission from the valence band maximum appears at  $E_V + h\nu$  in the spectrum. The spectral width or the distance between emission from the valence band maximum and the

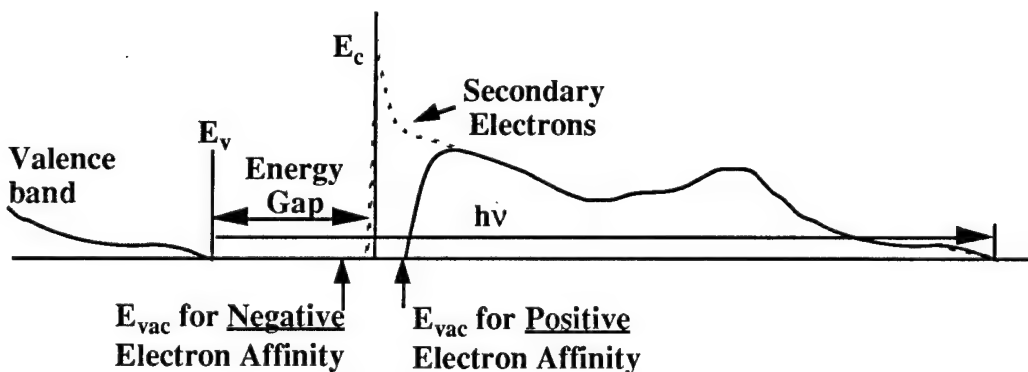


Figure 1. Schematic diagram of photoemission spectra for a negative electron affinity surface (dotted line) and a positive electron affinity surface (solid line).

conduction band minimum is, therefore,  $h\nu - E_G$ . With the values for He I radiation,  $h\nu = 21.21$  eV, and the bandgap of diamond,  $E_G = 5.45$  eV, a spectral width of  $\sim 15.7$  eV is determined for a NEA surface. However, for the case of a positive electron affinity surface the low energy cutoff will be determined by the position of the vacuum level and the spectral width will be smaller.

### C. Results and Discussion

AES spectra of the as-loaded samples exhibited features indicative of the presence of oxygen on the surface. Subsequent to the  $1150^\circ\text{C}$  anneal, no oxygen could be detected on the surface of the diamond substrates by means of AES. As evidenced by UPS, the surfaces exhibited a positive electron affinity, see Fig. 2. It has been previously reported that heating diamond (100) to  $1150^\circ\text{C}$  results in the removal of oxygen and a surface with a positive electron affinity [3, 9]. Upon deposition of  $2\text{\AA}$  of cobalt, a negative electron affinity (NEA) was observed and a Schottky barrier height of  $\Phi_B \approx 0.35$  eV was measured by means of UPS as shown in Fig. 2. Equation (1) gives an expression for the electron affinity  $\chi$  of a p-type semiconductor following the formation of a Schottky barrier [10]:

$$\chi = (\Phi_M + \Phi_B) - E_G. \quad (1)$$

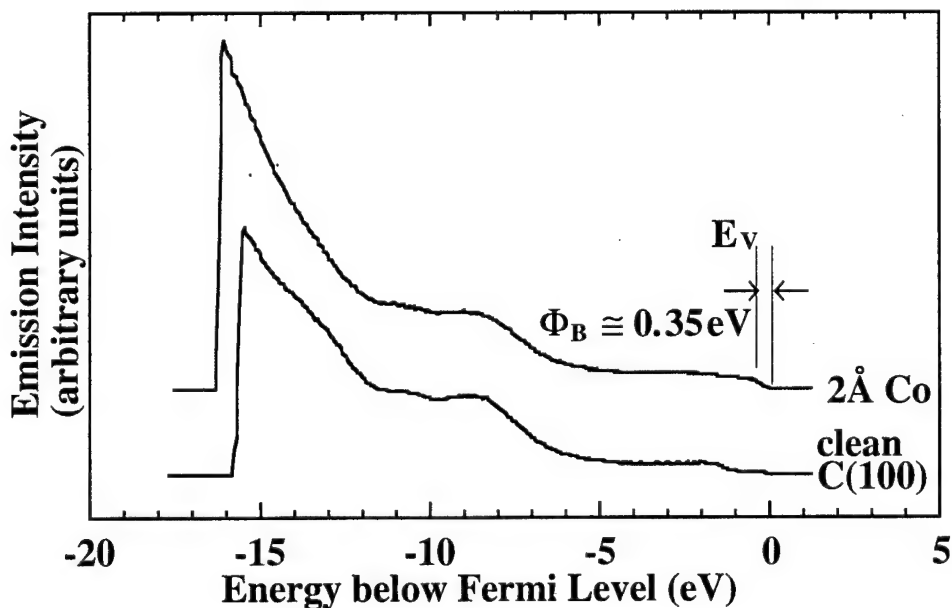


Figure 2. UV photoemission spectra of diamond (100) following a  $1150^\circ\text{C}$  anneal and of Co deposited on diamond.

With the value for the metal work function of cobalt  $\Phi_M = 5.00$  eV, the bandgap of diamond  $E_G = 5.45$  eV and the measured Schottky barrier height, an electron affinity of  $\chi \approx -0.1$  eV can be calculated. This result is in agreement with the experimental data. Previously, this simple work function model has been used to explain metal induced NEA effects for Ti and Ni deposited on diamond (111) [4, 5]. The presence of a cobalt layer was confirmed employing AES. AFM images of the diamond wafers clearly display linear grooves with a depth of  $\sim 20$  Å. These kind of features are due to the commonly applied procedure of polishing the samples with diamond grit. As evidenced by AFM, Co was deposited as uniform films replicating the grooves of the underlying diamond substrates, see Fig. 3.

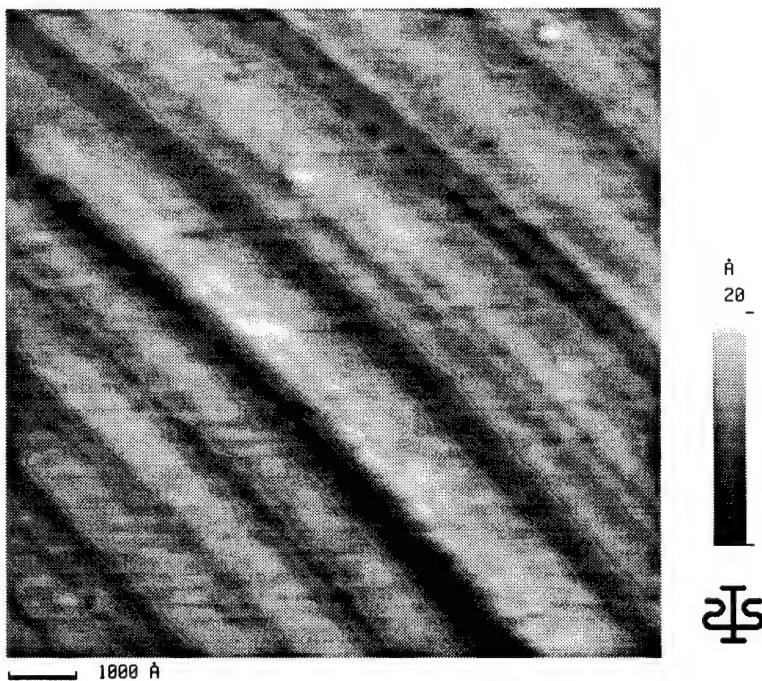


Figure 3. AFM micrograph of 2 Å of cobalt deposited on diamond (100).

#### D. Conclusions

Thin cobalt films have been deposited on diamond (100) crystals. A metal induced NEA was observed and a Schottky barrier height of  $\Phi_B \approx 0.35$  eV was determined by means of UPS. Furthermore, the cobalt layers were found to be uniform.

#### E. Acknowledgments

This work was supported by the Office of Naval Research (N00014-92-J-1477).

## F. References

1. P. K. Baumann, T. P. Humphreys and R. J. Nemanich, in Diamond, SiC and Nitride Wide Bandgap Semiconductors, edited by C. H. Carter, G. Gildenblat, S. Nakamura, R. J. Nemanich, Mater. Res. Soc. Proc. **339**, Pittsburgh, PA, 69 (1994).
2. J. van der Weide and R. J. Nemanich, Appl. Phys. Lett. **62**, 1878 (1993).
3. J. van der Weide, Z. Zhang, P. K. Baumann, M. G. Wensell, J. Bernholc and R. J. Nemanich, Phys. Rev. B **50**, 5803 (1994).
4. J. van der Weide and R. J. Nemanich, J. Vac. Sci. Technol. B **10**, 1940 (1992).
5. J. van der Weide and R. J. Nemanich, Phys. Rev. B, **49**, 13629 (1994).
6. F. J. Himpsel, P. Heimann and D. E. Eastman, Sol. State Commun. **36**, 631 (1980).
7. B. B. Pate, W. E. Spicer, T. Ohta and I. Lindau, J. Vac. Sci. Technol. **17**, 1087 (1980).
8. M. Marchywka, P. E. Pehrsson, S. C. Binari and D. Moses, J. Electrochem. Soc., Vol. **140**, No. 2 (1993) L19.
9. P. K. Baumann and R. J. Nemanich, Proc. of the Fifth European Conference on Diamond, Diamond-like and Related Materials (J. Diamond Rel. Mat., 1995) in press.
10. E. H. Rhoderick and R. H. Williams, *Metal-Semiconductor Contacts* (Clarendon, Oxford, 1988).

## VII. Diamond Negative Electron Affinity Surfaces, Structures and Devices

R. J. Nemanich, P. K. Baumann and J. van der Weide  
Department of Physics and Department of Materials Science and Engineering  
North Carolina State University  
Raleigh, NC 27695-8202

### Abstract

The electron affinity of a semiconductor relates the band structure of the semiconductor at the surface to the vacuum ground state near the surface. Wide bandgap semiconductors have the possibility of exhibiting a negative electron affinity (NEA) meaning that electrons in the conduction band are not bound by the surface. The surface conditions are shown to be of critical importance in obtaining a negative electron affinity. In this study, angle resolved UV-Photoemission Spectroscopy (ARUPS) is used to detect the effect. Surface terminations ranging from adsorbates, metals and insulators are shown to induce an NEA on diamond. In particular, it is demonstrated that hydrogen termination can induce a NEA on (111), (100), (110) and (311) surfaces. Theoretical studies have indicated a basis for the observed NEA effects. In contrast, as-prepared surfaces with oxygen termination often exhibit a positive electron affinity. It is shown that thin metal layers of Ti, Ni, Cu, and Co can induce a NEA on the (111) surface, and new evidence indicates NEA on the (100) surface. NEA materials could prove useful in cold cathode applications, and potential and limitations are discussed.

### A. Introduction

The electron affinity of a semiconductor is defined as the energy required to remove an electron from the conduction band minimum to a distance macroscopically far from the semiconductor (i.e. away from image charge effects). At the surface this energy can be shown schematically as the difference between the vacuum level and the conduction band minimum. The electron affinity is not, in general, dependent on the Fermi level of the semiconductor. Thus, while doping can change the Fermi level in the semiconductor and the workfunction will change accordingly, the electron affinity is unaffected by these changes. An alternative view is that the electron affinity is a measure of the heterojunction band offset between the vacuum and

---

To appear in the proceedings of the *3rd International Conference on the Applications of Diamond Films and Related Materials* at NIST Gaithersburg, MD (1995).

a semiconductor of interest. For most semiconductors, the conduction band minimum is below the vacuum level and electrons in the conduction band are bound to the semiconductor by an energy equal to the electron affinity. In some cases, surface conditions can be obtained in which the conduction band minimum is above the vacuum level. In that case, the first conduction electron would not be bound to the sample but could escape with a kinetic energy equal to the difference in energy of the conduction band minimum and the vacuum level. This situation is termed a negative electron affinity. (Note that the electron is still bound to the vicinity of the sample by coulomb forces.)

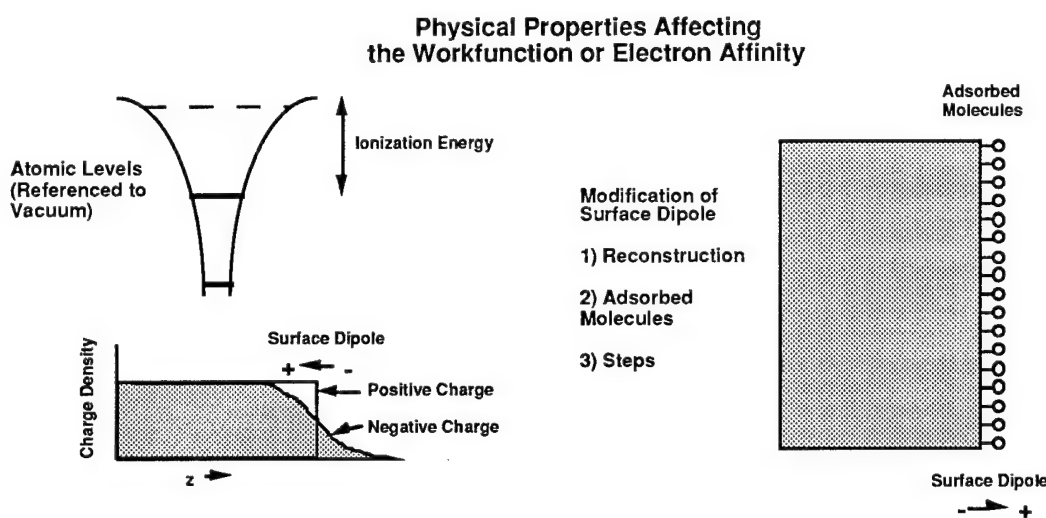


Figure 1. A representation of the effects which contribute to the workfunction (or electron affinity) of any material. While the atomic levels are an intrinsic property of the material, changes in the surface bonding can substantially affect the workfunction or electron affinity.

The electron affinity or work function of a material is usually ascribed to two aspects of the material: (1) the origin of the atomic levels, and (2) the surface dipole due to the surface termination [1]. These effects are shown schematically in Fig. 1. The atomic levels are more or less intrinsic to a material and cannot be changed. This is not the case for the surface dipole. The surface dipole can be substantially affected by surface reconstructions and surface adsorbates. As a simple example to illustrate the magnitude of this effect consider a surface with hydrogen termination, and assume that the average nuclear and electronic charges are point charges separated by  $0.5\text{\AA}$ . Then for a surface density of  $1\times 10^{15}\text{cm}^{-2}$ , we would find a  $\sim 9\text{eV}$  effect due to the surface dipole. (Certainly complete charge transfer is never a reasonable possibility, but this simple calculation demonstrates the significance of the surface dipole.) Because of the large effect of the surface dipole, it is essentially impossible to determine if a

material is “intrinsically NEA.” Thus the surface termination is critical in describing the electron affinity (or NEA) properties of a material.

One method to measure the electron affinity of a semiconductor is UV-photoemission [2,3]. The changes in the spectra due to NEA are indicated in Fig. 2 [4]. The electrons from the valence band are excited into the conduction band. In transiting towards the surface, electron scattering occurs and a large number of secondary electrons accumulate at the valence band minimum. For materials with a positive electron affinity, these electrons cannot escape. While for a NEA, the electrons can be emitted directly and will be observed with a low kinetic energy. Thus, the two effects which signify a NEA are an extension of the spectral range to lower energy and the appearance of a sharp peak at low kinetic energy. This feature will appear at the largest (negative) binding energy in typical presentations of UPS spectra.

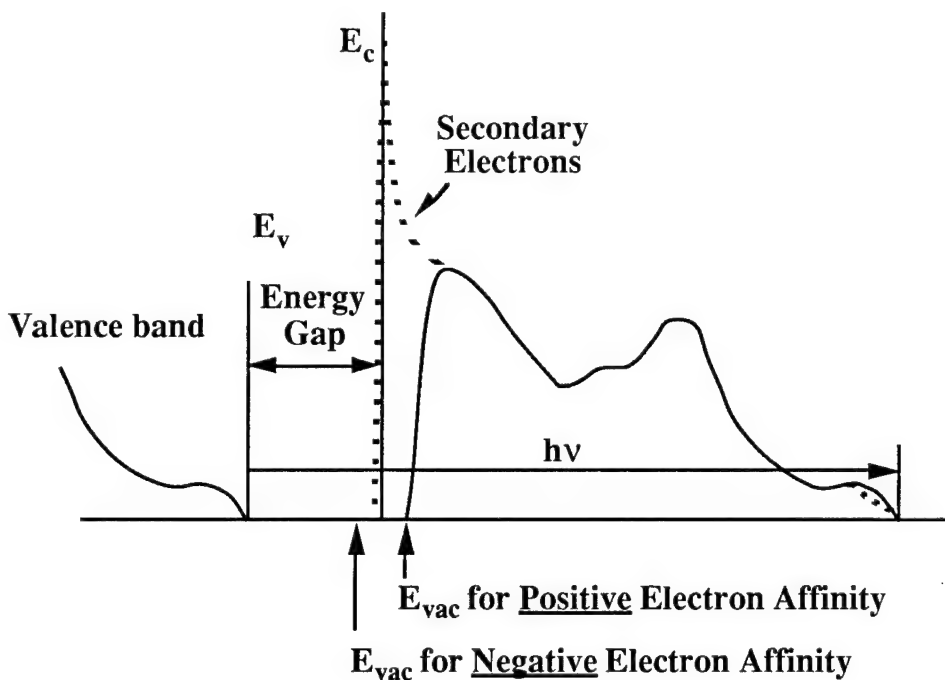


Figure 2. A schematic of how NEA affects the photoemission spectra. For a NEA surface the spectra is broadened to lower kinetic energy and a peak due to quasi thermalized electrons is detected also at the lowest kinetic energy.

In addition to the sharp feature that is often evident in the spectra of a NEA semiconductor, the width of the photoemission spectrum ( $W$ ) is related to the bandgap  $E_g$  and the excitation energy  $h\nu$ . The relation is that  $h\nu = E_g + W$ . Careful measurements of the width of the spectra are helpful in distinguishing whether the effect is direct emission of the electrons from conduction band states or whether excitons are involved in the emission process. The effects of excitons have recently been reported by Pate and co-workers [5].

## B. Experimental

The experiments described in this summary paper were carried out in an integrated UHV system with surface preparation, film growth and surface characterization capabilities. The system consists of eight chambers interconnected by a linear sample transfer mechanism. The overall length of the sample transfer chamber is ~35ft. A portion of the system is shown schematically in Fig. 3. This system shows the relations of the UV photoemission system, the plasma surface processing system, the LEED/Auger systems, and the metals MBE chamber. In the experiments described here, the UV-photoemission measurements were made with HeI (21.21eV) radiation and the electrons were analyzed with a VSW HAC50 50mm mean radius hemispherical electron analyzer. The spectra were collected at normal emission with a collection angle of ~2°. The sample was biased with ~1V so that the low energy electrons can overcome the workfunction of the analyzer. While higher sample bias can be employed, the low bias used here is to minimize spectral distortions that occur due to changes in the effective collection angle for the higher sample bias.

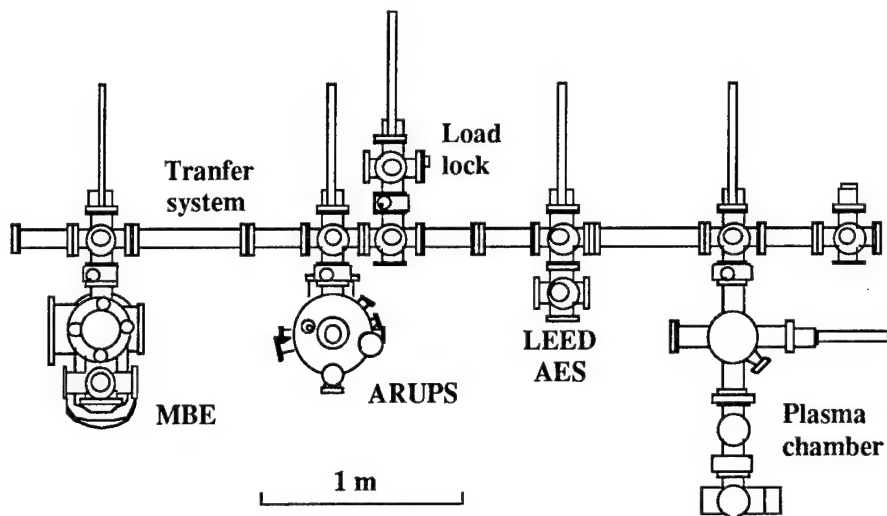


Figure 3. A schematic of a portion of the integrated surface processing and characterization system used in the studies described here.

## C. Surface Termination Effects

While the NEA of H-terminated diamond (111) has been established for many years [2,3,4,6], it has only recently been shown that H-terminated (100) surfaces exhibit a NEA [7,8,9]. The UV photoemission of a diamond (100) surface versus annealing is shown in Fig. 4. The results indicate the development of a sharp feature at the lowest kinetic energy (i.e. largest negative binding energy) of the spectra and an increase in the width of the

spectrum. Auger spectra obtained from the same surfaces indicated the presence of oxygen termination for the as-prepared surface, and the oxygen remained until  $\sim$ 1000°C. Thus, the presence of oxygen was correlated with a positive electron affinity. It is difficult to detect the presence of H by the techniques available in this study, but partial H termination is likely from the wet chemical surface preparation treatments employed in this study. A theoretical analysis reported in concert with the experimental study also supported the presence of H-termination in obtaining a NEA of the (100) surface [7]. The study proposed that the annealed (100) surface with a  $2\times 1$  reconstruction was monohydride terminated and exhibited a NEA.

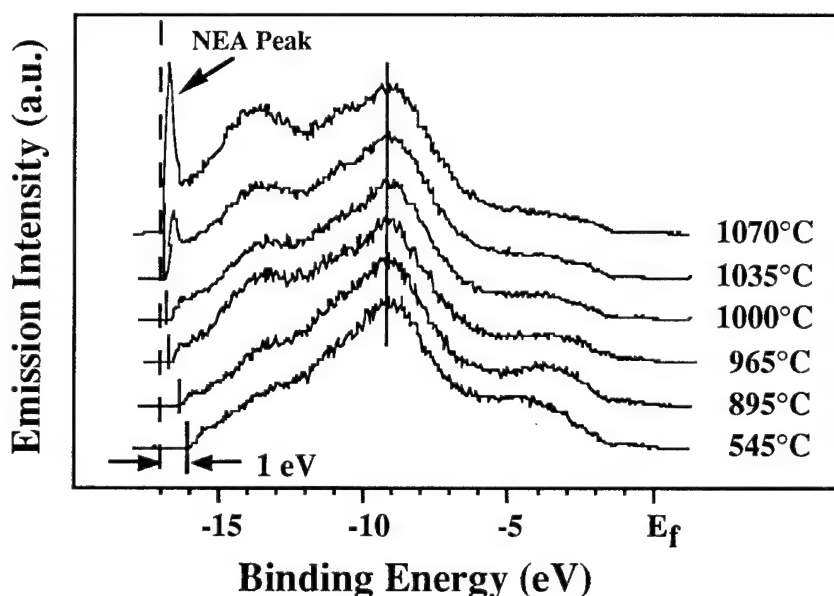


Figure 4. The photoemission of a diamond (100) surface as a function of annealing. The broadening of the spectral width and the sharp feature at high (negative) binding energy (i.e. low kinetic energy) are indicative of a NEA.

A schematic of the changes in the band alignment with H termination is indicated in Fig. 5. The band bending indicated is consistent with that expected for p-type (B doped) diamond. The two schematics have been aligned at the vacuum level to indicate the effect of the surface dipole. The H termination changes the surface dipole which results in a shift of the semiconductor bands with respect to the vacuum level.

UV-photoemission measurements of H-terminated (110) and (311) surfaces also exhibited the characteristics of a NEA. Future studies should focus on the stability of the H-terminated surfaces and the interactions with oxygen.

An alternative surface treatment that can be employed to induce a NEA on diamond is a thin metal layer. It is now well established that low workfunction metals such as Cs can be used to induce a NEA on III-V semiconductors such as GaAs. These surfaces are commonly employed

### Electronic Bands Near the Surface

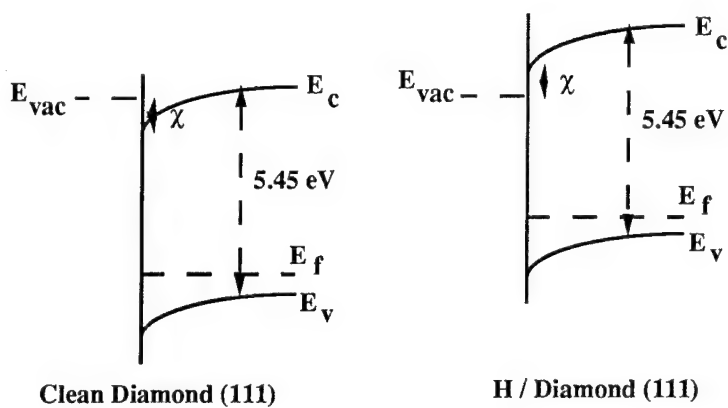


Figure 5. The band alignments of clean diamond and H terminated diamond surfaces. Note that the figures have been aligned at the vacuum level.

in high efficiency photocathodes. For diamond, it was initially shown that Ti on diamond (111) surfaces resulted in a NEA, [10] and Ni on diamond was also found to exhibit a NEA [11]. Recent studies have also indicated a NEA for Co or Cu on diamond (100) surfaces [12,13]. The photoemission spectra of diamond surfaces with a few monolayers of these different metals are summarized in Fig. 6. All spectra show the sharp feature associated with a NEA.

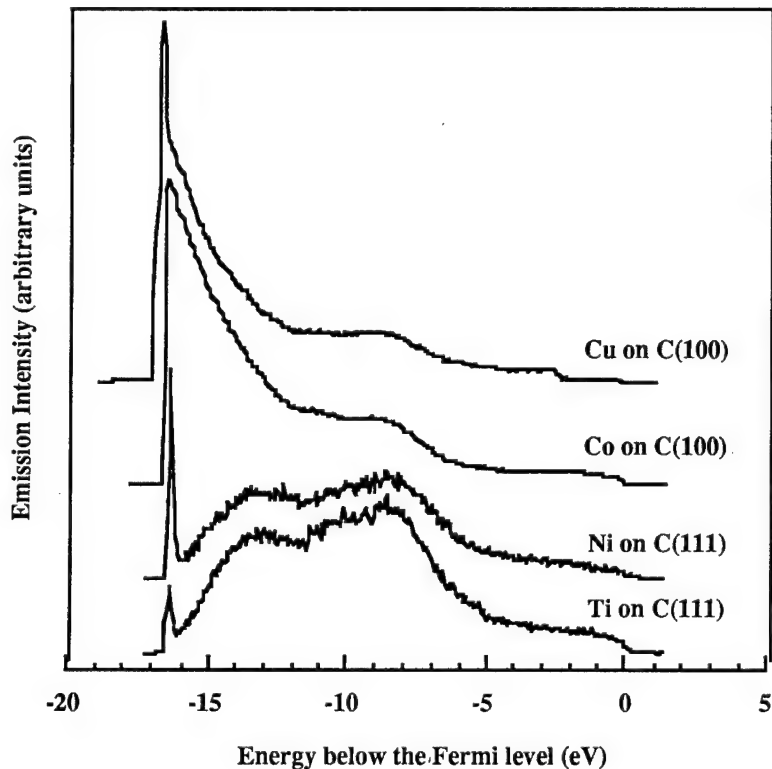
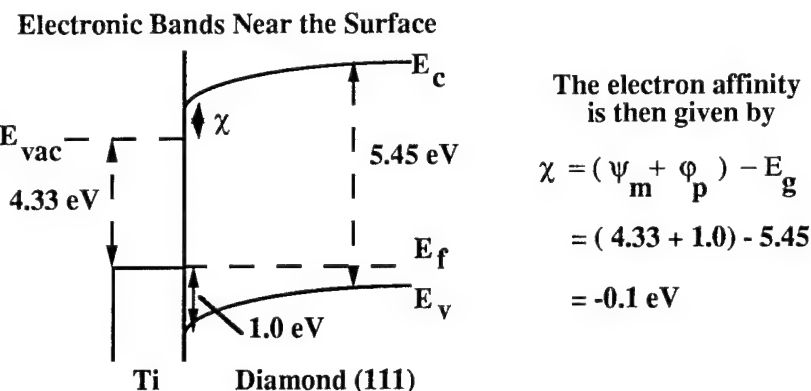


Figure 6. UV-photoemission spectra of diamond surfaces with thin metal overlayers. The metal thicknesses correspond to several monolayers.

A surface dipole, as noted in the introduction, is critical in establishing the relation between the band structure of the semiconductor and the vacuum. For the case of the metal overlayer, the dipole is actually established at the metal semiconductor interface. This is the same dipole that results in the Schottky barrier. The vacuum level is referenced to the metal through the metal workfunction and the interface dipole references the band structure of the semiconductor to the metal.

Of the results obtained to date, the most significant may be the observation of a NEA of Co on diamond (100) [13]. These films have been shown to be uniform with little tendency to islanding as has been observed for Ni and Cu [14]. In addition, it has been shown Ti-oxide will also cause an NEA on the (111) surface [15] and this surface could also prove more stable than the pure metal layers.



**Figure 7.** The band structure at the surface of diamond with a thin metal coverage. The electron affinity can be deduced from the Schottky barrier, the metal workfunction and the diamond bandgap. The numbers for Ti on diamond (100) are illustrated.

#### D. Device Issues

In the past few years, there has been significant interest in several applications that could involve vacuum electron emission. One of the most discussed applications is for displays [16]. There have been several recent demonstrations of field emission displays using arrays of point emitters. The sharp point emitters result in a field enhancement at the tip and a possible reduction in the workfunction due to the steps on the surface. The current versus voltage from a field emitter follows the Fowler-Nordheim expression. Other possible applications of field emitters is vacuum microelectronics and large-area cold cathodes for high-frequency or high-power applications.

The advantage of vacuum over semiconductor applications is in the breakdown field and the mobility of the electrons. The breakdown field of any vacuum device would be determined by the surfaces of cathode or anode rather than the semiconductor. Of course, the carriers are

free from phonon scattering in the vacuum and the trajectories would be essentially ballistic paths.

The I-V dependence of an ideal NEA-based emitter would exhibit emission at any (negative) voltage. At low fields the current would be limited by the space charge in the vacuum around the emitter (following Child's law) and at higher voltage the current would be limited by the resistance of the semiconductor and the contact. The energy distribution of the emitted electrons from a NEA cathode should be very narrow ( $\sim kT$ ), and it should exhibit a noise component related to the resistance of the semiconductor and contact. This is in contrast to either thermal emitters (i.e. hot cathodes) or field emitters that exhibit fluctuations based on the statistics of the highest energy part of the electron distribution.

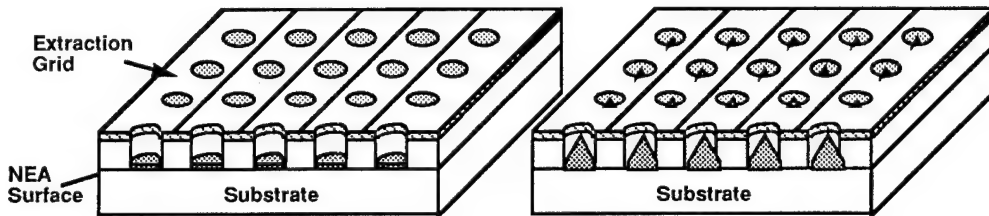


Figure 8. Schematic of cold cathode grid structures employing either a flat NEA surface or a pointed emitter.

An electron emitter based on a negative electron affinity material would have several unique advantages over pointed field emitters. These would include low turn-on voltage, high current, low erosion, and low noise. Figure 8 compares two structures that could be employed in the applications noted above. The field emitter would require a significant field established through a potential between the tip and grid layer. In contrast, the NEA device would be controlled by a small field established by the grid to balance the anode to cathode field.

The research described here and the advances of others has established that obtaining a NEA surface is achievable. It is likely that these surfaces could be made stable for relatively high current emission. The major technological problem is supplying electrons to the conduction band of diamond. The studies described here employed above bandgap light to excite carriers. There may be some applications where light excitation can be used in cathode structures. A more desirable situation is to obtain an ohmic contact to an n-type NEA semiconductor. This involves a true challenge for diamond since reliable n-type doping is not readily obtainable. Furthermore, the ohmic contact to the n-type semiconductor could also be troublesome since a very low workfunction material would be the obvious choice. This may not be necessary, though, if high levels of n-type doping are achievable.

### E. Acknowledgment

This work was supported in part by the Office of Naval Research and the Ballistic Missile Defense Organization.

### F. References

1. Zangwill, A (1988), *Physics at Surface*, (Cambridge).
2. F. J. Himpsel, J. A. Knapp, J. A. van Vechten and D. E. Eastman, Phys.Rev. **B20**, 624 (1979).
3. Pate, B.B. (1986). Surf. Sci. **165**, 83.
4. J. van der Weide and R. J. Nemanich, Applied Physics Letters **62**, 1878 (1993).
5. C. Bandis and B.B. Pate, Phys. Rev. Lett. **74**, 777 (1995).
6. R. J. Nemanich, L. Bergman, K. F. Turner, J. van der Weide and T. P. Humphreys, Trieste Semiconductor Symposium on Wide-Band-Gap Semiconductors, Physica B **185**, 528 (1993).
7. J. van der Weide, Z. Zhang, P. K. Baumann, M. G. Wensell, J. Bernholc and R. J. Nemanich, Physical Review B **50**, 5803 (1994).
8. J. van der Weide and R. J. Nemanich, J. Vac. Sci. Technol. B **12**, 2475 (1994).
9. P. K. Baumann and R. J. Nemanich, J. Diamond Mat. (in press).
10. J. van der Weide and R. J. Nemanich, J. Vac. Sci. Technol. B **10**, 1940 (1992).
11. J. van der Weide and R. J. Nemanich, Physical Review B**49**, 13629 (1994).
12. P. K. Baumann, T. P. Humphreys and R. J. Nemanich, Mat. Res. Soc Symp. Proc. **339**, 69 (1994).
13. P. K. Baumann and R. J. Nemanich, "Negative electron affinity effects and Schottky barrier height measurements of Co on diamond (100) surfaces," this Proceedings.
14. P. K. Baumann, T. P. Humphreys, R. J. Nemanich, K. Ishibashi, N. R. Parikh, L. M. Porter and R. F. Davis, J. Diamond and Related Materials **3**, 883 (1994).
15. C. Bandis, D. Haggery and B. B. Pate, Mat. Res. Soc. Symp. Proc. **339**, 75 (1994).
16. K. Derbyshire, Solid State Technology **37**, 55 (1994).

## VIII. Characterization of Electron Emission from Cold Cathode Emitters

### A. Introduction

The search for cold cathode devices has received much attention recently. To find a device that can emit electrons with just a few volts applied is a goal for both research and industry. In the past, there have been several potential solutions for electron emission. One method uses high electric fields produced by metal tips to cause electrons to tunnel into vacuum. However, these cathodes are unstable at high current densities. Another method uses conventional semiconductors such as Si or GaAs covered with a layer of Cs. Due to band bending, the conduction band of the material lies below the vacuum energy level. When a bias is applied, high current densities of greater than  $1500 \text{ A/cm}^2$  can be measured. The disadvantage of such a device is that it is easily contaminated after exposure to  $\text{O}_2$ . A third method would be to use wide bandgap materials such as AlN or diamond which can have their conduction band close to the vacuum energy level even in the presence of  $\text{O}_2$  or  $\text{H}_2\text{O}$ . These materials can be doped or grown in different ways to make them acceptable electron emitters [1]. Whatever the method employed, a testing station is needed to characterize the electron emission.

An example of a device pursued by M. Geis *et al.* [2] using diamond is shown in Fig. 1. The diodes are fabricated by carbon ion implantation into p-type diamond and covered with one micron of aluminum. The diode current  $I_D$  was varied from 0.1 mA to 10 mA with a bias voltage  $V_D$  of -60 to -150 V. The voltage between the anode and the p-type diamond substrate was usually 100V, and the anode current  $I_A$  varied from  $1e-13\text{A}$  to  $5e-7\text{A}$ .

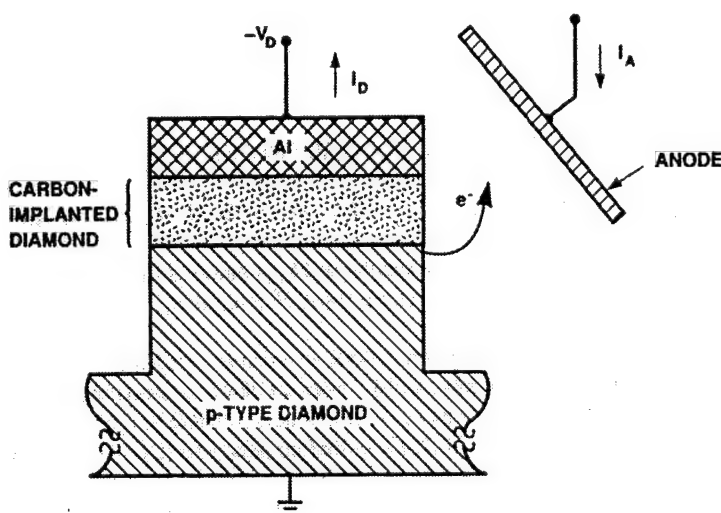


Figure 1. A typical diamond cold cathode built by M. Geis *et al.*

## B. Experimental Procedure

The layout of the High Vacuum I-V / Optics Station is shown in Fig. 2. The chamber, pumps, data acquisition, and source-measure components have been obtained and assembled. The vacuum chamber will be used for carrying out the measurements described below. With the existing pumps on the system, a pressure of 5e-8 Torr can be reached.

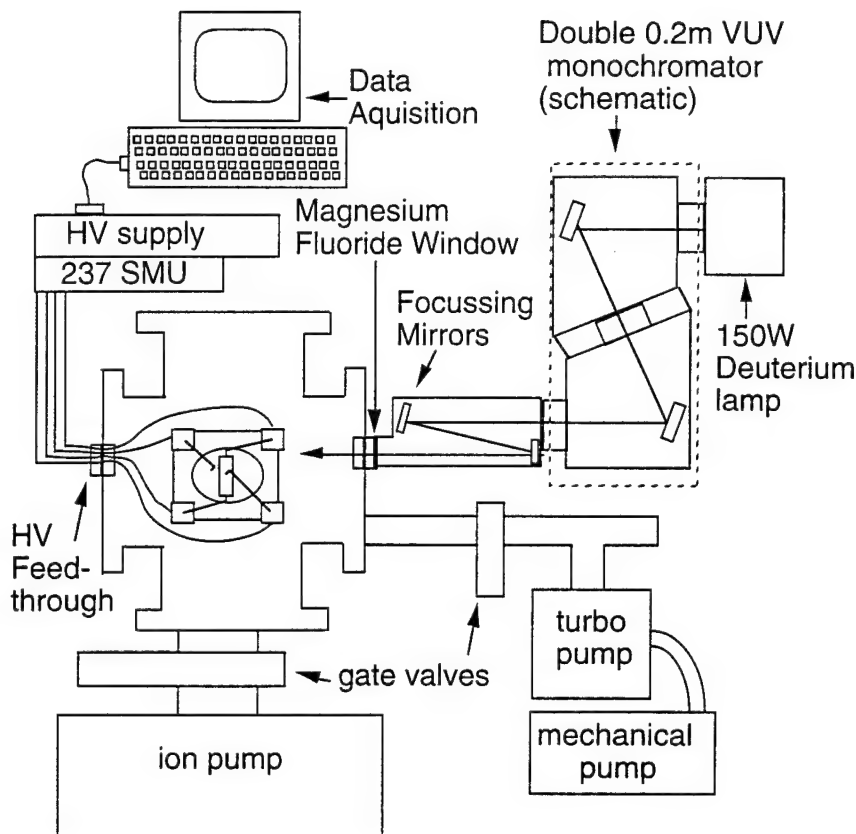


Figure 2. High Vacuum I-V / Optics Station.

The first of the measurements that will be attempted is a simple two-pole DC measurement as shown in Fig. 3. A collector will be used to draw the electrons out of the sample. The collector consists of a platinum wire imbedded in a Teflon block. The voltage between the anode and the sample can be varied between -1100 Volts and +1100 Volts using a Keithley 237 Source Measure Unit. The distance between the collector and the sample can be adjusted from outside of the vacuum chamber with an ultra-high vacuum stepper motor. With this motor, distances of a few microns can be achieved.

The second DC measurement to be carried out will be a three-pole measurement as shown in Fig. 4. The collector will be attached to a micrometer or a piezo-electric positioner. Electrons are emitted from the surface by applying a voltage across the sample. The current between the sample and the collector will be measured as a function of sample bias.

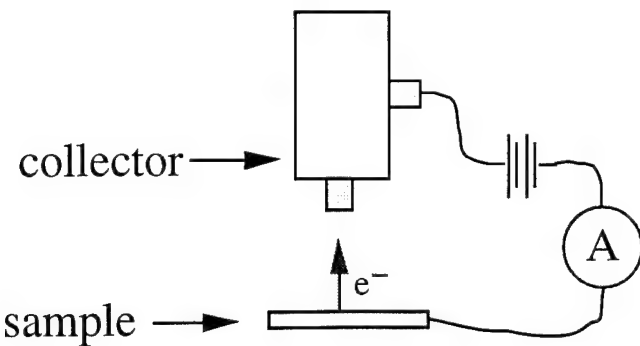


Figure 3. A two-pole DC measurement with a platinum wire imbedded in a Teflon block as a collector. The diameter of the platinum wire is 2.0mm.

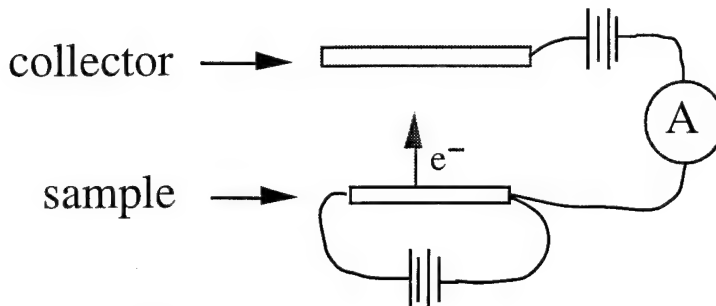


Figure 4. A three-pole DC measurement using a micrometer or piezo-electric positioner as a collector.

The third DC measurement will be a four-pole measurement where the set-up would be the same as that for the three-pole measurement with a gate included for amplification of the current. Current-voltage readings between the collector and the sample can be taken as a function of gate bias.

A fourth type of measurement is a quantum efficiency measurement. Quantum efficiency is defined as the ratio of the number of electrons emitted from a sample per photon incident on that sample. The photo-excitation of the sample will be carried out with a monochromatic light source. The wavelength range that can be covered with a high vacuum monochromator would be from 120nm to 400nm using a 150 W Deuterium light source. The bandgaps of both diamond and AlN fall well within this range. Operating in this wavelength range would give an understanding of any defect level that may be present in the bandgap of the material. If electrons are emitted from the sample, they can be collected with a grid as shown in Fig. 5.

### C. Discussion and Conclusion

The reason for the quantum efficiency measurement, other than applying a merit value to the device in question, would be to study any competing mechanisms which could inhibit

electron emission. A quantum efficiency number would indicate just how much these mechanisms inhibit electron emission.

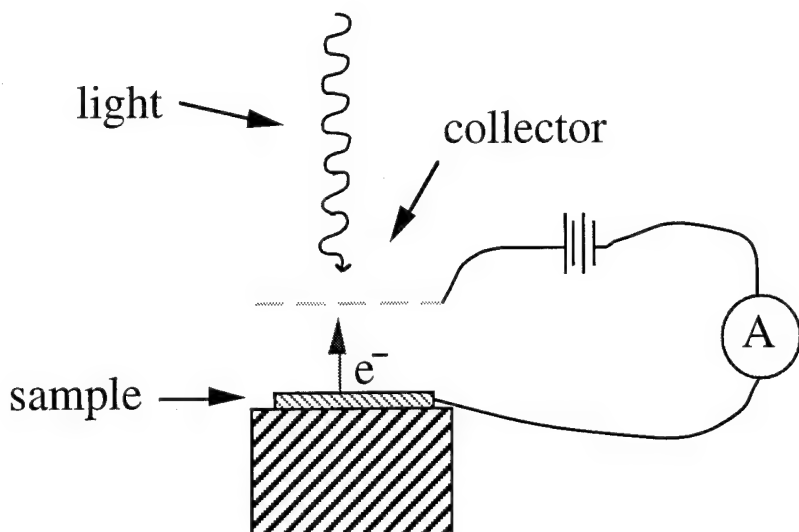


Figure 5. Photo-excitation of the sample with monochromatic light.

Two competing mechanisms are shown in Fig. 6. After an electron is excited into the conduction band from the valence band, one of three events can happen. One, if there is a defect level in the lattice, the electron can be captured at an empty center. If the defect level captures a hole from the valence band also, then an indirect transition has occurred. Two, the electron has a certain probability of decaying to the valence band instead of being emitted. The

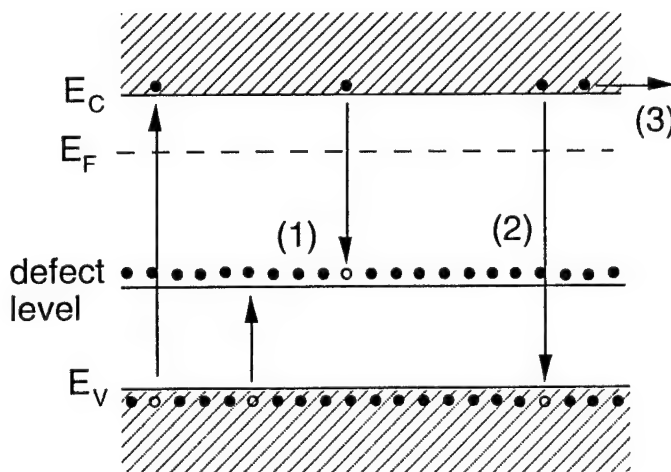


Figure 6. Two competing mechanisms: (1) indirect transition and (2) direct transition. If neither of these events occur then (3) the electron can be emitted.

electron has made a direct transition in this case. Three, if neither of the previous events occur, then the electron has a probability of being emitted. These two competing mechanisms, indirect transition through a defect level or direct transition to the valence band can inhibit electron emission and cause the device quality to be poor.

In conclusion, DC measurements and photo-excitation measurements can give us an understanding of how to design a cold cathode device. Each device that is fabricated can be characterized in vacuum using these methods.

#### D. Future Plans and Goals

Near future work includes annealing the sample to extreme temperatures to see how this affects the measurements discussed above.

#### E. References

1. M. W. Geis, N. N. Efremow, J. D. Woodhouse, M. D. McAleese, M. Marchywka, D. G. Socker and J. F. Hochedez, IEEE Electron Device Letters **12**, 456 (1991).
2. M. W. Geis, N. N. Efremow, J. D. Woodhouse and M. D. McAleese, "Diamond Cold Cathodes," in *Proceedings of the First International Conference on the Applications of Diamond Films and Related Materials*, Y. Tzeng, M. Yoshikawa, M. Murakawa and A. Feldman, Ed., Elsevier Science Publishers, 1991, pp 309-310.

## IX. Angular Resolved UPS (ARUPS) Investigation of 6H SiC Electronic Surface Structure

### A. Introduction

The necessity for electronic devices with higher performance characteristics is ever increasing, and thus, surface cleaning without damage becomes especially important. Electronic performance is related to electronic structure, therefore, electronic structure as a function of the cleaning process must be examined. Because SiC tends to graphitize with annealing, a cleaning procedure which allows replacement of lost Si is desirable. R. Kaplan investigated this by annealing  $\beta$  and 6H SiC samples in a silicon flux[1]. Hydrogen plasma processing has been demonstrated in cleaning silicon wafers[2]. The use of silane annealing (CVD cleaning) and a 1% silane/H<sub>2</sub> gas mixture has been discussed in a previous report[3]. This report focuses on the CVD cleaning process and characterization of the surface states.

UPS was used to examine the electronic states of the processed surface. Surface states, possibly caused by dangling bonds on a clean surface, were observed. Surface states appeared as distinctive features in the spectra. ARUPS was used to measure the dispersion of the surface momentum states. The surface state features of the spectra were sensitive to chemisorption of atoms or molecules to the surface[4]. Hydrogen termination was used in an attempt to further study Fermi level pinning by surface states[5].

### B. Experimental Procedures

These studies were performed in an integrated ultra high vacuum transfer system. The details of the system have been presented elsewhere[6]. The capabilities included plasma processing, UPS, XPS, MBE, LEED and Auger electron spectroscopy (AES).

The sample used for this study was a 1 inch (25 mm) n-type SiC wafer. The wafer was the Si-terminated (0001) surface oriented 3-4° towards the [11̄20] surface. Tungsten was deposited on the back of the wafer to allow for uniform heating of the sample. Earlier work involved Pt as the backing material. This proved unsatisfactory as the Pt-C compounds formed were not stable at experimental temperatures. In one case, Pt appeared to diffuse through the sample. The *ex situ* preparation was a 10 minute dip in 10% HF solution.

For cleaning in the Gas Source Molecular Beam Epitaxy (GSMBE) system, the following procedures were used. Once in vacuum, the SiC crystals were inserted into the ALE system where they were outgassed at 250°C, 450°C, and 700°C for 30 minutes prior to any silane cleaning. All samples treated in this manner exhibited (1×1) LEED patterns. For CVD cleaning in the GSMBE, we exposed the sample to 1200 Langmuirs of silane for 15 minutes.

The plasma system has a base pressure of  $1.0 \times 10^{-9}$  Torr but operates in the milliTorr range of pressure. Hydrogen of up to 100 sccm can flow into the system. One may also flow, at a rate of 10 sccm, a mixture of 1% silane/H<sub>2</sub>. Power is coupled into the chamber through rf

induction. Typical power rates are from 20 to 400 watts depending on the type of cleaning/etching desired. For CVD cleaning in the plasma chamber, 10 sccm of 1% SiH/H was used which gave a pressure of 25 mTorr. The annealing temperature was held at 825°C for 5 minutes. CVD cleaning in the plasma system was virtually identical to the GSMBE. However, the higher flux allows for quicker processing. Hydrogen termination was accomplished by 1 minute of flowing 86 sccm of H<sub>2</sub> (giving a pressure of 16 mTorr) with 20 Watts of power at a temperature of 450°C.

The UPS chamber had a base pressure of  $2 \times 10^{-10}$  Torr. Operating conditions involved pressures up to  $1 \times 10^{-9}$  Torr, but the higher pressure was due to the helium inflow and did not contaminate the sample. The UPS system utilized a helium resonance lamp (the He I line) to provide a source of 21.2 eV light. The ability existed to use the neon 16.8 eV emission line. This was useful for distinguishing between bulk and surface features. The bulk states will shift with respect to the Fermi level while surface features will not. Photoemitted electrons were measured with a 50 mm mean radius hemispherical electron analyzer operated at a 0.15 eV energy resolution and a 2° angular resolution. The analyzer (VSW HA50) is mounted on a double goniometer and can be tilted with respect to the sample in two independent directions. This capability was used to perform angular resolved UPS (ARUPS). Angles of up to 40° were examined for various reconstructions of the surface. The SiC samples were fastened by tantalum wire to a molybdenum sample holder. The sample holder was biased by up to 4 V to allow low energy electrons to overcome the work function of the analyzer. The Fermi level of the system (sample and analyzer) was determined by UPS measurement of the sample holder with no sample bias (i.e., grounded). The sample holder can be heated to 1150 °C.

The sample was examined in the case of the 3×3 reconstruction and the  $\sqrt{3} \times \sqrt{3}$  R30° reconstruction as well as the 1×1 case. In some cases annealing was required to obtain the 1×1 surface and was always necessary to obtain the  $\sqrt{3} \times \sqrt{3}$ .

### C. Results

The surface was cleaned by an *ex situ* 10% HF dip for 10 minutes to remove thick oxide. This was followed by annealing the sample in a silane flux. The silane flow was 10 sccm of 1% SiH<sub>4</sub>/H<sub>2</sub> for 5 minutes while a temperature of 825°C was maintained. AES of this process, along with the LEED pattern, is shown in Fig. 1 and compared to an *ex situ* clean alone. These parameters resulted in substantial removal of oxygen and surface hydrocarbons. The CVD clean resulted in a 3×3 reconstruction, possibly due to a silicon adatom structure, indicating a Si rich surface.[7]

The CVD clean removed substantial amounts of oxygen and hydrocarbons. This produced an ordered surface with a 3×3 reconstruction. From the Auger spectra, a Si/C ratio of 1.8

indicating a silicon rich surface was determined. The LEED pattern was attributed to a Si adatom structure. The  $1\times 1$  LEED pattern seemed to occur for a wide range of Si/C ratios. The  $\sqrt{3} \times \sqrt{3}$  surface arose from annealing the  $1\times 1$  and was shown by Auger to be Si deficient.

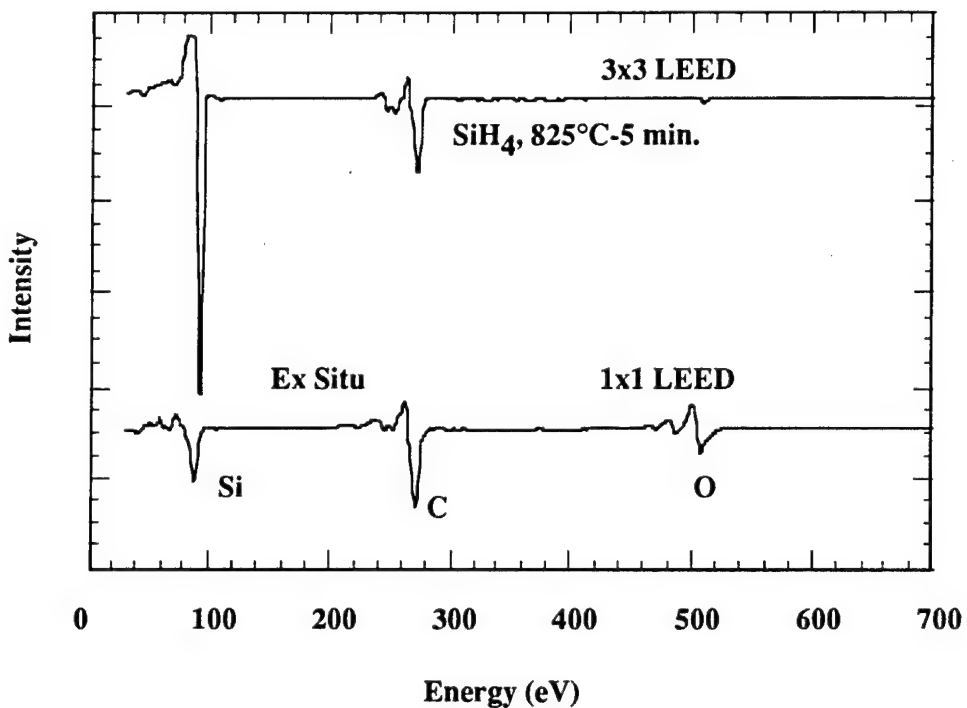


Figure 1. Silane CVD clean of 6H SiC.

ARUPS scans were performed on the CVD cleaned sample, a reconstructed sample, the unreconstructed  $1\times 1$  surface and a hydrogen terminated clean sample. The  $\sqrt{3} \times \sqrt{3}$  R $30^\circ$  surface was prepared by annealing to  $960^\circ\text{C}$  without a silane flow and was silicon deficient. The hydrogen terminated surface was a CVD cleaned sample which had a LEED pattern of  $1\times 1$ . It was exposed to a hydrogen plasma to investigate the role of dangling bonds in the UPS spectra. The UPS data for the three main surfaces appear in Fig. 2.

The angular dispersion of the  $3\times 3$  surface is shown as a representative spectra for the dispersion studies, see Fig. 3.

The UPS investigation yielded very interesting results. Features in the spectra were seen which may be surface states. Note that the substrate is n type, yet in all cases emission started near the Fermi level; this suggested Fermi level pinning. Surface states were distinguishable from those of the bulk by using light of a different energy, as discussed above. To test the origin of the state, the plasma system was used to terminate the surface with hydrogen. As seen in Fig. 4, this resulted in the partial removal of the feature and a shift of the spectra away from the Fermi level. This change was attributable to the passivation of the surface. The dangling

bonds were satisfied by the hydrogen atoms which terminated the surface. Without the H termination, Fermi level pinning was achieved.

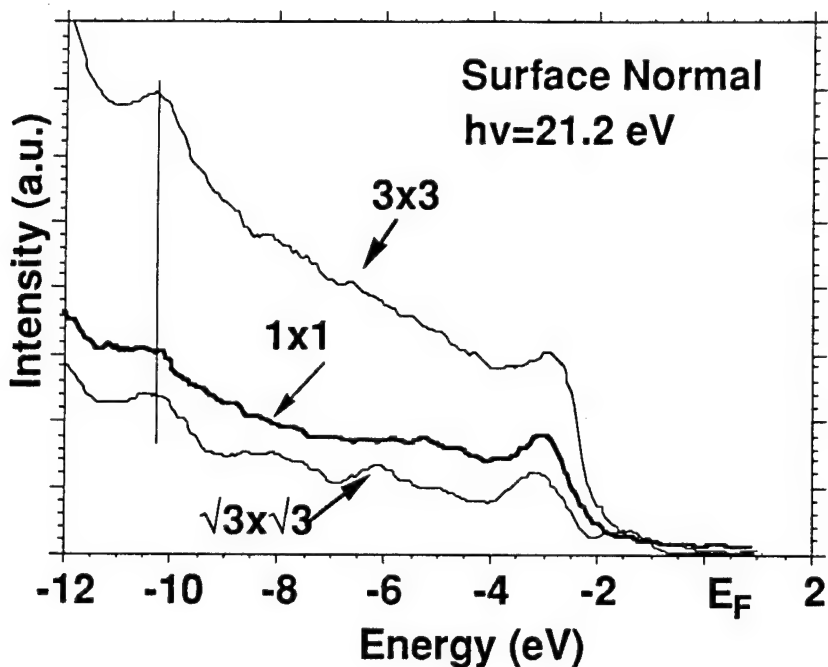


Figure 2. SiC electronic structure.

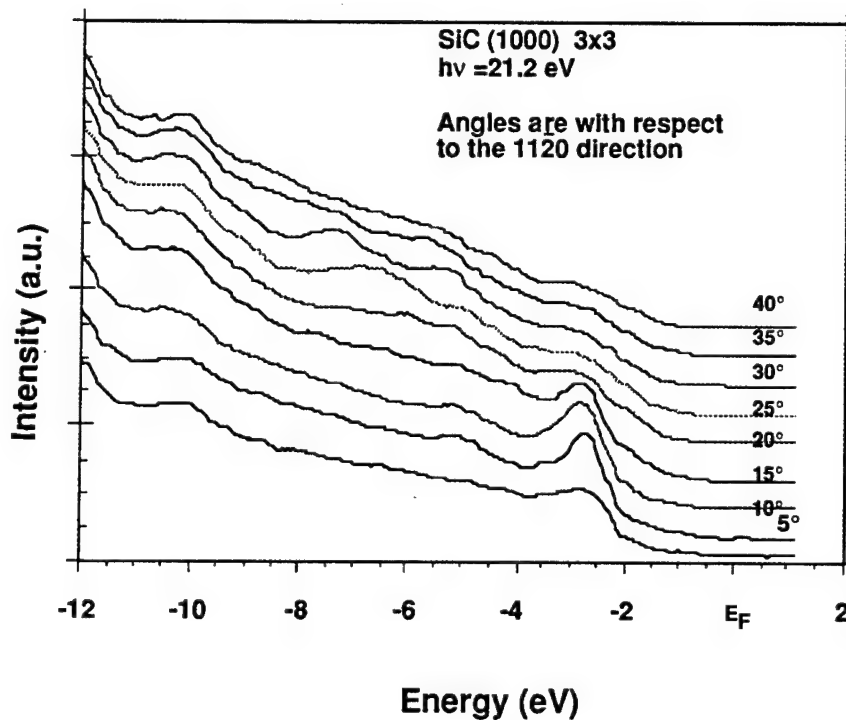


Figure 3. Angular dispersion of the  $3\times 3$  SiC surface.

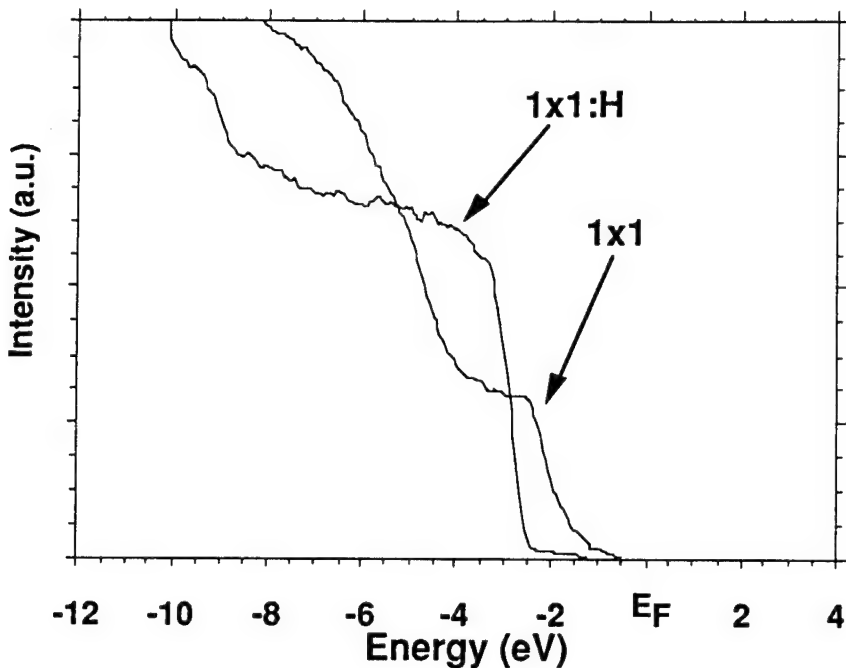


Figure 4. H termination unpins the Fermi level.

#### D. Discussion

Removing oxide and other contaminants from the surface allowed features in the spectra which were attributed to surface states in the electronic structure to be seen. These surface states were due to either dangling bonds on the surface or possibly back bonds to the C underlayer. The  $\sqrt{3} \times \sqrt{3}$  surface appeared to have the most structure. The  $1\times 1$  surface, as mentioned previously, did not seem to be a unique surface, i.e. different stoichiometry gives the same  $1\times 1$  LEED pattern.

The effect of hydrogen termination confirmed that the UPS features were due to surface states. XPS confirmed the shift in spectra and was followed by Thermal Programmed Desorption (TPD) which showed large amounts hydrogen desorption. After this treatment, the shift was removed.

The usefulness of ARUPS allows mapping of the dispersion of the  $k$  states parallel to the surface. A discussion of this can be found in Uhrberg and Hannson's review [4]. The relation between the energy and the momentum states is given by

$$k_{||} = \sin \theta e \sqrt{\frac{2mE_{kin}}{h^2}}$$

where  $\theta_e$  is the angle of emission with 0 degrees as normal emission and  $E_{kin}$  is the kinetic energy of the photoemitted electrons. Using this relation, the dispersion as a function of wavevector was plotted, see Fig. 5.

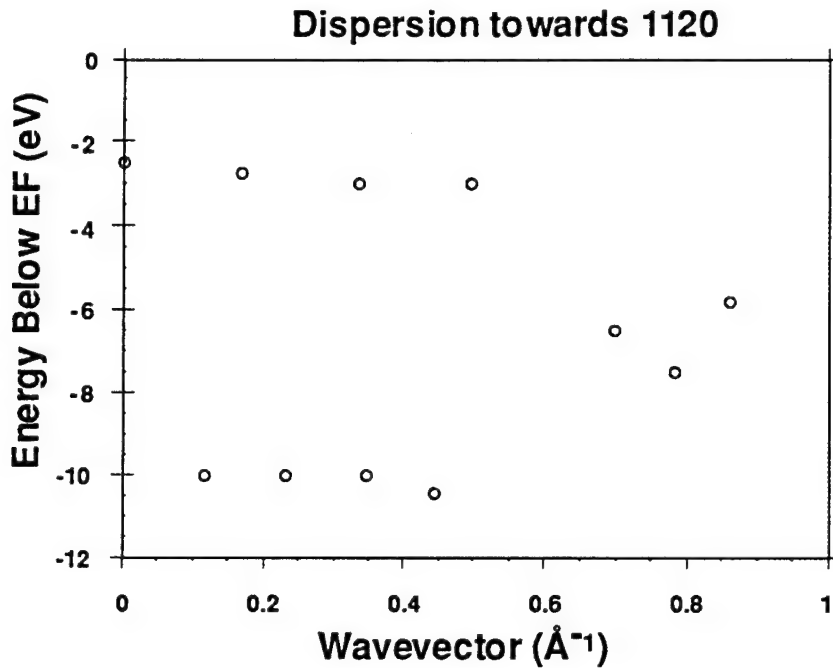


Figure 5. Wavevector dispersion.

#### E. Conclusions

Cleaning was demonstrated of 6H vicinal SiC substrates by silane CVD methods which have improved the pure chemical etch method. Substantial removal of surface hydrocarbons and oxides was shown. The  $1\times 1$  LEED pattern was not a good indicator of the surface cleanliness and, given the range of stoichiometries exhibited, it was not a useful indicator of surface condition.

The observation of surface states on SiC was made. All of the surfaces (except the hydrogen terminated) exhibited some degree of surface resonance (surface state). The  $\sqrt{3}\times\sqrt{3}$  surface showed the most structure. This might be due to a higher number of dangling bonds per area. The hydrogen termination of the surface unpins the Fermi level. This was confirmed by both UPS and XPS. The removal of termination and the subsequent return of surface state features further strengthen the argument for dangling bonds as the cause of the surface features.

#### F. Future Plans

Further investigation of the surface state structure will be made by UPS. The surface has sufficient study to include metal overlayers and to begin ARUPS studies of Schottky barriers

on 6H SiC. This probe of the surface structure should lead to a better understanding of surface kinetics which in turn should help further develop the contact and heterojunction processes. An additional metallization chamber which has come on line will speed this research thrust as more metals will be available at the same time.

A chamber for HF vapor phase cleaning is in development for addition to the integrated transfer system. This will present an opportunity to investigate this mode of processing.

#### G. Acknowledgments

This work was supported in part by the Office of Naval Research through grants N0014-92-J-1477 and N0014-92-J-1604. The SiC substrates used were supplied by Cree Research. S. W. King provided XPS and the GS-MBE work. J. P. Barnak provided assistance with the plasma chamber as well as discussion. R. S. Kern was a valuable source of information.

#### H. References

1. R. Kaplan, Surface Science **215**, 111 (1989)
2. R. A. Rudder, S. V. Hattangady, J. B. Posthill, and R. J. Markunas, Mat. Res. Soc. Symp. **116**, 529 (1988)
3. ONR Semiannual Technical Report December 1994
4. R. I. G. Uhrberg , G. V. Hansson, Critical Reviews in Solid State and Materials Sciences, **17** (2) 136 (1991)
5. J. Pelletier, D. Gervais, and C. Pomot, J. Appl. Phys. **55**, 994 (1994)
6. J. van der Weide, R. J. Nemanich, J. Vac. Sci. Technol. B **10** 1940 (1992)
7. R. Kaplan

## X. Homoepitaxial Growth of Silicon Carbide Polytypes by Gas-Source Molecular Beam Epitaxy

### A. Introduction

Silicon carbide (SiC) is a wide band gap material that exhibits polytypism, a one-dimensional polymorphism arising from the various possible stacking sequences of, e. g., the silicon and carbon layers along the directions of closest packing. There are approximately 250 SiC polytypes[1]. Included in these is one cubic polytype. This single cubic polytype,  $\beta$ -SiC, crystallizes in the zincblende structure, has a room temperature band gap of 2.3 eV, and is commonly referred to as 3C-SiC. (In the Ramsdell notation, the three (3) refers to the number of Si and C bilayers necessary to produce a unit cell and the C indicates its cubic symmetry.) The other rhombohedral and hexagonal polytypes are classed under the heading of  $\alpha$ -SiC. The most common of these latter polytypes is 6H-SiC with a room temperature band gap of  $\approx$  3.0 eV.

Since the 1950's, monocrystalline single crystals of 6H-SiC have been grown at using the Lely sublimation process[2]. However, nucleation was uncontrolled using this process and control of resultant polytypes was difficult. SiC single crystals inadvertently formed during the industrial Acheson process have also been used as substrates for SiC growth. However, neither these nor those formed using the Lely process are large enough for practical device applications. Recently, using a seeded sublimation-growth process, boules of single polytype 6H-SiC of >1 inch diameter of much higher quality of that obtained using the Lely process have been grown. The use of single crystals of the 6H polytype cut from these boules has given a significant boost to SiC device development.

SiC epitaxial thin film growth on hexagonal SiC substrates has been reported since the 1960's. The use of nominally on-axis SiC substrates has usually resulted in growth of 3C-SiC films. Films of 3C-SiC(111) grown by CVD have been formed on 6H-SiC substrates less than 1° off (0001)[3]. Films of 3C-SiC on 6H-SiC substrates have typically had much lower defect densities than those grown on Si substrates. The major defects present in  $\beta$ -SiC/6H-SiC films have been double positioning boundaries (DPB)[4]. Despite the presence of DPBs, the resultant material was of sufficient quality to further device development of SiC. The use of off-axis 6H-SiC(0001) substrates has resulted in growth of high-quality monocrystalline 6H-SiC layers with very low defect densities[5].

In addition, the use of more advanced deposition techniques, such as molecular beam epitaxy (MBE), has been reported for SiC in order to reduce the growth temperature and from about 1400-1500 °C on 6H-SiC substrates. Si and C electron-beam sources have been used to epitaxially deposit SiC on 6H-SiC (0001) at temperatures of 1150 °C[6]. Previous reports by all investigators have documented 3C-SiC growth only on 6H-SiC(0001) by MBE.

## B. Experimental Procedure

Thin, epitaxial films of SiC were grown on the Si-face of 6H-SiC(0001) substrates supplied by Cree Research, Inc. These vicinal 6H-SiC(0001) wafers, oriented 3-4° towards [1120], contained a 0.8 μm epitaxial 6H-SiC layer deposited via CVD and a thermally oxidized 75 nm layer to aid in wafer cleaning. A novel *in situ* cleaning procedure, described in previous reports, has been developed using reaction and desorption of the silicon-containing precursor (SiH<sub>4</sub>). The surface preparation procedure involves cleaning with 10% HF and a 10 minute anneal at 1050 °C in UHV, as well as a silane exposure and boil-off. This additional cleaning step, intended to remove any residual oxygen, fluorine or other contaminants and create a silicon terminated surface, exposes the substrate to 0.1 sccm SiH<sub>4</sub> for 2 minutes at 1050 °C until the surface undergoes a reconstruction from the 1×1 to 3×3 as observed by RHEED. This 3×3 reconstruction is indicative of a Si-rich surface. (For a description of the various surface reconstructions of SiC, please refer to Kaplan[7].) The 3×3 reconstructed samples were annealed at 1200 °C for 10 minutes causing them to revert to the 1×1 pattern. At this point the films were grown.

All growth experiments were carried out in the gas-source molecular beam epitaxy system detailed in previous reports. The new heater assembly[8], designed for high temperature attainment, has been installed and operates as expected allowing for substrate temperatures as high as 1500 °C. The sources of Si and C were SiH<sub>4</sub> and C<sub>2</sub>H<sub>4</sub> (both 99.99% pure), respectively. Flow ratios of SiH<sub>4</sub> and C<sub>2</sub>H<sub>4</sub> were varied from 2:1 to 2:3. Hydrogen (99.9995% pure) was also introduced at 5.0 sccm into the reaction chamber during some depositions. Substrate temperatures were varied from 1050-1450 °C. Typical base pressures of 10<sup>-9</sup> Torr were used. All experiments were performed for 2 hours on vicinal 6H-SiC(0001) substrates and examined by *in situ* reflection high-energy electron diffraction (RHEED) at the end of the growth run.

## C. Results

Most prior growth conditions have resulted in monocrystalline, epitaxial layers of 3C-SiC with rough surfaces and the appearance of three-dimensional growth originating at the terraces of the vicinal substrates. The resulting films have been generally cubic and contain double positioning boundaries as evidenced by the RHEED and HRTEM. These results have been detailed in previous reports. Sporadic deposition of 6H-SiC has also been achieved and described previously; however, a clear understanding of the growth conditions necessary to grow 6H-SiC had not been determined.

When no hydrogen was present in the reaction chamber, films of SiC grown at all temperatures and gas flow ratios were cubic. Experiments conducted when hydrogen was introduced into the reaction chamber resulted in cubic films at substrate temperatures below

1400 °C and 6H-SiC films at temperatures above this temperature. Although all SiC films were monocrystalline by RHEED analysis for all conditions studied, 6H-SiC was only achieved at substrate temperatures  $\geq$  1400 °C under 5.0 sccm hydrogen flow. Figure 1 shows representative patterns. There were essentially three different RHEED patterns that were observed. Figures 1a and 1b are characteristic of cubic SiC patterns. Figure 1a is typical of films grown at temperatures below 1100 °C; Figure 1b, higher temperatures. Figure 1c is characteristic of a hexagonal (6H) pattern.

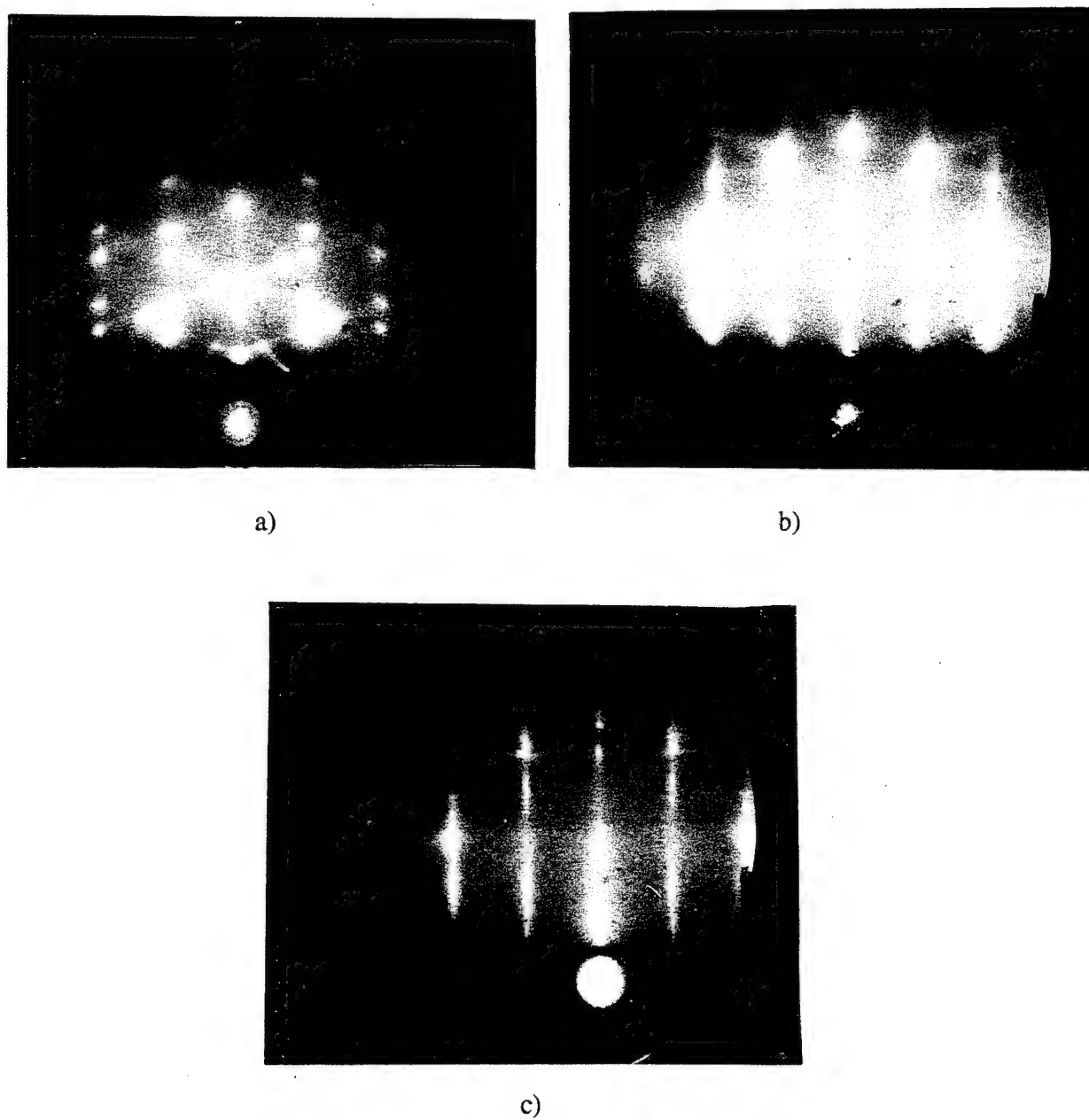


Figure 1. RHEED photographs for a) growth runs below 1100 °C, b) growth runs above 1100°C and c) growth runs above 1400°C in flowing H<sub>2</sub>.

#### D. Discussion

The use of hydrogen to produce homoepitaxial 6H-SiC is not a new technique. Hydrogen makes up the majority of the gas flow in CVD growth of SiC but has not been used previously in the MBE growth of SiC. The presence of hydrogen and the high temperatures of growth used here are necessary to achieve 6H-SiC films. It is expected that, at lower temperatures without the presence of atomic hydrogen, the decomposition of ethylene is incomplete without free silicon and, as a result, the films are a result of sporadic nucleation in locations where excess silicon species are present.

#### E. Conclusions

Preliminary studies into the growth conditions necessary to reproducibly achieve homoepitaxial 6H-SiC films have been performed. The initial results indicate that the most important factors in SiC polytype control (3C versus 6H) are the substrate temperature and the presence of hydrogen.

#### F. Future Research Plans and Goals

A study on both n- and p-type (with solid Al from a standard MBE effusion cell) is also underway. Further study of the effects of temperature, flow ratios and dopant incorporation are now being initiated.

#### G. References

1. G. R. Fisher and P. Barnes, *Philos. Mag. B* **61**, 217 (1990).
2. J. A. Lely, *Ber. Deut. Keram. Ges.* **32**, 229 (1955).
3. H. S. Kong, J. T. Glass, and R. F. Davis, *Appl. Phys. Lett.* **49**, 1074 (1986).
4. H. S. Kong, B. L. Jiang, J. T. Glass, G. A. Rozgonyi, and K. L. More, *J. Appl. Phys.* **63**, 2645 (1988).
5. H. S. Kong, J. T. Glass, and R. F. Davis, *J. Appl. Phys.* **64**, 2672 (1988).
6. S. Kaneda, Y. Sakamoto, T. Mihara, and T. Tanaka, *J. Cryst. Growth* **81**, 536 (1987).
7. R. Kaplan, *Surface Sci.* **215**, 111 (1989).
8. An invention disclosure explaining this heating element, made from SiC-coated graphite, has been submitted to the NCSU Technology Administration and Development Office.

## XI. Rectifying and Ohmic Contacts for P-Type Alpha (6H) Silicon Carbide

### A. Introduction

The formation of low resistivity and thermally stable ohmic contacts to 6H-SiC remains a serious problem in the development of SiC device technology. For SiC power devices to have the advantage over Si, the contact resistivities must be below  $1 \times 10^{-5} \Omega \text{-cm}^2$  [1]. In addition, the electrical characterization of state-of-the-art SiC films depends on the ability to fabricate ohmic contacts on material with low carrier concentrations. Therefore, better ohmic contacts are needed both for improving device performance and for improving the quality of films which can be grown. The thermal stability of ohmic contacts is of particular concern for p-type SiC, which have traditionally relied on Al or Al alloys to dope the SiC surface below the contacts. While the fabrication of ohmic contacts to SiC also has usually depended on very heavily-doped surfaces, the introduction of high levels of dopants in the near surface device region of the epilayer prior to the deposition of the contact or by ion implantation through the contact makes probable the introduction of point and line defects as a result of the induced strain in the lattice. Based on all of these issues and experiments already performed at NCSU, our goals are to produce contacts which are thermally stable and have low contact resistivities while also reducing the need for doping by ion implantation.

Low resistance contacts to p-type SiC remain a substantial challenge for high temperature and high-power devices. An Al-Ti alloy [2] annealed at 1000°C for 5 min. was reported to yield contact resistances ranging from  $2.9 \times 10^{-2} \Omega \text{ cm}^2$  for a carrier concentration of  $5 \times 10^{15} \text{ cm}^{-3}$  to  $1.5 \times 10^{-5} \Omega \text{ cm}^2$  for  $2 \times 10^{19} \text{ cm}^{-3}$ . The thermal stability of these contacts was not reported. Aluminum deposited on a heavily-doped 3C-SiC interlayer on a 6H-SiC substrate and subsequently annealed at 950°C for 2 min. reportedly yielded contact resistivities of  $2-3 \times 10^{-5} \Omega \text{ cm}^2$  [3]. Because of its low melting point (660°C), however, pure Al would be unsuitable for high temperature applications. Platinum contacts annealed from 450 to 750°C in 100°C increments were also used as ohmic contacts to p-type SiC [4]. These contacts, which rely on the combination of a highly-doped surface and the high work function of Pt, have not been known to yield contact resistivities as low as those for the contacts containing Al.

Because Ni forms stable silicides but not carbides, it has the potential to draw Si out of the lattice, allowing Al to diffuse into the SiC and occupy Si sites. In contrast, Ti forms a very stable carbide [5] in addition to silicides and therefore readily competes for the C in TiAl contacts. This report describes electrical characteristics and chemical profile results of as-deposited NiAl Schottky contacts and NiAl ohmic contacts annealed at 1000 °C (10 to 80 s) on p-type 6H-SiC (0001). Future experiments with these contacts are also discussed along with other contact schemes which do not incorporate Al.

## B. Experimental Procedure

Vicinal, single-crystal 6H-SiC (0001) wafers provided by Cree Research, Inc. were used as substrates in the present research. The wafers were doped with N or Al during growth to create n- or p-type material, respectively, with carrier concentrations of  $1\text{--}5 \times 10^{18} \text{ cm}^{-3}$ . Homoepitaxial layers (1–5  $\mu\text{m}$  thick) grown by chemical vapor deposition (CVD) were Al-doped with carrier concentrations ranging from  $1 \times 10^{16}$  to  $1 \times 10^{19} \text{ cm}^{-3}$ . The surfaces were oxidized to a thickness of 500–1000  $\text{\AA}$  in dry oxygen. The substrates were simultaneously cleaned and the oxide layer etched from the surface using a 10 min. dip in 10% hydrofluoric acid, transferred into the vacuum system, and thermally desorbed at 700 °C for 15 min. to remove any residual hydrocarbon contamination.

A UHV electron beam evaporation system was used to deposit the NiAl and Ni films. After depositing 1000  $\text{\AA}$  of NiAl, 500–1000  $\text{\AA}$  of Ni was deposited as a passivating layer. Pure Ni (99.99%) and pure Al (99.999%) pellets were arc melted to form alloyed pellets of 50:50 atomic concentration for evaporation of NiAl. The films were deposited onto unheated substrates at a rate of 10–20  $\text{\AA}/\text{s}$ . The pressure during the depositions was between  $5 \times 10^{-9}$  and  $5 \times 10^{-8}$  Torr.

Circular contacts of 500  $\mu\text{m}$  diameter were fabricated for electrical characterization by depositing the metal films through a Mo mask in contact with the substrate. Silver paste served as the large area back contact. For contact resistance measurements, TLM patterns [6] were fabricated by photolithography. The Ni/NiAl films were etched in phosphoric acid : acetic acid : nitric acid (12 : 2 : 3) at 50 °C (etch rate  $\approx 30 \text{ \AA}/\text{s}$ ). The contact pads were  $300 \times 60 \mu\text{m}$  with spacings of 5, 10, 20, 30 and 50  $\mu\text{m}$ . Mesas in the substrate were not fabricated. All subsequent annealing was conducted in a  $\text{N}_2$  ambient in a rapid annealing furnace.

Electrical characteristics were obtained from current-voltage and capacitance-voltage measurements. Current-voltage (I-V) measurements were obtained with a Rucker & Kolls Model 260 probe station in tandem with an HP 4145A Semiconductor Parameter Analyzer. Capacitance-voltage (C-V) measurements were taken with a Keithley 590 CV Analyzer using a measurement frequency of 1 MHz.

Auger electron spectroscopy (AES) was performed with a JEOL JAMP-30 scanning Auger microprobe. The films were sputtered with Ar ions at a beam current and voltage of 0.3  $\mu\text{A}$  and 3 kV, respectively, to obtain composition profiles through the thickness of the films.

## C. Results

*Chemical Characterization of As-deposited Films.* The composition of the NiAl films deposited at room temperature were analyzed with AES. The first films deposited were found to contain approximately 3 at. % O. This contamination was attributed to O found in the Ni source. Alloyed pellets were subsequently fabricated using a new Ni source (99.99%).

An Auger depth profile of a film deposited from the latter source is shown in Fig. 1. While there was some modulation of the intensities, the overall composition remained relatively stable. The relative intensities of Ni and Al calculated from pure Ni and pure Al standards and their corresponding sensitivity factors are shown in Fig. 2. The average atomic composition was approximately 50:50.

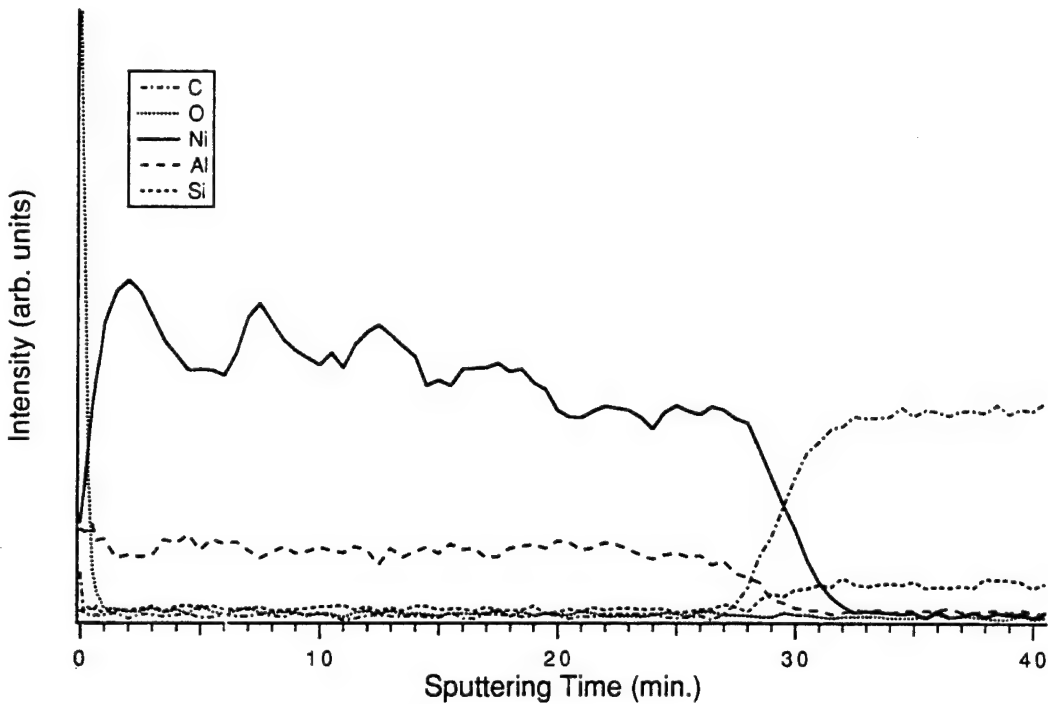


Figure 1. AES composition profile of 1000 Å of NiAl deposited at room temperature on (0001) 6H-SiC.

*Schottky contacts.* In the as-deposited condition the Ni/NiAl contacts were rectifying on p-type SiC with carrier concentrations of  $1.6 \times 10^{16}$  and  $3.8 \times 10^{18} \text{ cm}^{-3}$  in the epilayer. The sample with the lower carrier concentration displayed leakage current densities of  $\sim 1 \times 10^{-8} \text{ A/cm}^2$  at 10 V and ideality factors between 1.4 and 2.4, while the latter sample displayed approximately five orders of magnitude higher leakage current densities and similar ideality factors. The average Schottky barrier heights (SBH's) calculated for the samples with the lower and higher carrier concentrations were 1.37 and 1.26 eV, respectively. The lower SBH calculated for the former sample is likely due to enhanced thermionic field emission through the upper energy region of the barrier because of the narrower depletion region. Hence, the 1.37 eV value is believed to be more accurate.

Similar results were obtained for as-deposited Ni and Au contacts on p-type ( $2.1\text{--}4.5 \times 10^{16} \text{ cm}^{-3}$ ) 6H-SiC (0001). These samples displayed similar leakage currents and ideality factors of

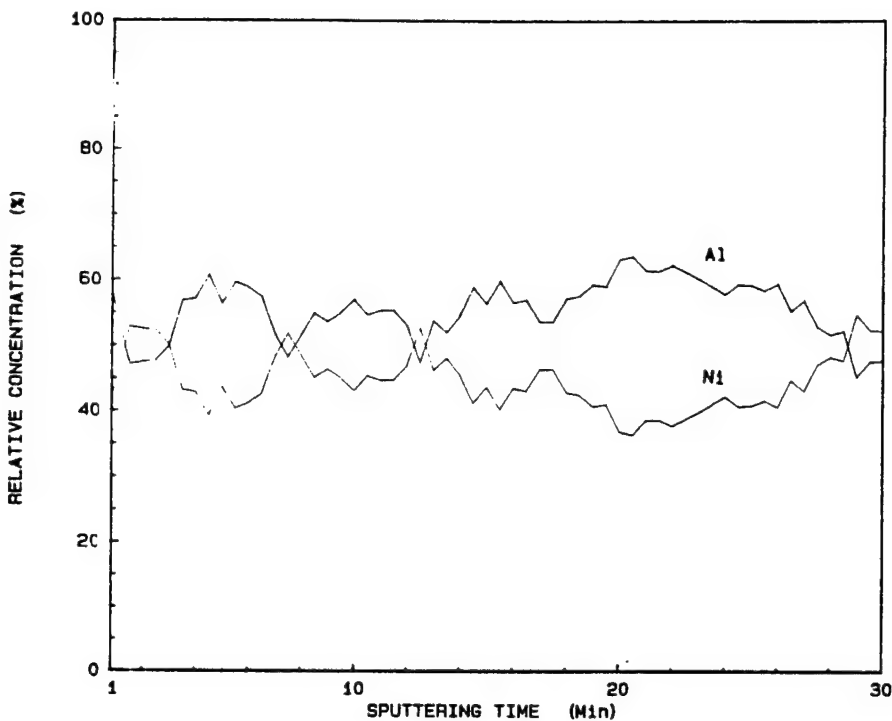


Figure 2. Relative concentrations of Ni and Al in the film represented in Fig. 1. The calculations were based on the signals from pure Ni and pure Al and their corresponding sensitivity factors.

1.3–2.1 and <1.1, respectively. From these measurements SBH's of 1.31 eV for the Ni contacts and 1.27 eV for the Au contacts were calculated. In comparison, as-deposited Ni on n-type ( $4.1 \times 10^{16} \text{ cm}^{-3}$ ) 6H-SiC (0001) yielded ideality factors below 1.1, similar leakage current densities to those stated above, and SBH's of 1.14 eV and 1.21 eV calculated from I-V and C-V measurements, respectively.

Our measurements on p-type SiC have shown consistent differences from measurements on n-type 6H-SiC. The SBH's tended to be higher on p-type than on n-type material. While leakage currents for Au, NiAl, and Ni contacts on p-type 6H-SiC were comparable to Ni contacts on n-type 6H-SiC, the ideality factors were higher on p-type SiC. The higher ideality factors for contacts on p-type SiC indicate that thermionic emission was not the dominant current transport mechanism. In the future we may investigate these contacts with deep level transient spectroscopy (DLTS) to determine whether recombination at deep levels accounts for the different electrical behavior of the contacts on p-type material.

*Ohmic Contacts.* The Ni/NiAl contacts were sequentially annealed for total times of 10–80 s at 1000 °C in a N<sub>2</sub> ambient. This temperature was used because (1) limited intermixing of Al and SiC was reported at 900 °C [7] and (2) other papers report annealing in this temperature range for Al-based ohmic contacts on p-type SiC [2, 3, 8]. Because of the extremely high thermodynamic driving force for Al to form an insulating oxide layer

$(\Delta G_f \text{ (Al}_2\text{O}_3) \sim -1300 \text{ kJ/mol at } 1000^\circ\text{C}$  [JANAF - Chase, M., et al., JANAF Thermochem. Tables, 3d Ed. J. Phys. Chem. Ref. Data, 1985, 14(Supp. 1)]), 1000 Å of Ni was deposited on top of the NiAl contacts to slow the oxidation process.

Table I summarizes the results of I-V measurements taken at selected intervals through the annealing series for three samples with various carrier concentrations in the SiC epitaxial layer ( $1.4 \times 10^{18}$ ,  $5.7 \times 10^{18}$ , and  $1.5 \times 10^{19} \text{ cm}^{-3}$ ). The two samples with the lower carrier concentrations were not truly ohmic but became ohmic-like after annealing for 80 s. This annealing series will be continued to determine whether ohmic behavior in these two samples will ensue; however, the additional force on the probes needed to obtain consistent results indicates that an oxide has begun to form at the surface and may cause problems with further annealing. The sample with the higher carrier concentration was ohmic after annealing for 10 s. The calculated specific contact resistivity remained approximately  $2.0 \times 10^{-2} \Omega \text{ cm}^2$  through annealing for 60 s. A slight increase to  $3.1 \times 10^{-2} \Omega \text{ cm}^2$  was calculated after annealing for 80 s. This increase is believed to be due to the surface oxide layer. These values of specific contact resistivity should only be considered as preliminary estimates since only one level of the TLM measurement pattern was used. In the near future we plan to employ a circular TLM measurement structure [9], which consists of only one level and does not involve etching of the substrate.

Table I. Estimated specific contact resistivities / electrical behavior of Ni (1000 Å) / NiAl (1000 Å) / p-SiC after annealing at  $1000^\circ\text{C}$  for 20, 40, 60, and 80 s for three samples with the carrier concentrations indicated. The specific contact resistivities were calculated from non-mesa etched linear TLM patterns.

Annealing Time	20 s	40 s	60 s	80 s
$1.4 \times 10^{18} \text{ cm}^{-3}$	non-ohmic	non-ohmic	non-ohmic	almost ohmic
$5.7 \times 10^{18} \text{ cm}^{-3}$	non-ohmic	non-ohmic	non-ohmic	almost ohmic
$1.5 \times 10^{19} \text{ cm}^{-3}$	$2.0 \times 10^{-2} \Omega \text{ cm}^2$	$1.9 \times 10^{-2} \Omega \text{ cm}^2$	$2.2 \times 10^{-2} \Omega \text{ cm}^2$	$3.1 \times 10^{-2} \Omega \text{ cm}^2$

#### D. Discussion

An Auger depth profile (Fig. 3) of Ni/NiAl/SiC annealed at  $1000^\circ\text{C}$  for 80 s shows that the surface oxide is thicker than that on the as-deposited sample (Fig. 1). After sputtering for a couple of minutes, the O concentration dropped to below detectable limits; however, the data shows a decreasing Al concentration in the direction toward the SiC interface. This indicates

that the kinetics are more favorable for the Al to diffuse toward the surface and react with O than for the Al to react with the SiC. Some of the Ni has probably reacted with Si at the interface to form a silicide, as indicated by the local maximum in the Ni intensity near the SiC interface, while the peak in the C intensity indicates the presence of an adjacent C-rich layer.

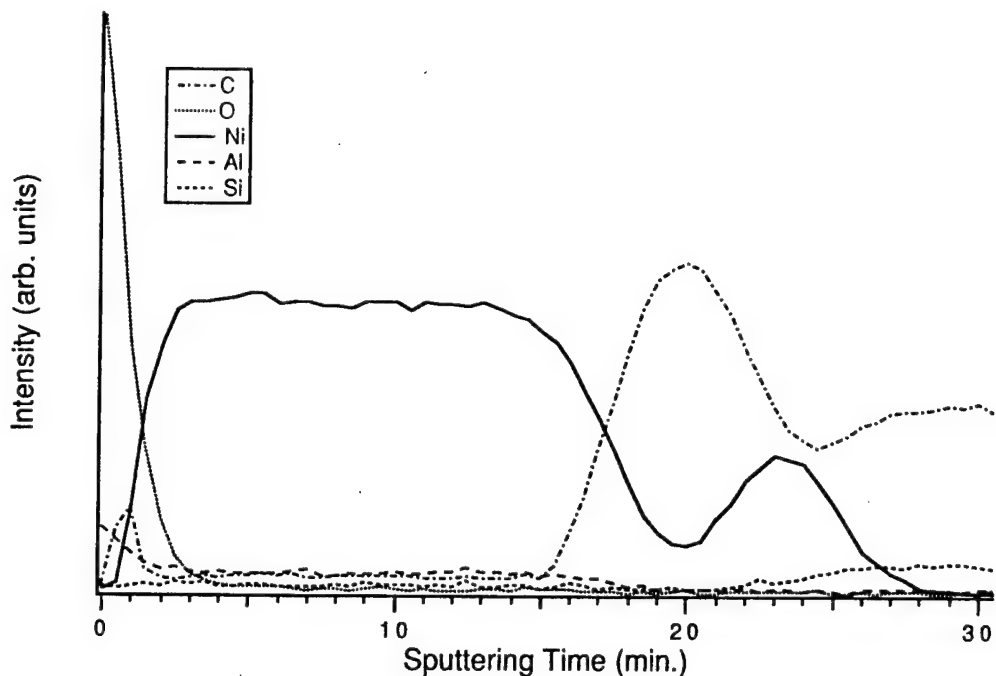


Figure 3. AES composition profile of Ni (1000 Å) / NiAl (1000 Å) / 6H-SiC annealed at 1000 °C for 80 s in N<sub>2</sub>.

The demonstrated oxidation problem with Al necessitates the development of ohmic contacts which do not consist of substantial concentrations of Al. The following section discusses future plans for finishing the experiments on NiAl contacts and for initiating experiments on novel contact materials.

#### E. Conclusions

Nickel-aluminum was investigated primarily as an ohmic contact for p-type 6H-SiC because of the p-type doping of Al in SiC, the high melting point of NiAl (as compared to Al), and the tendency of Ni to form silicides but not carbides. This latter property potentially could have resulted in extraction of Si from the SiC lattice in exchange for Al, thereby enhancing the p-type carrier concentration at the surface. Although the I-V measurements indicate that some Al may be diffusing into the SiC after the longest annealing time performed (80 s at 1000 °C), this potential for reaction between Al and SiC appears to be exceeded by the driving force for

Al to diffuse to the surface and react with O. A concentration profile obtained from AES analysis shows that Al has diffused through the 1000 Å Ni overlayer to form a thin (200 Å estimated) oxide layer.

In addition to the ohmic behavior resulting from annealing the NiAl contacts, as-deposited Ni, NiAl, and Au contacts deposited at room temperature on p-type ( $N_A < 5 \times 10^{16} \text{ cm}^{-3}$ ) 6H-SiC (0001) were rectifying with low leakage currents, ideality factors between 1.3 and 2.4, and SBH's of 1.31, 1.27, and 1.37 eV, respectively. These SBH's are higher than typically calculated for contacts on n-type 6H-SiC, as represented by the 1.14 eV value for Ni on n-type 6H-SiC and calculated from I-V measurements. A technique such as DLTS be used to explain the different behavior between Schottky contacts on n- and p-type SiC.

#### F. Future Research Plans and Goals

To complete our study on NiAl ohmic contacts for p-type SiC, the annealing series at 1000 °C will be extended. In addition, the specific contact resistivities will be remeasured using circular TLM patterns. This method consists of only one photolithographic level and should be more accurate than the single level, linear TLM patterns used for the calculations in this report. A photolithography mask with the circular TLM patterns is currently being designed and will be used in future research on ohmic contacts.

An alternate planned approach to Al-based ohmic contacts for p-type SiC will incorporate p-type semiconducting interlayers. The goal of this approach is to find a semiconducting material with a favorable band lineup with SiC (i.e., reduce the band bending) and to which an ohmic contact can easily be made. We have chosen to examine the  $\text{In}_x\text{Ga}_{1-x}\text{N}$  system for interlayer materials because of the lower density of surface states (and hence less band bending) and the range of band gaps over the composition range. We plan to measure the valence band offsets and electrical characteristics between various compositions of  $\text{In}_x\text{Ga}_{1-x}\text{N}$  (starting with  $x=0$ ) and SiC. If a low energy barrier at the interface results, metals will be investigated for ohmic contacts for the interlayer / SiC structure.

#### G. References

1. D. Alok, B. J. Baliga, and P. K. McLarty, IEDM Technical Digest, IEDM 1993, 691 (1993).
2. J. Crofton, P. A. Barnes, J. R. Williams, and J. A. Edmond, Appl. Phys. Lett. **62**(4), 384 (1993).
3. V. A. Dmitriev, K. Irvine, and M. Spencer, Appl. Phys. Lett. **64**(3), 318 (1994).
4. R. C. Glass, J. W. Palmour, R. F. Davis, and L. S. Porter, U.S Patent No. 5,323,022 (1994).
5. J. L. Murray, Ed. Phase Diagrams of Binary Titanium Alloys (ASM International, Metals Park, Ohio, 1987).
6. H. H. Berger, Solid State Electronics **15**(2), 145 (1972).
7. V. M. Bermudez, J. Appl. Phys. **63**(10), 4951 (1988).

8. T. Nakata, K. Koga, Y. Matsushita, Y. Ueda, and T. Niina, in *Amorphous and Crystalline Silicon Carbide and Related Materials II*, M. M. Rahman, C. Y.-W. Yang, and G. L. Harris, Eds., Vol. 43 (Springer-Verlag, Berlin, 1989).
9. G. K. Reeves, *Solid State Electronics* **21**, 801 (1978).

## XII. Fabrication and Characterization of MIS Diodes of Al/AlN/SiC by Gas-Source Molecular Beam Epitaxy

### A. Introduction

Silicon carbide (SiC) is a wide band gap material that makes it attractive for the fabrication of electronic devices that operate in a variety of harsh environments. SiC has a wide band gap ( $\approx 3.0$  eV at room temperature), excellent thermal stability[1-3], a high thermal conductivity ( $4.9$  W cm $^{-1}$ K $^{-1}$ )[4], a high breakdown field ( $2 \times 10^6$  V cm $^{-1}$ )[2] and a high saturated electron drift velocity ( $2 \times 10^7$  cm s $^{-1}$ )[3]. In the last few years, blue light emitting diodes (LEDs), junction field effect transistors (JFETs) and metal-oxide-semiconductor field effect transistors (MOSFETs) have become commercially available. Excellent reviews of these devices have been published[5-11].

Since metal-insulator-semiconductors (MIS) structures are an important part of today's microelectronics industry, MIS diodes (using SiO<sub>2</sub>, in particular, as the insulator) have been studied by a number of researchers. The majority of the studies have been done on 6H-SiC substrates. Although some work[12-16] has also been done on 3C-SiC, the defective nature of the material make most of the measurements difficult to interpret since the resulting interface state densities and fixed oxide charge densities were very high. Most of this work has centered around the optimization of the oxidation both kinetically and electrically; however, the chemical character of the oxide has also been studied by Auger electron spectroscopy[17, 18] and secondary ion mass spectroscopy[16, 19, 20]. Nearly all reports (see for example[21]) report that the MOS diodes can be easily accumulated and depleted at room temperature; however, inversion can only be obtained when the samples are illuminated by a UV light. The lowest reported values[22] of fixed charge densities and interface state densities are  $9 \times 10^{11}$  cm $^{-2}$  and  $1.5 \times 10^{11}$  cm $^{-2}$  eV $^{-1}$ , respectively. To date, there has only been one report[23] of a MIS diode made with an insulator other than SiO<sub>2</sub>. In this case, Si<sub>3</sub>N<sub>4</sub> was used, but had only minimal success due to very large density of defects and large leakage currents.

Aluminum nitride possesses a direct band gap of 6.28 eV at 300 K[24], a melting point in excess of 2275 K[25] and a thermal conductivity of 3.2 W cm $^{-1}$  K $^{-1}$ [26]. As such, it is a candidate material for high-power and high-temperature microelectronic and optoelectronic applications with the latter employment being particularly important in the ultraviolet region of the spectrum[24]. These properties strongly indicate that superior surface acoustic wave devices, operational in aggressive media and under extreme conditions both as sensors for high temperatures and pressures and as acousto-optic devices can be developed[27-29]. However, progress regarding these (and other) applications is hampered by the lack of good single crystal material.

## B. Experimental Procedure

Thin, epitaxial films of several thicknesses of AlN were grown on a variety of Si-face  $\alpha$ -SiC(0001) substrates supplied by Cree Research, Inc. The different  $\alpha$ -SiC(0001) wafers are listed in Table I. Each of the wafers contained a 0.8  $\mu\text{m}$  epitaxial SiC layer deposited via CVD and a thermally oxidized 75 nm layer to aid in wafer cleaning. The surfaces were prepared by a 10% HF dip and a 10 minute anneal at 1050 °C in UHV as well as a silane exposure and boil-off described in previous reports.

---

Table I. SiC Substrates used in this Research

---

on-axis, n-type ( $n = 2.8 \times 10^{16} \text{ cm}^{-3}$ ) 6H-SiC  
off-axis, n-type ( $n = 2.4 \times 10^{16} \text{ cm}^{-3}$ ) 6H-SiC  
off-axis, p-type ( $n = 2.1 \times 10^{16} \text{ cm}^{-3}$ ) 6H-SiC  
off-axis, n-type ( $n = 5.0 \times 10^{15} \text{ cm}^{-3}$ ) 4H-SiC

---

All growth experiments were carried out in the gas-source molecular beam epitaxy system detailed in previous reports. Films of AlN were grown at 1100 °C. Source were aluminum (99.9999% purity), evaporated from a standard MBE effusion cell operated in all cases at 1150°C, and 7.0 sccm ammonia (99.999% pure). Typical base pressures of  $10^{-9}$  Torr were used. Aluminum contacts (area =  $5 \times 10^{-3} \text{ cm}^2$ ) were deposited on the AlN by means of a standard evaporator and In-Sn solder was used a contact to the SiC.

High frequency capacitance-voltage measurements were performed on a HP 4275A C-V analyzer and the quasistatic C-V and I-V measurements were performed on a HP 4140B analyzer. Measurements were performed with the assistance of S. Cohen of IBM T. J. Watson Research Center in Yorktown Heights, NY. These analyzers were programmed to measure C-V and I-V characteristics of the diodes as well as to calculate the insulator thickness from the capacitance. Measurements were performed on diodes with AlN thicknesses of 1000 Å and 2500 Å.

## C. Results

In all cases, the diodes could be accumulated and depleted with the application of small gate voltages. Figure 1 shows C-V curves for a typical 1000 Å sample. However, deep depletion and inversion were not achieved in any case. For the 1000 Å samples, the leakage current was too high to accurately measure quasistatic C-V response.

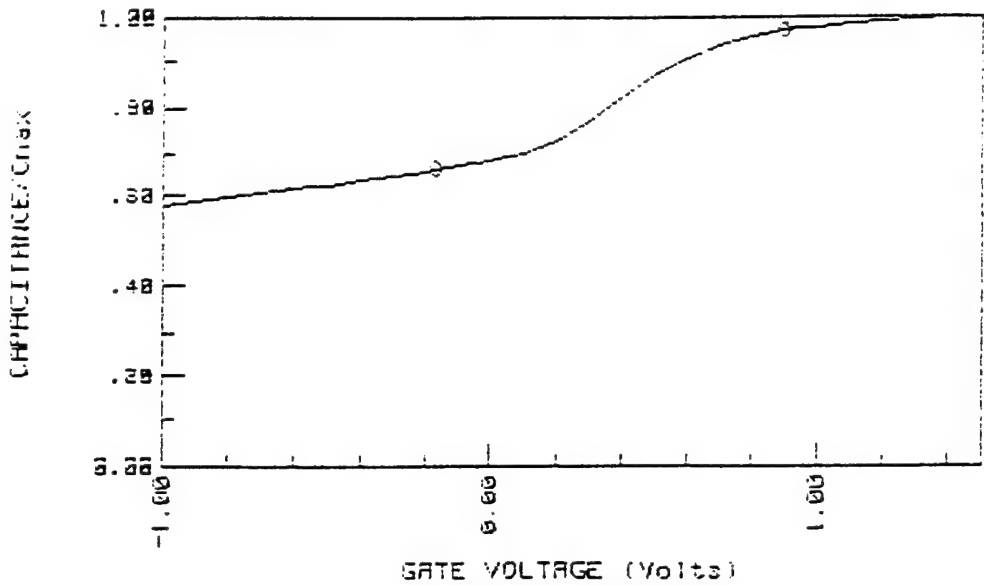


Figure 1. High frequency C-V curve for a typical Al/AlN/SiC diode. The AlN thickness is 1000 Å.

The leakage current was reduced by increasing the AlN thickness to 2500 Å. In this case, both the high frequency and the quasistatic C-V curves were measured. Figure 2 shows both of these curves on the same graph. At this thickness, the samples had low leakage currents (Fig. 3) but still did not undergo inversion.

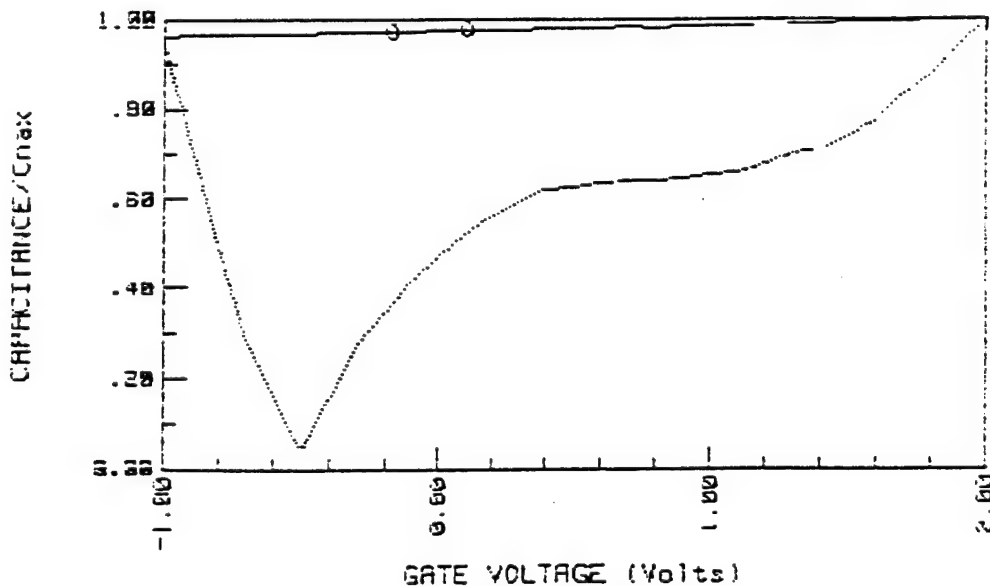


Figure 2. High frequency (solid line) and quasistatic (dotted line) C-V curves for an Al/AlN/SiC diode. The AlN thickness is 2500 Å.

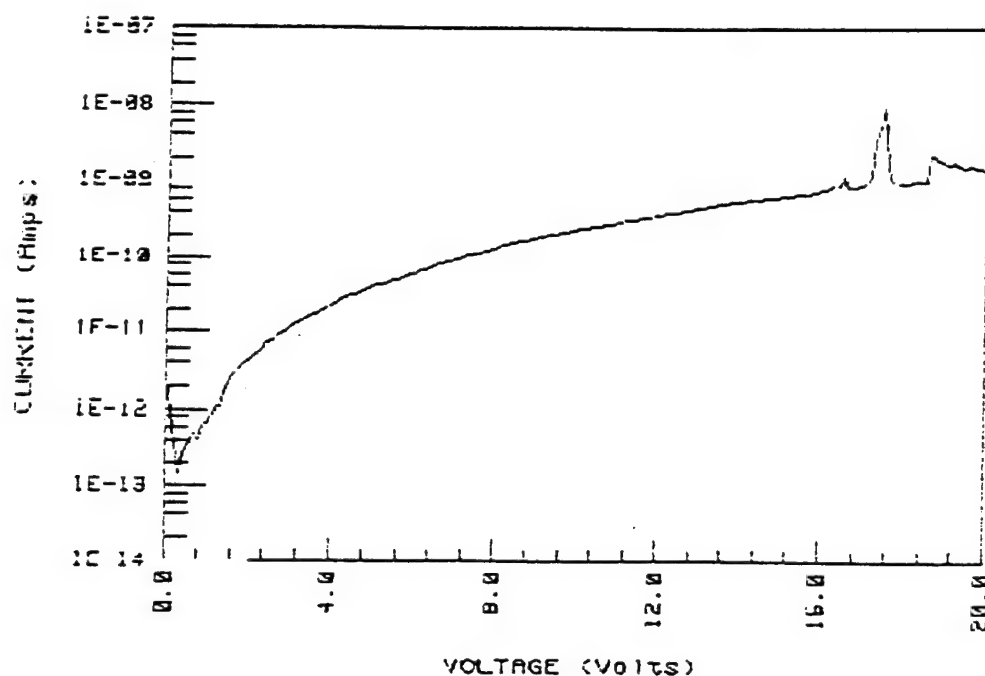


Figure 3. I-V curve for an Al/AlN/SiC diode. The AlN thickness is 2500 Å.

An interesting result of this work was that the capacitance showed a large dependency on applied frequency. When different frequencies were applied, the measured insulator capacitance was different each frequency.

#### D. Discussion

Figures 1 and 2 show the accumulation and depletion of Al/AlN/SiC diodes. Attempts to invert these samples at room temperature were unsuccessful. This is due to several factors. The extremely low intrinsic carrier concentration in SiC ( $\approx 10^{-6} \text{ cm}^{-3}$ ) and the low carrier generation significantly reduce the number of minority carriers available in the SiC surface region. Despite the inability to measure the interface state density due to the leakage in the insulator, the presumed high concentration of these states as well as traps and defects in the SiC (independent of the AlN insulator) may also prevent inversion. Thicker AlN layers show better leakage characteristics and may be necessary to achieve excellent insulating properties. The dependence of the capacitance on frequency implies a relationship between dielectric constant and frequency as well since the capacitance and the dielectric constant are related by insulator thickness only.

#### E. Conclusions

Thin AlN insulating layers on SiC have been used in MIS structures. The resulting diodes can be accumulated and depleted but cannot be inverted by high frequency C-V characterization. Layers thinner than 1000 Å are too leaky to perform quasistatic measurements to determine the density of interface states. A large dependency of AlN dielectric constant on frequency was also observed.

## F. Future Research Plans and Goals

The first priority is to reduce the leakage current and make accurate measurements of the interface state density. This will be accomplished by growing thicker layers ( $\approx 3000 \text{ \AA}$ ) of AlN on the same substrates and repeating the measurements. The second priority is to achieve inversion of the semiconductor. Effects of temperature and illumination will be determined.

## G. References

1. R. B. Campbell and H.-C. Chang, in *Semiconductors and Semimetals, Vol. 7B*, edited by R. K. Willardson and A. C. Beer (Academic Press, New York, 1971), p. 625.
2. W. von Muench and I. Pfaffeneder, *J. Appl. Phys.* **48**, 4831 (1977).
3. W. von Muench and E. Pettenpaul, *J. Appl. Phys.* **48**, 4823 (1977).
4. G. A. Slack, *J. Appl. Phys.* **35**, 3460 (1964).
5. R. F. Davis, J. W. Palmour and J. A. Edmond, *Mater. Res. Soc. Symp. Proc.* **162**, 463 (1990).
6. R. F. Davis, in *The Physics and Chemistry of Carbides; Nitrides and Borides*, edited by R. Freer (Kluwar Academic Publishers, The Netherlands, 1990), p. 589.
7. R. F. Davis, G. Kelner, M. Shur, J. W. Palmour and J. A. Edmond, *Proc. IEEE* **79**, 677 (1991).
8. R. F. Davis, J. W. Palmour and J. A. Edmond, *Diam. Rel. Mater.* **1**, 109 (1992).
9. R. F. Davis, *Phys. B* **185**, 1 (1993).
10. P. A. Ivanov and V. E. Chelnokov, *Semicond. Sci. Technol.* **7**, 863 (1992).
11. J. A. Powell, P. G. Neudeck, L. G. Matus and J. B. Petit, *Mater. Res. Soc. Symp. Proc.* **242**, 495 (1992).
12. K. Shibahara, S. Nishino and H. Matsunami, *Jpn. J. Appl. Phys.* **23**, L862 (1984).
13. R. E. Avila, J. J. Kopanski and C. D. Fung, *Appl. Phys. Lett.* **49**, 334 (1986).
14. S. M. Tang, W. B. Berry, R. Kwor, M. V. Zeller and L. G. Matus, *J. Electrochem. Soc.* **137**, 221 (1990).
15. M. Shinohara, M. Yamanaka, S. Misawa, H. Okumura and S. Yoshida, *Jpn. J. Appl. Phys.* **30**, 240 (1991).
16. C. Raynaud, J.-L. Autran, J.-B. Briot, B. Balland, N. Bécourt and C. Jaussaud, *J. Electrochem. Soc.* **142**, 282 (1995).
17. R. W. Kee, K. M. Geib, C. W. Wilmsen and D. K. Ferry, *J. Vac. Sci. Technol.* **15**, 1520 (1978).
18. R. Berjoan, J. Rodriguez and F. Sibieude, *Surf. Sci.* **271**, 237 (1992).
19. C. Raynaud, J.-L. Autran, B. Balland, G. Guillot, C. Jaussaud and T. Billon, *J. Appl. Phys.* **76**, 993 (1994).
20. C. Raynaud, J.-L. Autran, F. Seigneur, C. Jaussaud, T. Billon, G. Guillot and B. Balland, *J. Phys. III* **4**, 937 (1994).
21. A. Rys, N. Singh and M. Cameron, *J. Electrochem. Soc.* **142**, 1318 (1995).
22. J. N. Shenoy, G. L. Chindalore, M. R. Melloch, J. A. Cooper, Jr., J. W. Palmour and K. G. Irvine, *J. Electron. Mater.* **24**, 303 (1995).
23. G. E. Morgan, C. C. Tin, J. R. Williams and R. Ramesham, in *Silicon Carbide and Related Materials*, edited by M. G. Spencer, R. P. Devaty, J. A. Edmond, M. A. Khan, R. Kaplan, and M. Rahman (Institute of Physics, Bristol, 1994), p. 645.
24. W. M. Yim, E. J. Stofko, P. J. Zanzucchi, J. I. Pankove, M. Ettenberg and S. L. Gilbert, *J. Appl. Phys.* **44**, 292 (1973).
25. M. G. Norton, P. G. Kotula and C. B. Carter, *J. Appl. Phys.* **70**, 2871 (1991).
26. G. A. Slack, *J. Phys. Chem. Solids* **34**, 321 (1973).
27. J. K. Liu, K. M. Lakin and K. L. Wang, *J. Appl. Phys.* **46**, 3703 (1975).
28. M. Morita, N. Uesugi, S. Isogai, K. Tsubouchi and N. Mikoshiba, *Jpn. J. Appl. Phys.* **20**, 17 (1981).
29. G. D. O'Clock, Jr. and M. T. Duffy, *Appl. Phys. Lett.* **23**, 55 (1973).

# Nitrogen-based Materials

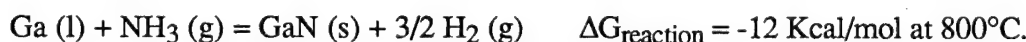
### XIII. Synthesis and Characterization of High Purity, Single Phase GaN Powder

#### A. Introduction

The recent fabrication of p-n junctions in gallium nitride thin films and the subsequent commercial realization of blue and green light emitting diodes based on this material have generated considerable interest and a growing number of research programs devoted to the III-V nitrides. In the wurtzite form, GaN has a band gap of 3.45 eV (near UV region) at room temperature. It also forms a continuous range of solid solutions with AlN (6.28 eV) and InN (1.95 eV). Thus, optoelectronic devices having specifically engineered band gaps with energies from the visible to the deep UV are theoretically possible with these materials. The wide band gaps of these materials and their strong atomic bonding also make them candidates for high power and high temperature devices. At present, GaN films are almost universally grown on foreign substrates such as sapphire and SiC. The mismatches in lattice parameters result in significant densities ( $\geq 10^8 \text{ cm/cm}^{-3}$ ) of dislocations in the films. As such, the availability of GaN bulk single crystals and wafers for homoepitaxial film growth has gained considerable importance. Crystal growth process routes applicable to GaN, e. g., sublimation and high pressure methods demand the availability of a high purity, single phase, well characterized powder source. This has been the objective of the research reported herein.

Our research has revealed only one supplier of GaN powder in the USA. The amount, purity and cost are limited, poor and extreme, respectively. The available X-ray and crystallographic data for GaN shown on PDF 2-1078 are also limited and date to 1938 [1]. This early data has a figure of merit of 14.

In the determination of viable methods of economically producing semiconductor purity GaN powder, the instability of this material to sublimation and the very low reactivity between Ga and N<sub>2</sub> ( $\Delta G_f = -4.4 \text{ Kcal/mol}$ ;  $K_p = 17$  at 500°C) must be considered. Initial research of Pichugin and Yas'kov [2] has shown that GaN powder can be obtained via the reaction:



The primary advantage of this process route is that it offers a viable method for the production of GaN which is as pure as the starting reactants. The availability of ultra pure Ga metal coupled with the recent advances in the reduction of both water and oxygen in the ammonia to <1 ppm allow the achievement of very high purity, single phase GaN powder at reasonable costs. The above reaction was employed in this research with several modifications to the experimental procedures used by the earlier investigators. An important product of these studies is a marked refinement of the existing crystallographic information and XRD as well as related microstructural information for the GaN powder which are reported below.

## B. Experimental Procedure

The precursor materials of 99.99% pure molten Ga metal contained in alumina or quartz reaction boats and 99.999% pure NH<sub>3</sub> gas were reacted in a 4 cm dia., 90 cm long horizontal tube furnace having a silica glass liner. A three dimensional matrix of boat position (5 cm intervals from the ammonia inlet), ammonia flow rate (200-500 sccm) and boat temperature (800-1200 °C) was employed to determine the optimum conditions for complete conversion of Ga to GaN. The Ga was heated to the desired temperature prior to reaction with the flowing NH<sub>3</sub>. Upon completion of each experiment, the samples were rapidly cooled to room temperature under an increased flow of ammonia (typically 1000 sccm) to minimize any GaN decomposition. No free Ga or other phase was observed in the XRD patterns of the GaN powder synthesized between 900 and 1050°C. The rapid formation of a gas permeable GaN layer was achieved within this temperature range such that the unreacted metal was continuously exposed to NH<sub>3</sub>. Similar studies between 1050 and 1200°C resulted in a small but X-ray detectable amount of free Ga in the powder, probably as a result of the decomposition of the GaN. At temperatures below 900°C, a GaN crust formed on the surface of the liquid Ga regardless of the flow rate of NH<sub>3</sub> (400-1000 sccm) or the reaction time (1-4 h) and stopped the reaction. For our system, the combination of optimum parametric values for the complete conversion of the Ga to GaN were 50 cm from the ammonia inlet, 400 sccm and 975°C. It was this material which was selected for determination of the XRD patterns. The design of the system used to produce GaN powder has been disclosed to North Carolina State University [3].

The as-prepared layers of GaN were porous and off-white in color. After removal from the boats, the material was crushed and slightly ground in an Agate Mortar. The XRD patterns of the GaN powder were obtained using a Rigaku (D/MAX-IIA) powder diffractometer equipped with an incident beam monochromator to obtain Cu K $\alpha_1$  radiation. The diffraction conditions were 0.02 degrees per step 2θ° scan with 4 s counting time. Systematic machine errors were determined using a 99.999% pure internal Si standard. Error corrections were subsequently made on the actual d spacings obtained from the XRD data. Both Appleman and Evans [4] and TREOR [5] cell refinement methods were used to perform least squares refinements of the data. Additional details regarding the XRD procedure are presented in Table I. Scanning electron microscopy (SEM) of the crushed GaN powder was obtained using a JEOL Model 6400 field emission microscope at 5 kV. Parameters obtained from SEM studies for size, size distribution and morphology are very important for the next step in the crystal growth research, namely, the consolidation of the powder into solid shapes having densities near theoretical.

---



---

Table I. Experimental Technique for X-ray Diffraction.

---

<i>Radiation type, source:</i>	X-ray, Cu
$\lambda$ value used:	1.540598 Å, K $\alpha$ 1
$\lambda$ Discrim.:	Incident beam, graphite mono
$\lambda$ Detector:	Scintillation
<i>Instrumental description:</i>	<i>Div.:</i> 0.8° <i>Rec.:</i> 0.3°
<i>Instrument profile breath:</i>	0.10 °2θ
<i>Temperature:</i>	22±1 °C
<i>Specimen form:</i>	Side loaded powder, packed for 2θ's
<i>Range of 2θ :</i>	30° 2θ to 130° 2θ
<i>Specimen motion:</i>	None
<i>Internal/external 2θ std.:</i>	Si (internal)
<i>Lattice parameter of 2θ std.:</i>	5.4315 Å
<i>2θ error correction:</i>	Interpolation from cubic regression equation of Si standard.
<i>Intensity measurement technique:</i>	Automated computer software (Rigaku D-MAX IIA), Peak heights
<i>Error (~):</i>	5%
<i>Cell refinement method:</i>	Least squares, Appleman and Evans (1973), Werner (1984)

---

### C. Results and Discussion

The unit cell data and data from a representative X-ray diffraction pattern of single phase GaN powder produced in this research are presented in Tables II and III, respectively. The latter represents a marked improvement in the crystallographic information available for this material. The PDF file 2-1078 reports a Smith-Snyder [6] figure-of-merit of F<sub>19</sub>=14, with 19 planes being indexed, and visual relative intensities. The diffraction data determined in this research are presented in Table III. All observed planes were indexed in the interval of 30°-130°.

---

---

Table II. Unit Cell Data for GaN.

---

$a = 3.18907 (8) \text{ \AA}$      $b = 3.18907 (8) \text{ \AA}$      $c = 5.1855 (2) \text{ \AA}$   
 $\alpha = 90^\circ$                            $\beta = 90^\circ$                            $\gamma = 120^\circ$   
 $V = 45.672 (2) (\text{\AA})^3$      $D_X = 6.0886 \text{ gr cm}^{-3}$      $Z = 2$                           Formula wt: 83.7297

Crystal System: Hexagonal

Figure of merit type  $F_N$ , Werner (1984)       $M_{23} = 374$  Werner (1984)  
Value :  $F_{23} = 174$  (0.004579, 29)

---

As there was no detectable interaction with or chemical interdiffusion between the boat used to contain the molten Ga and the metal or the GaN, the purity of the latter is controlled by the purity of the reactants. The Inductively Coupled Plasma technique employed for chemical analysis among 30 elements revealed only 100 ppm of manganese and 50 ppm of magnesium as detectable impurities. All other elements investigated as possible impurities were below the detection limits of this technique. As both precursors can now be purchased in very high purities, high purity GaN is now possible. At the present time, the only disadvantage of the procedure used in this study is that it is a batch process which limits the quantity of material produced to the size of the furnace and the container for the metal.

An SEM image typical of the optimized GaN powder is shown in Fig. 1. The particle size distribution of this material was narrow (1 to  $5\mu\text{m}$ ) with a majority of the particles being  $\approx 1 \mu\text{m}$ . The shapes of these particles were a mixture of various faceted polyhedra and rounded particles.

#### D. Summary

An economically viable process route has been established for producing single phase GaN powder from the reaction of liquid Ga metal with flowing ammonia. The optimum temperature, ammonia flow rate and boat position in the hot wall tube furnace relative to the ammonia inlet for the complete reaction to pure GaN for our system were  $975^\circ\text{C}$ , 400 sccm and 50 cm, respectively. The XRD data revealed the GaN to be single phase with figure of merit  $F_{23}=174$ . This research has resulted in both qualitative and quantitative improvements in the crystallographic and powder diffraction data available for this material. An SEM study of the ground powder revealed an average particle size and size distribution of  $\approx 1 \mu\text{m}$  and 1 to  $5 \mu\text{m}$ , respectively.

Table III. XRD Data for GaN.

$2\theta$ exp ( $^{\circ}$ )	I/I <sub>0</sub>	d <sub>exp</sub> ( $\text{\AA}$ )	<i>hkl</i>	$\Delta 2\theta$ ( $^{\circ}$ )
32.3904	56	2.762	100	-0.002
34.5702	45	2.593	002	-0.002
36.8465	100	2.437	101	0.000
48.0902	19	1.891	102	-0.001
57.7758	31	1.5945	110	+0.002
63.4492	27	1.4649	103	+0.019
67.8117	4	1.3809	200	+0.001
69.1040	22	1.3582	112	+0.005
70.5114	12	1.3345	201	-0.004
72.9062	3	1.2964	004	+0.003
78.3940	3	1.2186	202	+0.000
82.0349	2	1.1737	104	-0.009
91.1101	7	1.0790	203	-0.005
95.1200	3	1.0438	210	+0.010
97.6528	8	1.0234	211	-0.002
99.9511	5	1.0059	114	+0.004
105.0019	6	0.9709	105	+0.008
105.4025	5	0.9683	212	+0.001
109.1648	1	0.9452	204	-0.003
113.5807	4	0.9207	300	-0.011
119.0945	8	0.8936	213	+0.003
125.2224	4	0.8676	302	+0.000
126.0445	2	0.8644	006	-0.009

### E. Acknowledgments

The authors express their appreciation to Dr. A. Cuneyt Tas of the Middle East Technical University, Metallurgical Engineering Department, Ankara, Turkey for his valuable support in

the XRD characterization studies and to the Office of Naval Research for monetary support for this research under contract N00014-92-J-1477.



Figure 1. SEM image of the GaN powder produced at 975 °C.

#### F. References

1. H. Juza, Z. Anorg. Chem. **239**, 285 (1938).
2. I. G. Pichugin and D. A. Yaskov, Inorg. Mat. **6**, 1732 (1972).
3. C. M. Balkas and R. F. Davis, North Carolina State University, Invention Disclosure No: 95-06, Raleigh, North Carolina, (1994).
4. D. E. Appleman and H. T. Evans, U.S. Geological Survey, Computer Contribution 20, U.S. National Technical Information Service, Document No. PB-216188, (1973).
5. P. E. Werner, *Trial and Error Program for Indexing of Unknown Powder Patterns*, TREOR, University of Stockholm, Stockholm, Sweden (1984).
6. G. S. Smith and R. J. Snyder, J. Appl. Cryst. **12**, 60 (1979).

## XIV. Undoped and Doped GaN and $\text{Al}_x\text{Ga}_{1-x}\text{N}$ Thin Films Deposited on High-Temperature Monocrystalline AlN Buffer Layers on Vicinal and On-axis $\alpha$ (6H)-SiC(0001) Substrates via Organometallic Vapor Phase Epitaxy

M. D. Bremser, T. W. Weeks, Jr. and R. F. Davis

### Abstract

Monocrystalline GaN(0001) thin films have been grown at 950°C on high-temperature,  $\approx 100$  nm thick, monocrystalline AlN(0001) buffer layers pre-deposited at 1100°C on  $\alpha$ (6H)-SiC(0001)<sub>Si</sub> substrates via OMVPE in a cold-wall, vertical, pancake-style reactor. These films were free of low-angle grain boundaries and the associated oriented domain microstructure. The PL spectra of the GaN films deposited on both vicinal and on-axis substrates revealed strong bound excitonic emission with a FWHM value of 4 meV. This near band-edge emission from films on the vicinal substrates was shifted slightly to a lower energy, indicative of films containing residual tensile stresses. A peak attributed to free excitonic emission was also clearly observed in the on-axis spectrum. Undoped films were too resistive for accurate Hall-effect measurements. Controlled n-type, Si-doping in GaN was achieved for net carrier concentrations ranging from approximately  $1 \times 10^{17} \text{ cm}^{-3}$  to  $1 \times 10^{20} \text{ cm}^{-3}$ . Mg-doped, p-type GaN was achieved with  $n_{\text{A}} - n_{\text{D}} \approx 3 \times 10^{17} \text{ cm}^{-3}$ ,  $\rho \approx 7 \Omega \cdot \text{cm}$  and  $\mu \approx 3 \text{ cm}^2/\text{V} \cdot \text{s}$  as measured by Hall-effect. Double-crystal x-ray rocking curve measurements for simultaneously deposited 1.4  $\mu\text{m}$  GaN films revealed FWHM values of 58 and 151 arc sec for deposition on on-axis and off-axis 6H-SiC(0001)<sub>Si</sub> substrates, respectively. The corresponding FWHM values for the AlN buffer layers were approximately 200 and 400 arc sec, respectively.

$\text{Al}_x\text{Ga}_{1-x}\text{N}$  films have been grown for  $0 \leq x \leq 1$ . Abrupt heterojunctions have been demonstrated in this system. Cathodoluminescence spectra of  $\text{Al}_x\text{Ga}_{1-x}\text{N}$  films for  $x < 0.5$  showed intense near band-edge emission. Double-crystal x-ray rocking curve measurements revealed increasing FWHM values with increasing values of x. The FWHM values were smaller for AlGaN films grown on on-axis substrates than for simultaneously deposited films grown on vicinal substrates. As-deposited Si-doped  $\text{Al}_{0.75}\text{Ga}_{0.25}\text{N}$  exhibited negative electron affinity.

---

\*Portions of this report have been submitted as separate papers to *Applied Physics Letters* and the *Journal of Materials Research*.

## A. Introduction

Recent research regarding II-VI compound semiconductors and device structures has culminated in the successful fabrication of the first blue-green[1] and blue[2] injection laser diodes (LDs) and high-efficiency blue[3] light emitting diodes (LEDs). Comparatively, the direct band gap III-V nitrides possess greater physical hardness, much larger heterojunction offsets, higher melting temperatures and higher thermal conductivities[4]. GaN (wurtzite structure), the most studied of the III-V nitrides, has a room temperature band gap of 3.39 eV and forms continuous solid solutions with both AlN (6.28 eV) and InN (1.95 eV). As such, materials with engineered band gaps are feasible for optoelectronic devices tunable in wavelength from the visible (600 nm) to the deep UV (200 nm). The relatively strong atomic bonding and wide band gaps of these materials also points to their potential use in high-power and high-temperature microelectronic devices. Specific applications for these wide band gap semiconductors include UV, blue and blue-green light emitting diodes, UV photodetectors, short-wavelength laser diodes and transit time limited microwave power amplifiers[5]. Concomitant with the realization and/or optimization of these devices is the present need for improved film quality.

Bulk single crystal wafers of AlN and GaN are not commercially available[6]. Sapphire(0001) is the most commonly used substrate, although its a-axis lattice parameter and coefficient of thermal expansion are significantly different from that of GaN (Table I). It was first observed by Yoshida *et al.*[7,8] that the electrical and luminescence properties of GaN films grown via reactive molecular beam epitaxy improved markedly when an AlN “buffer layer” was initially deposited on the sapphire(0001) substrate. Amano *et al.*[9,10] and Akasaki *et al.*[11] were the first to use an AlN buffer layer for improving GaN films deposited via organometallic vapor phase epitaxy (OMVPE). By decreasing the growth temperature of the AlN buffer layer from 1000°C to 600°C, further improvements in surface morphology, electrical measurements and luminescence properties of the GaN were observed[10,11]. At present, for OMVPE growth of GaN on sapphire(0001) substrates, the need for low-temperature (450°C-600°C) buffer layers of AlN[10-15] or GaN [13-16] appears paramount.

The growth process, transformations and resulting microstructures in the AlN and GaN films on sapphire(0001) substrates have been extensively investigated[10,11,14,15,17]. Specifically, the description given in Ref. 15 states that the low-temperature AlN is deposited as an amorphous film which undergoes solid phase epitaxy upon being annealed at the GaN growth temperature. The annealed AlN buffer layer has slightly misoriented (<3° in the basal plane[14]) columnar grains preferentially oriented along [0001] with a domain microstructure and associated low-angle boundaries. Subsequent GaN growth occurs by first nucleating on the individual AlN columns. These initial crystallites of the GaN epilayer reportedly undergo

Table I. Comparison of III-Nitride Material Properties with Various Substrate Materials.<sup>a</sup>

Material	Lattice Parameter at RT	Thermal Conductivity at RT	Coefficients of Thermal Expansion
2H-GaN	$a = 3.189 \text{ \AA}$ $c = 5.185 \text{ \AA}$	$1.3 \text{ W/cm}\cdot\text{K}^b$	$5.59 \times 10^{-6}/\text{K}$ $7.75 \times 10^{-6}/\text{K}^b$
2H-AlN	$a = 3.112 \text{ \AA}$ $c = 4.982 \text{ \AA}$	$2.5 \text{ W/cm}\cdot\text{K}^b$	$4.15 \times 10^{-6}/\text{K}$ $5.27 \times 10^{-6}/\text{K}$
6H-SiC	$a = 3.08 \text{ \AA}$ $c = 15.12 \text{ \AA}$	$4.9 \text{ W/cm}\cdot\text{K}$	$4.2 \times 10^{-6}/\text{K}$ $4.68 \times 10^{-6}/\text{K}$
$\alpha$ -sapphire	$a = 4.758 \text{ \AA}$ $c = 12.99 \text{ \AA}$	$0.5 \text{ W/cm}\cdot\text{K}$	$7.5 \times 10^{-6}/\text{K}$ $8.5 \times 10^{-6}/\text{K}$
MgO	$a = 4.216 \text{ \AA}$		$10.5 \times 10^{-6}/\text{K}$
ZnO	$a = 3.252 \text{ \AA}$ $c = 5.213 \text{ \AA}$		$2.9 \times 10^{-6}/\text{K}$ $4.75 \times 10^{-6}/\text{K}$

<sup>a</sup> From *Landolt-Börnstein*, Vol. 17, edited by O. Madelung (Springer, New York, 1982)

<sup>b</sup> From *Properties of Group III Nitrides*, edited by J.H. Edgar (INSPEC, London, 1994).

geometric selection[18] via grain orientation competition until an oriented domain structure emerges. Subsequently, lateral growth and coalescence of GaN islands occurs resulting in uniform films having smooth surfaces. However, as a result of the slight misorientation in the annealed AlN buffer layers, low-angle grain boundaries persist in the GaN films[14]. A similar growth mode is proposed for GaN growth on low-temperature GaN buffer layers[13,19-21].

However, until ongoing crystal growth research leads to larger GaN crystals and more easily achieved homoepitaxial deposition, closely matched substrates, in terms of lattice parameters and coefficients of thermal expansion, are desirable. Candidate materials include MgO, ZnO and SiC[4]. Significant improvements in film quality have not been reported using MgO[22] and ZnO[23-25]. As with sapphire, these insulating substrates also prohibit the use of backside electrical contacts. However, commercially available conductive 6H-SiC(0001) substrates[26], which are more closely matched in both lattice parameter and coefficient of thermal expansion to AlN and GaN (Table I), show considerable promise[27,28].

In the present research, GaN thin films were deposited on monocrystalline high-temperature (HT) AlN buffer layers previously deposited on the Si- or C-polar planes of vicinal and on-axis 6H-SiC substrates. Likewise, AlN buffer layer growth was investigated on the various wafer types. The n- and p-type doping of GaN using Si and Mg dopants, respectively,

was also accomplished. However, since AlN has not been effectively doped n- or p-type, these insulating buffer layers prohibit front-and-backside electrical contacts, which are desirable for optoelectronic devices. As such, conductive  $\text{Al}_x\text{Ga}_{1-x}\text{N}$  buffer layers which do not compromise the resultant GaN film quality are sought.

## B. Experimental Procedure

As-received vicinal and on-axis 6H-SiC(0001)<sub>Si</sub> and 6H-SiC(0001)<sub>C</sub> wafers[26] were cut into 7.1 mm squares. Vicinal 6H-SiC wafers were oriented 3°-4° off-axis toward the <11̄20>. These pieces were degreased in sequential ultrasonic baths of trichloroethylene, acetone and methanol and rinsed in deionized water. The SiC substrates were then dipped into a 10% HF solution for 10 minutes to remove the thermally grown oxide layer and blown dry with N<sub>2</sub> before being loaded onto a SiC-coated graphite susceptor contained in a cold-wall, vertical, pancake-style, OMVPE reactor. The system was evacuated to less than  $3 \times 10^{-5}$  Torr prior to initiating growth. The continuously rotating susceptor was RF inductively heated to the AlN deposition temperature of 1100°C or 1200°C (as measured optically on the susceptor) in 3 SLM of flowing H<sub>2</sub> diluent. Hydrogen was also used as the carrier gas for the various metalorganic reactants and dopants. Deposition of each AlN buffer layer was initiated by flowing triethylaluminum (TEA) and ammonia (NH<sub>3</sub>) into the reactor at 23.6 μmol/min and 1.5 SLM, respectively. The system pressure during AlN growth was 45 Torr. Each AlN buffer layer was grown for 30 minutes resulting in a thickness of ≈100 nm. The TEA flow was subsequently terminated, the susceptor temperature decreased to 950°C and the system pressure increased to 90 Torr for the GaN growth. The flow rate of triethylgallium (TEG) was maintained at 24.8 μmol/min. The growth rate for GaN was ≈0.9 μm/hr. Silicon doped GaN films were grown by additionally flowing SiH<sub>4</sub> (8.2 ppm in balance of N<sub>2</sub>) at flow rates between ≈0.05 nmol/min and ≈15 nmol/min. Magnesium doping was accomplished by introducing bis-cyclopentadienylmagnesium (Cp<sub>2</sub>Mg) at a flow rate of 0.2 μmol/min.

Deposition of  $\text{Al}_x\text{Ga}_{1-x}\text{N}$  was initiated by flowing triethylaluminum (TEA) and triethylgallium (TEG) into the reactor at flow rates between 0 to 23.6 μmol/min and 0 to 24.8 μmol/min, respectively, corresponding to various alloy concentrations. TEA and TEG flow rates as a function of  $\text{Al}_x\text{Ga}_{1-x}\text{N}$  alloy composition are shown as a graph in Fig. 1.

Prior to being introduced into the reactor, the metalorganic precursors were fed into a gas mixing manifold, designed with a significantly reduce dead volume, to facilitate the deposition of abrupt heterojunctions. Ammonia (NH<sub>3</sub>) flowing at 1.5 SLM was the source of nitrogen. The system pressure was 45 Torr. Silicon doping was accomplished by flowing silane (SiH<sub>4</sub>) at 8.2 ppm in a balance of nitrogen into the reactor.

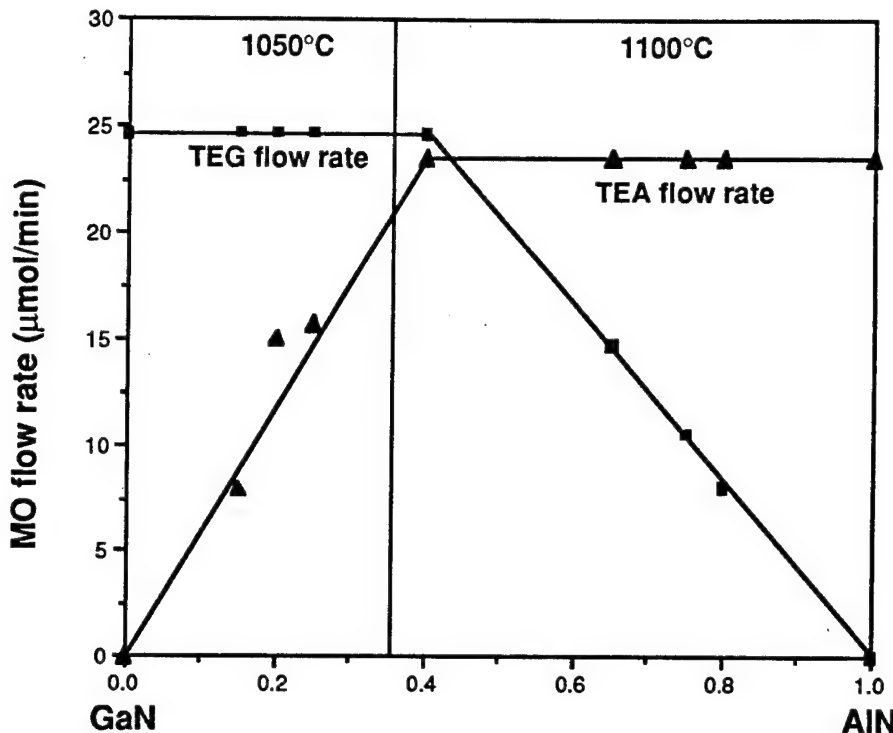


Figure 1. TEA and TEG flow rates as a function of  $\text{Al}_x\text{Ga}_{1-x}\text{N}$  alloy composition.

Four sets of undoped samples were examined on both vicinal and on-axis 6H-SiC(0001)<sub>Si</sub> and 6H-SiC(0001)<sub>C</sub> substrates: (1) 1100°C AlN buffer layer, (2) 1200°C AlN buffer layer, (3) 950°C GaN on 1100°C AlN buffer layer and (4) 950°C GaN on 1200°C AlN buffer layer. Additionally, samples of  $\text{Al}_x\text{Ga}_{1-x}\text{N}$  for various compositions were grown on both vicinal and on-axis 6H-SiC(0001)<sub>Si</sub> and 6H-SiC(0001)<sub>C</sub> substrates *without* a HT-AlN buffer layer.

The structural, microstructural, optical and electrical characteristics of the epitaxial GaN thin films were analyzed using several techniques. Scanning electron microscopy (SEM) was performed using a JEOL 6400FE operating at 5 kV. Conventional and high resolution transmission electron microscopy (TEM) were performed on a Topcon EM-002B microscope operating at 200 kV. Double-crystal x-ray rocking curve (DCXRC) measurements for the GaN(0004) and AlN(0002) reflections were made on a double-crystal diffractometer using Cu K $\alpha$ . The  $\text{Al}_x\text{Ga}_{1-x}\text{N}$  alloy concentrations were determined using Auger Electron Spectrometry (AES). The photoluminescence (PL) properties of the GaN films were determined at 8K using a 15 mW He-Cd laser ( $\lambda = 325 \text{ nm}$ ) as the excitation source. The cathodoluminescence (CL) properties of the GaN films were determined at 8K using a Kimball Physics electron gun operating at 7 keV. NEA was investigated by ultraviolet photoemission spectroscopy (UPS) using a helium resonance lamp (the He I line) to provide a source of

21.2 eV light. Spectroscopic ellipsometry (SE) was performed in a dry nitrogen ambient on a rotating analyzer ellipsometer with an angle of incidence of 67.08° and equipped with a xenon arc lamp having a spectral range of 1.5eV-6 eV. The carrier concentrations and mobilities in the Si-doped GaN films were characterized by Hall-effect measurements (Van der Pauw geometry) using a modified Keithley Model 80 equipped with a sensitive digital voltmeter (Keithley Model 182DMM). Thermally evaporated Al served as the ohmic contacts to these films. Mg-doped GaN samples were tested using a Hg-probe C-V system (MDC CSM/2), a 4-point probe system (VEECO FPP-5000) and the above mentioned Hall system using thermally evaporated In contacts. Separately deposited AlN buffer layers were characterized via reflection high-energy electron diffraction (RHEED), SEM and DCXRC measurements.

### C. Results and Discussion

*High-Temperature AlN Buffer Layers.* The surfaces of the 1100°C and 1200°C AlN buffer layers were mottled and textured with very small hillocks, respectively, on both the vicinal and on-axis 6H-SiC(0001)<sub>C</sub> wafers as observed via SEM. These growth templates yielded hexagonal hillocks, nominally 10 μm wide, on the surfaces of the subsequently grown GaN films. However, the AlN grown on the vicinal and on-axis 6H-SiC(0001)<sub>Si</sub> substrates had a smooth surface morphology. RHEED studies indicated that these films were monocrystalline as-deposited. In contrast, RHEED results indicated that AlN deposited on 6H-SiC(0001)<sub>Si</sub> substrates in the range of 500°C-1050°C resulted in polycrystalline material. Subsequent GaN deposition on these lower temperature buffer layers consisted essentially of the random nucleation and growth of isolated islands. The enhanced surface mobility of the adatoms at temperatures  $\geq$ 1100°C and the relatively small mismatch in lattice parameters between AlN(0001) and 6H-SiC(0001) ( $\Delta a/a_0 \approx 1\%$ ) promoted the growth of monocrystalline AlN(0001) films[27,28]. However, many small pits, nominally 30 nm in diameter, were observed on the AlN surfaces when using both Si-face wafer types. The pit density was decreased by increasing the AlN deposition temperature from 1100°C to 1200°C. This decrease was greater in on-axis than in off-axis films.

*Initial Growth of GaN on HT-AlN.* Coalescence of GaN islands occurred on monocrystalline HT-AlN buffer layers on vicinal and on-axis 6H-SiC(0001)<sub>Si</sub> substrates within the first several hundred angstroms of growth. The SEM image in Fig. 2 shows an intermediate stage of coalescence of  $\approx$ 150Å thick GaN islands after one minute of growth.

After this initial coalescence, GaN growth occurred by a layer-by-layer mechanism. In contrast, for GaN film growth on low-temperature buffer layers on sapphire(0001), a similar growth scenario pertains but requires  $\geq$ 30 minutes, several thousand angstroms of deposition and crystallographic geometric selection by the depositing atoms before island coalescence and layer-by-layer growth result[11,15].

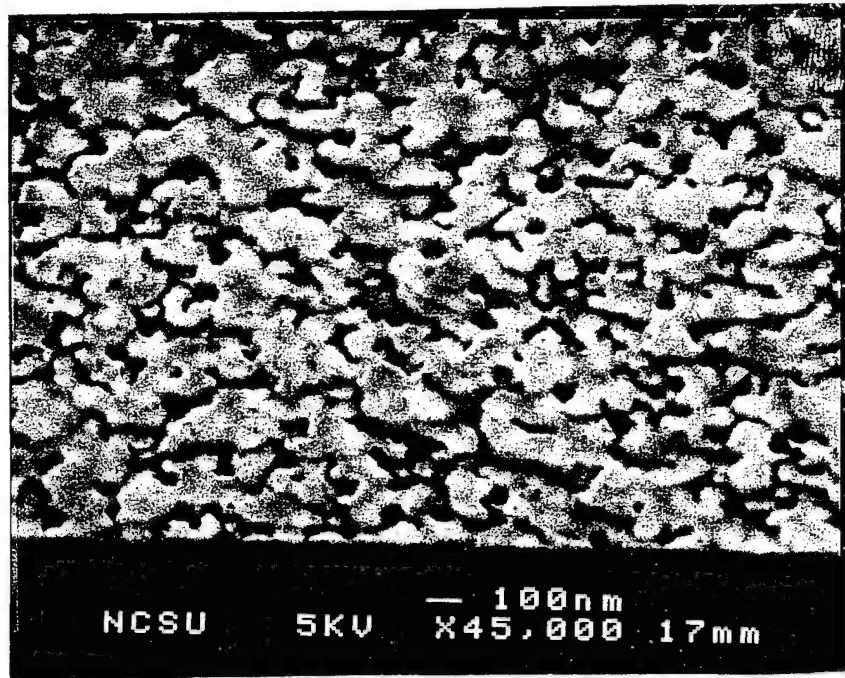


Figure 2. SEM image showing an intermediate stage of coalescence of  $\approx 150\text{\AA}$  thick GaN islands after 1 minute of growth on a monocrystalline AlN buffer layer deposited at  $1100^\circ\text{C}$  on a 6H-SiC(0001)Si substrate.

*GaN Surface Morphology.* The GaN films deposited on the HT-AlN buffer layers on the on-axis 6H-SiC(0001)Si substrates had very smooth surfaces as shown in Figs. 3(a) and 3(b).

Random pinholes, possibly caused by incomplete coalescence of the GaN, were observed on the otherwise featureless surface. A slightly mottled surface for GaN films grown on vicinal 6H-SiC(0001)Si substrates was observed in plan view SEM (Fig. 4(a)), probably as a result of the higher density of steps coupled with the mismatch in the Si/C and Al/N bilayer stacking sequences at selected steps[29] on the growth surface of this substrate. However, only the surface steps were seen in the corresponding higher resolution cross-sectional TEM images, as shown by the representative micrograph in Fig. 4(b). For the vicinal and on-axis growth, there was no apparent difference in surface morphology between the GaN films deposited on the  $1100^\circ\text{C}$  and  $1200^\circ\text{C}$  AlN buffer layers.

*TEM of GaN on HT-AlN.* GaN films deposited directly on 6H-SiC(0001)Si substrates at  $900^\circ\text{C}$  and 45 Torr had columnar-like grains, faceted surfaces and high net carrier concentrations ( $n_D - n_A > 1 \times 10^{19} \text{ cm}^{-3}$ ) [30]. In contrast, films deposited at  $950^\circ\text{C}$  on HT-AlN layers on similar 6H-SiC(0001)Si substrates were monocrystalline with no misorientation or low-angle grain boundaries, as determined via TEM by selected area diffraction and microstructural analysis. The stacking fault density was noticeably very low. These results are apparent in the cross-sectional TEM micrographs shown in Figs. 5(a) and 5(b) for on- and off-axis growth, respectively.

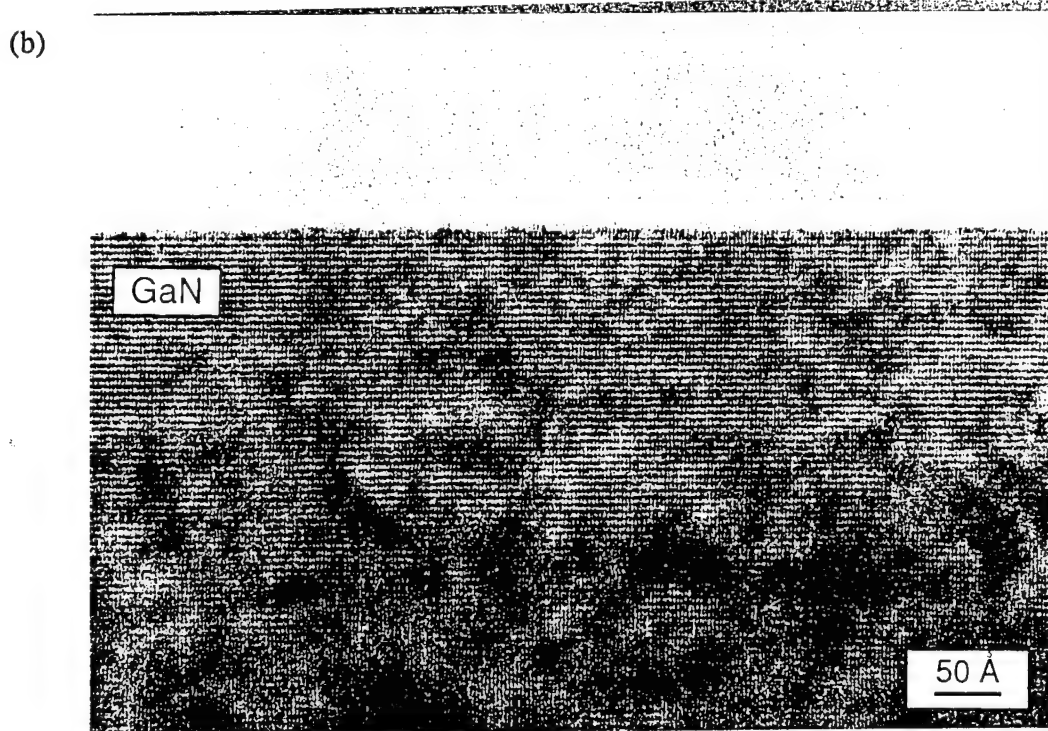
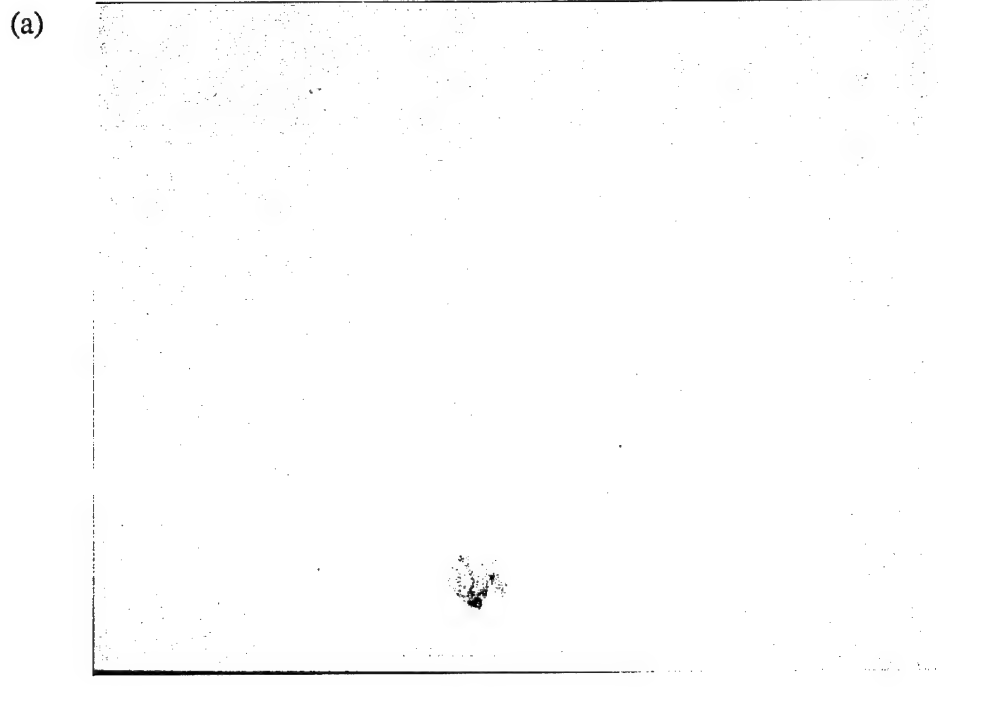


Figure 3. Plan view SEM (a) and cross-sectional TEM micrographs (b) of the surface of GaN deposited at 950°C on an AlN buffer layer grown at 1100°C on on-axis 6H-SiC(0001)Si substrates.

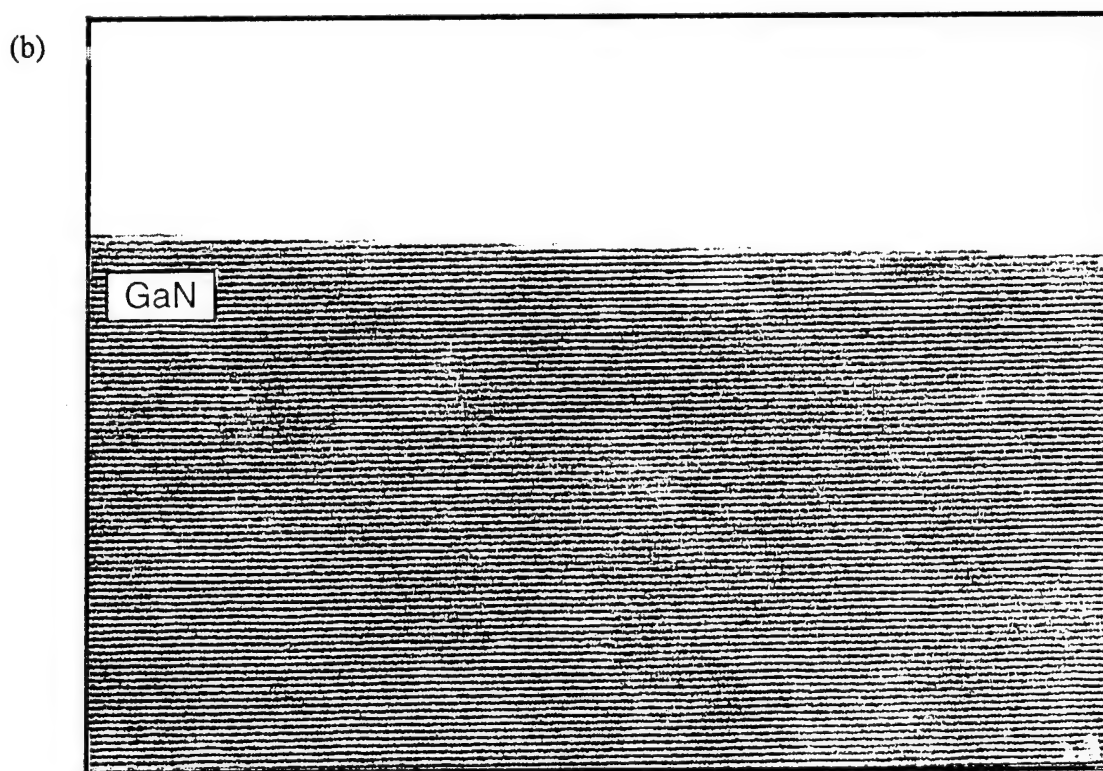
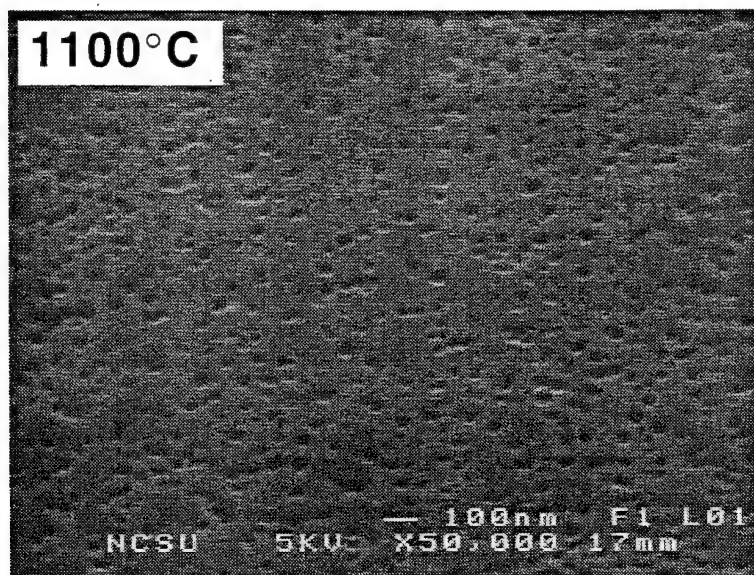


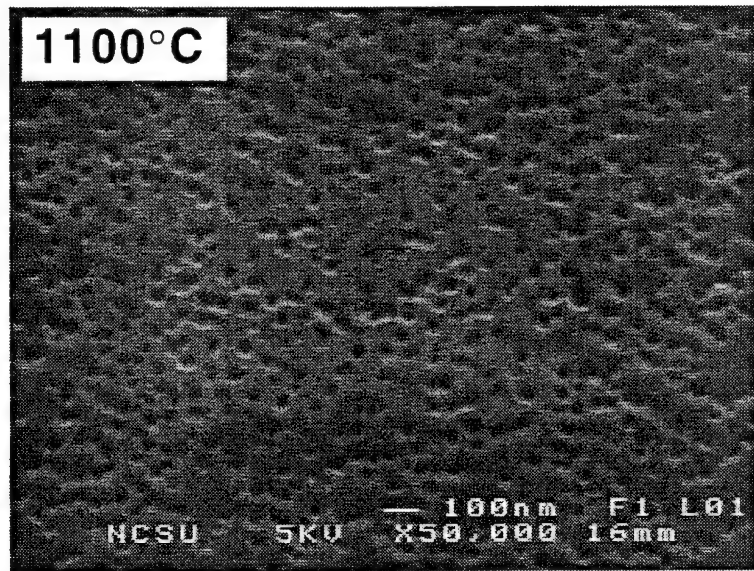
Figure 4. Plan view SEM (a) and cross-sectional TEM micrographs (b) of the surface of GaN deposited at 950°C on an AlN buffer layer grown at 1100°C on vicinal 6H-SiC(0001)<sub>Si</sub> substrates.

(a)



**on-axis**

(b)



**off-axis**

Figure 5. Cross-sectional TEM micrographs of GaN grown at 950°C via OMVPE on a monocrystalline AlN buffer layer deposited at 1100°C on (a) on-axis and (b) vicinal 6H-SiC(0001)Si substrates.

Residual lattice strain resulting from double positioning boundaries (DPBs)[29], generated at the SiC steps as a result of the difference in the Si/C and Al/N bilayer stacking sequence along [0001], and resultant threading dislocations were apparent in the AlN buffer layers. The dislocation density within the first 0.5  $\mu\text{m}$  of the GaN film on the vicinal 6H-SiC(0001)Si

substrate was approximately  $1 \times 10^9 \text{ cm}^{-2}$ , as determined from initial plan view TEM analysis by counting the number of dislocation per unit area. This value is approximately an order of magnitude lower than that reported[14] for thicker GaN films deposited on sapphire(0001) substrates using low-temperature buffer layers. As shown in Fig. 4(b), the dislocation density of the GaN film deposited on the vicinal 6H-SiC(0001)<sub>Si</sub> substrate decreased rapidly as a function of thickness. In contrast, since the on-axis wafers had less step and terrace features, the HT-AlN buffer layers on these substrates were of higher microstructural quality with smoother surfaces and fewer DPBs. Consequently, the microstructural quality of the GaN films and the AlN buffer layers were better for on-axis growth as shown by the DCXRC data noted below. As shown in Fig. 4, the dislocation density of the GaN film grown on-axis is comparable to the much thicker GaN film grown on the off-axis 6H-SiC(0001)<sub>Si</sub> substrate.

**XRC Measurements.** DCXRC measurements taken on simultaneously deposited 1.4  $\mu\text{m}$  GaN films on HT-AlN (1100°C) buffer layers revealed FWHM values of 58 and 151 arc sec for deposition on the on-axis and off-axis 6H-SiC(0001)<sub>Si</sub> substrates, respectively. The FWHM values of the DCXRC values for the corresponding  $\approx 100 \text{ nm}$  AlN buffer layers were approximately 200 and 400 arc sec, respectively. These latter values were unchanged by increasing the growth temperature to 1200°C. The 2.7  $\mu\text{m}$  GaN film deposited under identical conditions on a vicinal 6H-SiC(0001)<sub>Si</sub> substrate and shown in Fig. 5(b) yielded a FWHM value of 66 arc sec. The reduction in FWHM values from 151 to 66 arc sec is consistent with the decrease in the dislocation density as a function of thickness for GaN films grown on vicinal 6H-SiC(0001)<sub>Si</sub> substrates, as noted above. Likewise, the FWHM value (58 arc sec) of the thinner (1.4  $\mu\text{m}$ ) GaN film grown on-axis is comparable to the FWHM value (66 arc sec) of the thicker (2.7  $\mu\text{m}$ ) GaN film grown off-axis.

**Photoluminescence and Spectroscopic Ellipsometry** The low-temperature (8K) PL spectra (Fig. 6) of the simultaneously deposited 1.4  $\mu\text{m}$  GaN films on the (a) on-axis and (b) vicinal 6H-SiC(0001)<sub>Si</sub> substrates showed strong near band-edge emission at 357.74 nm (3.466 eV) and 358.00 nm (3.463 eV), respectively (Fig. 7), which has been attributed to an exciton bound to a neutral donor[31].

The FWHM values of these I<sub>2</sub> bound exciton peaks were 4 meV. The near band-edge peak on the vicinal samples was significantly stronger than that from the on-axis films (see Fig. 6). Additionally, the spectrum of the material on the vicinal substrate was shifted to a slightly lower energy, indicative of the tensile stresses in the film. This finding was independently verified by SE[32]. A peak centered at 357.14 nm (3.472 eV) attributed to free excitonic emission was also clearly observed in the on-axis spectrum by PL. This free excitonic emission in the vicinal sample was dominated by the very intense I<sub>2</sub> peak. SE further resolves the A and B free excitons at room temperature for films grown on both vicinal and on-axis substrates.

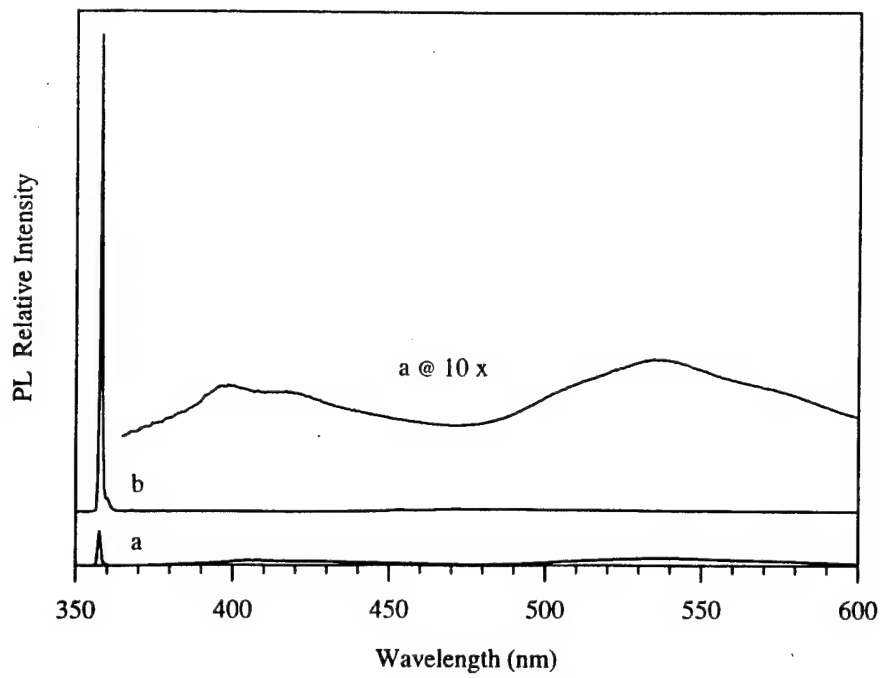


**Figure 6.** The low-temperature (8K) PL spectra of the GaN films on (a) on-axis and (b) vicinal 6H-SiC(0001)Si substrates. Inset shows details of the near band-edge region.

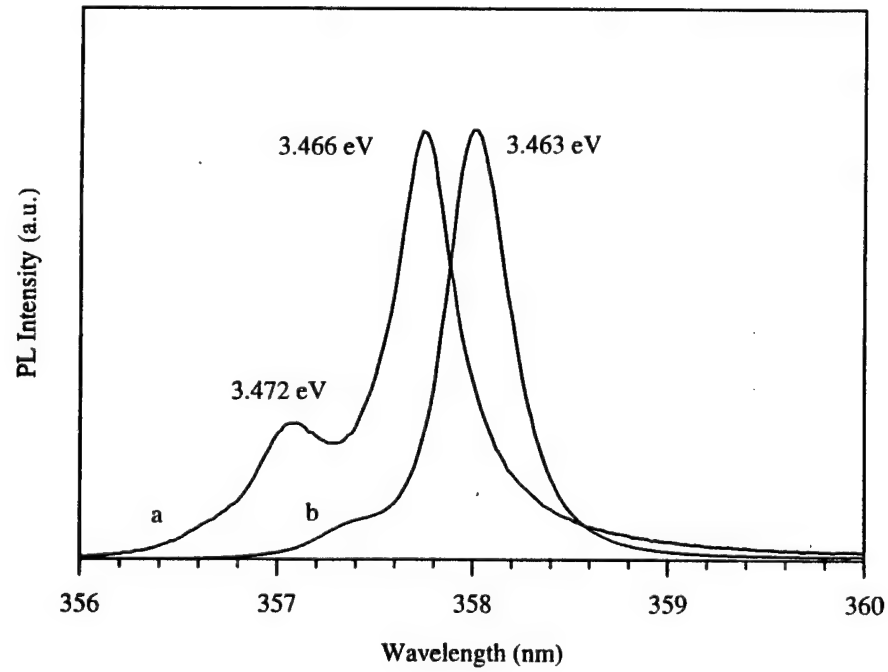


**Figure 7.** The low-temperature (8K) PL spectra of near bandedge emission of the GaN films on (a) on-axis and (b) vicinal 6H-SiC(0001)Si substrates.

Using SE, work is in progress to quantify both the hydrostatic and non-hydrostatic components of the residual strain in these films, as well as those grown on on-axis substrates[32]. The spectrum from the GaN film on the vicinal substrate revealed no observable emission at  $\approx 545$  nm (2.2 eV), commonly associated with deep-levels (DL) in the band gap[33]. A very weak 2.2 eV peak was observed in the GaN film grown on-axis. Similar variations in the PL spectra were also observed for GaN films grown on the vicinal and on-axis 6H-SiC(0001)<sub>Si</sub> substrates. However, the peak associated with the free exciton was not clearly observed in the latter spectra. The causes of these PL spectral differences are under investigation.

*Si-doping in GaN.* Undoped high quality GaN films grown on HT-AlN buffer layers on both vicinal and on-axis 6H-SiC(0001)<sub>Si</sub> substrates were too resistive for Hall-effect measurements. Controlled n-type doping was achieved using SiH<sub>4</sub> for net carrier concentrations ranging from  $\approx 1 \times 10^{17}$  cm<sup>-3</sup> to  $\approx 1 \times 10^{20}$  cm<sup>-3</sup> in GaN films grown on vicinal 6H-SiC(0001)<sub>Si</sub> substrates. The net carrier concentrations and room temperature mobilities versus SiH<sub>4</sub> flow rate are plotted in Fig. 8. Films with a net carrier concentration of  $n_D - n_A = 2 \times 10^{17}$  cm<sup>-3</sup> had a room temperature Hall mobility of  $\mu = 375$  cm<sup>2</sup>/V·s.

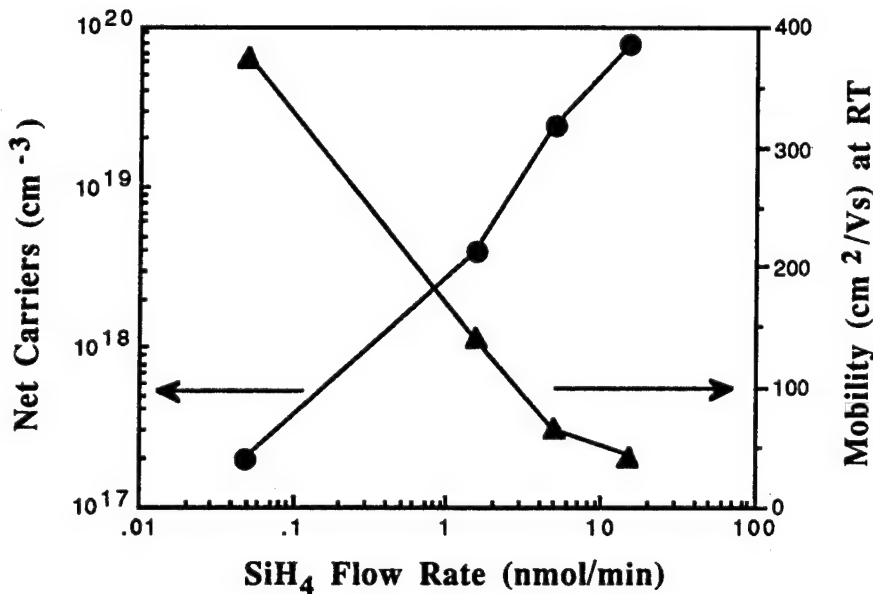
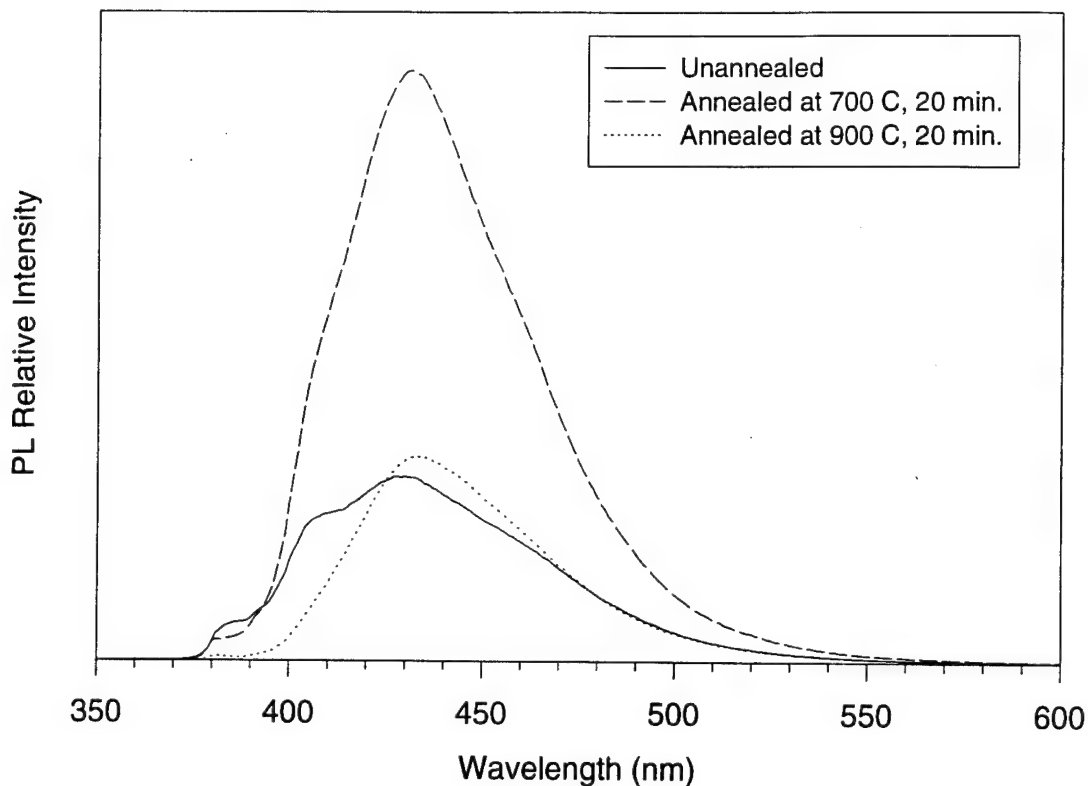


Figure 8. Net carrier concentration and room temperature mobilities in Si-doped, n-type GaN as a function of SiH<sub>4</sub> flow rate.

*Mg-doping in GaN.* Mg-doped GaN films were deposited at 950°C on HT-AlN (1100°C) buffer layers on vicinal 6H-SiC(0001)<sub>Si</sub> substrates by introducing Cp<sub>2</sub>Mg at a flow rate of 0.2  $\mu$ mol/min. These samples were subsequently annealed at 700°C at 700 Torr in 3 SLM of N<sub>2</sub> for 20 minutes. These same samples were re-annealed at 900°C for 20 minutes under

identical conditions. Figure 9 shows the PL (8K) spectra of the unannealed, 700°C annealed and 900°C annealed samples.



**Figure 9.** Low-temperature (8K) PL spectra of an unannealed, 700°C annealed and 900°C annealed Mg-doped GaN film.

Similar to the results of Nakamura *et al.*[34], the PL intensity of the blue emission was increased by the 700°C anneal and was dramatically decreased by the subsequent 900°C anneal. Hall-effect measurements made on the annealed samples revealed p-type GaN with a net hole carrier concentration of  $n_{A-ND} \approx 3 \times 10^{17} \text{ cm}^{-3}$ , a resistivity of  $\rho \approx 7 \Omega \cdot \text{cm}$  and a hole mobility of  $\mu \approx 3 \text{ cm}^2/\text{V}\cdot\text{s}$ . Likewise, 4-point probe and Hg-probe C-V measurements verified p-type GaN.

Additionally, Mg-doped GaN films were deposited at 1100°C on HT-AlN (1100°C) buffer layers on vicinal 6H-SiC(0001)<sub>Si</sub> substrates by introducing Cp<sub>2</sub>Mg at a flow rate of 0.2  $\mu\text{mol}/\text{min}$ . C-V measurements revealed p-type GaN *as-deposited* with  $n_{A-ND} \approx 2 \times 10^{16} \text{ cm}^{-3}$ . These samples were subsequently annealed at 600°C at 700 Torr in 3 SLM of N<sub>2</sub> for 20 minutes. The PL intensity of the blue emission was found to be the most intense after annealing at 600°C. P-type GaN with  $n_{A-ND} \approx 1 \times 10^{18} \text{ cm}^{-3}$  was revealed by C-V measurements of the annealed films.

$Al_xGa_{1-x}N$  Film Growth. As shown in Fig. 1,  $Al_xGa_{1-x}N$  films have been grown for Al mole fractions of  $0 \leq x \leq 1$ . The alloy concentrations were determined via AES by depth profiling through multi-layer heterostructures, one of which is shown in Fig. 10.

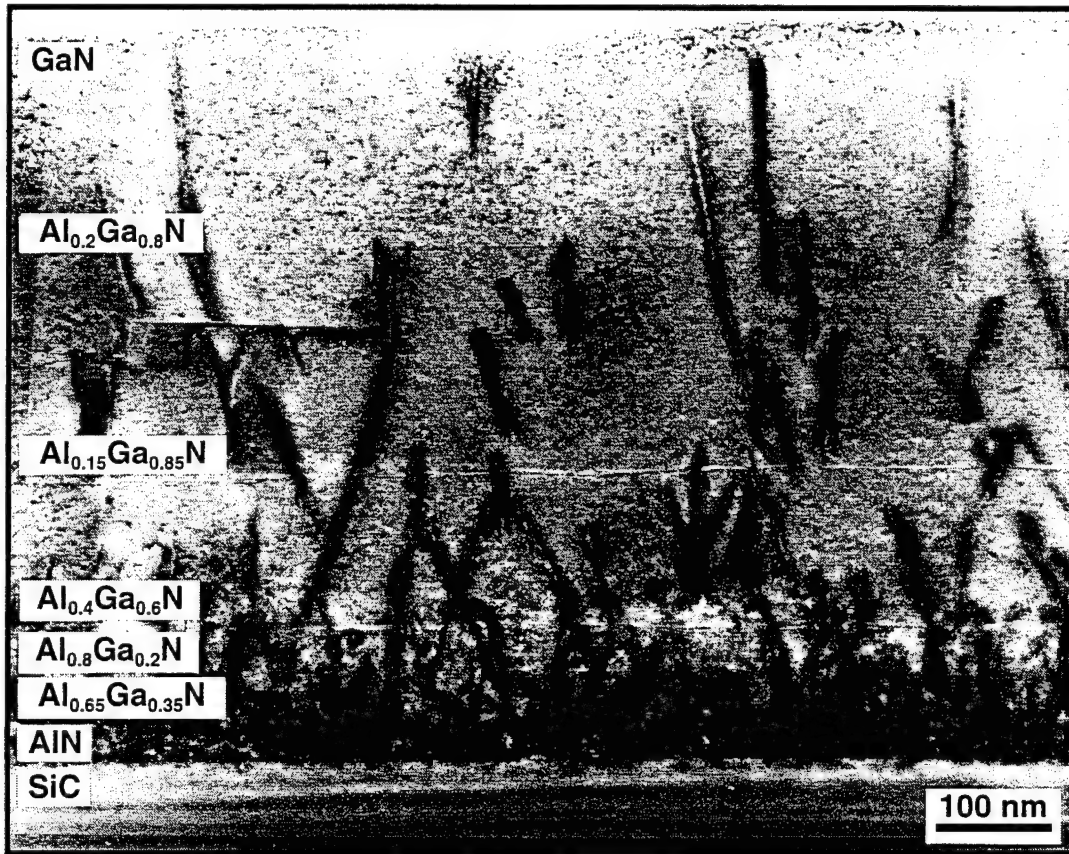


Figure 10. Cross-section TEM micrograph of a 7-layer  $Al_xGa_{1-x}N$  heterostructure.

GaN and AlN served as the necessary standards.  $Al_xGa_{1-x}N$  films for  $0 < x < 0.3$  were then simultaneously deposited directly on vicinal and on-axis 6H-SiC(0001) substrates *without* the use of the customary high-temperature AlN buffer layers[28]. These films were electrically insulating as-grown. As shown in Fig. 11, SEM revealed a smooth surface for a  $0.8 \mu m$  thick  $Al_{0.12}Ga_{0.88}N$  film deposited directly on an on-axis substrate.

The Al mole fractions were determined by low-temperature CL measurements as described below. Similar to findings for GaN film growth[28], the DCXRC measurements revealed smaller FWHM values for AlGaN films grown on on-axis substrates as compared to simultaneously deposited films grown on vicinal substrates. Also, the FWHM values expand with increasing Al mole fraction. These results are shown in Fig. 12 where FWHM values are plotted versus alloy concentration for  $Al_xGa_{1-x}N$  films simultaneously deposited on vicinal and on-axis 6H-SiC(0001) substrates.

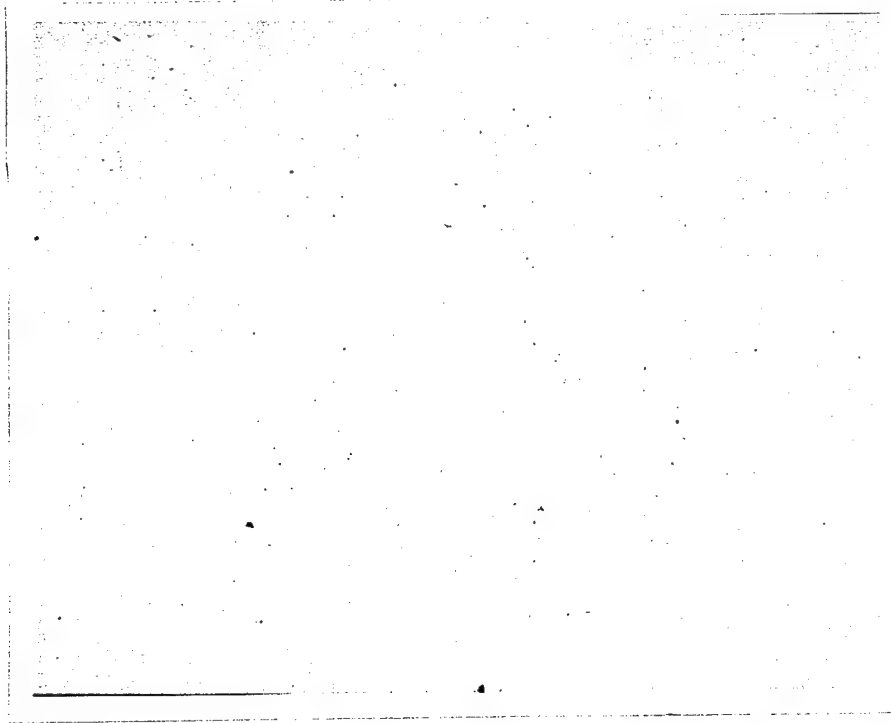


Figure 11. Plan-view SEM of a 0.8 micron thick Al<sub>0.12</sub>Ga<sub>0.88</sub>N film deposited directly on an on-axis substrate.

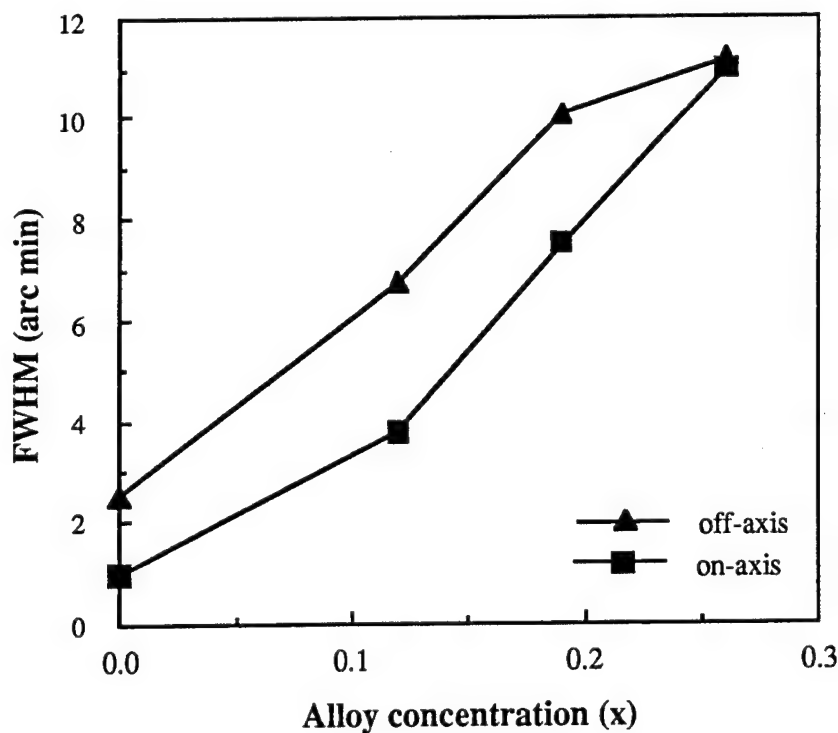


Figure 12. DCXRC FWHM values versus alloy concentration for Al<sub>x</sub>Ga<sub>1-x</sub>N films simultaneously deposited on vicinal and on-axis 6H-SiC(0001) substrates.

*CL of  $\text{Al}_x\text{Ga}_{1-x}\text{N}$ .* The low-temperature (8K) CL spectra of the  $\text{Al}_x\text{Ga}_{1-x}\text{N}$  films with  $x < 0.5$  showed strong near band-edge emission. Films with  $x \geq 0.5$  are currently being investigated. As expected, the energy positions of these peaks shifted towards higher energy with increasing  $x$ , as shown in Fig. 13.

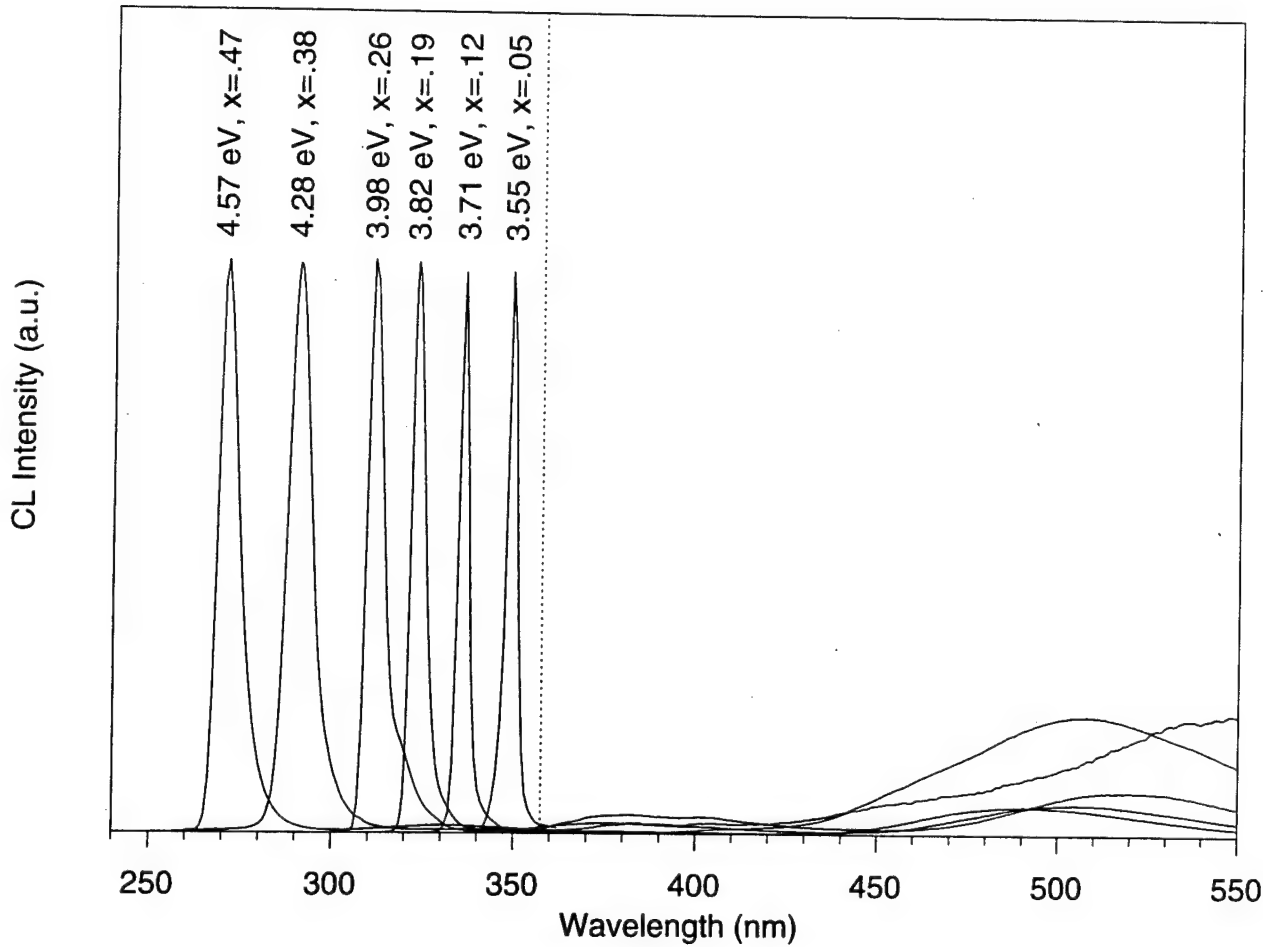


Figure 13. Low-temperature (8K) CL of  $\text{Al}_x\text{Ga}_{1-x}\text{N}$  films with  $x < 0.5$ .

The dashed line in the graph shows the peak position for  $\text{Al}_x\text{Ga}_{1-x}\text{N}$  where  $x = 0$ . Al mole fractions were assigned from the near band-edge peak positions using a bowing parameter of  $b = 0.98 \text{ eV}$ , as determined by Khan *et al* [35]. Apparent in Fig. 14 is the increased FWHM values of the energy peaks with increasing values of  $x$ . Thus, Fig. 14 graphs the increasing FWHM values of these near band-edge peaks for undoped  $\text{Al}_x\text{Ga}_{1-x}\text{N}$  films grown on vicinal 6H-SiC(0001) substrates.

AlGaN films grown on on-axis substrates showed a similar trend. The broadening of the near band-edge peak is possibly due to increased fluctuations in the alloy compositions of  $\text{Al}_x\text{Ga}_{1-x}\text{N}$  films for increasing values of  $x$  [35]. Also, the CL peak intensities were 0.1 to 1

order of magnitude stronger for undoped AlGaN films grown on vicinal substrates than for films grown on on-axis substrates. This phenomenon is being investigated further.

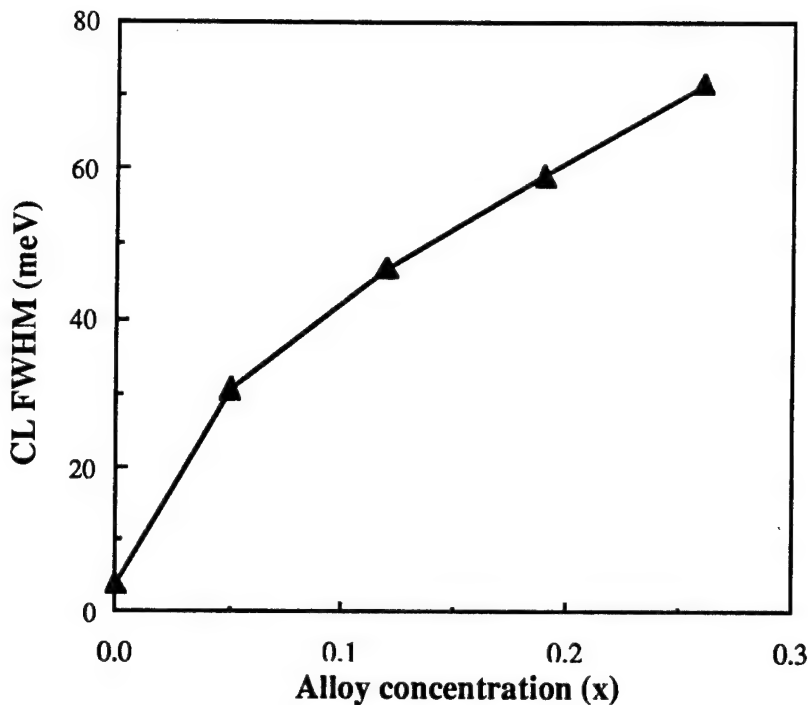


Figure 14. FWHM values of the CL near band-edge peak from  $\text{Al}_x\text{Ga}_{1-x}\text{N}$  films grown on vicinal 6H-SiC(0001) substrates.

*Heterostructures of  $\text{Al}_x\text{Ga}_{1-x}\text{N}$ .* For the successful fabrication of super-lattices and multiple quantum well structures, abrupt heterojunctions are important. Thus, as shown in the cross-section SEM micrograph of Fig. 15, a multi-layer heterostructure was grown. The cross-sectional TEM image of this structure is shown in Fig. 16.

Including the initial AlN buffer layer, five distinct layers are observable. Therefore, using the reduced dead volume gas mixing manifold, abrupt heterojunctions were fabricated, similar to the AlN/GaN interface shown in Fig. 17.

*Negative Electron Affinity in Si-doped  $\text{Al}_{0.75}\text{Ga}_{0.25}\text{N}$ .* A Si-doped  $\text{Al}_{0.75}\text{Ga}_{0.25}\text{N}$  film grown directly on vicinal 6H-SiC(0001) exhibited a NEA effect in the as-deposited state as determined by UPS. Because charging problems with insulating AlGaN can quickly quench the photoemission, the film was intentionally Si-doped to minimize this effect. Figure 18 shows the UV photoemission of this sample exhibiting a distinctive peak indicative of the presence of NEA. A large sample bias (3 V) was needed to overcome the work function of the electron analyzer. Thus, the work function of  $\text{Al}_{0.75}\text{Ga}_{0.25}\text{N}$  is apparently less than that of the analyzer, which is between 4 and 5 eV. Subsequent vacuum annealings at  $475^\circ\text{C}$  and  $580^\circ\text{C}$  quenched the NEA.

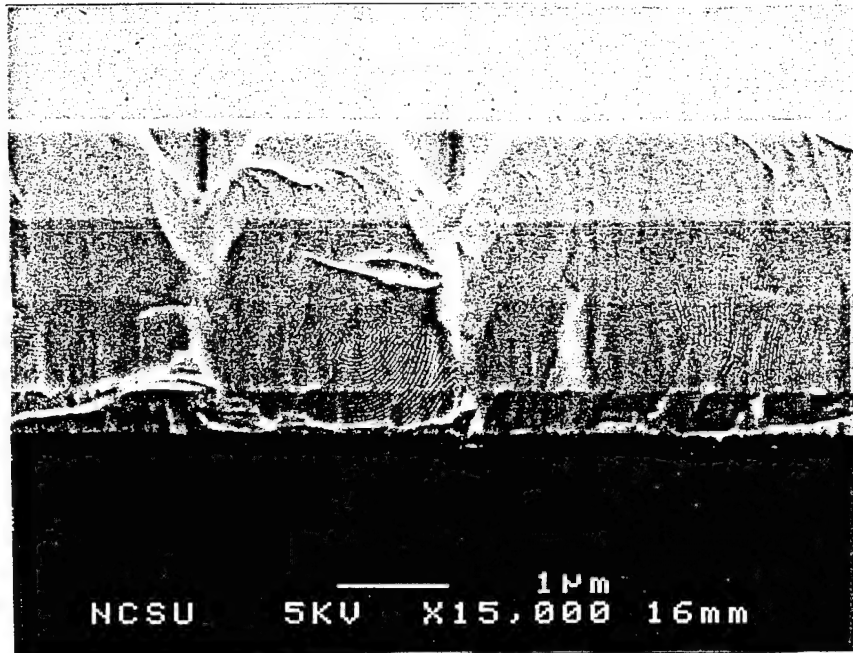


Figure 15. Cross-section SEM micrograph of a 5-layer heterostructure.

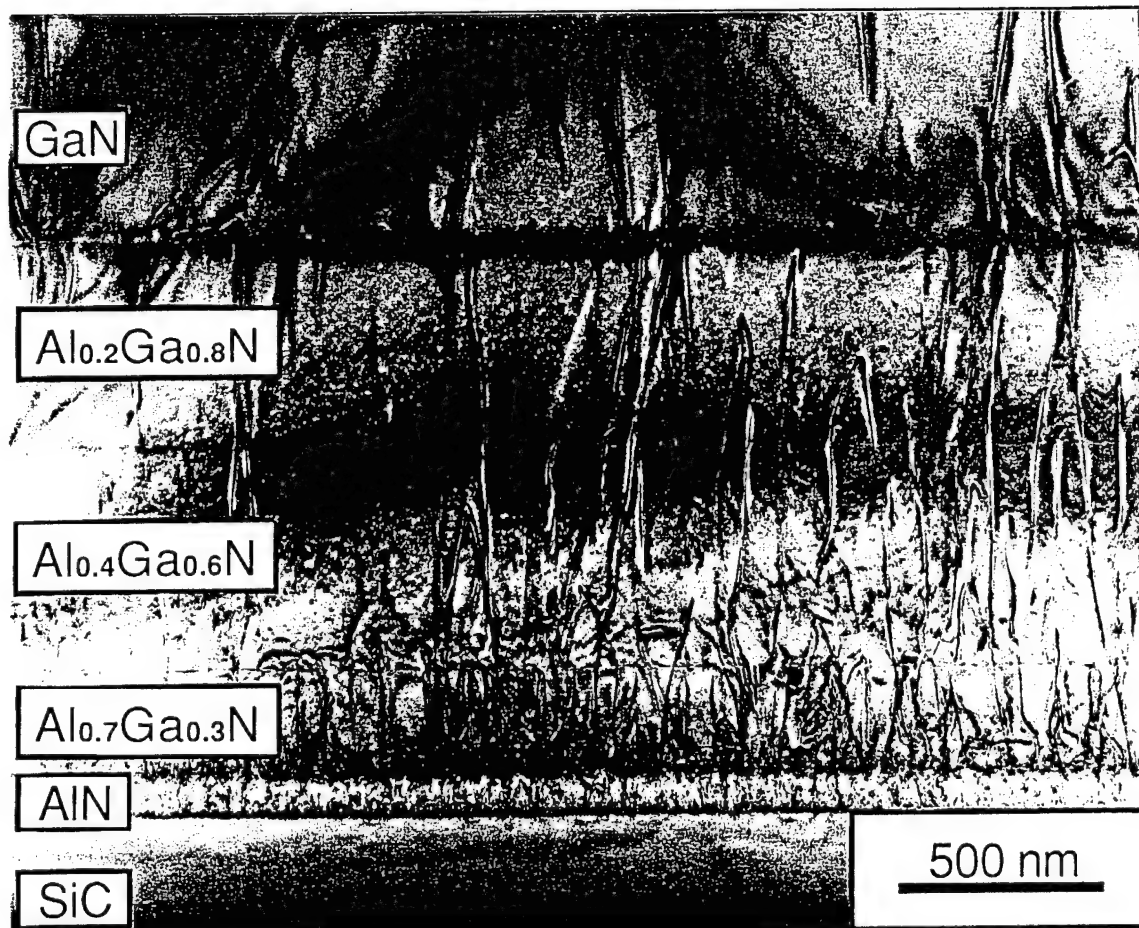


Figure 16. Cross-sectional TEM image of the heterostructure shown in Fig. 15.

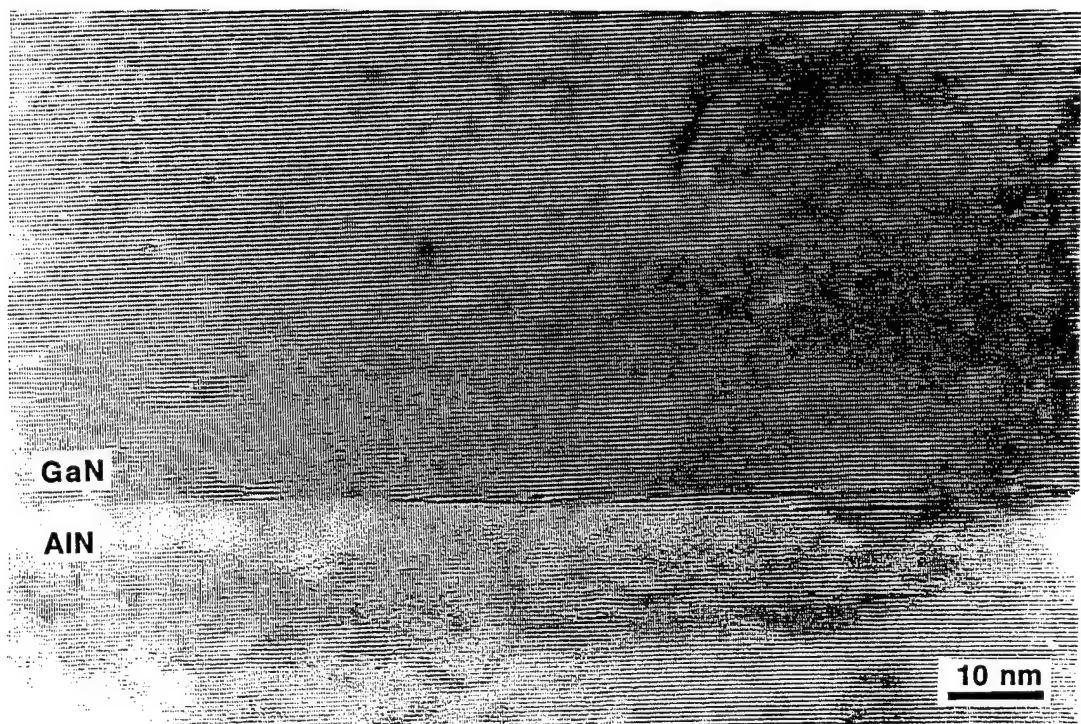


Figure 17. TEM micrograph showing the abruptness of an AlN/GaN interface.

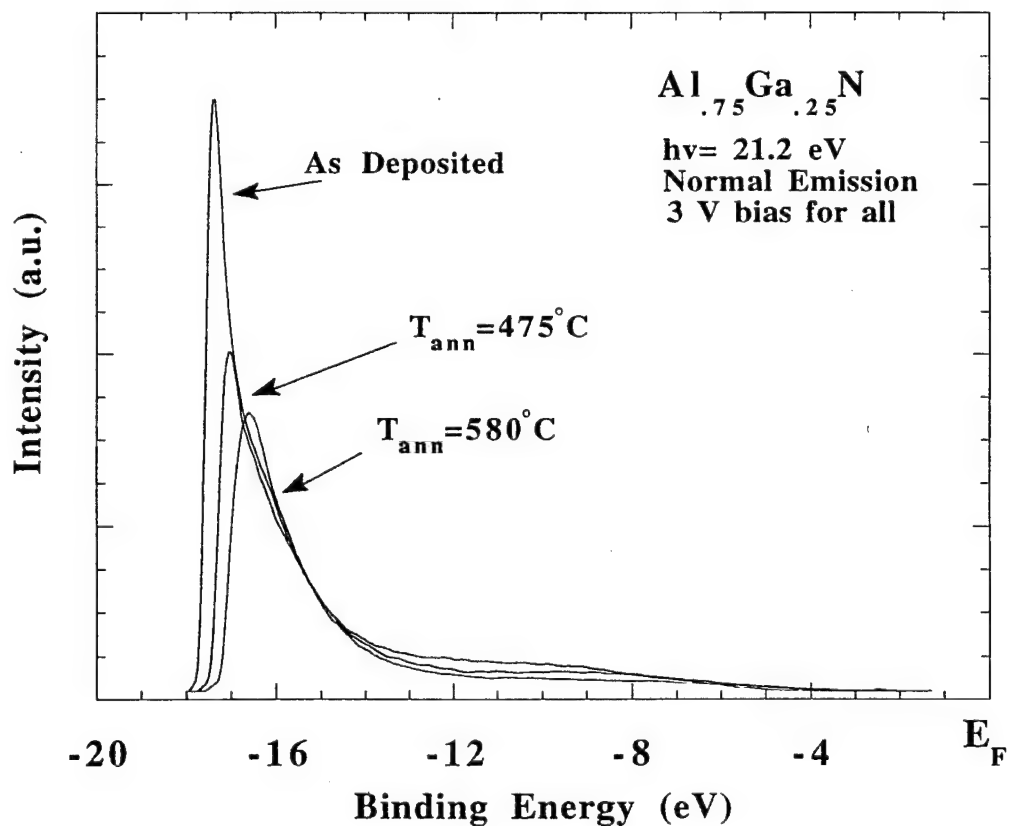


Figure 18. UV photoemission of  $\text{Al}_{0.75}\text{Ga}_{0.25}\text{N}$  on 6H-SiC(0001) with a sample bias of 3 V. UPS spectra for the as-deposited state and subsequent anneals at  $475^\circ\text{C}$  and  $580^\circ\text{C}$  are shown.

#### D. Conclusions

GaN(0001) thin films void of low-angle grain boundaries and associated oriented domain microstructures have been grown at 950°C via OMVPE on monocrystalline AlN(0001) buffer layers previously deposited at 1100°C on vicinal and on-axis  $\alpha$ (6H)-SiC(0001)<sub>Si</sub> substrates. The improved GaN film quality is a direct result of the achievement of monocrystalline HT-AlN buffer layers with no misorientations or low-angle grain boundaries. The GaN films grown on the vicinal substrates contained both a higher density of dislocations in the interface region and a higher residual stress. The latter was manifest in both a broader DCXRC FWHM value and a shift in the PL spectrum. Controlled n-type Si-doping of GaN was demonstrated for net carrier concentrations ranging from approximately  $1 \times 10^{17}$  cm<sup>-3</sup> to  $1 \times 10^{20}$  cm<sup>-3</sup>. Mg-doped p-type GaN was obtained as-deposited and upon annealing,  $n_A$ -nD as high as  $1 \times 10^{18}$  cm<sup>-3</sup> was achieved. For simultaneously deposited 1.4  $\mu$ m films, DCXRC measurements for the GaN(0004) reflection indicated FWHM values of 58 and 151 arc sec for films grown on on-axis and off-axis 6H-SiC(0001)<sub>Si</sub> substrates, respectively. The corresponding FWHM values of the AlN(0002) reflection for the  $\approx$ 100 nm buffer layers were approximately 200 and 400 arc sec, respectively. Each low-temperature (8K) PL spectrum of the GaN films deposited on both on-axis and vicinal substrates showed a strong bound exciton peak having a FWHM value of 4 meV. The spectrum of the material on the vicinal substrates was shifted to a lower energy, indicative of the tensile stresses in the film. The on-axis spectrum also contained a peak believed to be associated with free excitonic emission.

$Al_xGa_{1-x}N$  films have been grown for  $0 \leq x \leq 1$ . Abrupt heterojunctions have been demonstrated in this system. DCXRC measurements revealed smaller FWHM values for  $AlGaN$  films grown on on-axis 6H-SiC(0001) substrates as compared to simultaneously deposited films grown on vicinal substrates. Also, the FWHM values increase with increasing values of x. The CL spectra of the  $Al_xGa_{1-x}N$  films for  $x < 0.5$  showed strong near band-edge emission. FWHM values of the main energy peak increased with increasing Al mole fraction. Si-doped  $Al_{0.75}Ga_{0.25}N$  exhibited a NEA effect in the as-deposited state.

#### E. Future Research Plans and Goals

With the achievement of both p- and n-type GaN, the fabrication of p-n homojunctions is possible, but mesa isolation of these junctions is needed for electrical testing. Further work will be undertaken to increase the maximum achievable net carrier concentration in p-type GaN. By demonstrating the growth of high quality  $Al_xGa_{1-x}N$  films for  $x < 0.3$  directly on 6H-SiC, doping of these films will allow for their use as a conducting buffer layer. Additionally, the growth of high quality  $Al_xGa_{1-x}N$  for  $x > 0.3$  is needed. Also, the electrical characterization of p- and n-type doping of  $Al_xGa_{1-x}N$  must be demonstrated. This will allow for the fabrication of single and double heterostructures for ultraviolet LEDs, photodetectors, and laser diodes.

These efforts will require the ability to grow thin quantum well structures. Concurrently, microelectronic devices such as MESFETs, MISFETs, and HBTs can be demonstrated. Ultimately, to be able to achieve these devices, preparation of the nitride surfaces which are free of post-deposition overlayers must be achieved. By using spectroscopic ellipsometry in concert with other analytical techniques, this can be accomplished.

#### F. References

1. M. A. Haase, J. Qui, J. M. DePuydt and H. Cheng, *Appl. Phys. Lett.* **59**, 1272 (1991).
2. H. Jeon, J. Ding, A. V. Nurmikko, W. Xie, D. C. Grillo, M. Kobayashi, R. L. Gunshor, G. C. Hua and N. Otsuka, *Appl. Phys. Lett.* **60**, 2045 (1992).
3. W. Xie, D. C. Grillo, R. L. Gunshor, M. Kobayashi, H. Jeon, J. Ding, A. V. Nurmikko, G. C. Hua and N. Otsuka, *Appl. Phys. Lett.* **60**, 1999 (1992).
4. S. Strite and H. Morkoc, *J. Vac. Sci. Technol. B* **10**, 1237 (1992).
5. M. Gershenson, D. E. Wang, L. Ta, in *Proceedings 1981 International Optoelectronics Workshop, Tainan, Taiwan, December 1981*, edited by D. Y. Chang (National Cheng Kung University, Tainan, Taiwan) p. 139.
6. R. F. Davis, *Physica B* **185**, (1993).
7. S. Yoshida, S. Misawa and S. Gonda, *Appl. Phys. Lett.* **42**, 427 (1983).
8. S. Yoshida, S. Misawa and S. Gonda, *J. Vac. Sci. & Technol. B* **1**, 250 (1983).
9. H. Amano, N. Sawaki, I. Akasaki and Y. Toyoda, *Appl. Phys. Lett.* **48**, 353 (1986).
10. H. Amano, I. Akasaki, K. Hiramatsu, N. Koide and N. Sawaki, *Thin Solid Films* **163**, 415 (1988).
11. I. Akasaki, H. Amano, Y. Koide, K. Hiramatsu and N. Sawaki, *J. Cryst. Growth* **98**, 209 (1989).
12. M. A. Khan, J. N. Kuznia, D. T. Olson and R. Kaplan, *J. Appl. Phys.* **73**, 3108 (1993).
13. J. N. Kuznia, M. A. Khan, D. T. Olson, R. Kaplan and J. Freitas, *J. Appl. Phys.* **73**, 4700 (1993).
14. W. Qian, M. Skowronski, M. De Graef, K. Doverspike, L. B. Rowland and D. K. Gaskill, *Appl. Phys. Lett.* **66**, 1252 (1995).
15. K. Hiramatsu, S. Itoh, H. Amano, I. Akasaki, N. Kuwano, T. Shiraishi and K. Oki, *J. Crystal Growth*, **115**, 628 (1991).
16. S. Nakamura, *Jpn. J. Appl. Phys.*, **30**, L1705 (1991).
17. N. Kuwano, T. Shiraishi, A. Koga, K. Oki, K. Hiramatsu, H. Amano, K. Itoh and I. Akasaki, *J. Cryst. Growth*, **115**, 381 (1991).
18. A. A. Chernov, *Modern Crystallography III: Crystall Growth* (Springer, Berlin, 1984) p. 283.
19. S. Nakamura, *Jpn. J. Appl. Phys.*, **30**, 1620 (1991).
20. A. E. Wickenden, D. K. Wickenden and T. J. Kistenmacher, *J. Appl. Phys.*, **75**, 5367 (1994).
21. D. K. Wickenden, J. A. Miragliotta, W. A. Bryden and T. J. Kistenmacher, *J. Appl. Phys.* **75**, 7585 (1994).
22. R. C. Powell, G. A. Tomasch, Y.-W. Kim, J. A. Thornton and J. E. Greene, *Mater. Res. Soc. Symp. Proc.* **162**, 525 (1990).
23. P. J. Born and D. S. Robertson, *J. Mater. Sci.* **15**, 30003 (1980).
24. K. Matsubara and T. Takagi, *Jpn. J. Appl. Phys.* **22**, 511 (1982).
25. Z. Sitar, M. J. Paisley, B. Yan and R. F. Davis, *Mater. Res. Soc. Symp. Proc.*, **162**, 537 (1990).
26. Cree Research, Inc., 2810 Meridian Parkway, Suite 176, Durham, NC 27713
27. T. W. Weeks, Jr., M. D. Bremser, K. S. Ailey, E. Carlson, W. G. Perry and R. F. Davis (unpublished).

28. T. W. Weeks, Jr., M. D. Bremser, K. S. Ailey, E. Carlson, W. G. Perry, L. L. Smith, J. A. Freitas, Jr., R. F. Davis, Second Nitride Workshop, St. Louis, MO, October 17-18, 1994.
29. S. Tanaka, R. S. Kern and R. F. Davis, *Appl. Phys. Lett.* **66**, 37 (1995).
30. T. W. Weeks, Jr., D. W. Kum, E. Carlson, W. G. Perry, K. S. Ailey and R. F. Davis, Second International High Temperature Electronics Conference, Charlotte, NC, June 5-10, 1994.
31. R. Dingle, D. D. Sell, S. E. Stokowski and M. Illegems, *Phys. Rev. B* **4**, 1211 (1971).
32. N. V. Edwards, T. W. Weeks, Jr., M. D. Bremser, H. Liu, R. A. Stall, R. F. Davis and D. E. Aspnes, Materials Research Society Spring Meeting, San Francisco, CA, April 17-20, 1995.
33. W. Götz, N. M. Johnson, R. A. Street, H. Amano and I. Akasaki, *Appl. Phys. Lett.* **66**, 1340 (1995).
34. S. Nakamura, T. Mukai, M. Senoh and N. Iwasa, *Jpn. J. Appl. Phys.* **31**, L139 (1992).
35. M. R. H. Khan, Y. Koide, H. Itoh, N. Sawaki and I. Akasaki, *Solid State Commun.* **60**, 509 (1986).

## XV. Novel Computer-controlled CVD System for the Deposition and Doping of III-V Nitride Thin Films

### A. Introduction

With recent world-wide research efforts, the III-V nitride compounds have shown their potential for optoelectronic and microelectronic semiconductor device applications. With band-gap energies ranging from 1.9 and 3.4 eV for InN and GaN, respectively, to 6.2 eV for AlN, optical devices can be made covering the entire visible light range through the UV range. Also, the III-V nitrides are well suited to high-temperature, high-power microelectronic applications. Production and commercial availability of nitride-based optoelectronic devices is now possible because earlier materials problems, such as p-type doping of GaN, have been overcome. As a result of these advancements, high-power, high-brightness LEDs have been produced in the blue-green, blue and violet-blue spectral ranges [1-4]. Also, Amano *et al.* have shown violet stimulated emission from a photopumped AlGaN/GaInN heterostructure demonstrating optical confinement and the feasibility of laser structures in this material system [5]. Other work on microelectronic devices by Khan *et al.* includes a AlGaN/GaN-based heterostructure field effect transistor (HFET) [6]. Although progress has been made in both optoelectronic and microelectronic devices, further developments are possible, such as complete compositional control of the nitride alloys and doping of AlN. To address these problems and to further demonstrate the capabilities of the III-V nitrides, a novel CVD system has been developed and built. Progress made in the growth of AlN and GaN films will be discussed.

### B. Experimental Procedure

An inverted flow rotating disc MOCVD system was used to grow the AlN and GaN films. The design and features of the CVD system have been described in detail in a previous report [7]. The reactants used in the film growth were trimethylaluminum (TMA), triethyl-gallium (TEG) and ammonia ( $\text{NH}_3$ ). Hydrogen was used as the diluent and carrier gas. The deposition pressure was varied between 45 and 90 torr. The system was operated under both manual and computer control.

The films were grown on Si-face SiC(0001) substrates cut 3-4° off-axis towards the  $<11\bar{2}0>$ . The as-received wafers were cut using a diamond saw into 7.1mm square pieces and degreased. The SiC pieces were then dipped into a 10% HF solution for 10 minutes to remove the thermally grown oxide and blown dry with  $\text{N}_2$ . After, the substrates were mounted on the SiC-coated graphite substrate holder and loaded in the system. The reactor chamber was evacuated to less than  $2 \times 10^{-6}$  torr before initiating growth. The substrate holder was rotated continuously at approximately 45 rpm while being heated with a resistance heater to 1100°C in 2000 sccm of  $\text{H}_2$ . In addition, 10 sccm of  $\text{H}_2$  was flowed continuously through the radial precursor mixing manifold, acting as a purge between gas source switching. The temperature

of the substrate was measured using an Ircon Ultimax Infrared Thermometer. While the growth temperature was being obtained, the flow of the carrier gas through the metalorganic bubblers was established. The temperature and pressure of each bubbler were independently controlled at 20°C and 300 torr. Once the growth temperature was reached, AlN deposition was started by flowing TMA and NH<sub>3</sub> into the reactor at 12.7 μmol/min and 1500 sccm, respectively. The AlN was grown for five minutes corresponding to a thickness of approximately 1000 Å. After five minutes, the TMA flow was switched off and the temperature was lowered to 1000°C. Once this temperature was obtained, GaN deposition was started by flowing TEG at a rate of 23.7 μmol/min. After the prescribed time, the TEG flow was switched off and the film was cooled to room temperature in flowing H<sub>2</sub> and NH<sub>3</sub>. The growth rate of the GaN film was approximately 5 μm/hour. Scanning Electron Microscopy (SEM) was performed on a JEOL 6400 FE operating at 5kV.

### C. Results and Discussion

*Film Growth.* Figures 1 and 2 are SEM micrographs representative of the quality of the preliminary growth of AlN and GaN films, respectively. The AlN film has few distinguishable features on the relatively flat surface. Deposition of a flat, monocrystalline buffer layer is necessary in order to deposit high-quality GaN films. SiC has an advantage over sapphire in this respect, since monocrystalline AlN films can be deposited directly at high temperatures, rather than depositing a low temperature, amorphous layer that crystallizes at higher temperatures. These crystallized films on sapphire have been shown to be highly oriented

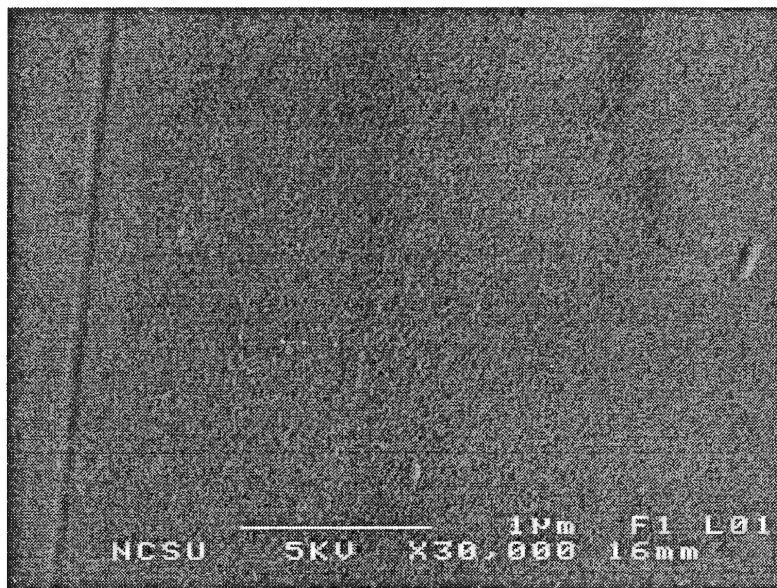


Figure 1. SEM micrograph of surface of AlN film.

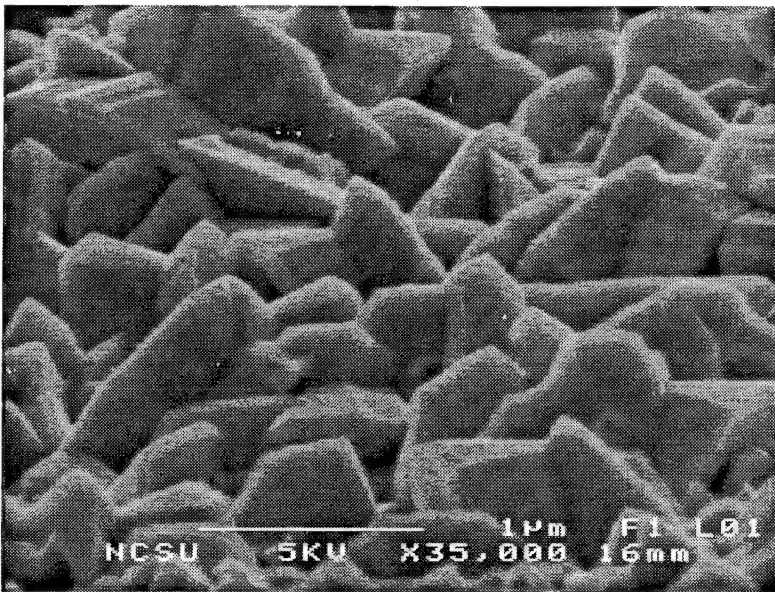


Figure 2. SEM micrograph of surface of GaN film.

polycrystals with low-angle grain boundaries and threading dislocations. This leads to higher defect density GaN films [8-10]. While the initial results are promising, the AlN buffer layers will be further investigated using high-resolution transmission electron microscopy (HRTEM) to examine the surface and microstructure of the films.

Figure 2 shows the random polycrystalline nature of the GaN film grown on the AlN buffer layer in Fig. 1. The morphology of the film is attributed to the high growth rate of the GaN film (approximately 5  $\mu\text{m}/\text{hour}$ ). Reducing the growth rate the GaN should yield smoother films, reflecting the high quality of the AlN buffer layer. Further optimization of the growth parameters will be investigated.

*System Operation.* Using the LabVIEW software package from National Instruments, computer control of the CVD system has been demonstrated for the system temperature, valve operation, and gas flow rate control. Integration of these control programs will lead to the operation of the system under complete computer control.

#### D. Conclusions

The growth of AlN and GaN films on Si-face SiC(0001) using a novel CVD system design has been investigated. SEM micrographs show relatively flat AlN films and random polycrystalline GaN films. With further work, the quality of both films should improve. Computer control of key system components has been demonstrated.

## E. Future Research Plans and Goals

As noted, the quality of the GaN films grown depends greatly on the quality of the buffer layer. Future plans include further growth and characterization of the AlN buffer layer, as well as investigating the use of AlGaN alloys and graded buffer layers for the growth of GaN and nitride alloys. N-type and p-type doping of GaN will also be investigated. Obtaining high quality GaN will provide a template for work on InN and InGaN alloys, with concentration on green and blue-green spectral emission. This will lead to growing device structures, including Schottky diodes, HFETS, photodetectors and LEDs and lasers. Finishing the work to establish complete computer control of the system will help in the fabrication of device structures. Film and device characterization techniques will include Photoluminescence, Secondary Ion Mass Spectroscopy, SEM, HRTEM, X-ray Rocking Curves, and Capacitance-Voltage and Hall-effect measurements.

## F. References

1. S. Nakamura, T. Mukai, M. Senoh. *Appl. Phys. Let.* **64** (13), 1687 (1994).
2. S. Nakamura. *J. Cryst. Growth.* **145**, 911 (1994) .
3. M. A. Khan, Q. Chen, R. A. Skogman, J. N. Kuznia. *Appl. Phys. Let.* **66** (16), 2046 (1995).
4. S. Nakamura, T. Mukai, M. Senoh. *J. Appl. Phys.* **76** (12), 8189, (1994).
5. H. Amano, T. Tanaka, Y. Kuni, K. Kato, S. Kim, I. Akasaki. **61** (11), 1377 (1994).
6. M. A. Kahn, J. N. Kuznia, D. T. Olson, W. J. Schaff, J. W. Burm, M. S. Shur. *Appl. Phys. Let.* **65** (9), 1121 (1994) .
7. Nitride Semiconductors for Ultraviolet Detection. Semiannual Report 1994.
8. T. W. Weeks, M. D. Bremser, K. S. Ailey, E. Carlson, W. G. Perry, R. F. Davis. Submitted to *Appl. Phys. Let.*
9. S. Tanaka, R. S. Kern, R. F. Davis. *Appl. Phys. Let.* **66** (1), 37 (1995).
10. K. Hiramatsu, S. Itoh, H. Amano, I. Akasaki, N. Kuwano, T. Shirashi, K. Oki. *J. Cryst. Growth* **115**, 628 (1991) .
11. W. Qian, M. Skowronski, M. De Graef, K. Doverspike, L. B. Rowland, D. K. Gaskill. *Appl. Phys. Let.* **66** (10), 1252 (1995).

## XVI. New Buffer Layers for GaN on Sapphire by Atomic Layer and Molecular Stream Epitaxy

### A. Introduction

Good quality GaN has been grown by conventional MOCVD and ECR-assisted MBE. For GaN/InGaN grown on sapphire using an AlN/GaN buffer, the large lattice mismatch between GaN and sapphire can enhance three-dimensional nucleation that may lead to polycrystalline material. The most common buffer layer growth method involves depositing an amorphous AlN or GaN film at low temperature (less than 500°C), then anneal at 1000°C or higher to recrystallize before depositing the GaN film [1-3].

This approach has worked very well and several device structures including a blue LED based on the AlGaN/InGaN/AlGaN double heterostructure was produced in Japan based on this buffer layer growth method. However, this method suffers from several problems. First, the electrical properties of the GaN critically depend on the thickness of this buffer layer. Second, the recrystallization of this buffer layer produces low angle grain boundaries that can be a source of dislocation nucleation and propagation to the epilayer surface with a density of  $10^{10} \text{ cm}^{-2}$ . And third, these dislocations can be perpendicular to the GaN/buffer layer interface and thread to the growing surface making their reduction by dislocation interaction and annihilation less probable.

In this paper, we report on two different approaches for buffer layer growth: Atomic Layer Epitaxy (ALE) and Molecular Stream Epitaxy (MSE). Both techniques were developed by our group in the epitaxial growth of GaAs and their related compounds [4-7]. In ALE, the substrate rotates between two streams: one containing metalorganics (MO) and the second, NH<sub>3</sub>, as shown in Fig. 1a. ALE offers the advantage of reactant gas separation, thereby eliminating gas-phase reactions which can hinder high quality material growth. The MSE process is shown in Fig. 1b where the substrate rotates crossing one stream containing both MO and NH<sub>3</sub> thus depositing a few monolayers of AlN or GaN for each rotation. The deposited layer is being annealed during the rest of the cycle and, for example, for a 30 rpm rotational speed growing by MSE, the growth time is 0.2 seconds followed by an annealing time of 1.8 seconds. In this report, comparative analysis of the buffer layers grown by MSE and ALE is discussed.

The design of our reactor allows the growth of thin films by either conventional MOCVD, MSE, ALE, or any combination of the three. The column III and V reactant gases enter the reactor growth chamber through separate tubes and contact the substrate placed on the susceptor which is either rotating or stationary, depending on the mode of growth. For conventional MOCVD, the susceptor is stationary and both reactant gases flow over the substrate simultaneously. With MSE and ALE the susceptor rotates, however, in the MSE

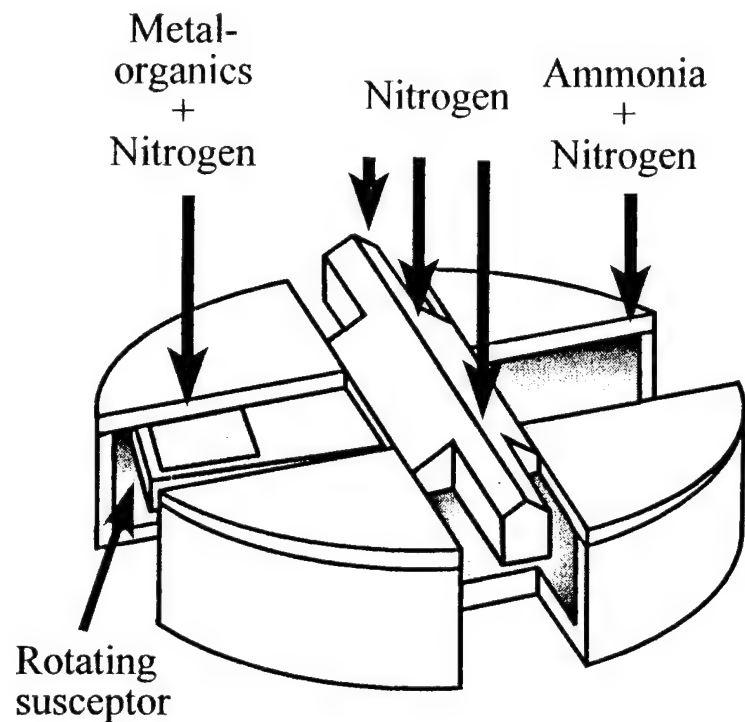


Figure 1a. Schematic of the susceptor and gas flow locations for ALE growth method.

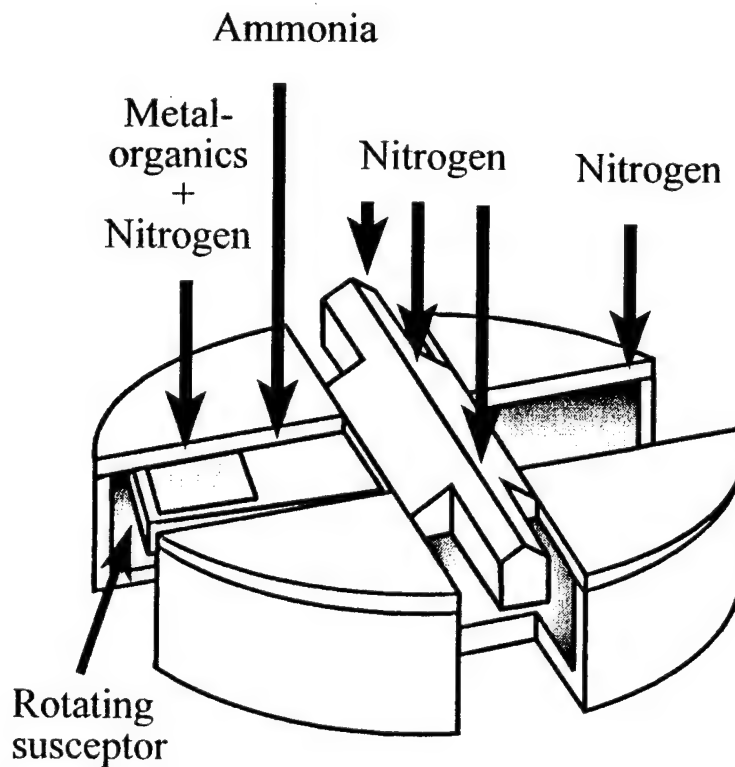


Figure 1b. Schematic of the susceptor and gas flow locations for MSE growth method.

growth mode, the reactant gases flow similar to conventional MOCVD whereas with ALE, they are kept separate from one another contacting the substrate independently. Typical rotation rates are 30 to 60 rpm.

### B. Experimental Procedure

The nitride films are grown on on-axis (0001) sapphire substrates. Prior to growth, the substrate is cleaned and etched in  $H_2SO_4:H_2O_2$  (1:1) for 45 minutes at 120°C. It is then annealed at 1050°C for 15 minutes in the reactor growth chamber followed by ammonia passivation for 1 minute. The layers are grown at temperatures ranging from 550 to 900°C. Column III reactants are TMAI (+18°C), TMGa (-10°C), and EDMIn (+10°C) flowing at 3-15, 1-8, and 15-120 sccm, respectively. The column V reactant is  $NH_3$  with flows in the range of 0.5-2 slm. The carrier and purge gases are purified nitrogen. The pressure in the growth chamber can also be varied from less than 100 torr to atmospheric. All samples grown are characterized by double crystal x-ray diffraction (DCXRD) and  $\theta$ - $2\theta$  x-ray diffraction. The  $\theta$ - $2\theta$  scans are used to determine the films crystalline quality. Photoluminescence (PL) is used to assess the optical properties. Transmission electron microscopy (TEM) is also used for interface and microstructural analysis on some samples.

### C. Results and Discussion

To compare the effect that the buffer layer has on the GaN film, buffer layers grown by MSE and ALE were grown and observed in cross-sectional TEM. For all samples the substrate was (0001) sapphire and the GaN was grown on the buffer layer by conventional MOCVD at 900°C. The GaN films are single crystalline as determined by x-ray diffraction and selected area diffraction in the TEM.

*MSE Grown Buffer Layer.* Figure 2 shows a XTEM brightfield micrograph of GaN grown on an AlN/GaN buffer layer deposited at 900°C by MSE. Threading dislocations are observed as a result of the misfit strain caused by the mismatch between the epilayer and substrate lattices, and also a few low angle grain boundaries are present. The defect density is highest at the GaN/buffer layer interface and decreases with increasing thickness of the GaN layer as observed by other reports [8]. PL data indicates strong band edge emission for GaN grown on MSE buffer layers as shown in Fig. 3 with a peak height greater than 30 volts.

Several samples were grown for the purpose of optimizing the growth conditions of the MSE buffer layer. A growth temperature of 900°C for the buffer layers was kept constant while the pressure and gas flows of the system and the thickness of the buffer layer were varied. In one experiment, an AlN/GaN buffer layer was grown for a high number of cycles using  $N_2$  as the carrier gas without a GaN epilayer. From the x-ray diffraction analysis of the sample, shown in Fig. 4, it was found to be single crystalline but with very low counts. Low counts

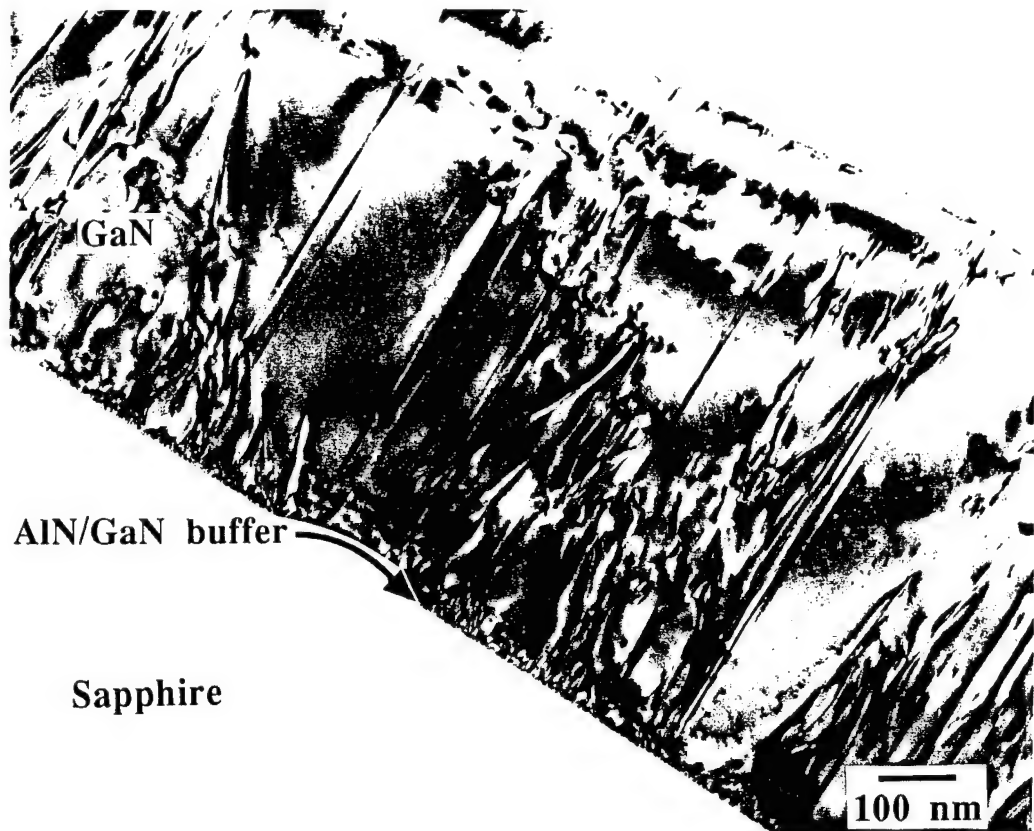


Figure 2. Cross-sectional TEM micrograph of GaN grown on an on-axis (0001) sapphire substrate at 900°C by MOCVD buffered by an AlN/GaN layer grown at 900°C by MSE.

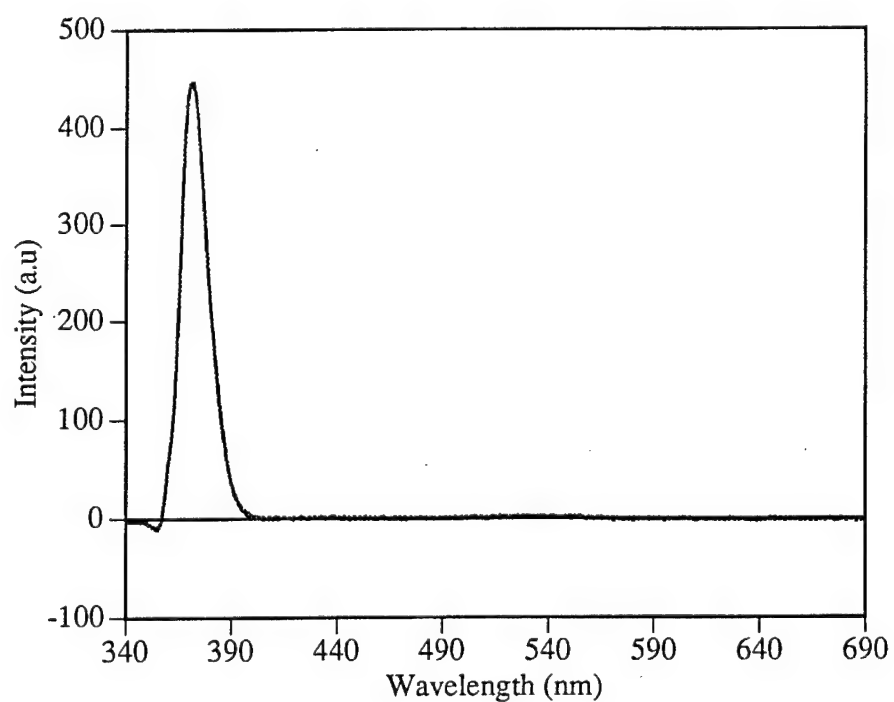


Figure 3. Photoluminescence spectra of GaN grown by MOCVD on an AlN/GaN layer grown at 900°C by MSE.

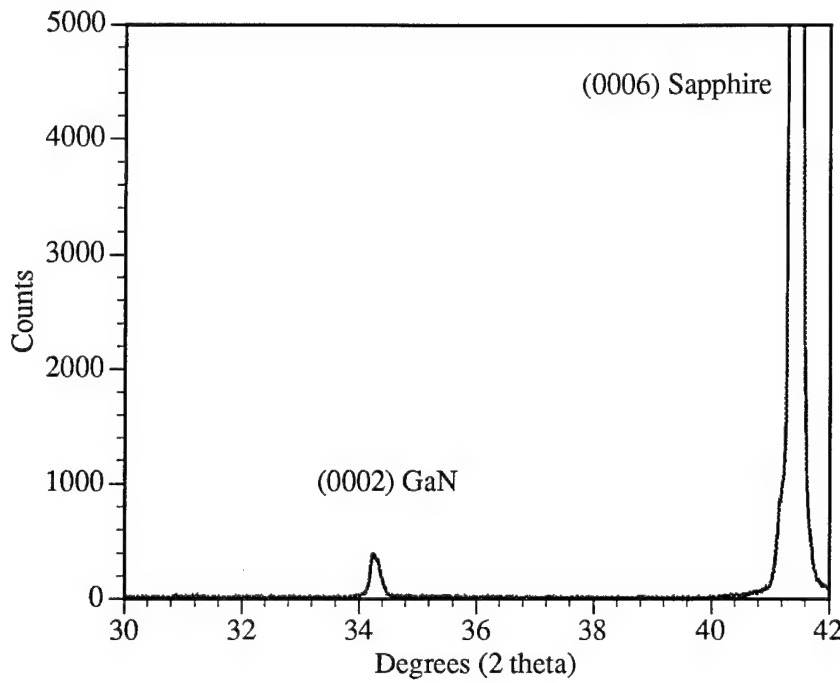


Figure 4.  $\theta$ - $2\theta$  x-ray diffraction analysis of AlN/GaN buffer grown on (0001) sapphire at 900°C by MSE.

usually indicates a thin or very poor quality layer. This may suggest the possibility of an upper limit on the thickness attainable for an AlN/GaN buffer layer grown by MSE or a thickness threshold above which the material reduces in quality. Further study is underway to better qualify this result.

*ALE Grown Buffer Layer.* Figure 5 shows an XTEM brightfield micrograph of GaN grown on an AlN/GaN buffer layer deposited at 700°C and 100 torr by ALE. The threading dislocations is markedly reduced or nonexistent compared to MSE grown material shown in Fig. 2. However, another type of defect has greatly increased in density and occurs uniformly across, as well as through, the GaN film. Preliminary results associate these defects with either low angle grain boundaries, anti-phase domain boundaries, twinning, or double positioning boundaries. Further investigation into the exact nature of these defects is currently underway.

#### D. Conclusions

The preliminary results of several studies into the effect the buffer layer has on the quality of GaN films has been presented. Comparative analysis of MSE and ALE grown buffer layers using XTEM was shown with some interesting differences noted. A possible upper limit on the thickness or a thickness threshold for good quality material by MSE grown AlN/GaN buffer layers has been identified. Further study in both areas discussed in this report is planned and should help in the understanding of the causes producing these results. Optimization of the growth conditions for obtaining good quality buffer layers and GaN/InGaN films is ongoing.

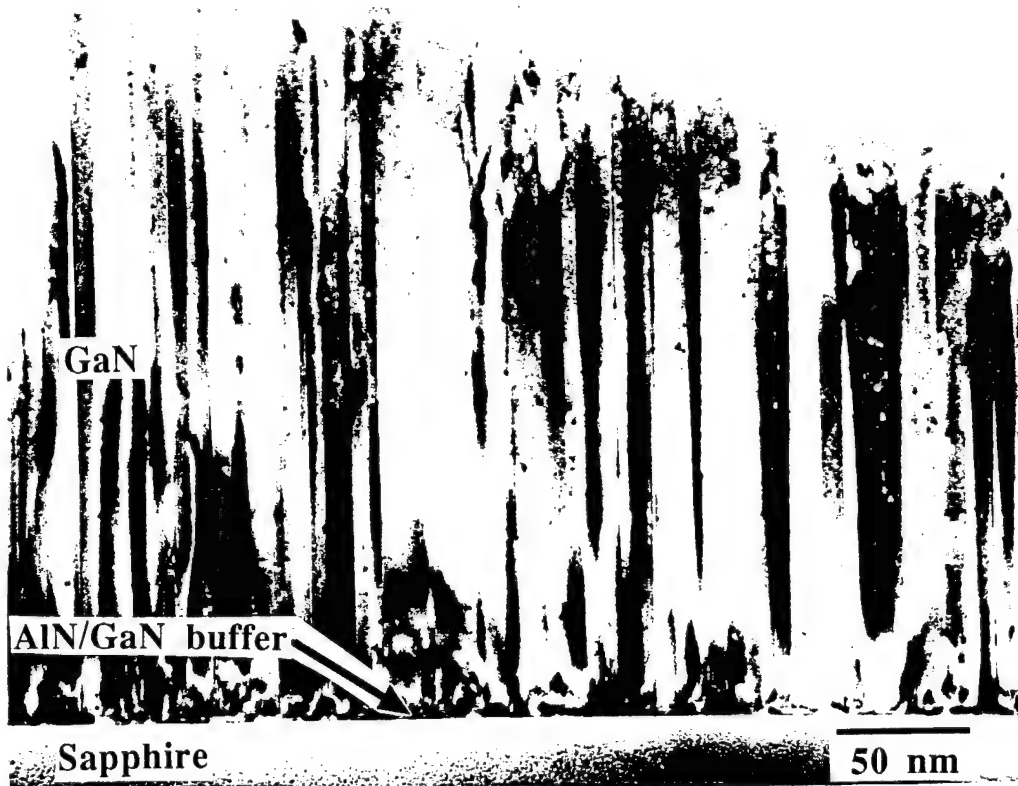


Figure 5. Cross-sectional TEM micrograph of GaN grown on an on-axis (0001) sapphire substrate at 900°C by MOCVD buffered by an AlN/GaN layer grown at 700°C and 100 torr by ALE.

#### E. Future Work

Considerably more research and analysis will be necessary for a better understanding of the topics presented in this report. Other areas of future work include optimizing the thickness of the buffer layer and studying its effect on the dislocation density, microstructure, electrical and optical properties of device quality GaN and InGaN grown on the buffer layers.

#### F. References

1. H. Amano, T. Asahi, and I. Akasaki, Jpn. J. Appl. Phys. **29**, L205 (1990).
2. S. Nakamura, Y. Harada, and M. Seno, Appl. Phys. Lett. **58**, 2021 (1991).
3. J. N. Kuznia, M. Asif Khan, D.T. Olson, R. Kaplan, and J. Freitas, J. Appl. Phys. **73**, 4700 (1993).
4. S. M. Bedair, M. A. Tischler, N. Katsuyama, and N. A. El-Masry, Appl. Phys. Lett. **47**, 51 (1985).
5. N. Katsuyama, M. A. Tischler, N. Karam, N. A. El-Masry, and S. M. Bedair, Appl. Phys. Lett. **51**, 529 (1987).
6. S. M. Bedair, B. T. McDermott, Y. Ide, M. A. Tischler, and N. A. El-Masry, J. Cryst. Growth **93**, 182 (1988).
7. S. M. Bedair, and N. A. El-Masry, Appl. Surf. Sci. **82**, 7 (1994).
8. W. Qian, M. Skowronski, M. De Graef, K. Doverspike, L. B. Rowland, and D. K. Gaskill, Appl. Phys. Lett. **66**, 1252 (1995).

## XVII. Low Temperature Atomic Layer Epitaxy of GaN and InGaN

K. S. Boutros, F. G. McIntosh, J. C. Roberts and S. M. Bedair  
Electrical and Computer Engineering Department  
North Carolina State University  
Raleigh, NC 27695

E. L. Piner and N. El-Masry  
Material Science and Engineering Department  
North Carolina State University  
Raleigh, NC 27695

### Abstract

GaN and InGaN single crystal films have been grown in the temperature range between 600 and 700 °C by Atomic Layer Epitaxy (ALE). InGaN films with composition up to 30% InN have been achieved. The FWHM of double crystal X-ray diffraction of these films was as small as 5 minutes, the lowest value reported for this ternary alloy. Strong photoluminescence band edge emission between 365 nm and 446 nm was observed at room temperature. Excessive flows of the indium organometallic source was not needed for this low temperature growth, emphasizing the ALE technique as a unique approach for the growth of InGaN over the entire composition range.

### A. Introduction

GaN, AlN, InN and their ternary and quaternary alloys are excellent candidates for the development of full-color displays, high-density optical data storage, and high-temperature/radiation hard electronics due to their wide band gap which covers the entire visible-near UV range and their high-thermal conductivity and melting point.

Good quality GaN with both n and p-type conduction has been achieved by conventional MOCVD, as well as reactive-MBE [1-4]. Also, there have been several reports on the growth of AlGaN, InGaN and devices fabricated on these layers [5-8]. Typical growth temperatures at which high-quality materials can be achieved are in the range of 900-1050 °C for the MOCVD environment. Lower temperatures result in polycrystalline films, poor optical properties, and low growth rates due to the low decomposition efficiency of ammonia. At these typical growth temperatures, the vapor pressure of ammonia is very high which causes the GaN films to have a high concentration of nitrogen vacancies, leading to a high background carrier concentration. Also, the growth of InGaN becomes inhibited at these temperatures because of the reevaporation of indium from the film.

---

To be submitted to the Journal of Electronic Materials

Growth of indium-compounds at low temperature is, therefore, desirable. However, due to intense gas phase reaction causing the formation of polymers which affect the quality of the epitaxial layers, little success has been achieved in the growth of InGaN by conventional MOCVD, with the exception of the work done by Nakamura *et al.*, who was able to achieve good quality InGaN up to 25% indium in a modified 2-flow MOCVD reactor [9]. Several attempts have been made by others to reduce the gas phase reaction between column III and column V reactants by the use of high speed nozzles [10], separation of reactants inlets to the chamber [11], and fast gas switching between col. III and col. V reactants [12].

Atomic layer epitaxy (ALE), which relies on continuously flowing col. III and V reactants and a rotating substrate holder exposed alternately to the separate streams of col. III and V, is potentially suitable for the growth of GaN and InGaN at low temperature. ALE of GaAs, InGaP, and other III-V compounds has been previously demonstrated in our lab and has proven to be effective in growing high-quality materials at reduced temperature [13,14]. Also, the inherent self-limiting mechanism offered by the ALE process allows for monolayer control of the growing material over a wide range of growth parameters which is advantageous for the growth of quantum-well type structures. In the case of GaN/InGaN growth, ALE is especially advantageous because it allows for the separation of reactant gases and the possible elimination of gas phase reaction and adduct formation, proven to inhibit the growth of good-quality material. ALE also offers very high effective V/III ratios that can be obtained by varying the dwell times under col. V versus col. III reactants, and enhanced surface diffusion during layer-by-layer growth.

This report presents the growth of GaN and InGaN by ALE using the rotating substrate approach. Preliminary growth parameters required for single crystal growth in a nitrogen atmosphere have been established. It is demonstrated that ALE allows for low temperature growth of GaN and InGaN with good crystal and optical quality and that low temperature is required for achieving higher indium incorporation in the film. Structural, electrical, and optical characterization of the films is presented along with a discussion on the effect of growth parameters on the film quality. Finally, the areas requiring further investigation and the questions to be addressed in future work have been identified.

## B. Experimental Procedure

ALE of GaN was carried out entirely in a nitrogen atmosphere in an ALE reactor that was designed by our group and has been previously proven to allow the low temperature growth of several III-V compounds [14]. The reactor relies on the introduction of col. III and V reactants in separate inlets to the growth area, and the substrate, carried on a rotating susceptor, is exposed sequentially to the reactants in each rotation cycle. Between each exposure, the boundary layer over the substrate is mechanically sheared off to allow for total removal of

reaction products. Then a purging step is achieved by exposing the substrate to nitrogen gas before exposing it to the next reactant. A schematic representation of our susceptor and the configuration of the reactant inlets is shown in Fig. 1. Typically, 30 to 60 cycles are executed per minute, which lead to a growth rate of approximately 0.1 to 0.5  $\mu\text{m}/\text{hr}$ , depending on the growth conditions.

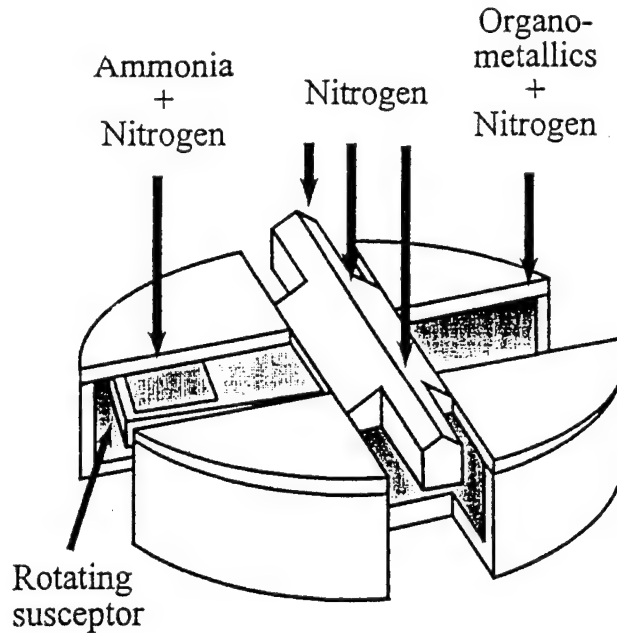


Figure 1. Schematic representation of the ALE susceptor used for the growth of GaN and InGaN and the different gas inlets.

We have expended a great deal of effort in the reactor design and in modifications of the original design to insure total isolation of col. III and col. V reactants to eliminate the gas phase reactions which have a big effect on the quality of growth at low temperatures. We established from this set of experiments a base line for the growth of GaN and InGaN by ALE. The heteroepitaxy of GaN on sapphire substrates was carried out on an AlN buffer layer grown also by ALE, unlike the conventional growth method which relies on depositing an amorphous AlN layer by MOCVD followed by recrystallization at high temperature [11].

We have used for this work on-axis (0001) oriented sapphire substrates which were degreased and etched in (1:1)  $\text{H}_2\text{SO}_4:\text{H}_2\text{O}_2$  @ 120 °C for 45 minutes prior to growth. The substrate is annealed @ 1050 °C in the reactor in a nitrogen atmosphere for 15 minutes, then it is exposed to ammonia for 1 minute to passivate the surface before the deposition starts. A thin AlN buffer is deposited by ALE @ 700 °C and a subsequent GaN buffer layer is deposited at the same temperature. The temperature is then reduced to the appropriate growth temperature for the subsequent growth sequence. Column III reactants used are trimethylaluminum (TMAI) (+18 °C) with flows ~ 7-15 sccm, trimethylgallium (TMGa) (-10 °C) with flows ~ 1-8 sccm,

and ethyldimethylindium (EDMIn) (+10 °C) with flows ~ 15-120 sccm. The col. V reactant used is ammonia with flows ~ 0.5-2 slm, and all carrier and purge gases are purified nitrogen. V/III ratios were varied between  $10^3$  and  $10^5$ , depending on the dwell time under col. V. The pressure used for this set of experiments was 100 torr, in order to minimize reactant mixing and resulting parasitic gas phase reactions. Typical growth temperatures were between 600 and 700 °C. All the layers grown were typically characterized by double crystal X-ray diffraction (DC-XRD) for identifying the crystal quality, room temperature photoluminescence (PL) for optical properties and Hall and conductivity measurements to assess electrical properties. Scanning electron microscopy and TEM were also used in some occasions to assess the surface morphology and defect types in the material.

### C. Results and Discussion

*ALE of GaN with Nitrogen Carrier Gas.* Single crystal GaN with specular surface has been achieved by ALE at growth temperatures as low as 600 °C in a nitrogen ambient. At lower temperatures, the growth rate becomes extremely small if single crystal is to be achieved. This is due to the limited decomposition of TMGa in nitrogen at these temperatures [15]. Usually, at temperatures lower than 600 °C the films appear yellow in color and are optically dead. GaN grown between 600 and 700 °C is single crystal with a reasonable growth rate, and shows DC-XRD line width of approximately 7 minutes. This value is comparable to that obtained from GaN grown by conventional MOCVD at 1000 °C [16]. A typical DC-XRD curve of these GaN films is shown in Fig. 2.

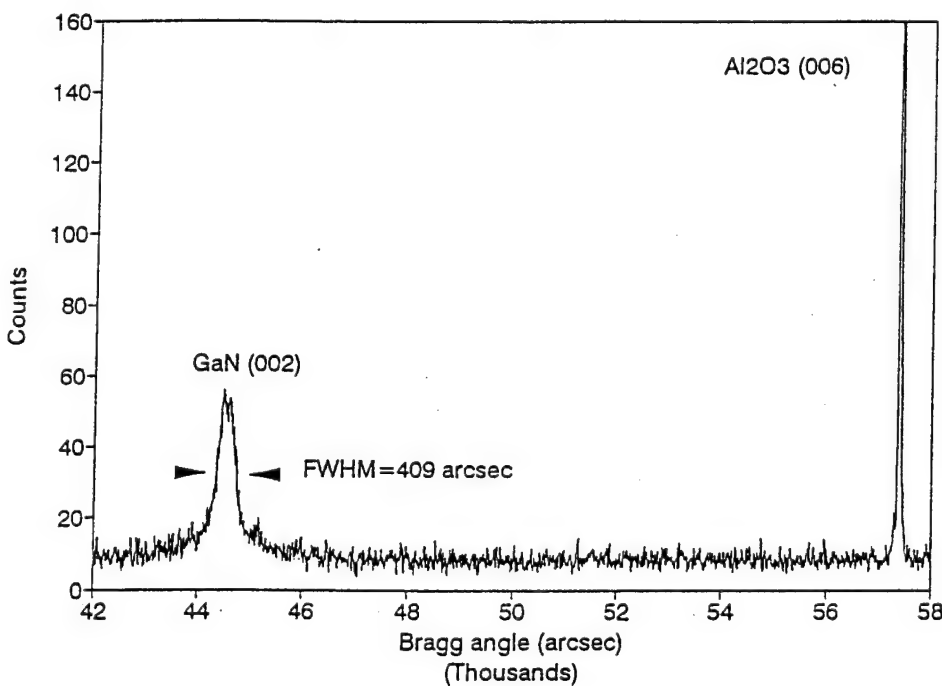


Figure 2. DC-XRD curve of GaN grown by ALE at 700 °C in a nitrogen atmosphere.

PL emission of films grown at lower than 700 °C is dominated by a broad deep level emission centered at 430 nm. Crystals grown at 700 °C, however, have a strong band edge (BE) emission with FWHM ~ 150 meV at room temperature, in addition to a yellow emission at 545 nm. Figure 3 shows the results of a typical room temperature PL emission from these films. The BE emission of these films is of comparable intensity to that obtained from films grown by MOCVD in our lab and by others. This indicates that the film properties obtained by MOCVD can be achieved by ALE with a reduction of about 300 °C in the growth temperature.

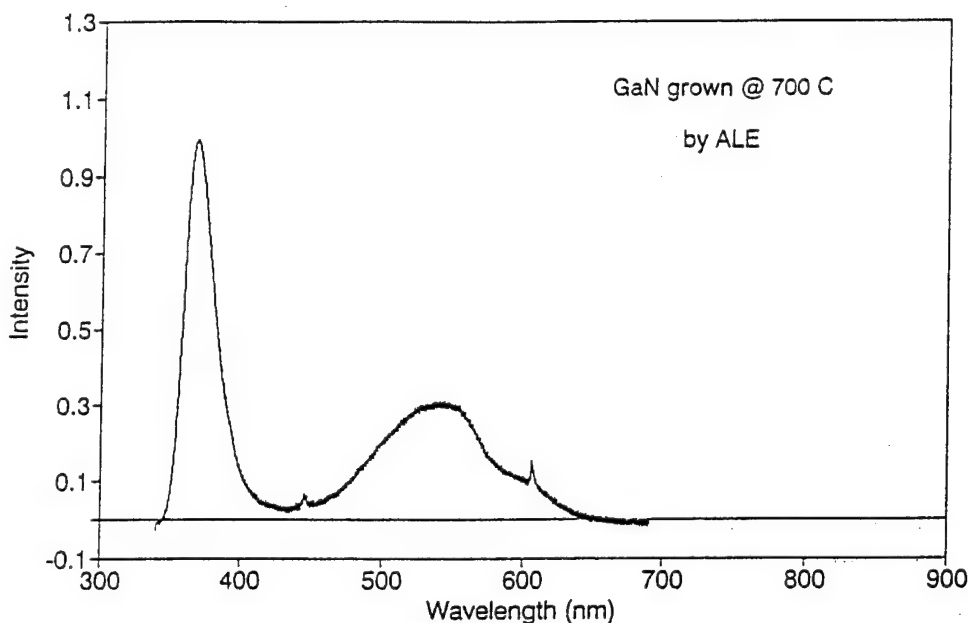


Figure 3. Room temperature photoluminescence plot of GaN films grown by ALE at 700 °C in a nitrogen atmosphere.

The origin of the 430 nm deep level emission is not clear. But its intensity becomes much weaker if it does not totally disappear for samples that have band edge emission which may suggest that it is related to high density of defects in the film caused by the very low growth temperature or by the non-optimum conditions used for the buffer layer growth. This deep level has been previously reported by others and it has been attributed to contaminants present in the organometallic bubblers [17]. The other deep level related emission is the yellow emission at 545 nm. This emission is present with band edge emission and can be variable in intensity relative to BE emission depending on growth conditions. We have observed a trend relating this yellow emission to the gallium flux during growth. Given that all other parameters are fixed, as shown in Fig. 4, the relative BE-to-yellow intensity is strongly dependent on the TMGa flux. This might relate the enhancement of this yellow emission to an increase in carbon incorporation in the film during growth, due to a higher concentration of reaction products. The

nature of this yellow emission is still a subject of controversy, but it has been previously reported to be possibly due to carbon incorporation in the film [18].

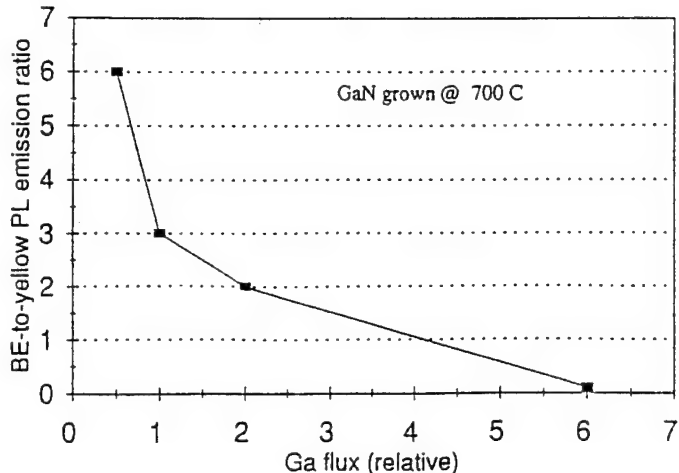


Figure 4. Effect of the gallium flux at the Col. III side during growth on the relative intensities of band edge and deep level PL emission.

Most GaN samples grown below 700 °C had a yellow color and were insulating. A high carbon contamination level is probably the cause for this yellow color and for the high compensation of the material. Samples grown at 700 °C with present BE emission are conducting and the conductivity has been identified by Hall measurements to be n-type. Carrier concentration is typically on the order of  $10^{19}$  per  $\text{cm}^3$ , with mobilities ranging between 5 and 25  $\text{cm}^2/\text{V.sec}$ . The poor electrical properties can be due to several reasons, such as the fairly thin film or the non-optimized buffer layer on which the GaN films are grown.

*ALE of InGaN.* We have also achieved single crystal growth of InGaN with Indium content up to 30% as indicated by XRD, under the same growth conditions as for GaN between 600 and 700 °C. Fig. 5 shows the DC-XRD curve for the InGaN films grown on sapphire substrate. Curve (a) is for a sample grown at 700 °C. We estimated the InN mole fraction in the InGaN films by calculating the difference between the peak positions between the InGaN and sapphire peaks and assuming that Vesgard's Law is valid for this ternary alloy. The calculated value for InN mole fraction from Fig. 2(a) is 7%. Curves (b) and (c) of Fig. 5 are for samples grown at 650 and 600 °C respectively with the same gas flows as for the first sample. The calculated (x) are 14 and 25%, respectively. This indicates, as will be further demonstrated, that the incorporation efficiency of indium in this ternary alloy seems to increase with decreasing growth temperature for the same organometallic vapor pressure ratio. The FWHM of the DC-XRD is about 8, 5, and 17 minutes for the  $\text{In}_{0.07}\text{Ga}_{0.93}\text{N}$ ,  $\text{In}_{0.14}\text{Ga}_{0.86}\text{N}$ , and  $\text{In}_{0.25}\text{Ga}_{0.75}\text{N}$  films, respectively. These values of FWHM are comparable to the

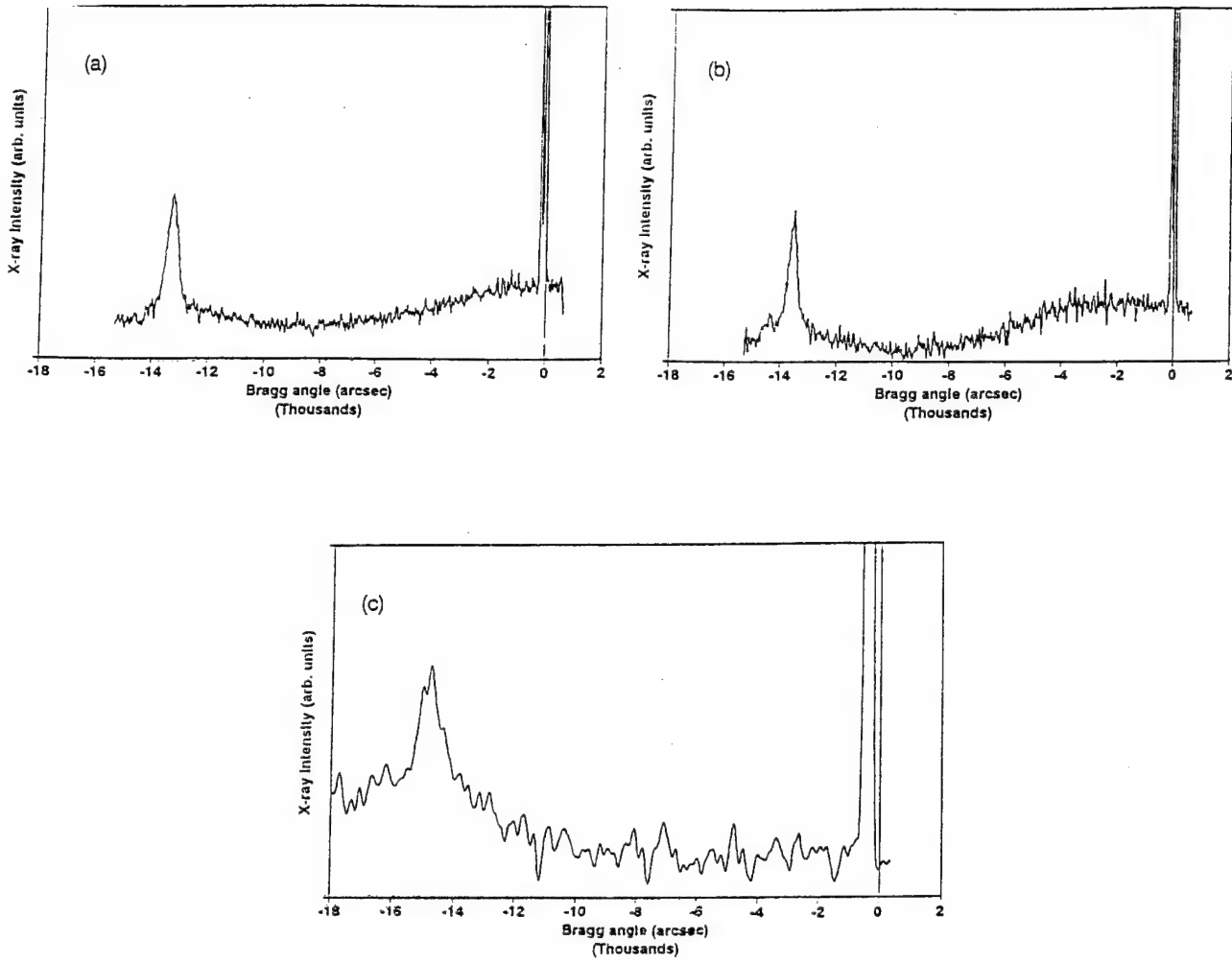


Figure 5. DC-XRD of InGaN films grown by ALE with different InN composition.  
 (a) InN=7%, (b) InN=14%, (c) InN=25%

and  $\text{In}_{0.25}\text{Ga}_{0.75}\text{N}$  films, respectively. These values of FWHM are comparable to the previously reported FWHM in the MOCVD grown InGaN at 800 °C with comparable compositions [9].

PL peaks for films grown at the earlier stages of this work were typically broad, single peaks, that shift with indium concentration, but were usually below the band gap. PL plot for an InGaN film with In~15%, grown at 650 °C, is shown in Fig. 6. Although some band edge emission can be observed, the emission is dominated by a broad deep level emission. Figure 7 shows the PL peak location for different concentrations of indium in InGaN, indicating that most PL emission obtained is sub-band-edge emission. In this plot, the indium concentration is determined from XRD, and data points are presented for InGaN grown at 600, 650, and 700 °C. The theoretical PL emission vs. indium composition curve shown along with the data is obtained from earlier work performed on polycrystals [19].

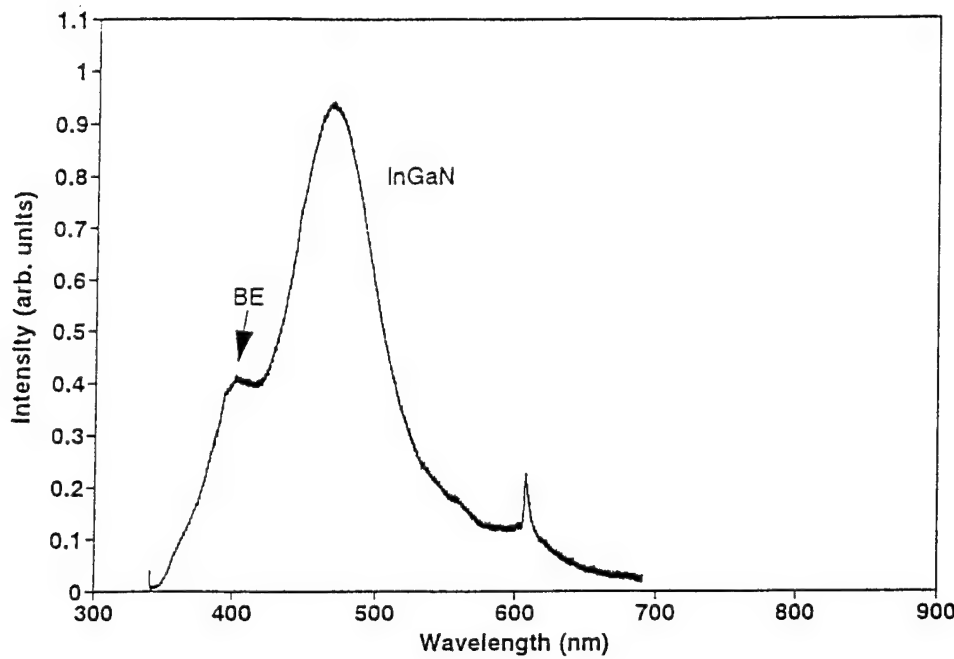


Figure 6. PL emission from InGaN films grown before optimization of the growth conditions. Some BE emission is present, but the PL is dominated by deep levels.

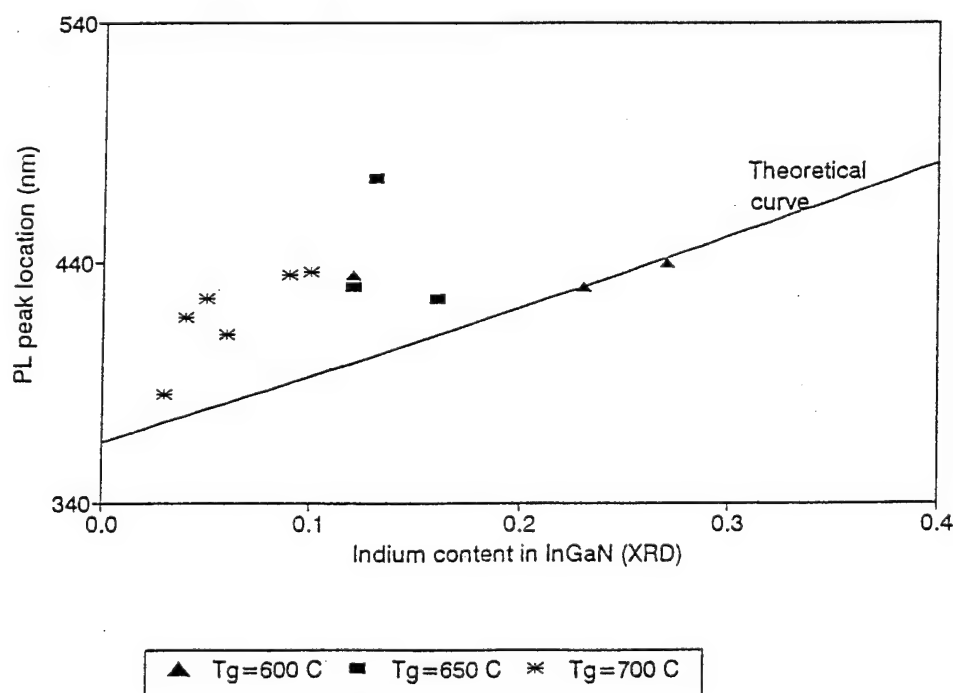


Figure 7. PL peak location vs. indium content in InGaN grown at different temperatures, indicating the PL emission is mainly due to deep levels.

Further optimization of the growth parameters, such as stopping for 1 second under the ammonia flux during the ALE cycle, reducing the total col. III flux, and minimizing carry over of gases from ammonia to the organometallic stream resulted in improvements in the PL spectrum as shown in Fig. 8. In this figure, PL band edge emission at room temperature is presented for  $\text{In}_{0.14}\text{Ga}_{0.86}\text{N}$  and  $\text{In}_{0.27}\text{Ga}_{0.73}\text{N}$  films with FWHMs  $\sim 200$  meV. Nakamura has been the only one thus far to obtain band edge emission from InGaN films with comparable composition [9].

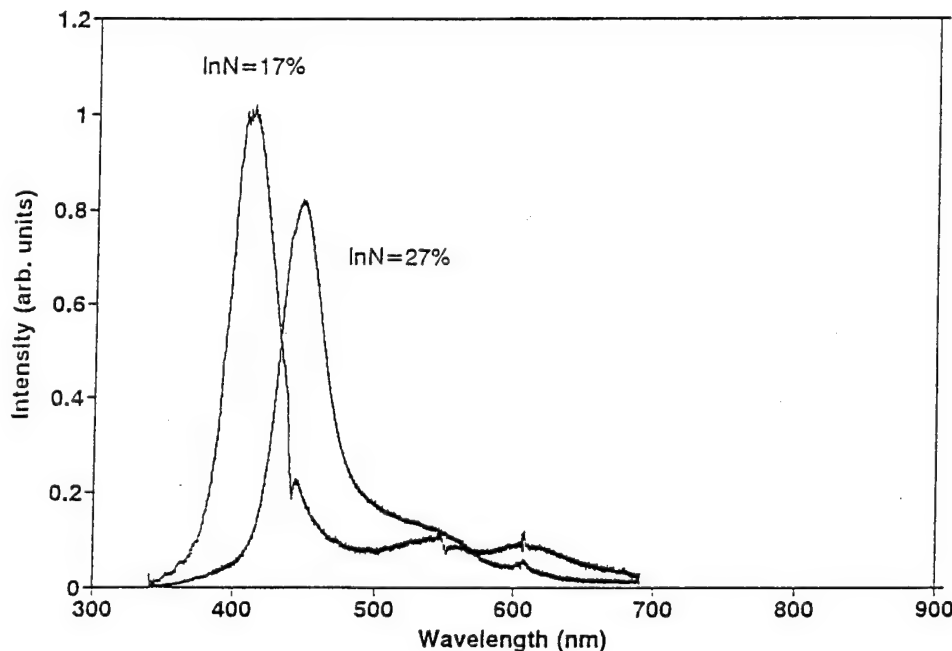


Figure 8. Room temperature PL of  $\text{In}_{0.17}\text{Ga}_{0.83}\text{N}$  and  $\text{In}_{0.27}\text{Ga}_{0.73}\text{N}$  indicating strong band edge emission from these films.

The efficiency of the incorporation of indium in the growing InGaN film is shown in Fig. 9 as a function of In/Ga+In molar ratio in the gas phase with the growth temperature as a second parameter. It can be observed that the incorporation of indium in the film is linearly related to the In/Ga+In molar ratio at a given temperature. But only at 600 °C does the solid composition approach the gas phase composition of EDMIn and TMGa in a 1:1 relation. This indicates that at growth temperatures higher than 600 °C, the indium incorporation efficiency becomes much less than that of gallium, possibly due to the reevaporation of indium from the growth surface during the ALE rotation cycle or to the formation of indium droplets in the InGaN film by segregation during growth [20]. The In/Ga ratios that we have used are much lower than those previously reported to achieve comparable compositions by MOCVD at 800 °C [9]. These results indicate that the ALE process is capable of cracking ammonia at lower

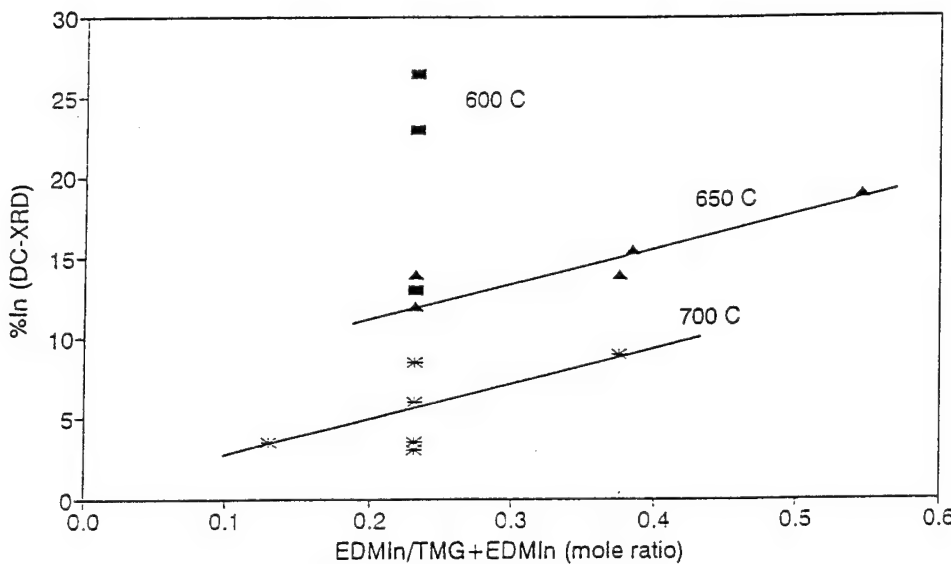


Figure 9. Effect of the In/Ga ratio in the Gas phase and growth temperature on the solid composition of InGaN grown by ALE.

temperatures than that required for the MOCVD technique. In the ALE process, the ammonia is cracked on a more active surface: a surface covered with gallium and indium atoms or their monomethylmetal radicals. The reactivity of this surface seems to be much higher than that of one covered or partially covered by the more inert GaN or InGaN molecules. The sensitivity of indium concentration in InGaN to the growth temperature emphasizes the importance of the ALE technique as a unique approach for the growth of InGaN.

A thorough investigation of our buffer layer has not been completed at this time. Further optimization of this layer is required to improve the quality of the GaN and InGaN films as it is expected that it strongly affects the properties of subsequent layers.

#### D. Conclusion and Future Work

The feasibility of ALE of single crystal GaN and InGaN with high percentage indium at low temperature in a nitrogen atmosphere has been demonstrated. Several key issues have been addressed in the ALE process such as gas phase reaction elimination and reaction product removal by mechanical shearing and gas purging. Consequently, low temperature growth has been made possible.

Strong band edge emission from GaN grown at 700 °C was obtained. These films showed single crystal XRD peaks with FWHM of ~ 7 minutes, and carrier concentration in the order of  $10^{19}$  with mobility of ~ 25 cm<sup>2</sup>/V.sec. Single crystal  $\text{In}_x\text{Ga}_{1-x}\text{N}$  ( $0 < x < 0.3$ ) was also grown by ALE between 600 and 700 °C. The indium concentration in the film has been shown to strongly depend on both the growth temperature and In/Ga ratio in the gas phase. PL emission of these films has been shown to strongly depend on the growth conditions. BE emission from

these films has been achieved with peak emission varying between 365 nm and 446 nm, opening the possibility for the fabrication of blue LEDs.

Further optimization of the growth conditions is necessary to improve the electrical properties of the GaN films, including a thorough investigation of the buffer layer and its effect on film properties. Also, additional investigation of growth temperature, V/III ratio, and growth pressure is necessary to further improve the optical properties of the InGaN films.

Future work will include the investigation of the use of hydrogen as a carrier gas during growth to improve the properties of InGaN and further optimization of the growth parameters to obtain higher InN% in InGaN. We will also attempt to incorporate these InGaN layers in quantum-well structures, study the electrical properties of InGaN and investigate the possibility of p-type doping of both GaN and InGaN.

#### E. References

1. S. Yoshida, S. Misawa and S. Gonda, *Appl. Phys. Lett.* **42**(5), 427 (1983).
2. R. J. Molnar, R. Singh and T. D. Moustakas, *Journ. Elect. Mat.* **24**(4), 275 (1995).
3. M. Rubin, N. Newman, J. S. Chan, T. Fu and J. Ross, *Appl. Phys. Lett.* **64**(1), 64 (1994).
4. S. Nakamura, M. Senoh, and T. Mukai, *Jap. Journ. App. Phys.* **30**(10A), L1708 (1991).
5. M. A. Khan, A. Bhattacharai, J. N. Kuznia and D. T. Olson., *Appl. Phys. Lett.* **63**(9), 1214 (1993).
6. M. A. Khan, J. N. Kuznia, A. R. Bhattacharai and D. T. Olson, *Appl. Phys. Lett.* **62**(15), 1786 (1993).
7. T. Matsuoka, N. Yoshimoto, T. Sasaki and A. Katsui, *Journ. Elect. Mat.* **21**(2), 157 (1992).
8. S. Nakamura, T. Mukai and M. Senoh, *Appl. Phys. Lett.* **64**(13), 1687 (1994).
9. S. Nakamura and T. Mukai, *Jap. J. Appl. Phys.* **31**, L1457, 1992.
10. S. Nakamura, Y. Harada and M. Seno, *Appl. Phys. Lett.* **58**(6), 2021 (1991).
11. H. Amano, N. Sawaki, I. Akasaki and Y. Toyoda, *Appl. Phys. Lett.* **48**(5), 353 (1986).
12. M. A. Khan, R. A. Skogman, J. M. Van Hove, D. T. Olson and J. N. Kuznia, *Appl. Phys. Lett.* **60**(11), 1366 (1992).
13. M. A. Tischler and S. M. Bedair, *Atomic Layer Epitaxy*, T. Suntola and M. Simpson, eds., Chap. 4 Blackie & Son (1990).
14. S. M. Bedair, B. D. McDermott, Y. Ide, M. A. Tischler, N. H. Karam, M. Timmons, and N. El-Masry, "Recent Progress in Atomic Layer Epitaxy of III-V Compounds," Proc. 4th Int. Conf. MOVPE, 1988.
15. M. Yoshida, H. Watanabe and F. Uesugi, *J. Electrochem. Soc.* **123**(3), 677, (1985).
16. J. N. Kuznia, M. A. Khan and D. T. Olson, *J. Appl. Phys.* **73**(9), 4700, (1993).
17. T. Sasaki and S. Zembutsu, *J. Appl. Phys.* **61**(7), 2533, (1987).
18. T. Ogino and M. Aoki, *Jap. Journ. Appl. Phys.* **19**(12), 2395, (1980).
19. K. Osamura, S. Naka and Y. Murakami, *Journ. Appl. Phys.* **56**, 3432 (1972).
20. T. Matsuoka, H. Tanaka, T. Sasaki and A. Katsui, *Inst. Phys. Conf. Ser.* No 106: Chap. 3, 141 (1990).

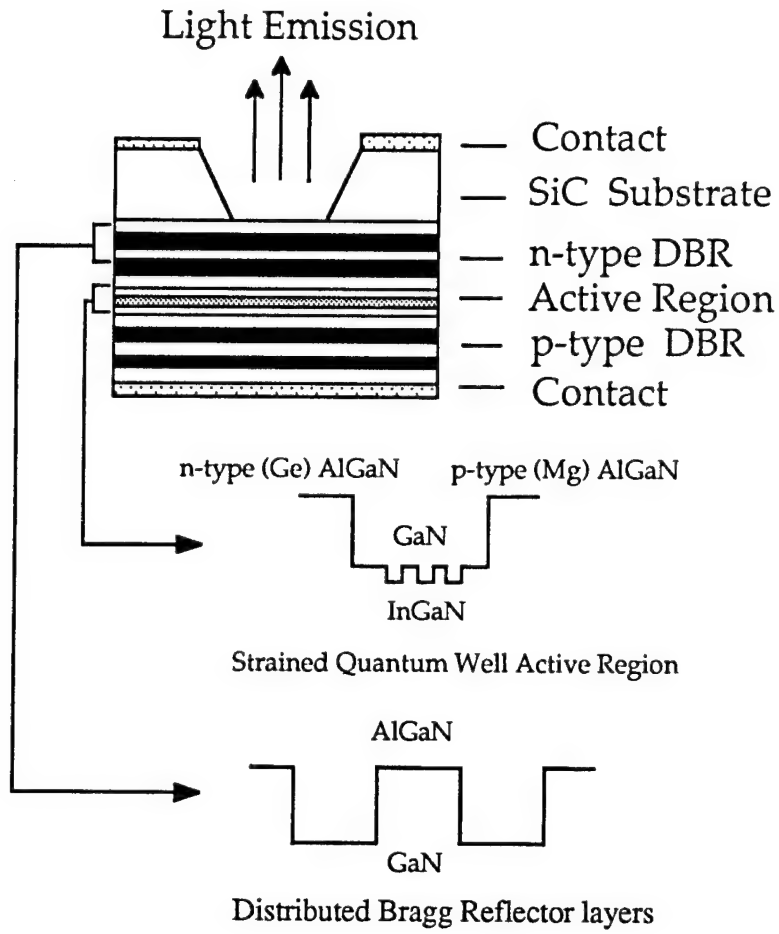
## XVIII. Growth of AlN and GaN Thin Films via Gas Source Molecular Beam Epitaxy

### A. Introduction

Recent research efforts in the wide-bandgap, III-V nitride, semiconductor field have concentrated on the development of light-emitting diodes (LEDs) that emit in the blue spectral region. An AlGaN/InGaN/AlGaN double heterostructure blue LED has been developed in Japan and is now commercially available. The logical next step is the fabrication of blue and UV lasers. The III-V nitrides are most promising candidate materials for these devices because they possess three favorable characteristics: (1) they all have direct transition band structures, (2) their bandgap energies range from the deep UV (6.2 eV (AlN)) to the orange (2.8 eV (InN)) regions of the spectrum, and (3) they can be mixed to form solid solutions allowing for the tailoring of bandgap energies to specific wavelengths.

One of the promising optical devices ideally suited for fabrication using the III-V nitrides is the Vertical Cavity Surface Emitting Laser (VCSEL). VCSELs have significant advantages over edge-emitting lasers for optoelectronic communications. The laser beam emitted from the VCSEL propagates normal to the plane of the substrate, thereby making alignment for chip-to-chip communication much simpler. Additionally, the chip area occupied by a VCSEL is relatively small compared to one required by an edge-emitter [1]. One unique feature of these VCSELs is that both the central light-emitting active region and the outermost distributed Bragg reflectors (DBRs) which form the Fabry-Pérot cavity are all dimensionally defined in one integrated crystal growth sequence performed over the entire wafer using epitaxial techniques such as Molecular Beam Epitaxy (MBE), Gas Source Molecular Beam Epitaxy (GSMBE) and CBE [2]. Efficient performance of such a device requires both high-quality crystalline microstructures and precise control of layer thickness and alloy composition to obtain the highly reflective mirrors and to ensure that the Fabry-Pérot resonance is placed at the exact wavelength for lasing. A typical schematic of a VCSEL structure is shown below. By incorporating a strained MQW active region and by varying the compositional ratios of the group III elements (Al, Ga, and In), the emission wavelength can be tailored to emit in the UV, blue and blue-green spectra.

AlN, GaN and InN thin films are presently grown by various techniques including MOVPE, RF sputtering, and electron cyclotron resonance (ECR) plasma assisted GSMBE. Within the past several years, significant advances in GaN and AlN growth techniques have been achieved [4-12]. Consequently, high quality GaN epitaxial films that exhibit remarkably improved surface morphologies can now be produced by CVD growth techniques. We are currently employing GSMBE to determine the optimal growth parameters for the binary



Schematic of a typical VCSEL structure.

compounds, selected solid solutions of these compounds and multilayer heterostructures of these materials in terms of microstructure and optical and electrical properties. Additionally, researchers have successfully doped the III-V nitrides and their alloys creating n-type (Si, Ge) doped films [13-15] and more notably, p-type magnesium doped films [6,11,14]. Although these recent developments have provided all of the material ingredients necessary for the fabrication of efficient LEDs, further refinement in film quality, namely GaN and InN, is still needed for the GSMBE growth and fabrication of VCSEL structures. This report presents the current research aimed at optimizing the microcrystalline and optical quality of GaN by employing thermally cracked ammonia as an alternative to our ECR plasma source used in III-V nitride thin-film growth.

## B. Experimental Procedure

GaN and AlN thin-films were grown on (0001) oriented  $\alpha$ (6H)-SiC wafers provided by Cree Research, Inc. The films were grown by GSMBE using a commercial Perkin-Elmer 430 system. The Al and Ga fluxes were provided by standard Knudson effusion cells. Nitride grade ammonia is used as the source gas and is further purified by a Nanochem ammonia purifier. The gas enters the MBE chamber through an experimental ammonia cracker cell manufactured by Effusion Science Inc. The cracker cell was designed with a Re filament and fits inside a standard effusion cell sleeve (2.25" diameter) [3]. All substrates were cleaned by a standard degreasing and RCA cleaning procedure prior to loading into the system. Additionally, the substrates were degassed at 700°C for 30 minutes prior to transferring to the deposition chamber.

Reflection high-energy electron diffraction (RHEED) was used to determine the crystalline quality of the films. Scanning electron microscopy (SEM) was used to analyze the films microstructures, and photoluminescence analysis was performed on the GaN films.

## C. Results and Discussion

Figure 1 shows the resulting surface morphologies of deposited GaN grown at 800°C using either ammonia cracked directly on the surface of the substrate, or precracked in the ammonia cracker cell as well as the substrate surface.

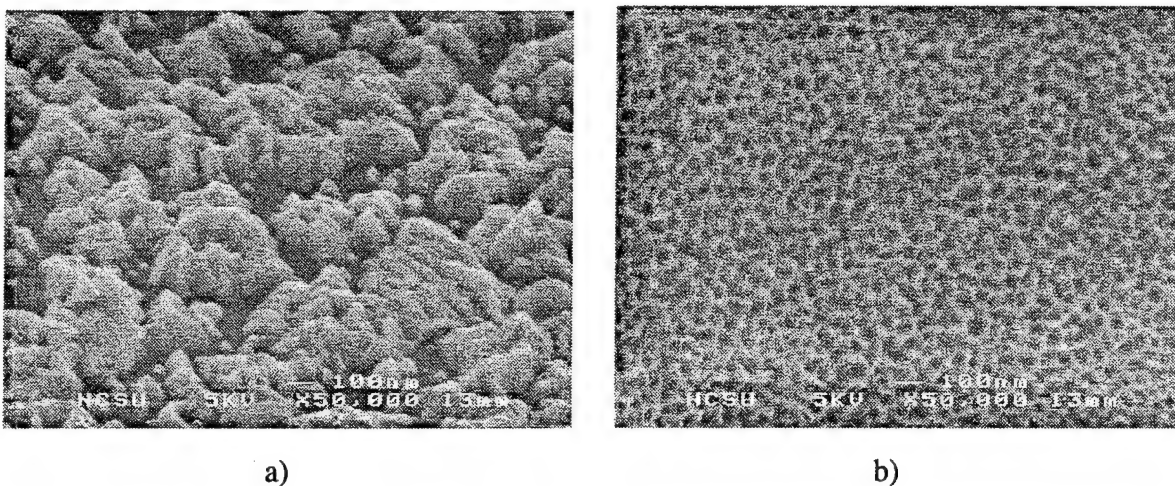


Figure 1. Comparison of GaN grown a) with precracked  $\text{NH}_3$ , and b) without precracked  $\text{NH}_3$ .

SEM image analysis of the GaN reveals smoother surface morphologies and enhanced growth rates were achieved when growth was performed without precracking the ammonia prior to cracking on the substrate. It is suspected that the reduced growth rate resulting from precracking occurs due to an effective reduction of NH radicals reaching the substrate surface.

RGA characterization of the cracker cell revealed that the primary constituents of the cracked ammonia flux were N<sub>2</sub> and H<sub>2</sub>, most likely resulting from recombination of NH molecules leaving the surface of the Re filament. N<sub>2</sub> and H<sub>2</sub> do not contribute to film growth, and thus the only relative source of NH radicals available are those produced from cracking on the substrate surface of any ammonia not previously cracked by the cracker cell.

Figure 2 shows the PL spectrum of GaN grown using ammonia as the nitrogen source. Prior PL of our GaN grown by ECR assisted GSMBE has resulted only in defect peaks and deep level emission. By switching over to ammonia as the nitrogen source, we have for the first time achieved PL emission near the band edge, 354 nm.

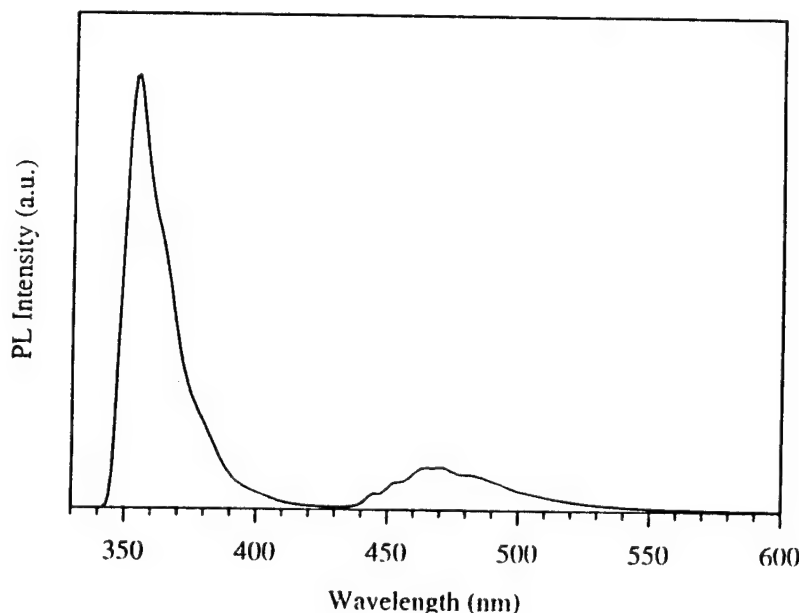
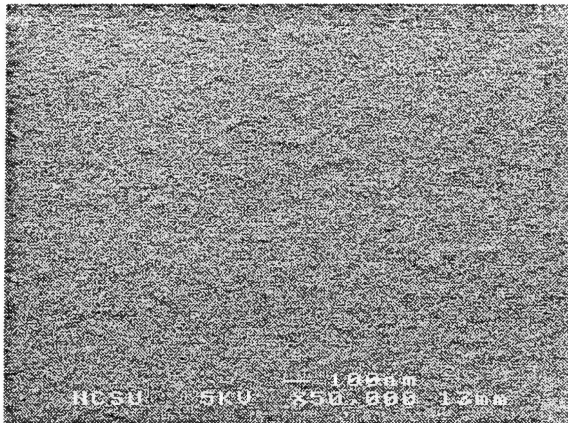


Figure 2. PL of GaN at 8K.

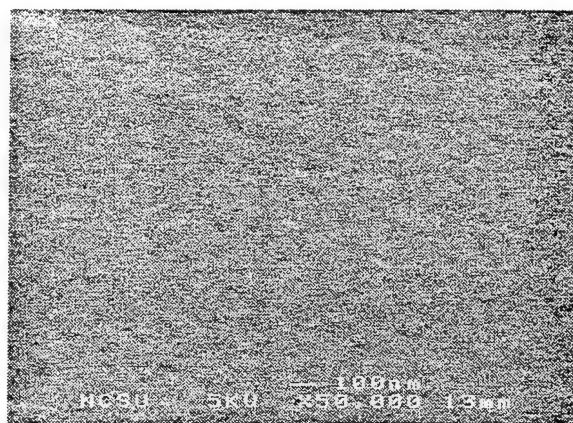
Figure 3 shows the results of SEM analysis performed on AlN grown using ammonia (with and without the assistance of precracking) as the source for nitrogen. In this case, no difference in either surface morphology or growth rate was found using the two methods. Further analysis by TEM may be used in the future to determine this issue. However, by using ammonia instead of the ECR plasma source, we were able to increase our growth rate from 1000Å/hr with the ECR, to 3000Å/hr with the ammonia.

#### D. Conclusions

The use of ammonia (NH<sub>3</sub>) thermally cracked on the substrate surface (6H-SiC) has lead to a marked improvement in the optical properties of GSMBE grown GaN as characterized by the



a)



b)

Figure 3. Comparison of AlN grown a) with precracked  $\text{NH}_3$ , and b) without precracked  $\text{NH}_3$ .

PL spectrum exhibiting a sharp peak at 354 nm in our films for the first time. By using  $\text{NH}_3$  as an alternative source for the ECR, the growth rate of AlN has increased from 1000Å to 3000Å an hour.

The use of a high-temperature ammonia-cracking source to precrack the ammonia has resulted in the degradation of both the film morphology and growth rate for GaN. The effects of the cracker cell on AlN growth is still inconclusive. Analysis of RGA spectra reveal that molecular nitrogen and hydrogen are the primary constituents resulting from decomposition of the ammonia. Recombination of NH molecules leaving the Re filament surface are thought to be the source of the  $\text{N}_2$  and  $\text{H}_2$ . This subsequently leads to a reduced growth rate for GaN films.

#### E. Future Research Plans and Goals

Over the next few months, further improvement of the GaN film quality will be studied by incorporating the use of AlN and AlGaN buffer layers. We will continue to optimize the quality (microstructurally, optically, and electrically) of our GaN, AlN and their solid solutions grown by using ammonia as the source of the group V species. We will then investigate methods of doping the films to obtain n- and p-type carriers. Once we have established these abilities, we will begin studies aimed at precise *in situ* film thickness monitoring. This will be necessary for fabrication of the Fabry-Pérot cavity and DBR mirrors necessary for efficient lasing of the VCSEL structures.

The possibility of using a nitride to replace the Re filament is under consideration at this time. This may allow for an increase in the ratio of atomic N and NH radicals produced by the

ammonia cracker which will be required for the efficient growth of InN grown at lower growth temperatures.

#### F. References

1. T. Miyamoto, T. Uchida, N. Yokouchi and K. Iga, *J. Crystal Growth* **136**, 210 (1994).
2. Y. M. Houn, M. R. T. Tan, B. W. Liang, S. Y. Wang, L. Yang and D. E. Mars, *J. Crystal Growth* **136**, 216 (1994).
3. Effusion Science Inc., 1994.
4. K. Hirosawa, K. Hiramatsu, N. Sawaki and I. Akasaki, *Jpn. J. Appl. Phys.* **32**, L1039 (1993).
5. S. Yoshida, S. Misawa and S. Gonda, *J. Appl. Phys.* **53**, 6844 (1982).
6. C. Wang and R. F. Davis, *Appl. Phys. Lett.* **63**, 990 (1993).
7. S. Nakamura and T. Mukai, *Jpn. J. Appl. Phys.* **31**, L1457 (1992).
8. T. Nagatomo, T. Kuboyama, H. Minamino and O. Omoto, *Jpn. J. Appl. Phys.* **28**, L1334 (1989).
9. M. A. Khan, J. M. Van Hove, J. N. Kuznia and D. T. Olson, *Appl. Phys. Lett.* **58**, 2408 (1991).
10. N. Yoshimoto, T. Matsuoka, T. Sasaki and A. Katsui, *Appl. Phys. Lett.* **59**, 2251 (1991).
11. S. Nakamura, M. Senoh and T. Mukai, *Jpn. J. Appl. Phys.* **30**, L1708 (1991).
12. J. Sumakeris, Z. Sitar, K. S. Ailey-Trent, K. L. More and R. F. Davis, *Thin Solid Films* **225**, 244 (1993).
13. S. Nakamura, P. Mukai, M. Senoh, *Jpn. J. Appl. Phys.* **31**, L139 (1992).
14. I. Akasaki, H. Amano, N. Koide, M. Kotaki and K. Manabe, *Physica B* **185**, 428 (1993).
15. N. Koide, H. Kato, M. Sassa, S. Yamasaki, K. Manabe, M. Hashimoto, H. Amano, K. Hiramatsu and I. Akasaki, *J. Crystal Growth* **115**, 639 (1991).
16. Semiannual Technical Report, Grant #N00014-90-J-1427.
17. Semiannual Technical Report, Grant #N00014-92-J-1720.

## XIX. Electron Cyclotron Resonance Growth of AlN, GaN and InN

### A. Introduction

In CVD systems, energy must be supplied to whatever reaction is producing the growth. In thermal CVD, substrate heating provides energy to these surface reactions. Plasma-enhanced CVD provides another method of energy input, a plasma of activated species; therefore, lower substrate temperatures can be used during growth. In an ECR plasma, a magnetic field is added to confine and direct the particles from the plasma. This method will be used to grow the III-V nitrides.

### B. Experimental Procedure

The plasma source is an ASTeX ECR diamond deposition chamber (see Figure 1). A 2.45GHz microwave source excites a nitrogen plasma in a 875G magnetic field created by two coils. A nitrogen plasma will provide activated nitrogen to the surface reaction. This activated nitrogen flows into a larger growth chamber where the substrate is mounted.

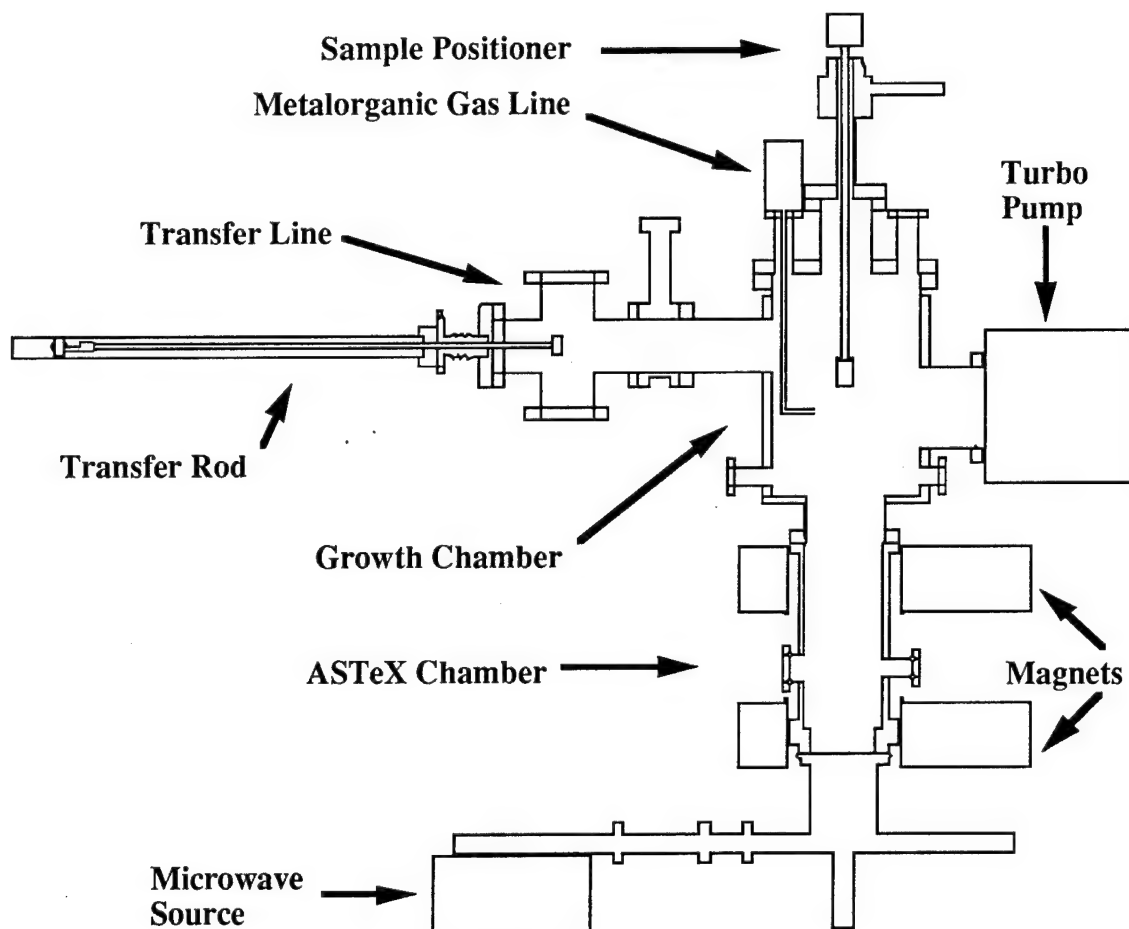


Figure 1. ECR growth system schematic.

The metalorganic precursors will be trimethylaluminum (TMA), trimethylgallium (TMG), and trimethylindium (TMI) using a nitrogen carrier gas. The metalorganics are kept in constant temperature baths, allowing control of their vapor pressures. The metalorganic injection point is a few inches below the substrate position. The reaction between the metalorganics and the activated nitrogen occurs just below the substrate. The metalorganic gas line is mounted to a Z-stage on the top flange to allow varying the substrate to gas inlet distance.

The growth chamber has a 10-3/4" ID and is watercooled. An XYZ stage at the center of the growth chamber's top flange supports the substrate which faces down during growth. The sample holder can flip up 90 degrees so samples can be transferred from the transfer line. The Z motion of the sample holder allows varying the substrate distance from the plasma.

Laser Reflectance Interferometry (LRI) will be used *in situ* to monitor the crystal growth rate and thickness [1]. This technique requires only a laser, photodetector and a computer for recording the photodetector voltage. The incident laser beam reflects at the vacuum-crystal and crystal-substrate boundaries. These two reflected beams will cycle through constructive and destructive interference as the crystal thickness increases with time. The photodetector records the cyclical intensity of the superposed reflected beams. The film thickness and growth rate can be determined knowing the crystal's index of refraction, the incident angle of the laser beams and also the laser wavelength.

### C. Results

The growth chamber, system stand and transfer rod mechanism have been designed and constructed. A mechanism for flipping the sample 90 degrees to allow sample transfers is being designed with Kurt J. Lesker. The microwave source, magnets, and plasma chamber are mounted on an aluminum stand housing the equipment. At present, a simplified nitrogen gas flow system is being used to test this plasma portion of the system. The final gas system is designed and will be assembled after further plasma testing.

### D. Discussion

*Applications of the Nitrides.* All of the nitrides have optoelectronic applications because of their direct bandgaps. Another important application is negative electron affinity (NEA). GaN has an NEA when cesium is adsorbed on its surface [2]. AlN deposited on alpha(6H)-SiC exhibits an NEA directly [3]. Therefore, it can be used to produce cold cathode emitters. The nitride alloys with large bandgaps (see Figure 2) may also exhibit an NEA, and would, therefore, have device applications similar to AlN.

*Progress in the Plasma Growth of the Nitrides.* Several groups have grown nitrides using plasma-enhanced CVD. These attempts are being used as models for the growth system being built. Single crystal n-type GaN was grown on sapphire using ECR plasma MOCVD [4]. The

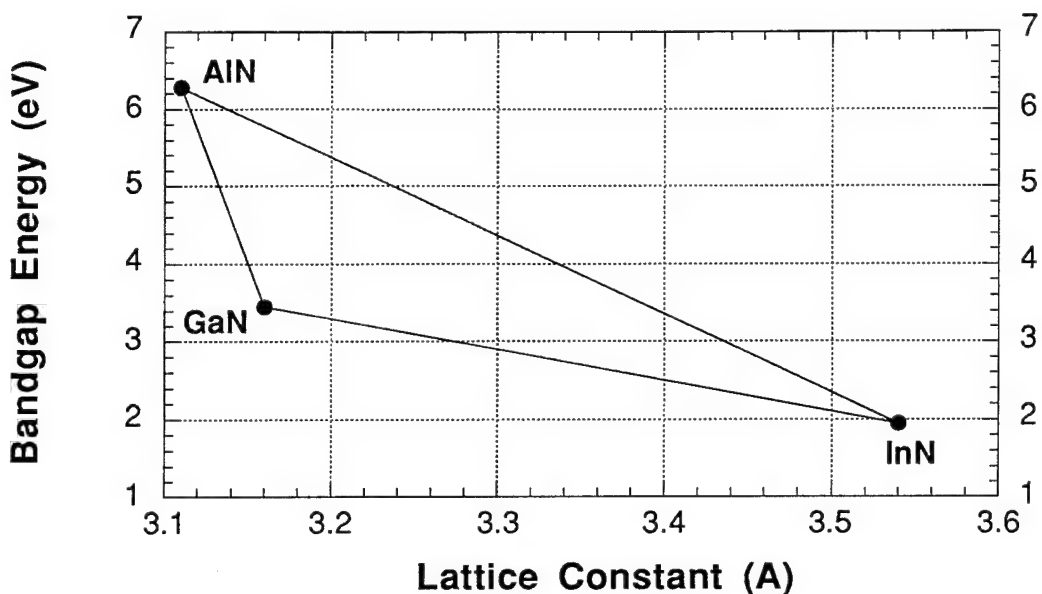


Figure 2. III-V nitride bandgap vs. lattice constant.

precursors were TMG (nitrogen carrier) with an ammonia plasma. The  $\text{NH}_3$  to TMG ratio was about 100. Epitaxial growth occurred from 300-400°C at pressures of .1-1 mTorr.

Single crystal InN was grown on sapphire using microwave plasma (non-ECR) MOCVD [5]. The precursors were TMI (nitrogen carrier) in a nitrogen plasma. The  $\text{N}_2$  to TMI ratio was 5000. Epitaxial growth occurred from 400-600°C at 1.3 Torr.

Thin AlN films were grown using ECR plasma MOCVD [6]. The precursors were TMA (nitrogen & hydrogen carriers) and a  $\text{N}_2/\text{H}_2$  plasma. Growth was at 10mTorr and only at 500°C. At higher growth temperatures, epitaxial growth of AlN may be attained.

AlN, GaN, and InN are completely miscible, so four different alloys can be formed. Single crystals of AlGaN, InGaN, and InGaAlN have been grown using MOCVD [7,8].

#### E. Conclusions

AlN, GaN, InN and their alloys will be grown by the method of ECR plasma-enhanced MOCVD. The ECR method especially suits growth of InN which dissociates at low temperatures. The nitride growth system will eventually be part of the transfer line, thus, connecting it to characterization and plasma cleaning systems.

#### F. Future Research Plans and Goals

The nitrides will be used to make devices and will be studied for their NEA properties. One specific device of interest is the cold cathode emitter.

## G. References

1. B. R. Stoner, B. E. Williams, S. D. Wolter, K. Nishimura and J. T. Glass, *J. Mater. Res.* **7**, 257 (1992).
2. J. I. Pankove and H. E. P. Schade, *Appl. Phys. Lett.* **25**, 53 (1974).
3. M.C. Benjamin, Cheng Wang, R. F. Davis, and R. J. Nemanich, *Appl. Phys. Lett.* **64**, 3288 (1994).
4. S. Zembutsu and T. Sasaki, *Appl. Phys. Lett.* **48**, 870 (1986).
5. A. Wakahara, T. Tsuchiya and A. Yoshida, *J. Crystal Growth* **99**, 385 (1990).
6. H. Nomura, S. Meikle, T. Nakanishi and Y. Hatanaka, *J. Appl. Phys.* **69**, 990 (1990).
7. M. Matloubian and M. Gershenson, *J. Electron. Mater.* **14**, 633 (1985).
8. T. Matsuoka, N. Yoshimoto, T. Sasaki, and A. Katsui, *J. Electron. Mater.* **21**, 157 (1992).

## XX. Native Defects in Gallium Nitride

P. Bogusławski<sup>1,2</sup>, E. L. Briggs<sup>1</sup>, and J. Bernholc<sup>1</sup>

1. *North Carolina State University, Raleigh, NC 27695-8202*

2. *Institute of Physics PAN, 02-668 Warsaw, Poland*

### Abstract

The results of an extensive theoretical study of native defects in hexagonal GaN are presented. We have considered cation and anion vacancies, antisites, and interstitials. The computations were carried out using *ab initio* molecular dynamics in supercells containing 72 atoms. N vacancy introduces a shallow donor level, and may be responsible for the *n*-type character of as-grown GaN. Due to the wide gap of nitrides, self-compensation effects strongly reduce both *n*-type and *p*-type doping efficiencies due to the formation of gallium vacancy and interstitial Ga, respectively.

71.55.Eq, 61.72.Ji, 64.80.Eb

Gallium nitride, together with other wide gap nitrides, holds substantial promise for electronic applications.<sup>1</sup> As-grown undoped samples of GaN are almost always *n*-type, with the concentration of conduction electrons ranging typically from  $10^{17}$  to  $10^{20}$  cm<sup>-3</sup>. These values are much higher than concentrations of detected impurities.<sup>2,3</sup> This strongly suggests that the doping is due to native defects. The residual donor was tentatively identified with the nitrogen vacancy.<sup>2-6</sup> The present calculations support this possibility. We point out, however, that among the point defects another candidate is the interstitial Ga. Like  $V_N$ , Ga(*I*) is an effective-mass donor, and its calculated abundance is comparable to that of  $V_N$  under certain conditions. It is also well-known that GaN is difficult to dope *p*-type. According to the present results, this behavior may be due to an efficient intrinsic compensation mechanism involving the formation of native defects that introduce shallow donor levels. This is a much more serious problem in the wide band-gap GaN (and even more in AlN) than in, say, GaAs, although a reduction of the *n*-type doping efficiency by the formation of Ga vacancies was observed in GaAs.<sup>7</sup> In this Communication we summarize the results of an extensive study of native defects in wurtzite GaN. We describe their electronic structure and use the calculated formation energies to identify the dominant native defects and to evaluate doping efficiencies and stoichiometry effects. The results compare well with the experimental data and lead to a tentative identification of the dominant native defects in as-grown GaN.

The calculations were carried out using *ab initio* molecular dynamics,<sup>8</sup> using an efficient relaxation procedure for optimization of the atomic geometries.<sup>9</sup> For Ga, a standard non-local Ga pseudopotential was used,<sup>10</sup> while a soft non-local pseudopotential was generated for N.<sup>11</sup> The kinetic energy cutoff for the plane wave basis set was 30 Ry. Tests for pure GaN show that these potentials reproduce well previous theoretical and experimental results.<sup>12</sup> Calculations for defects were carried out in a large supercell that would contain 72 atoms in the case of the perfect crystal. Due to the size of the cell, only the  $\Gamma$  point was used for Brillouin zone summations. Some results for the Ga interstitials were corroborated by a newly developed multigrid method,<sup>13</sup> that allows for the use of a much higher cutoff and

the explicit inclusion of Ga 3d electrons.

Assuming that the GaN crystal is in equilibrium with an atomic reservoir of either Ga or N, the formation energy of a defect in a charge state  $q$  is given by

$$E_{form}(q) = E_{tot}(q) - n_{Ga}\mu_{Ga} - n_N\mu_N + qE_F, \quad (1)$$

where  $E_{tot}$  is the total energy of the supercell with the defect,  $n_{Ga}$  and  $n_N$  are the numbers of Ga and N atoms,  $\mu_{Ga}$  and  $\mu_N$  are the chemical potentials, and  $E_F$  is the Fermi energy. The chemical potentials must satisfy the relation  $\mu_{Ga} + \mu_N = \mu_{GaN}$ .<sup>14</sup> Assuming elemental bulk sources for either Ga or N, the computed range of the allowed values for  $\Delta\mu$ , the difference between the chemical potentials of Ga and N, is from -1.8 eV (N-rich limit) to +1.8 eV (Ga-rich limit), since it is bound by the theoretical value of the heat of formation of GaN.

The equilibrium concentration of a defect is given by

$$C = N_{sites} \exp(S_{form}/k_B - E_{form}/k_B T) \quad (2)$$

where  $N_{sites}$  is the concentration of sites, and  $S_{form}$  is its formation entropy. Here, we assume a typical value of  $6 k_B$  for all defects. Since the formation energies of defects in GaN are much greater than the usual entropic contributions ( $4-10 k_B T$ ), this choice does not significantly affect the results. The concentrations of defects are thus determined by three independent parameters: temperature,  $\Delta\mu$ , and the number of carriers supplied by external dopants. The position of the Fermi level and the formation energies of charged defects (cf. eq. (1)) are self-consistently determined as a function of  $\Delta\mu$  from the charge neutrality condition, given the temperature and the number of external dopants.

Density functional theory (DFT) is well-known to underestimate semiconductor band gaps. In the present case, the calculated gap of 2.5 eV is smaller by 1 eV than the experimental value. This error does not influence the formation energies of neutral defects, but may strongly affect those of charged defects. For example,  $E_{form}$  of a shallow donor should be reduced by essentially the energy of the band gap in *p*-type samples. Thus, an underestimate of  $E_{gap}$  by 1 eV overestimates  $E_{form}$  by the same amount. For higher charge states the

error is even greater. We have attempted to partially eliminate this error by correcting both the band gap value and the positions of the gap states of charged defects by the following procedure: For the perfect GaN crystal, GW calculations<sup>15</sup> obtain the correct band gap and show that the major difference with DFT is a rigid upward shift of the conduction bands. Thus, the relevant level(s) is first projected onto valence and conduction states of perfect GaN, which form a complete basis. We then correct the formation energy by assuming that the level(s) has shifted upwards by the fraction of the band gap correction given by its conduction band content.

It is convenient to analyze the results obtained for the wurtzite structure in terms of zinc-blende symmetry with a superimposed hexagonal perturbation. In the zinc-blende structure, a substitutional defect, *e.g.*, a vacancy, has four equivalent nearest neighbors. In the wurtzite structure, the atom along the *c* axis relative to the defect (called here type-1 neighbor) becomes inequivalent to the three remaining neighbors (called here type-2 neighbors). The lowering of the point symmetry is also reflected in the electronic structure: the defect states that are three-fold degenerate in the zinc-blende structure split into singlets and doublets in the wurtzite structure. In the following, we refer to such singlet and doublet pairs as quasi-triplets. The resulting energy levels are schematically shown in Fig. 1, with the hexagonal splittings given in parentheses.

For the vacancies, we expect an  $A_1$  singlet and a quasi-triplet, corresponding to the  $T_2$  state in zinc-blende symmetry. As in the zinc-blende structure, the  $A_1$  state is in the valence bands for both vacancies. Since the electronic states of  $V_N$  are mainly composed of Ga dangling bonds, the energy of the quasi-triplet is quite high. The singlet state of the quasi-triplet is about 0.8 eV above the bottom of the conduction band. The hexagonal splitting is 0.5 eV and the quasi-triplet level contains one electron. However, since the quasi-triplet is a resonance, the electron autoionizes to the bottom of the conduction band, where it forms an effective mass state bound by the Coulomb tail of the vacancy potential.

Since the formation of the Ga vacancy creates  $N$  dangling bonds, its levels should be close to the top of the valence bands. Indeed, the quasi-triplet is located about 0.3 eV above

the valence bands edge, and the hexagonal splitting is only 0.1 eV. Since the quasi-triplet is populated by three electrons in the neutral charge state,  $V_{Ga}$  can trap both electrons and holes.

The gallium antisite introduces a quasi-triplet close to the middle of the band gap. In the neutral charge state, the singlet at  $E_v+1.4$  eV and the doublet at  $E_v+2.1$  eV contain two electrons each. The outward relaxation around  $Ga_N$  is large. The bond lengths with type-1 and type-2 neighbors increase from the ideal value of 3.70 a.u. to 4.12 and 4.27 a.u., respectively.

In the neutral charge state,  $N_{Ga}$  introduces a doubly occupied singlet at  $E_v+0.4$  eV, and an empty doublet at  $E_c-0.2$  eV. The  $N_{Ga}$  strongly distorts along the  $c$  axis. The bond distance to the type-1 neighbor is reduced by 29% and becomes comparable with the bond length in the  $N_2$  molecule, 2.07 a.u. Due to the distortion, the remaining bond lengths increase by 11%. The empty doublet at  $E_c-0.2$  eV cannot be occupied even by one electron, due to the large value of the electron-electron repulsion parameter for this level (0.95 eV).

We now turn to interstitials. In the wurtzite structure, there are two high-symmetry interstitial positions,  $T$  and  $O$ , shown in Fig. 2. The point symmetry is  $C_{3v}$  in both cases. The  $T$  site is located in the middle of the line connecting non-bonded Ga and N atoms. An atom at the  $T$  site has two nearest neighbors and six next nearest neighbors. The  $O$  site has six nearest neighbors, with distances greater by 28% than at the  $T$  site, and 7% greater than the equilibrium bond length. Due to the lack of a reflection plane perpendicular to the  $c$  axis, neither site can be the equilibrium position of an interstitial defect, except by accident. In particular, a relaxation along the  $c$  axis is expected. Indeed, we find that both the  $T$  and  $O$  positions are highly unstable for native interstitials.

The equilibrium position of the interstitial Ga is strongly charge-dependent. Fig. 2 shows both the initial and the relaxed configurations of the neutral  $Ga(T)$ . The relaxation leads to an upward displacement of three atoms:  $Ga(T)$ , the host Ga, and the host N. The  $Ga(T)$  moves by 1.2 a.u., gaining 11 eV. After the relaxation, the Ga-Ga distance increases to 4.17 a.u., which is close to the average Ga-Ga distance for  $Ga_N$  antisite. This configuration is

similar to the bridge-bond geometry of interstitial Ga in GaAs.<sup>16</sup> With an increasing charge the complex moves down, assuming an off-axis position for  $\text{Ga}^{3+}(T)$ .  $\text{Ga}_T^0$  introduces a deep level at  $E_c - 1.8$  eV, occupied by two electrons, and a resonance at  $E_c + 1.0$  eV. The one electron that should occupy the resonance autoionizes and is trapped in an effective mass level. Finally,  $\text{Ga}(T)$  exhibits a negative U behavior, since the +2 charge state is unstable for all positions of the Fermi level. The energy gain for the reaction  $2 \text{Ga}^{2+}(T) \rightarrow \text{Ga}^{3+}(T) + \text{Ga}^+(T)$  is 1.8 eV. The (+/3+) level is located at 1.7 eV above the top of the valence band.

In the case of  $\text{Ga}(O)$  shown in Fig. 2c, the relaxation is much weaker. The interstitial is displaced upwards by 0.55 a.u. and the first three Ga neighbors move down by 0.5 a.u. The change of the charge state has only a minor effect on the relaxation pattern. The electronic structures of  $\text{Ga}(T)$  and  $\text{Ga}(O)$  are quite similar, despite the very different surroundings.  $\text{Ga}(O)$  also introduces a resonance in the conduction bands that leads to an effective mass state, and a deep level at  $E_c - 0.8$  eV. The (+/3+) level is located at about  $E_v + 1.7$  eV and the U parameter is nearly zero. Finally, the computed formation energy of the neutral  $\text{Ga}(O)$  is only 0.2 eV greater than that of  $\text{Ga}(T)$ , which falls within the margin of error of our calculations.

For the N interstitial, starting from either the  $T$  or  $O$  site leads to the same final configuration, shown in Fig. 2d. A similar split-interstitial geometry has been obtained for the As interstitial in GaAs.<sup>16</sup> The displacement from the ideal  $T$  site is over 2 a.u., and the relaxation energy is 7.6 eV. The final N-N bond length is 2.64 a.u., which is very close to the N-N distance in the case of  $\text{N}_{\text{Ga}}$ . Considering the electronic structure,  $\text{N}(T)$  introduces a nearly degenerate pair of deep levels at about  $E_v + 1.0$  eV, separated by 0.1 eV and occupied by three electrons.

The calculated formation energies were used to study stoichiometry effects and to identify the dominant defects in GaN. Bulk samples are grown at  $T_g = 1300\text{-}1500$  °C and under Ga-rich conditions,<sup>6</sup> while MBE and CVD proceed typically at 600-950 and 900-1100 °C, respectively. We have considered several temperatures in the 600-1300 °C range, and com-

puted defect concentrations assuming equilibrium thermodynamics (cf. eq. (2)). However, GaN is currently grown under conditions that deviate significantly from equilibrium (see below). Nevertheless, the results still provide an indication of the identity of the dominant defects and of general effects governing their formation. We describe below the results for  $T_g=1300$  °C, and examine three scenarios: (i) no doping, *i.e.*, intrinsic sample, (ii) *n*-type, and (iii) *p*-type samples with concentrations of external carriers of  $10^{18} - 10^{21}$  cm<sup>-3</sup>. Lowering of temperature to 900 °C results in an overall decrease of defect concentrations by a few orders of magnitude, but trends remain the same.

Our results reveal that the stoichiometry and the doping efficiency of GaN are strongly influenced by the large value of the band gap, and have properties that should be universal for all wide band-gap semiconductors. The formation energies of neutral N and Ga vacancies are 3.2 and 8.1 eV, respectively, at Ga-rich conditions. We thus expect a negligible concentration of  $V_{Ga}$ . However, according to eq. (1), formation energies of defects in highly charged states may be reduced by an energy of up to 2-3 times the band gap, *i.e.*, of the order of 10 eV. In *n*-type samples, the energy gain associated with transferring three electrons from the Fermi level to the low-lying acceptor states of the vacancy makes  $V_{Ga}^{-3}$  the prevalent native defect. In *p*-type samples, this effect occurs for  $Ga^{+3}(I)$ , where three donor electrons are transferred to acceptor levels. Therefore, *doping of wide band gap semiconductors under conditions of thermal equilibrium leads to very strong self-compensation effects*. An attempt to dope the crystal will result in an increasing concentration of the appropriate compensating defect rather than an increase of free carriers. Consequently, one should expect low doping efficiencies and high doping-induced deviations from the ideal stoichiometry. Growth under conditions far from thermal equilibrium or introduction of dopants by ion implantation may lead to greater doping efficiency.

We illustrate the above ideas for GaN at  $T_g = 1300$  °C. In both intrinsic and doped material, the concentration of  $N(I)$  decreases from about 10<sup>17</sup> cm<sup>-3</sup> at N-rich conditions to about 10<sup>11</sup> cm<sup>-3</sup> at Ga-rich conditions. In an intrinsic crystal,  $V_N^+$  is a dominant defect for  $-1.0 \leq \Delta\mu \leq 1.8$  eV, with concentration of about 10<sup>18</sup> cm<sup>-3</sup> in the Ga-rich limit.

Accordingly, the concentration of  $V_{Ga}^{-3}$  is about three times smaller. The concentration of conduction electrons increases with  $\Delta\mu$  from  $10^{14}$  to  $10^{16} \text{ cm}^{-3}$ , and intrinsic GaN is slightly *n*-type, in qualitative agreement with experiment.

Doping of GaN substantially modifies its stoichiometry. The *n*-type crystal is N-rich over almost the whole range of  $\Delta\mu$ , and the dominant defect is  $V_{Ga}$ . Assuming the concentration of ionized external donors of  $10^{18} \text{ cm}^{-3}$  we find that the concentration of  $V_{Ga}^{-3}$  is nearly three times smaller, and is practically constant over the entire range of  $\Delta\mu$ . Only in the Ga-rich limit  $V_N$  starts to dominate and reaches a concentration of about  $10^{18} \text{ cm}^{-3}$ . The *p*-type crystal is Ga-rich, due primarily to the formation of  $\text{Ga}(I)$ , although  $V_N$  again starts to dominate at the Ga-rich limit. As in the case of *n*-doping, the concentration of  $\text{Ga}(I)$  is determined by the concentration of external acceptors.

Compensation effects due to intrinsic defects are very large for both types of doping, leading to a very small doping efficiency, see Fig. 3. This is particularly true for *p*-type doping in the Ga-rich limit, where, *e.g.*,  $10^{21} \text{ cm}^{-3}$  acceptors result in  $10^{14} \text{ cm}^{-3}$  holes. The computed very low *p*-type doping efficiency is in agreement with the experimental data for Mg doping, even in cases where no post-growth electron beam activation is required.<sup>17</sup> The efficiency of *n*-type doping is significantly larger, see Fig. 3b.

Comparing to previous theoretical results, a recent *ab initio* study of native defects in GaN by Neugebauer and Van De Walle<sup>18</sup> obtained results similar to ours for both vacancies and antisites, but there are differences for interstitials. Vacancies and antisites were also studied by Jenkins and Dow<sup>19</sup> using a model tight-binding hamiltonian. Their results differ significantly from those based on *ab initio* methods. Turning to the experiment, as-grown undoped samples of GaN are almost always *n*-type, which was suggested to be due to the formation of nitrogen vacancies,<sup>2-6</sup> but the residual donor(s) were not positively identified. The experimental donor energies are strongly scattered, falling in three ranges:<sup>4,20</sup> 10-40, about 100 and 200-400 meV. Possible explanations include the presence of more than one type of point defect, and/or interaction between point defects and extended defects, which

could lead to energy shifts. According to our calculations, under the usual Ga-rich conditions there are two prevalent shallow donors,  $V_N$  and  $\text{Ga}(I)$ , but the concentration of  $V_N$  is in general higher. The presence of either defect can explain the recently observed pressure-induced freeze-out of free electrons.<sup>6,21</sup> However, the computed formation energies are too large to account for the observed high electron concentrations. This discrepancy may be due to far-from-equilibrium growth conditions, that are also suggested by the large number of extended defects present in even state-of-the-art samples. Further experimental work is needed to positively identify the residual donor in GaN. Most likely the donor is a native one, but the *n*-type character of high-resistance samples could be due to residual impurities. The ODMR data of Glaser *et al.*<sup>5</sup> indicate the presence of a deep donor level as well as a shallow one for a wide variety of samples. The level structure of  $\text{Ga}(I)$ , unlike that of  $V_N$ , could account for this observation. Turning to acceptors, luminescence measurements<sup>22,23,4</sup> systematically find a residual acceptor at  $\sim 0.2$  eV. Lagerstedt and Monemar<sup>22</sup> suggested that it is a native defect, which was later assigned to the gallium vacancy.<sup>4</sup> Our calculations indeed show that  $V_{\text{Ga}}$  induces a shallow acceptor level.

In summary, we have reported the results of large scale *ab initio* calculations for native point defects in GaN. The results suggest that the residual donors responsible for the *n*-type character of as-grown GaN are nitrogen vacancies. However, the concentration of Ga interstitials under equilibrium conditions in the usual Ga-rich material can become comparable to that of the vacancy. Both *n*- and *p*-doping efficiencies are substantially reduced by the formation of  $V_{\text{Ga}}$ ,  $\text{Ga}(I)$ , and  $V_N$ , even in the absence of passivating impurities, such as hydrogen.

This work was supported in part by Grants ONR N00014-92-J-1477, NSF DMR 9408437, and KBN 2-P302-124-07. The calculations were carried out at the Pittsburgh Supercomputing Center and ICM, Warsaw.

## REFERENCES

- <sup>1</sup> R. F. Davis, Physica B **185**, 1 (1993); S. Strite and H. Morkoc, J. Vac. Sci. Technol. B **10**, 1237 (1992); H. Morkoc *et al.*, J. Appl. Phys. **76**, 1363 (1994).
- <sup>2</sup> H. P. Maruska and J. J. Tietjen, Appl. Phys. Lett. **15**, 327 (1969). B. Monemar and O. Lagerstedt, J. Appl. Phys. **50**, 6480 (1979).
- <sup>3</sup> M. Illegems and M. C. Montgomery, J. Phys. Chem. Solids, **34**, 885 (1973).
- <sup>4</sup> T. L. Tansley and R. J. Egan, Phys. Rev. B **45**, 10942 (1992), and the references therein.
- <sup>5</sup> E. R. Glaser *et al.*, Appl. Phys. Lett. **63**, 2673 (1993).
- <sup>6</sup> P. Perlin *et al.*, Proc. 22 Int. Confer. Phys. Semicond. Vancouver 1994, in print.
- <sup>7</sup> W. Walukiewicz, Appl. Phys. Letters, **54**, 2094 (1989).
- <sup>8</sup> R. Car and M. Parrinello, Phys. Rev. Lett. **55**, 2471 (1985).
- <sup>9</sup> C. Wang, Q.-M. Zhang, and J. Bernholc, Phys. Rev. Lett. **69**, 3789 (1992).
- <sup>10</sup> G. B. Bachelet, D. R. Hamann, and M. Schluter, Phys. Rev. B **26**, 4199 (1982); X. Gonze, R. Stumpf, and M. Scheffler, Phys. Rev. B **44**, 8503 (1991).
- <sup>11</sup> G. Li and S. Rabii, unpublished.
- <sup>12</sup> See P. Bogusławski *et al.*, Mat. Res. Soc. Symp. Proc. **339**, 693 (1994).
- <sup>13</sup> E. L. Briggs, D. J. Sullivan, and J. Bernholc, to be published.
- <sup>14</sup> S. B. Zhang and J. E. Northrup, Phys. Rev. Lett. **67**, 2339 (1991). D. B. Laks *et al.*, *ibid.* **66**, 648 (1991).
- <sup>15</sup> A. Rubio *et al.*, Phys. Rev. B **48**, 11810 (1993).
- <sup>16</sup> J. D. Chadi, Phys. Rev. B **46**, 9400 (1992).
- <sup>17</sup> T. W. Weeks, Jr., M. Bremser and R. F. Davis, unpublished.

<sup>18</sup> J. Neugebauer and C. G. Van de Walle, Phys. Rev. B **50**, 8067 (1994).

<sup>19</sup> D. W. Jenkins and J. D. Dow, Phys. Rev. B **39**, 3317 (1989).

<sup>20</sup> R. J. Molnar, T. Lei, T. D. Moustakas, Appl. Phys. Lett. **62**, 72 (1993).

<sup>21</sup> P. Bogusławski and J. Bernholc, unpublished.

<sup>22</sup> O. Lagerstedt and B. Monemar, J. Appl. Phys. **45**, 2266 (1974).

<sup>23</sup> R. Dingle *et al.*, Phys. Rev. B **4**, 1211 (1971); M. Illegems, R. Dingle, and R. A. Logan, J. Appl. Phys. **43**, 3797 (1972).

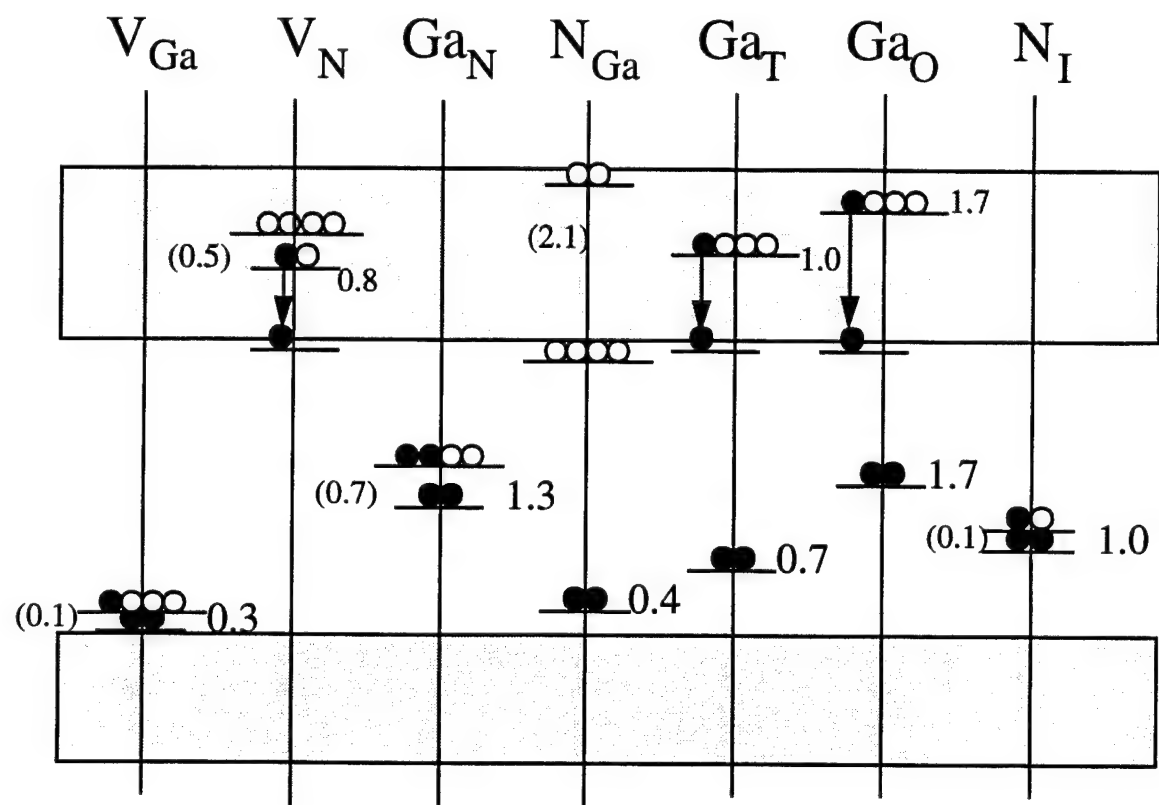


Figure 1. Energy levels of neutral native point defects in GaN.

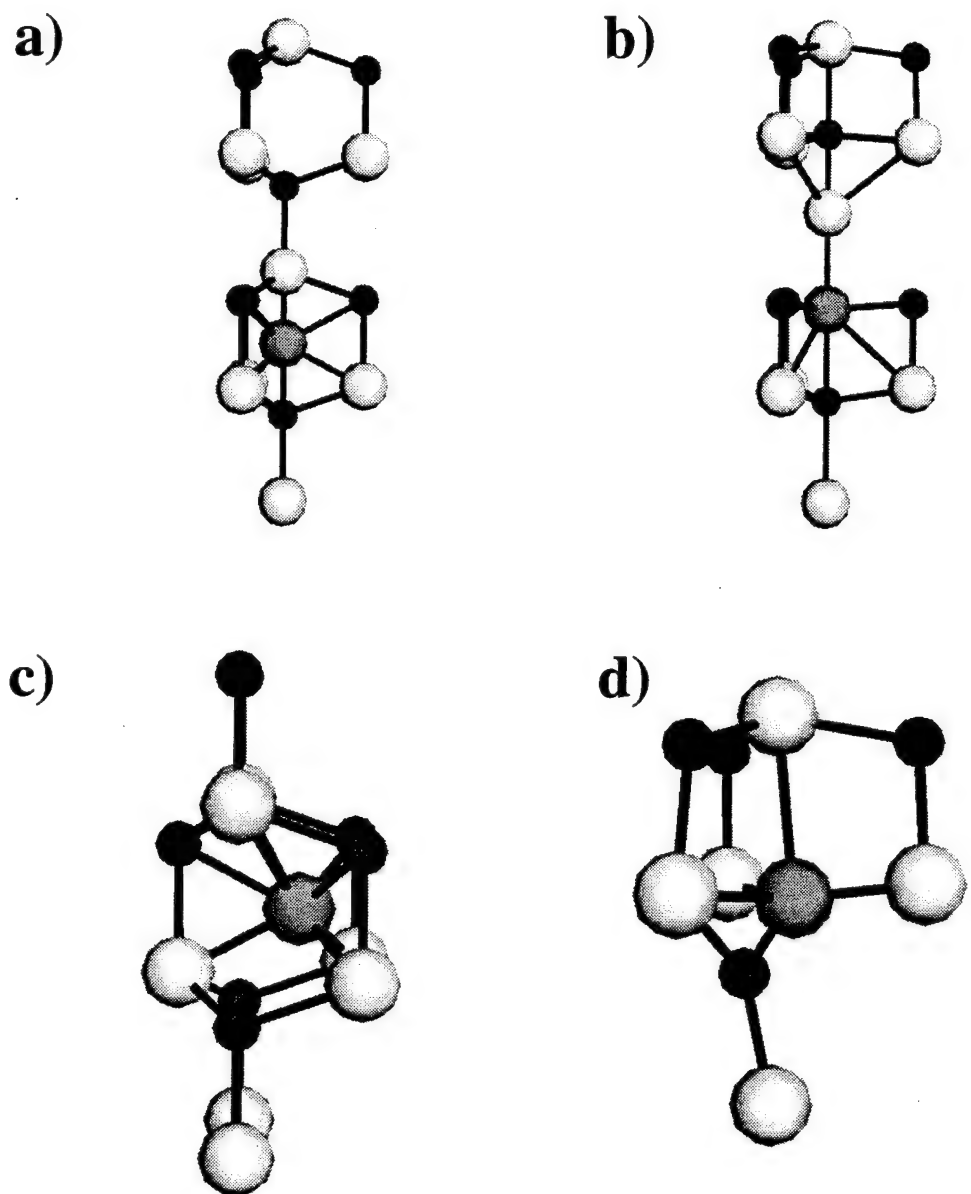


Figure 2. Atomic configurations of interstitials: (a) the ideal and (b) the relaxed Ga(*T*) interstitial, (c) the ideal Ga(*O*) interstitial, and (d) the relaxed N interstitial. Big and small spheres represent Ga and N atoms, respectively.

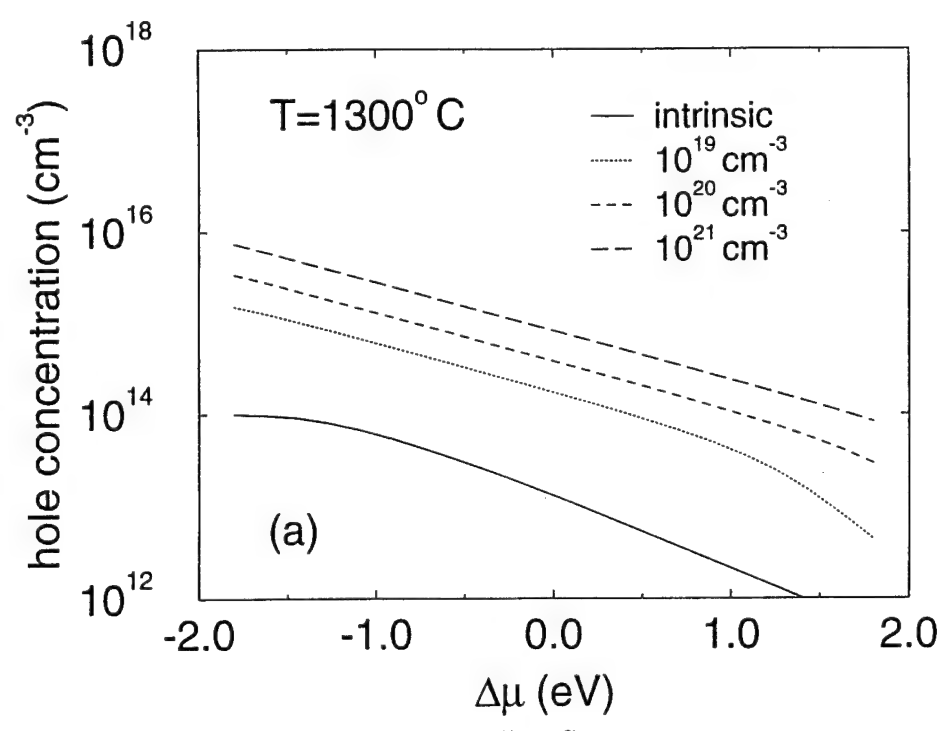
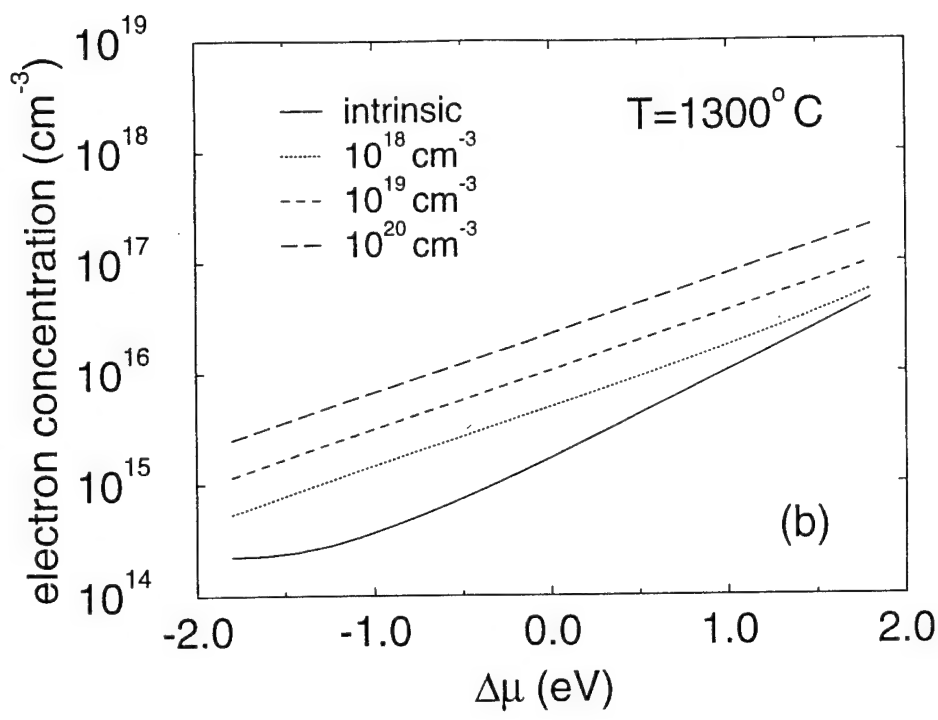


Figure 3. Calculated concentration of (a) free electrons and (b) free holes for various doping rates.

## **XXI. Towards the Identification of the Dominant Donor in GaN**

P. Perlin,<sup>1</sup> T. Suski,<sup>1</sup> H. Teisseyre,<sup>1</sup> M. Leszczynski,<sup>1</sup> I. Grzegory,<sup>1</sup> J. Jun,<sup>1</sup> S. Porowski,<sup>1</sup>

P. Boguslawski,<sup>2,3</sup> J. Bernholc,<sup>3</sup> J. C. Chervin,<sup>4</sup> A. Polian,<sup>4</sup> T. D. Moustakas<sup>5</sup>

1. *UNIPRESS, High Pressure Research Center, Polish Academy of Sciences, 01-142 Warsaw, Poland*

2. *Institute of Physics, Polish Academy of Sciences, 02-668 Warsaw, Poland*

3. *Department of Physics, North Carolina State University, Raleigh, NC 27695-8202*

4. *Physique Des Milieux Condenses, Universite Pierre et Marie Curie, 75252 Paris CEDEX 05, France*

5. *Department of Electrical, Computer and System Engineering, Boston University, Boston, MA 02215*

### **Abstract**

We analyze optical absorption, transmission, luminescence, and Raman scattering in *n*-type GaN at hydrostatic pressures up to 30 GPa. The results show a freeze-out of free carriers at the pressure of about 20 GPa. This effect is explained by trapping of electrons in a level that is a resonance at ambient pressure, but becomes a gap state at high pressures. *Ab initio* calculations indicate that the nitrogen vacancy has an appropriate electronic structure and is the best candidate to be the dominant native donor responsible for the autodoping of GaN.

71.55.Eq, 61.72.Ji, 78.30.Fs, 78.55.Cr

Gallium nitride is considered to be one of the most promising materials for the construction of short-wavelength light emitting devices, such as blue diodes and lasers [1]. In spite of impressive technological achievements of a last few years (*e.g.*, the production of the first commercially available blue diode), there are still substantial gaps in our knowledge of the basic physical properties of this material. One of them concerns the origin of *n*-type conductivity in undoped GaN crystals. Experimentally, room temperature concentrations of conduction electrons range from  $10^{17}$  to  $10^{20} \text{ cm}^{-3}$  independently of the method of growth, *i.e.*, they have been observed in both bulk crystals and in MBE- or OMCVD-grown epitaxial films. Maruska and Tietjan [2] and Ilegems and Montgomery [3] proposed that the autodoping is due to native defects, since concentrations of contaminants are lower by a few orders of magnitude than the highest concentrations of conduction electrons. Furthermore, the electron concentration is sensitive to the growth parameters (temperature and growth rate), which is easier to explain by a varying rate of creation of defects than by a varying incorporation of contaminants. The residual donor was tentatively identified with the nitrogen vacancy [2–5]. Technologically, it is very likely that  $\text{V}_N$  appears during the growth because of the very high nitrogen equilibrium pressure at the growth temperatures; this implies that the growth occurs under Ga-rich conditions. So far, however, the dominant donor was not positively identified with the nitrogen vacancy.

Recently, *ab initio* calculations of electronic structure of native defects in GaN were performed by Bogusławski *et al.* [6] and Neugebauer and Van de Walle [7]. They have shown that  $\text{V}_N$  introduces a resonant level inside the conduction bands at about 0.8 eV above the band minimum. In the neutral charge state, the one electron that should occupy this resonance autoionizes to bottom of the conduction bands and becomes bound by the Coulomb tail of the vacancy potential, forming a shallow level. Thus, at atmospheric pressure, the vacancy behaves like a shallow effective-mass donor. When the concentration of vacancies exceeds the critical Mott value, which is about  $10^{18} \text{ cm}^{-3}$  for GaN, the sample should become metallic.

In order to confirm the presence of a resonant level predicted by the theory we have

performed experiments under high hydrostatic pressures. Our method is based on the fact that the pressure coefficient of the bottom of the conduction band is usually higher than that of the resonance. Consequently, at sufficiently high pressures a crossover should occur between the two levels, and the resonance should become a genuine gap state that may trap electrons. After the crossover, free electrons would disappear from the conduction band and would occupy the deep-defect-induced state. To induce the crossover, the conduction band minimum should rise by at least 0.8 eV, assuming that the resonance does not move. Since the pressure coefficient of the gap is about 40 meV/GPa [8], one has to apply a pressure of about 20 GPa. Such high pressures necessitate the usage of diamond anvils, which practically excludes transport measurements. In this Letter we discuss the results of four optical experiments under pressure, which both probe for the existence of the resonant-deep transition and shed light on the origin of the so-called yellow luminescence at about 2.3 eV [10], which acts as a lifetime killer and suppresses the important blue luminescence. The first experiment measures the absorption due to free electrons in the infrared (IR) region of the spectrum ( $0.9\text{--}1.6 \mu\text{m}$ ). The second, complementary experiment measures the far-infrared ( $2\text{--}20 \mu\text{m}$ ) transmission. The third one investigates the variation with pressure of the yellow photoluminescence. Finally, we analyze our earlier Raman experiments on bulk samples [11].

We have used two types of GaN samples. The first samples were bulk GaN crystals grown at the nitrogen pressure of about 1.5 GPa and temperature of  $1500^\circ\text{C}$  [12]. These samples are characterized by free electron concentration of about  $5\times 10^{19} \text{ cm}^{-3}$ . The second type was a  $2.5 \mu\text{m}$  epitaxial film grown by MBE on a sapphire substrate. The Hall concentration of electrons was  $4\times 10^{17} \text{ cm}^{-3}$ . For the purpose of high pressure measurements, the substrate was thinned to about  $20 \mu\text{m}$ . The experiments were performed in diamond anvil cells (Mao-Bell-like [13] or Letoullec-Pinceaux [14] designs were used). We have employed a 4:1 methanol-ethanol mixture as a pressure-transmitting medium. A small piece of ruby was placed in the cell to monitor the pressure. Linear ruby scale ( $3.65 \text{ \AA/GPa}$ ) was used to determine the pressure from the energy of ruby luminescence.

To measure the absorption, the light beam from a 150 W halogen lamp was focused on a 100  $\mu\text{m}$  pinhole, whose image was projected on the sample. The outgoing light was dispersed by a Spex 500M spectrometer and detected by a Peltier-cooled PbS detector. This experimental setup limited the available spectral range to  $\lambda \leq 1.6 \mu\text{m}$ . Since this represents only a very small part of the free carrier absorption, we have decided to expand the examined spectral range by measuring the transmission. In this experiment we used a Perkin-Elmer 1600 Series Fourier spectrometer equipped with an IR microscope. The microscoping system allowed us to determine very accurately the ratio of the light intensity transmitted through the sample to that passing through the pressure-transmitting medium close to the sample. We measured the total IR transmission of the sample, *i.e.*, the ratio of intensities of the "white" light in the spectral range limited by the sensitivity of our IR detector (2-20  $\mu\text{m}$ ). The yellow luminescence was excited either by the 333-363 nm UV light of an argon laser or, at higher pressures, by the 325 nm line of a He-Cd laser. The Raman scattering measurements were performed with the use of a triple Dilor-XY spectrometer. The details of this experiment are given elsewhere [11].

Free-carrier absorption in the near IR region was measured in a bulk single crystal with  $n \simeq 5 \times 10^{19} \text{ cm}^{-3}$ . Figure 1 shows the absorption spectra at various pressures. For pressures lower than 15 GPa there is no substantial change in the shape of the absorption. However, between 15 GPa and 20 GPa the intensity of the absorption decreases and practically disappears above 20 GPa.

Figure 2 shows the pressure dependence of the total transmission of a thin (15  $\mu\text{m}$ ) bulk single crystal. For pressures lower than about 20 GPa, the transmission is practically constant and close to 15%. The transmission increases rapidly starting at 20 GPa. At the highest pressures the transmission exceeds 100%, which simply means that the absorption of the pressure-transmitting medium is higher than that of the sample.

The pressure dependence of the "yellow" luminescence is shown in Fig. 3. In this experiment we have used both an epitaxial film and a bulk sample. The mechanism of this luminescence will be discussed below. From Fig. 3 it follows that the energy of

the luminescence band changes linearly with pressure up to about 18 GPa. (Thus, at the highest pressures, the "yellow" luminescence becomes blue). Its pressure coefficient, about 30 meV/GPa, is very close to the pressure coefficient of the band gap [8]. At about 20 GPa, the slope changes and the peak position does not change with pressure.

Figure 4 compares the Raman spectra of GaN at low (2 GPa) and very high (32.2 GPa) pressures [11] for a sample with electron concentration exceeding  $10^{19} \text{ cm}^{-3}$ . It shows that new phonon peaks appear in the high pressure spectrum. Here we are interested in the peak labeled  $L_5$  with wavenumber of about  $850 \text{ cm}^{-1}$  at 32.2 GPa. By extrapolating its position to the ambient pressure we obtain an energy of  $740 \text{ cm}^{-1}$ , see inset. Since this energy is very close to the  $738\text{-}741 \text{ cm}^{-1}$  energy of the LO phonon in GaN recently measured in epitaxial samples [15], we assign the  $L_5$  peak to the LO phonon. The presence of this peak was detected only for pressures higher than 22 GPa, as shown in the inset of Fig. 4.

The experimental results can be consistently explained by the presence of a resonant state in the conduction band. Hydrostatic pressure induces a crossover of the resonance with the bottom of the conduction band at about 20 GPa. After the crossover, conduction electrons become trapped in the resonance-derived gap level. Consequently, since practically all electrons disappear from the conduction band, the concentration of defects giving rise to the resonance must be equal or higher than the concentration of dominant native donors. We propose here that it is the native donor that induces the resonance and we identify it with the nitrogen vacancy.

We will now discuss each case in more detail. Both absorption and transmission measurements show that at pressures higher than about 20 GPa the IR absorption in the  $0.9\text{-}1.5 \mu\text{m}$  range abruptly decreases. There are two main mechanisms of absorption in the IR region, phonon absorption and free carrier absorption. The former mechanism is important only in the far IR region (*i.e.*, for  $\lambda \geq 0.18 \mu\text{m}$ ), and should not change substantially with pressure. In contrast, free carrier absorption can change considerably when the concentration of free electrons changes. Therefore, we interpret the quenching of the IR absorption as due to a freeze-out of electrons from the conduction band. More precisely, we estimate from our data

that the electron concentration decreases by at least two orders of magnitude.

This picture explains also the Raman experiment. Our interpretation is based on the work of Mooradian and Wright [16], who observed and discussed the plasmon-phonon coupling in GaAs. They show that the plasmon-phonon coupling shifts the LO mode to higher energies and reduces its oscillator strength. This occurs at low pressures, when the concentration of free carriers is higher than  $10^{18} \text{ cm}^{-3}$  [17]. The pressure-induced freezout of electrons leads to a reappearance of the LO mode.

We now turn to the luminescence data. Two mechanisms of the "yellow" luminescence have been proposed in the literature. In the first one, the luminescence is due to a transition from the conduction band or a shallow donor state to a deep localized state [10]. The second mechanism [18] assumes a transition from a deep gap state to a shallow acceptor. The agreement of the pressure coefficient of the yellow luminescence reported here with that of the band gap supports the former mechanism. Note that this interpretation implies that the pressure coefficient of the deep final state is very small, which is indeed plausible for deep states. For example, this is the case for the zinc-related luminescence in GaN [19]. In contrast, it is difficult to explain the observed pressure dependence of the this luminescence in the framework of the second mechanism.

Accordingly, at low pressures the pressure coefficient of the luminescence is equal to the pressure coefficient of the band gap. After the emergence of the resonance from the conduction band into the gap, the luminescence is due to a transition from the resonance-derived deep state to the same final gap state. This explains the change of slope occurring at about 20 GPa.

To confirm the proposed interpretation we have calculated the electronic structure of the nitrogen vacancy under hydrostatic pressure. The calculations were performed by quantum molecular dynamics, in large unit cells corresponding to 72 atoms in the perfect crystal. We used norm-conserving pseudopotentials, plane-wave basis, and  $\Gamma$ -point sampling of the Brillouin zone. The calculated pressure coefficient of the band gap is 43 meV/GPa, in good agreement with the experimental value [8]. Our results show that the vacancy-induced

resonance, located at 0.8 eV above the bottom of the conduction band at zero pressure, moves down with pressure at a rate of 5 meV/GPa. The resonance crosses the bottom of the conduction band at a pressure of about 18 GPa.

We have considered two other explanations of our data. First, we have found that the interstitial Ga also introduces a resonance which crosses the bottom of the conduction band at about 20 GPa. However, the calculated concentrations of Ga(I) in undoped samples are lower than those of  $V_N$  by a few orders of magnitude [6]. A second possibility is a pressure-induced crossover of the conduction band minimum at  $\Gamma$  with one of the secondary minima at the edge of the Brillouin zone. According to our results, this crossover occurs at about 60 GPa, which is too high.

In summary, our high pressure optical experiments show that a freeze-out of electrons from the conduction band occurs at about 20 GPa. We propose that this effect is due to an emergence of a conduction band resonance into the forbidden gap. The resonance-derived deep state captures free electrons, leading to the freeze-out of free carriers. *Ab initio* calculations show that the nitrogen vacancy is a shallow donor at ambient pressures, and introduces a resonance that crosses the bottom of the conduction band at  $\sim 20$  GPa. The good agreement between experiment and theory strongly supports both the proposed interpretation and the hypothesis that the nitrogen vacancy is the residual donor responsible for the observed *n*-type character of bulk GaN samples.

This work was supported in part by grants KBN 2-P302-064-07 and 2-P302-124-07, NSF DMR-9408437, and ONR N00014-92-J-1477.

## REFERENCES

- [1] R. F. Davis, Physica B **185**, 1 (1993); S. Strite and H. Morkoc, J. Vac. Sci. Technol. B **10**, 1237 (1992).
- [2] H. P. Maruska and J. J. Tietjen, Appl. Phys. Lett. **15**, 327 (1969).
- [3] M. Illegems and M. C. Montgomery, J. Phys. Chem. Solids **34**, 885 (1973).
- [4] B. Monemar and O. Lagerstedt, J. Appl. Phys. **50**, 6480 (1979).
- [5] T. L. Tansley and R. J. Egan, Phys. Rev. B **45**, 10942 (1992), and the references therein.
- [6] P. Bogusławski, E. Briggs, T.A. White, M.G. Wensell, and J. Bernholc, Mat. Res. Soc. Symp. Proc. **339**, 693 (1994); P. Bogusławski, E. Briggs, and J. Bernholc, to be published.
- [7] J. Neugebauer and C. G. Van de Walle, Phys. Rev. B **50**, 8067 (1994).
- [8] The linear pressure coefficient of the band gap, 47 meV/GPa, has been determined in Ref. [9] by fitting the gap with a quadratic function of pressure. A linear fit to the same data gives a value of 36 meV/GPa.
- [9] P. Perlin, I. Gorczyca, N.E. Christensen, I. Grzegory, H. Teisseire, and T. Suski, Phys. Rev. B **45**, 13307 (1992).
- [10] T. Ogino and M. Aoki, Jpn. J. Appl. Phys. **19**, 2395 (1980).
- [11] P. Perlin, C. Jauberthie-Carillon, J.P. Itie, A. San Miguel, and I. Grzegory, A. Polian, Phys. Rev. B **45**, 83 (1992).
- [12] I. Grzegory and S. Krukowski, Physica Scripta **T39**, 242 (1991).
- [13] H.K. Mao and P.M. Bell, Carnegie Inst. Washington Yearbook **77**, 904 (1978).
- [14] R. Letoullec, J.P. Pinceaux and P. Loubeyre, High Pressure Research **1**, 77 (1988).

- [15] H. Sobotta, H. Neuman, R. Franzheld, and W. Seifert, Phys. Stat. Solidi (b) **174**, K57 (1992).
- [16] A.A. Mooradian and G.B. Wright, Phys. Rev. Lett. **16**, 999 (1967).
- [17] T. Kozawa *et al.*, J. Appl. Phys. **75**, 1098 (1994).
- [18] E. R. Glaser *el al.*, Appl. Phys. Lett. **63**, 2673 (1993); and to appear in Phys. Rev. B.
- [19] H. Teisseyre, P. Perlin, T. Suski, I. Grzegory, J. Jun, and S. Porowski, J. Phys. Chem. Solids, in press.

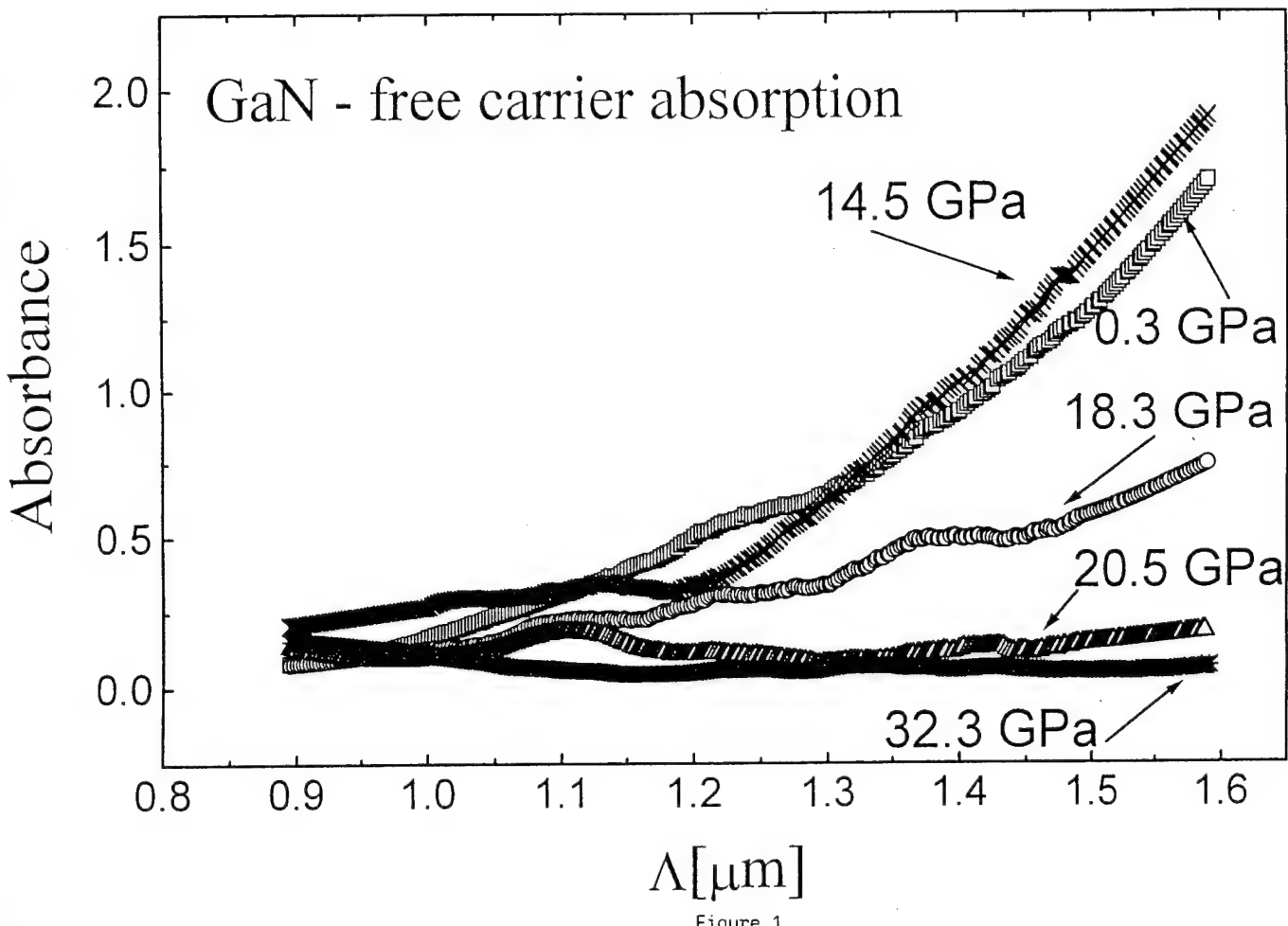


Figure 1. Free carrier absorption spectra of single crystal bulk GaN at  $T=300$  K for various pressures.

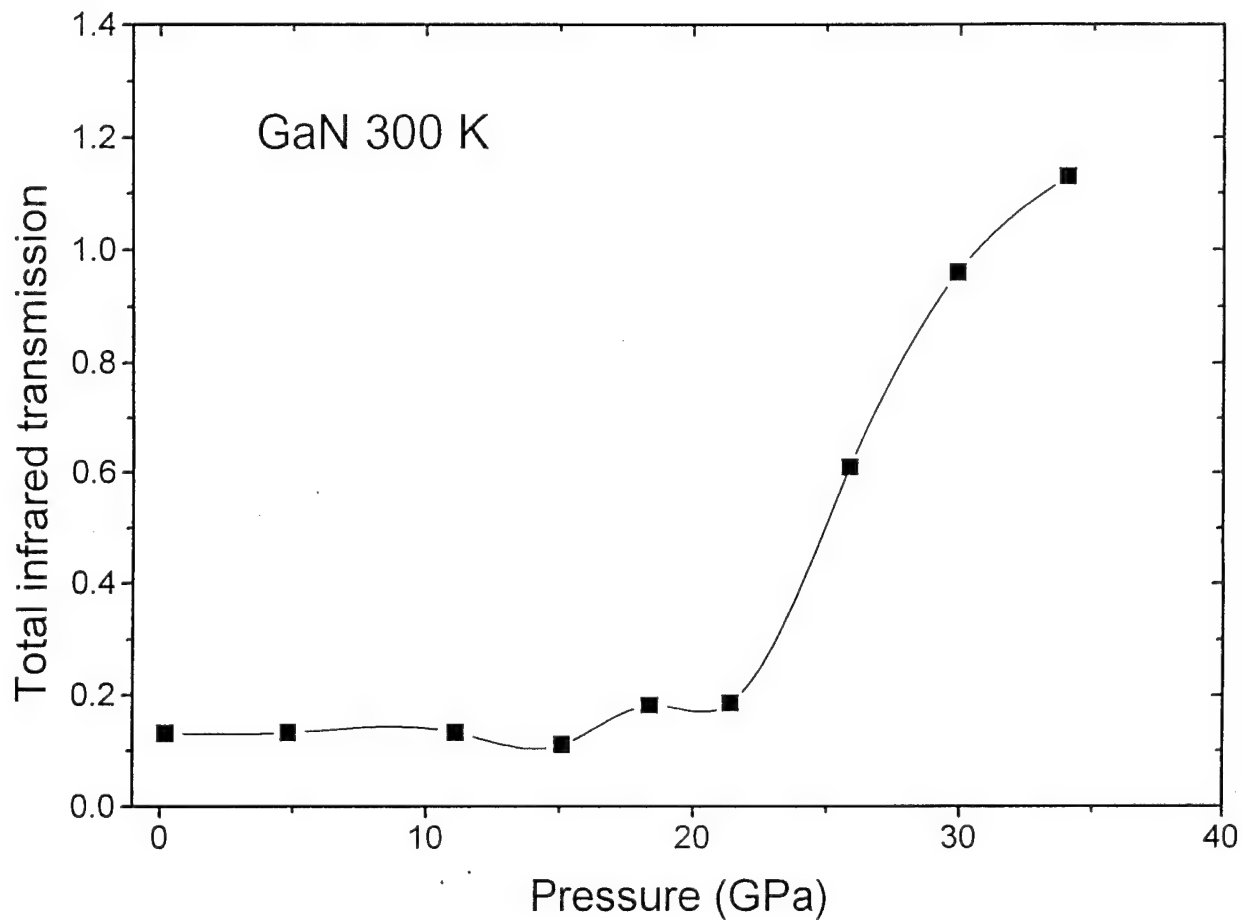


Figure 2. Pressure dependence of the total infrared transmission of a bulk GaN single crystal at T=300 K.

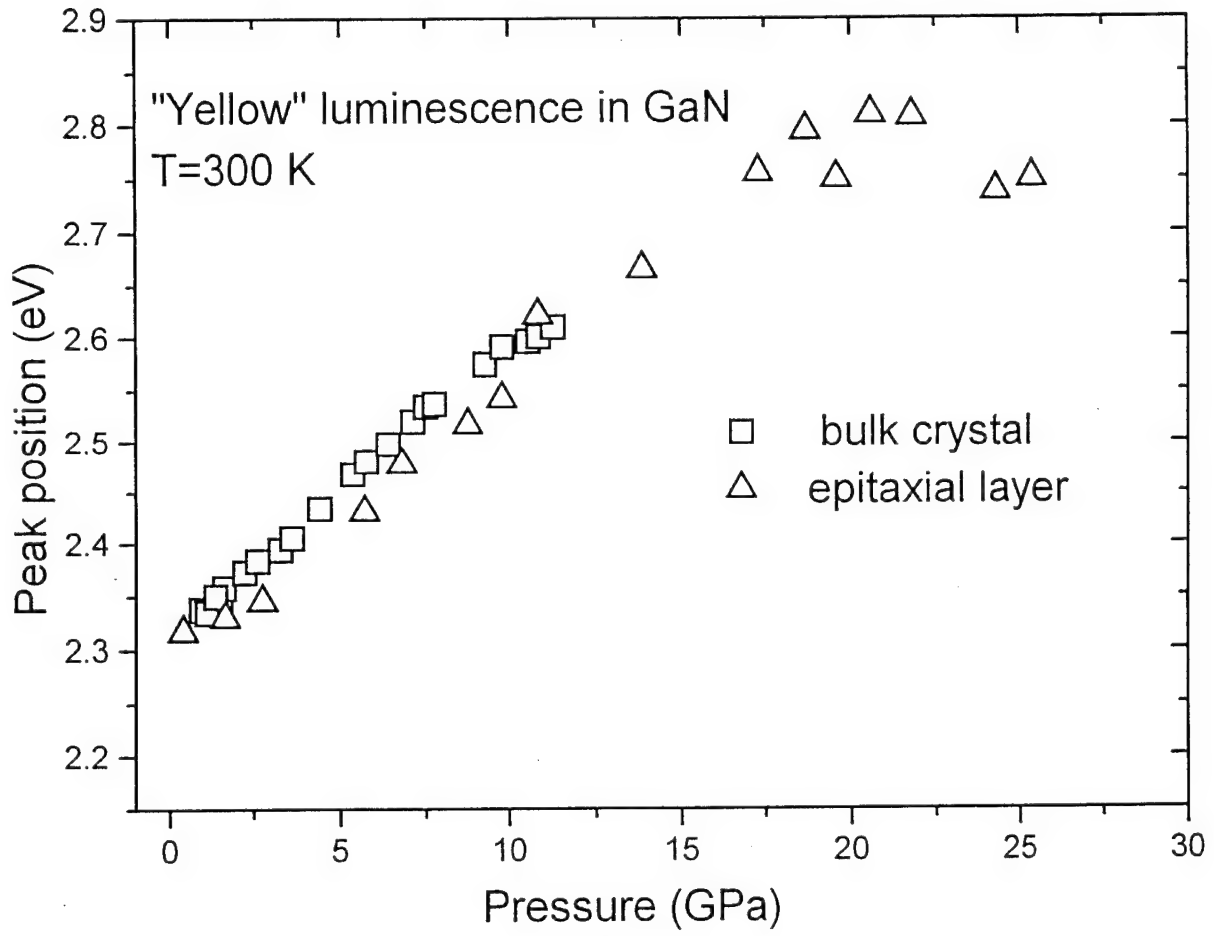


Figure 3

Figure 3. Pressure dependence of the energy of the “yellow” luminescence for a bulk sample and an epitaxial film of GaN.

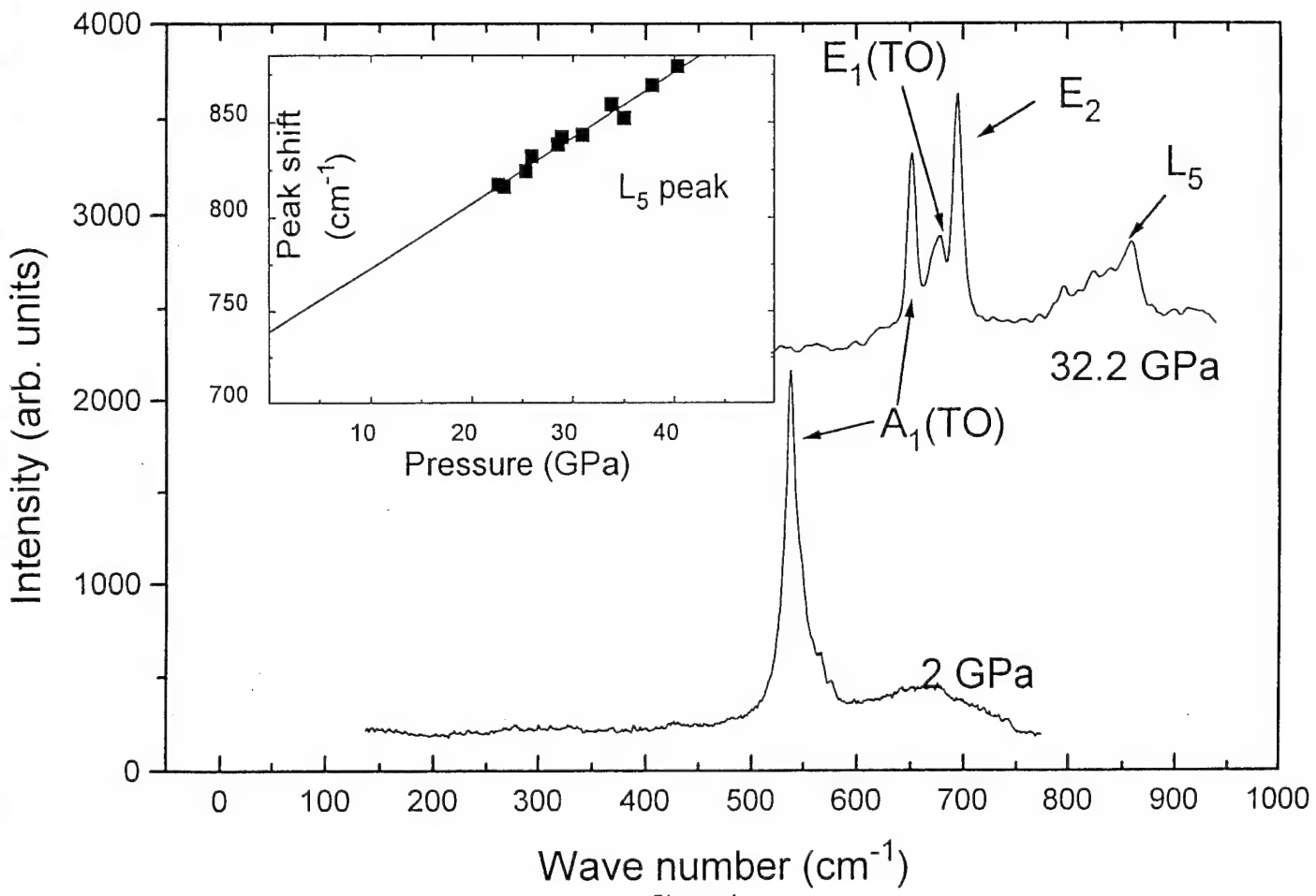


Figure 4

Figure 4. Raman spectra of a bulk single crystal at low (2 GPa) and high (32.2 GPa) pressures. The peaks labeled  $A_1(\text{TO})$ ,  $E_1(\text{TO})$ , and  $E_2$  reflect the phonon modes of GaN. Their appearance results from depolarization of the laser light due to strain in the diamond anvils [11]. The peak  $L_5$  appears above about 20 GPa. Insert: pressure dependence of the  $L_5$  peak energy. The solid line represents a linear extrapolation of the peak energy to ambient pressure.

## XXII. Luminescence Studies of GaN, AlN, InN and Their Solid Solutions

### A. Introduction

Luminescence is the emission of photons due to excited electrons in the conduction band decaying to their original energy levels in the valance band. The wavelength of the emitted light is directly related to the energy of the transition, by  $E=h\nu$ . Thus, the energy levels of a semiconductor, including radiative transitions between the conduction band, valance band, and exciton, donor, and acceptor levels, can be measured.[1,2] Various methods exist to excite the electrons, including photoluminescence (photon excitation), and cathodoluminescence (electron-beam excitation). In each technique, signal intensity is measured at specific wavelength intervals using a monochromator and a detector. The intensity versus wavelength (or energy) plot can then be used to identify the characteristic energy band gap and exciton levels (intrinsic luminescence) of the semiconductor, and the defect energy levels (extrinsic luminescence) within the gap .[1]

Both photo- and cathodoluminescence analysis has been performed on AlN, GaN, InN and their solid solutions.[3-20] Much of the work has been in the measurement the low temperature luminescence of GaN. High quality, unintentionally doped GaN exhibits a strong donor-bound exciton peak at 357.3 nm (3.47 eV).[16] Defect peaks due to donor-acceptor (DA) transitions and accompanying phonon replicas are also prevalent, with peak wavelengths at 380.3, 391.2 and 402.9 nm. The identity of the acceptor is not clear. A deep emission at 540 nm (2.2 eV) is also common in GaN. Currently the source of this emission is not known, although various models exist to explain it.[19,20] It is of utmost importance to limit the defect transitions, as it can reduce the transition probability of the near-gap emission.

Although undoped GaN is always n-type, recent advances in film growth have lowered the carrier concentration to  $10^{16}/\text{cm}^3$ . For device applications it is important to have a high carrier concentration at a controlled level. Common dopants for n-type doping of GaN include Si and Ge. Nakamura, *et al.* found that for Si-doped GaN, two peaks dominate the spectrum.[12] The first is a UV emission peak at 380 nm. The second peak is the deep level (DL) emission previously discussed; this transition is enhanced by Si-doping. Conflicting results were shown by Murakami, *et al.*, who saw a band edge peak at 358 nm dominate their spectrum.[8] The DL emission at 540 nm in their samples was very weak.

The development of light emitting diodes (LEDs) and laser diodes using GaN-based materials has been limited by the difficulty in obtaining quality p-type films.[12] Common dopants include Zn, Cd, and Mg.[3] Recent work has proven successful, with low resistivity Mg-doped GaN obtained by thermal annealing or low energy electron beam irradiation

(LEEBI) as a post-growth process step. The luminescence from these films typically show a broad peak located at 450 nm, with no emission near the band-edge.

Work on AlN and  $\text{Al}_x\text{Ga}_{1-x}\text{N}$  has been limited by the energy gap of 6.2 eV for AlN. This corresponds to a wavelength (200 nm) that is lower than most of the optical light sources. An excimer laser using the ArF line (193 nm) could possibly be used, although very little work on this has been done to date.[30] Cathodoluminescence of AlN and  $\text{Al}_x\text{Ga}_{1-x}\text{N}$  is possible, however, and most of the results have been obtained via this method.[16-18,30-33]  $\text{Al}_x\text{Ga}_{1-x}\text{N}$  with low amounts of Al can also be investigated using frequency doubled and tripled lasers that have lines down to 244 nm.

## B. Experimental Procedures

A combined photo- and cathodoluminescence system is used to measure the luminescence from the III-V nitrides. A schematic view is shown in Fig. 1, and a block diagram is shown in Fig. 2. Each sample is attached to a cryostat that allows for a test temperature range of 6 to 300 K. A McPherson model 219 vacuum monochromator with a focusing mirror chamber is used to collect the emitted light. The focal length of the monochromator is .5 m, with a wavelength resolution of .04 nm at 313.1 nm for a 1200 G/mm grating. A photon counting detection scheme is used to measure the light intensity, with a Photomultiplier tube (PMT) used that has a wavelength range of 180-650 nm.

A Liconix He-Cd laser is the photoexcitation source. It is a continuous wavelength laser that operates at a wavelength of 325 nm (3.8 eV), with a power of 15 mW. It is used for PL of GaN and  $\text{In}_x\text{Ga}_{1-x}\text{N}$ , but a lower wavelength source is needed to test the full range of  $\text{Al}_x\text{Ga}_{1-x}\text{N}$  solid solutions.

A Kimball Physics electron gun is used for cathodoluminescence measurements. It has maximum beam voltage of 10 keV and a maximum beam current of 450 uA. By varying the beam voltage it is possible to perform depth-resolved spectroscopy. The beam blanking capability of the electron gun will allow for time-delay studies of the semiconductors.

## C. Results and Discussion

*Undoped GaN.* Photoluminescence measurements were performed on GaN films grown via OMVPE on vicinal  $\alpha$ (6H)-SiC(0001)Si wafers. The buffer layer for each sample was AlN. All of the tests were performed at 8 K, unless otherwise noted.

The photoluminescence of undoped GaN grown at 950 °C is shown in Fig. 3. The sample thickness was 1  $\mu\text{m}$ . The peak at 357.36 nm was attributed to the recombination of excitons at neutral donors.[27] The FWHM of this peak, 4 meV, indicates the high quality of the sample. A weak defect peak ascribed to donor-acceptor (DA) pair recombination was observed at 379 nm (3.26 eV) with two associated LO-phonon replicas only after a 250X magnification of

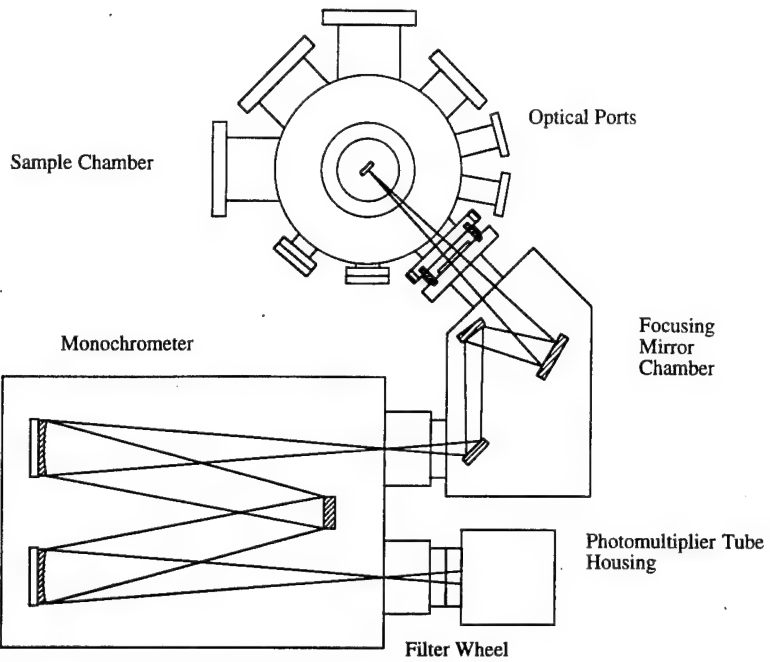


Figure 1. Schematic view of combined photo- and cathodoluminescence system.

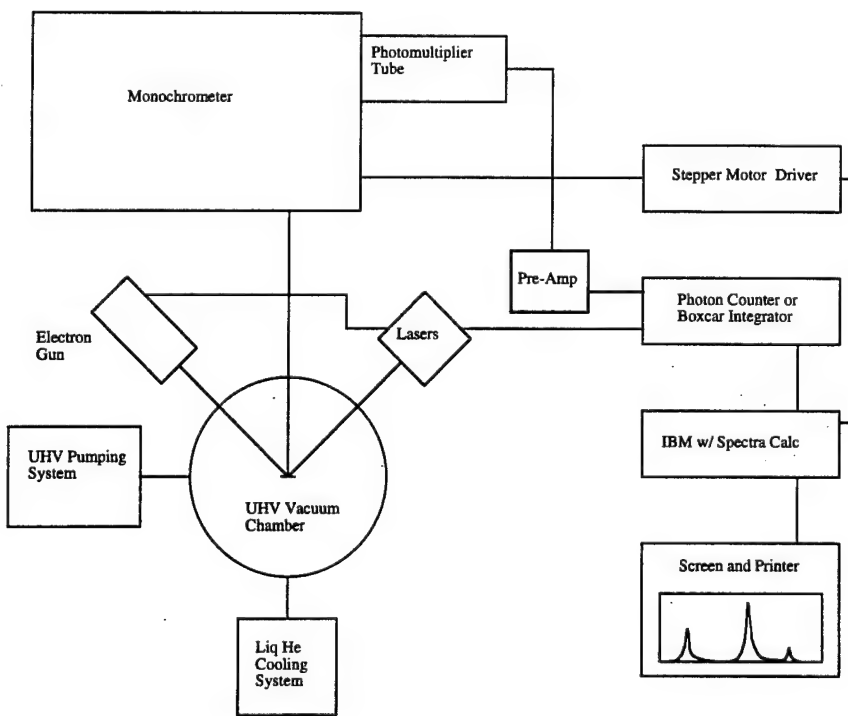


Figure 2. Block diagram of combined photo- and cathodoluminescence system.

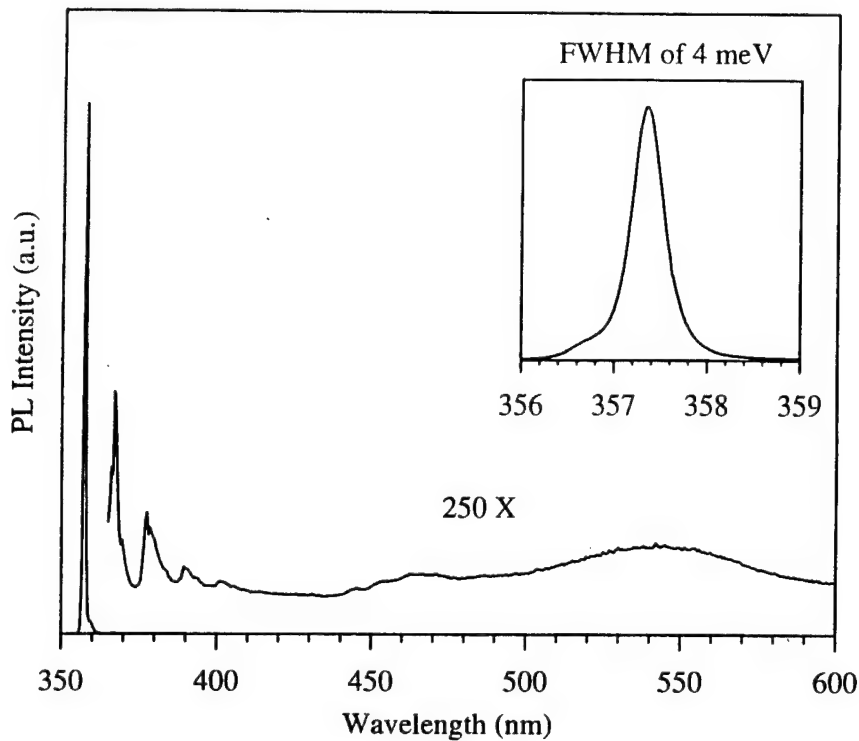


Figure 3. PL of GaN on SiC(0001) at 8 K.

the spectrum.[25] The origin of the D-A pair is attributed to residual donors and acceptors. Two LO-phonon replicas of the bound-exciton peak and a broad peak centered at 545 nm ( $\approx 2.2$  eV), commonly associated with deep-levels (DL) in the bandgap, were also observed at this magnification.[26]

Photoluminescence of GaN at various film thicknesses revealed a shift in the donor-bound exciton peak to lower energy as film thickness increased. The results are shown in Fig. 4, and the thickness and peak position for each film is given in Table I. The shift may be attributed to a change in the bandgap due to tensile strain in the film.[29] This is ascribed to the thermal expansion mismatch between GaN and the SiC substrate, which upon cooling of the film after growth results in the films being under tension. From this data it appears that as thickness increases the tension in the film also increases. Further studies will be done in the future to verify this.

*Mg-doped GaN.* The doping of GaN with magnesium to obtain p-type electrical behavior proved to be successful. The PL of Mg-doped GaN at 8 K as a function of annealing conditions is shown in Fig. 5. The growth temperature was 1050 °C, and the  $Cp_2Mg$  flow rate was .5  $\mu$ moles/min. The sample as-grown was p-type, but electrical measurement could not be made because the structural quality of the material was poor (possibly due to the high concentration of Mg).

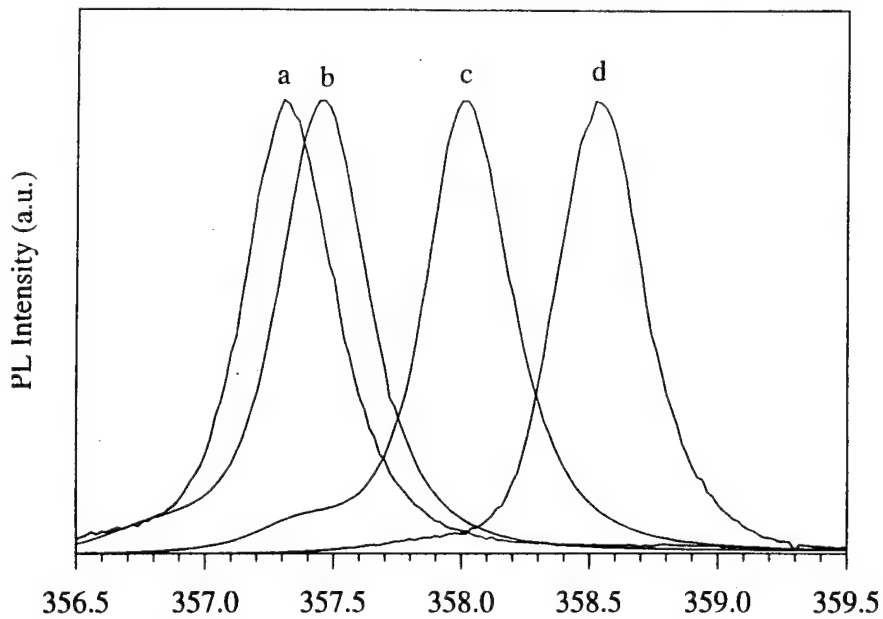


Figure 4. PL of GaN on SiC(0001) at 8 K for various thicknesses.

Table I

Sample	Film Thickness ( $\mu\text{m}$ )	Peak Location (nm)
a	.7	357.30
b	.9	357.46
c	1.4	358.00
d	2.7	358.52

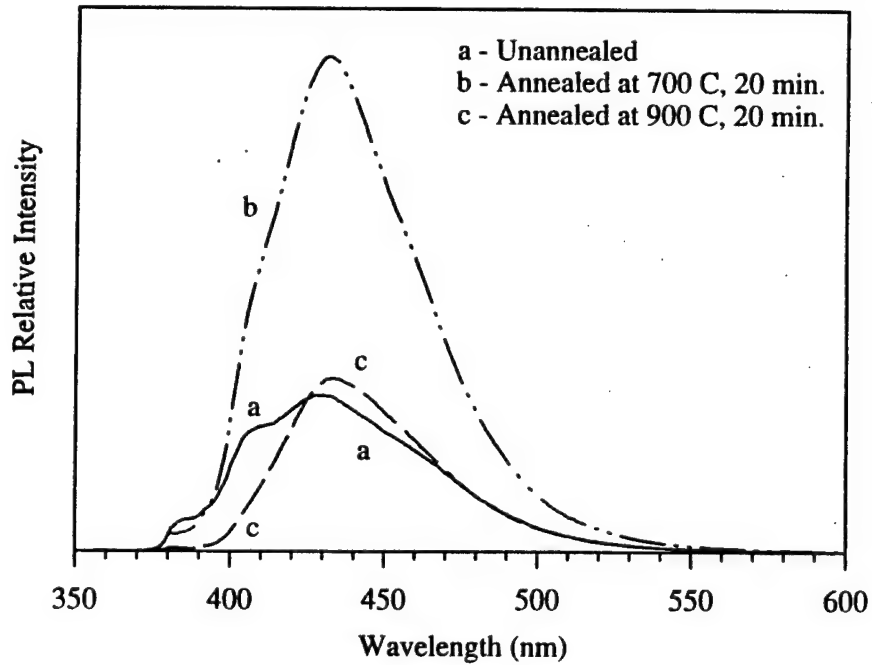


Figure 5. PL at 8 K of p-type Mg-doped GaN.

Annealing at 700 °C for 20 minutes enhanced the luminescence intensity by 250 %. Post-growth annealing is thought to release Mg from Mg-H complexes, which passivate the acceptors [22]. Recent work has shown that Mg-H complexes form at 500-600 °C for MBE-grown samples annealed in H<sub>2</sub> [24].

Annealing at 900 °C for 20 minutes resulted in a sharp decrease in the PL intensity compared to the sample annealed at 700 °C. This result is in line with previous work, which showed that PL intensity decreased gradually as the annealing was increased past 500 °C, while the resistivity of the sample did not change [22]. Thus the decrease in PL intensity is not due to a change in the number of active acceptor levels through compensation or other mechanisms.

One possibility is the thermal expansion mismatch between the GaN and the SiC substrate. As the annealing temperature is increased the temperature range over which the sample is later cooled is also increased. This leads to an increase in the stresses generated by the mismatch in thermal expansion. The resulting elastic strain is thought to lower the overall PL efficiency of the sample by increasing the rate of non-radiative transitions.

The effect of growth temperature for Mg-doped GaN was also investigated. The Cp<sub>2</sub>Mg flow was .2 μmoles/min at each temperature, which was lower than the sample discussed previously. Previous work has shown that Mg concentration in GaN at a given flow rate is almost independent of substrate temperature for a range of 850-1100 °C [23].

The PL spectrum of the sample grown at 975 °C is shown in Fig. 6. The unannealed sample exhibited relatively weak donor-acceptor (D-A) pair emission, along with its LO-phonon replicas, and a broad peak at 481 nm. The origin of the D-A pair was attributed to residual donors and the doped Mg-acceptors. The origin of the 481 nm peak was unknown, but it has been seen in other samples that were grown at lower temperatures. After annealing at 900 °C for 20 minutes the PL emission was very weak. This indicates that a sample growth temperature of 975 °C is too low.

The PL spectrum of the sample grown at 1050 °C is shown in Fig. 7. For the unannealed sample the D-A peak and its LO-phonon replicas were the dominate feature in the spectrum, and the peak intensity was 320 times stronger than the sample grown at 975°C. There was no evidence of the peak at 481 nm, although it could have been overwhelmed by the intensity of the D-A peaks.

Annealing of the sample at 900 °C for 20 minutes results in a shift of the PL spectrum to lower energy, with the peak emission at 406 nm. The peak intensity of this sample is .6 % of the unannealed sample. Annealing of the sample for an additional 20 minutes further decreased the PL intensity.

The PL spectrum for the sample grown at 1100 °C before annealing is shown in Fig. 8. The peak emission is at 429 nm. This sample was p-type as-grown, with a room-temperature hole concentration of  $2 \times 10^{16}/\text{cm}^3$ .

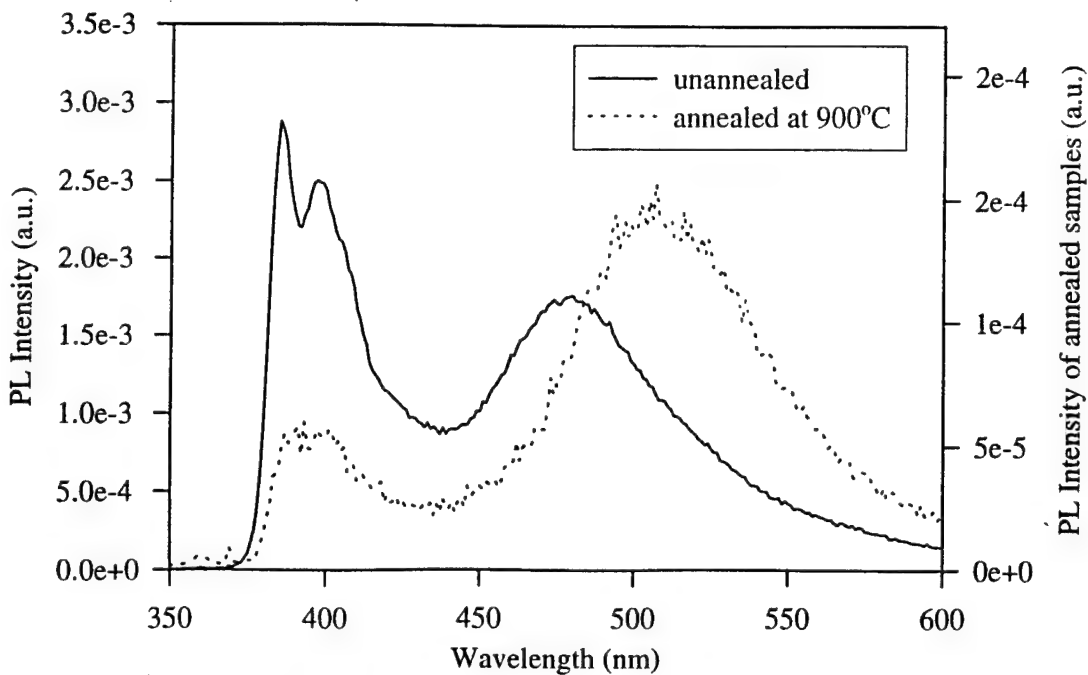


Figure 6. PL at 8 K of p-type Mg-doped GaN grown at 950°C.

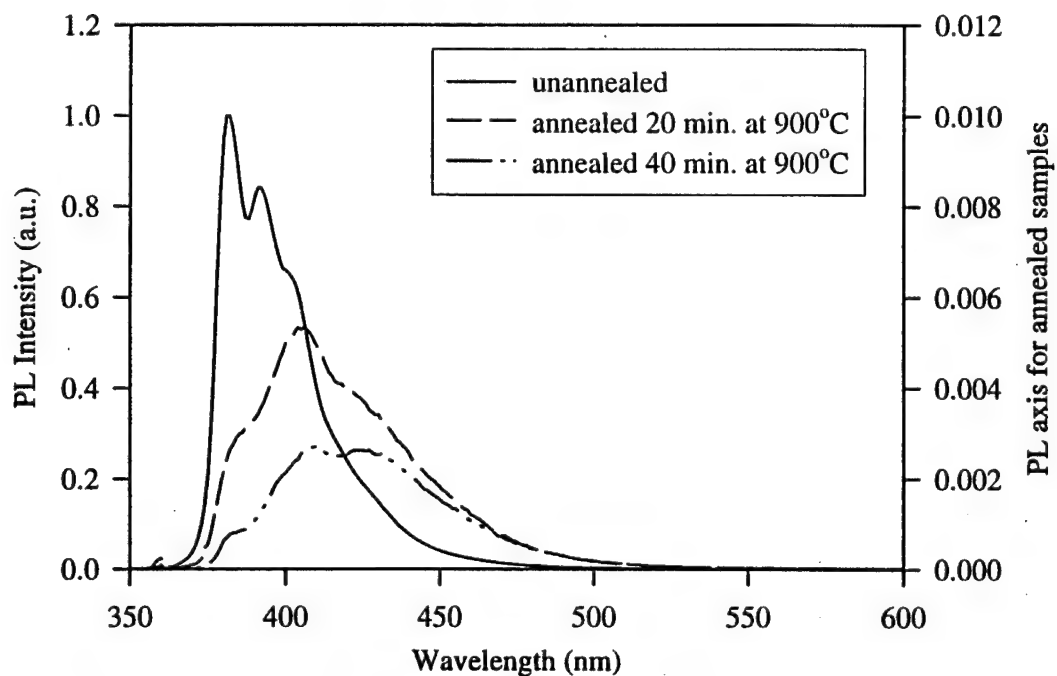


Figure 7. PL at 8 K of p-type Mg-doped GaN grown at 1050°C.

The PL spectrum at room temperature of the Mg-doped GaN as-grown and annealed at 600 and 700 °C is shown in Figure 9. The peak emission was at 460 nm for the as-grown sample and at 456 nm for the two annealed samples. The PL intensity was highest for the sample annealed at 600 °C and decreased at 700 °C, confirming that the PL intensity decreases for

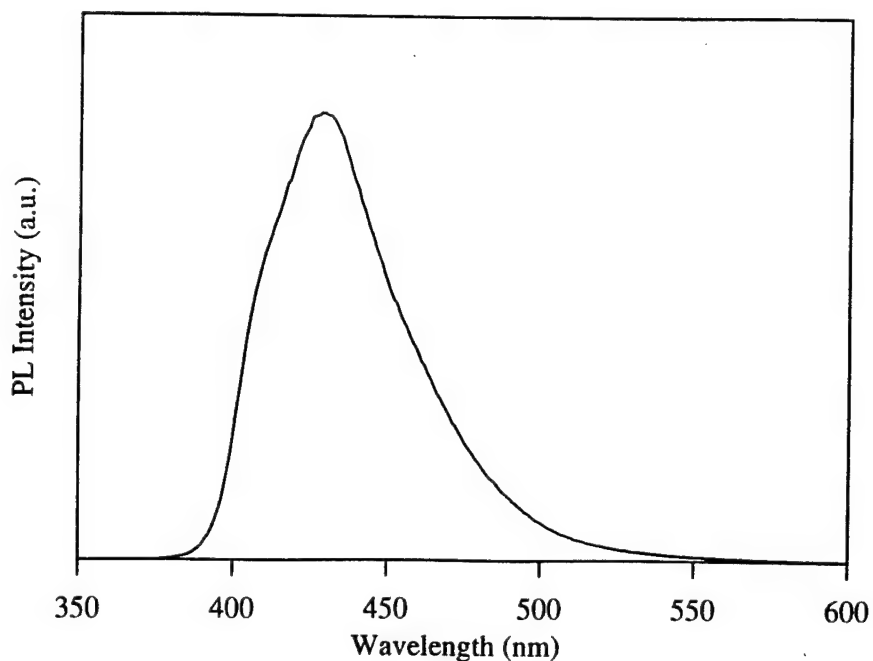


Figure 8. PL at 8 K of p-type Mg-doped GaN unannealed, grown at 1100°C.

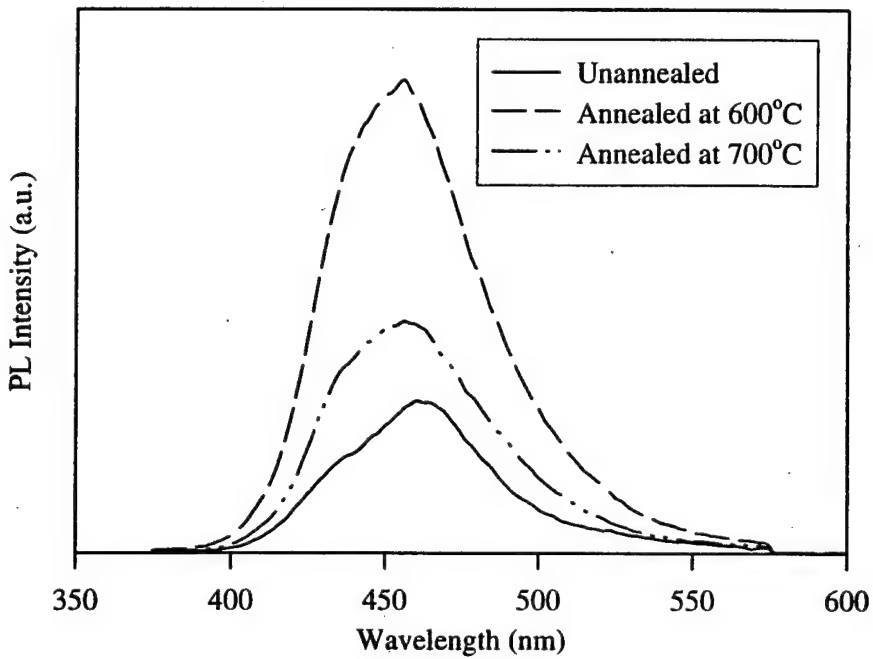


Figure 9. PL at room temperature of p-type Mg-doped GaN grown at 1100°C.

higher annealing temperatures. The room temperature hole concentration was  $1 \times 10^{18}/\text{cm}^3$  for the sample annealed at 600 °C. This value did not change for higher annealing temperatures, as seen in previous work.

*CL of Al<sub>x</sub>Ga<sub>1-x</sub>N.* Cathodoluminescence was performed on Al<sub>x</sub>Ga<sub>1-x</sub>N samples grown directly on vicinal  $\alpha$ (6H)-SiC(0001)Si wafers. Each test was performed at 8K with a beam voltage of 7 keV and a beam current of 200  $\mu$ A. Four samples were tested, and the results are shown in Fig. 10. The band-edge peak location, the peak FWHM, and the thickness of each sample is presented in Table II. The composition of each sample is not known, but it will be measured using SIMS in the future.

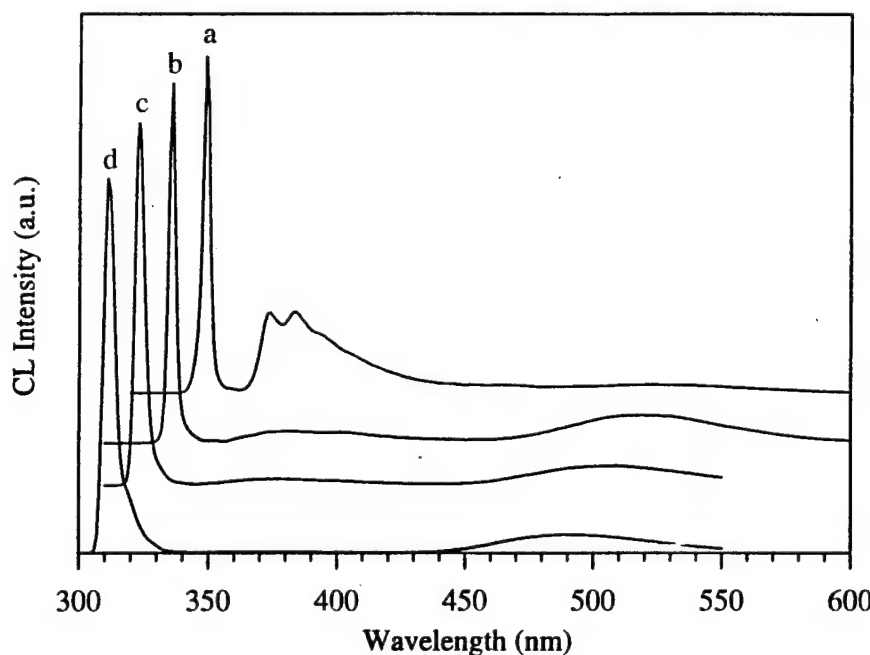


Figure 10. CL of Al<sub>x</sub>Ga<sub>1-x</sub>N at 8 K.

Table II

Sample	Peak Location (nm)	FWHM (meV)
a	349.3	31
b	334.6	46
c	324.5	59
d	311.4	64

As expected, the FWHM of the band-edge peak increases as x increases due to alloy broadening.[28] Given this, along with the absence of a buffer layer, the CL for these samples is still quite strong. Samples grown on on-axis SiC exhibited weaker band-edge CL emission.

Figure 11 shows the spectrum below the band-edge enhanced. Sample *a* exhibits relatively strong emission at 374 nm with two phonon replicas that are attributed to D-A pair emission.

As  $x$  increases the peaks attributed to D-A pair emission move to higher energies, but they are not as easily resolved. This could also be attributed to alloy broadening.

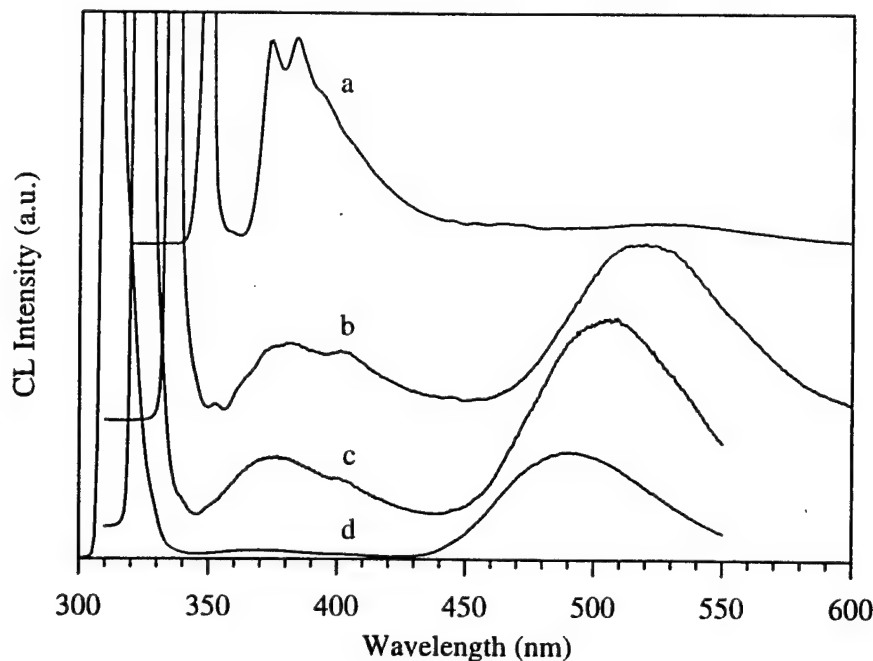


Figure 11. CL of  $\text{Al}_x\text{Ga}_{1-x}\text{N}$  at 8 K.

As  $x$  increases the DL emission centered at 540 nm for GaN also moves to higher energy. Previous work has studied the PL of GaN as a function of pressure to model the  $\text{Al}_x\text{Ga}_{1-x}\text{N}$  system.[34] Results showed that for pressures up to 20 GPa the pressure coefficient of the DL luminescence is equal to the pressure coefficient of the band gap. Using the pressure coefficient of 30 meV/GPa for the band gap they found that the change in the energy of the DL emission is equal to the change in the energy of the band-gap up to .6 eV. After 20 GPa they propose that a resonant state in the conduction band crosses over into the gap, and then the DL luminescence should be due a transition from the resonance-derived deep state to the same deep acceptor state. This resonant state is due to the nitrogen vacancy, which they suggest is the native donor in GaN.

This model for  $\text{Al}_x\text{Ga}_{1-x}\text{N}$  was tested using the CL data for samples *a-d*, along with other alloy samples grown on both vicinal and on-axis  $\alpha(6\text{H})\text{-SiC}(0001)\text{Si}$  wafers. PL of AlGaN tested at OSU are also included (discussed in next section). The results are shown in Fig. 12. The change in energy of the DL emission ( $E_{\text{DL}}$ ) follows the change in energy of the band-edge emission ( $E_{\text{BE}}$ ) initially, but after .2 eV it begins to lag behind. Thus it does appear that the luminescence of AlGaN follows the behavior seen in the pressure experiments of GaN, although further testing will be done to confirm this.

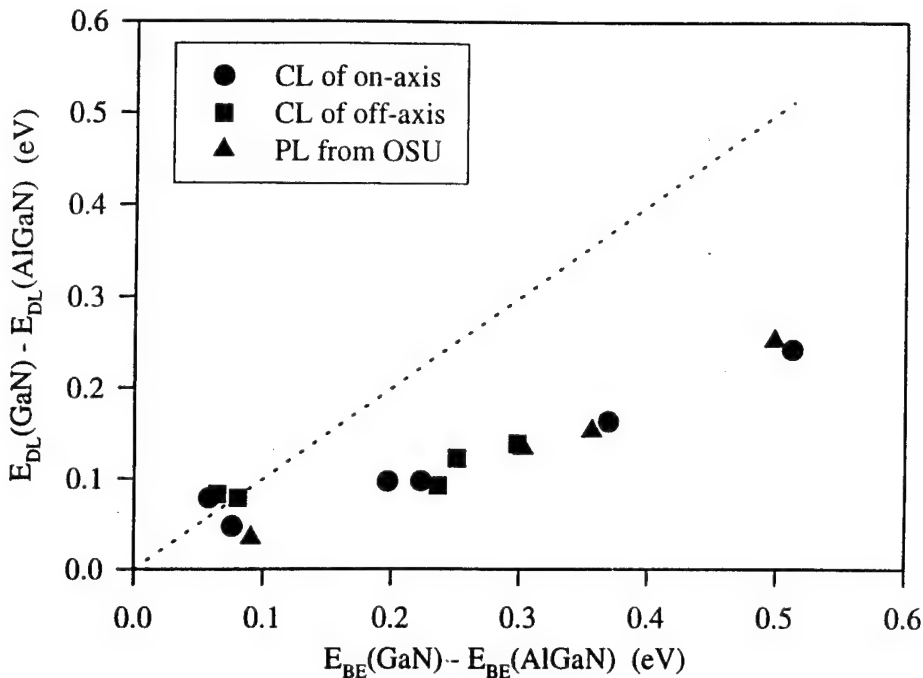


Figure 12. Change in deep level peak emission vs. change in band-edge emission.

*PL of AlGaN (In Collaboration with Oklahoma State University).* Photoluminescence of  $Al_xGa_{1-x}N$  through a collaboration with the Center for Laser Research at Oklahoma State University was performed. The excitation source is a frequency-doubled 488 nm line of an Ar-ion laser, which results in an output wavelength of 244 nm. Each test was performed at 10 K. PL of two samples is shown in Figure 13, these are samples *c* and *d* from the previous section.

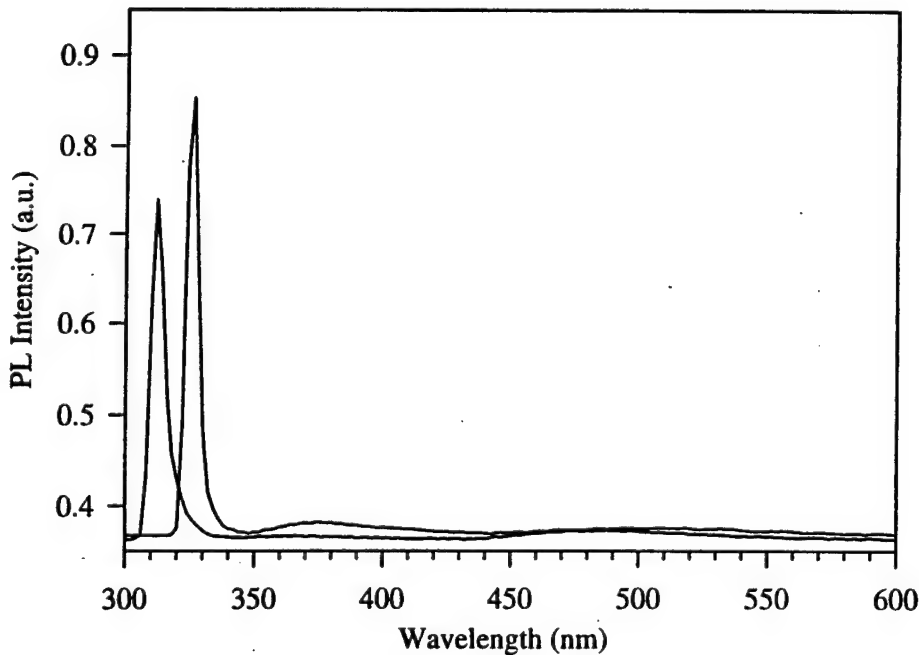


Figure 13. Photoluminescence of  $Al_xGa_{1-x}N$  at 10 K using a frequency-doubled 488 nm.

The results indicate that photoluminescence and cathodoluminescence of  $\text{Al}_x\text{Ga}_{1-x}\text{N}$  give complimentary results. In the future, time-resolved PL will be performed on these and other samples using the frequency-doubled laser.

#### D. Conclusions

Low temperature (8K) photoluminescence has been used to characterize both undoped and doped GaN films deposited on vicinal  $\alpha$ (6H)-SiC(0001)<sub>Si</sub> wafers by OMVPE. Unintentionally doped GaN exhibited a sharp peak at 357.36 nm for a 1  $\mu\text{m}$  film that is due to the recombination of excitons at neutral donors. The peak FWHM of 4 meV is an indication of the high quality of the film. The donor-acceptor pair emission and deep level emission at 2.2 eV were very weak for this sample, a further indication of its high quality.

A shift in the donor bound exciton peak to lower energies was found as film thickness increased. This may be due to an increase in residual tensile strain due to the thermal expansion mismatch between GaN and the SiC substrate.

Magnesium doping of GaN proved to be successful. Annealing of GaN at 700°C improved the PL emission by 250 %, but annealing at higher temperatures decreased the PL intensity. Residual strain due to the cooling of the sample after annealing may lead to an increase in non-radiative transitions.

The optimal growth temperature of Mg-doping of GaN was found to be 1100°C. This sample proved to be p-type as grown, with a room-temperature hole concentration of  $2 \times 10^{16}/\text{cm}^3$ . The PL emission peak was located at 429 nm at 8K and 460 nm at room temperature. Annealing at 600°C improved the room temperature hole concentration to  $1 \times 10^{18}/\text{cm}^3$ , this value did not improve with annealing at higher temperatures. From this information and the room temperature PL data it is concluded that 600°C is the optimal annealing temperature.

Cathodoluminescence at 8 K was used to characterize  $\text{Al}_x\text{Ga}_{1-x}\text{N}$  grown directly on vicinal  $\alpha$ (6H)-SiC(0001)<sub>Si</sub> wafers. The results showed strong emission at the band edge relative to deep level emission. The FWHM of the band edge peak increased with x, as expected.

The shift in the deep level (DL) emission relative to the shift in the band edge emission was investigated and compared to recent work on the pressure dependence of the PL of GaN. The results show that the shift in the DL emission does not keep up with the shift in the band edge emission past .1 eV. Further work will be performed to verify and understand this.

Photoluminescence of  $\text{Al}_x\text{Ga}_{1-x}\text{N}$  was performed in collaboration with the Center for Laser Research at Oklahoma State University. The results were very similar to CL performed on the same samples. Future work will center on using the PL system to perform time-resolved spectroscopy of  $\text{Al}_x\text{Ga}_{1-x}\text{N}$ .

### E. Future Research Plans and Goals

Photoluminescence and cathodoluminescence will continue to be used to measure the quality of GaN films grown by OMVPE and MBE. Work on both p- and n-type doped GaN will also continue. In addition, PL will be used to guide the growth of  $In_xGa_{1-x}N$ .

Extensive work will be done to study the  $Al_xGa_{1-x}N$  alloy system. CL measurements of  $Al_xGa_{1-x}N$  films through the full composition range will be performed, and the bowing parameter will be calculated. SIMS and Auger spectroscopy will be performed on the films to measure their exact composition to assist in this work. Ellipsometry and X-ray diffraction will also be used to study these films.

Future collaboration include working with Dr. J.J. Song and Dr. Wei Shan at Oklahoma State on photopumping and time-resolved spectroscopy of  $Al_xGa_{1-x}N$  and  $In_xGa_{1-x}N$ . Deep level transient spectroscopy (DLTS) measurements on  $Al_xGa_{1-x}N$  will be made with the assistance of Dr. Nobel Johnson at Xerox PARC. Photoluminescence excitation (PLE) spectroscopy and Optically detected magnetic resonance (ODMR) will be used to study the nature of the deep level emissions in  $Al_xGa_{1-x}N$ . This work will be done with Dr. Jaime Freitas and Dr. Evan Glaser at the Naval Research Laboratory.

### F. References

1. B. G. Yacobi and D. B. Holt, *Cathodoluminescence Microscopy of Inorganic Solids*, Plenum Press, New York (1990).
2. Micheal D. Lumb, Ed., *Luminescence Spectroscopy*, Academic Press, New York (1978).
3. S. Strite and H. Morkoç, *J. Vac. Sci. Technol. B* **10** (4), 1237 (1992).
4. R. A. Youngman and J. H. Harris, *J. Am. Ceram. Soc.* **73** [11], 3238 (1990).
5. S. Nakamura, T. Mukai, and M. Senoh, *Jpn. J. Appl. Phys.* **30** (10A), 1708 (1991).
6. V. F. Veselov, A. V. Dobrynin, G. A. Naida, P. A. Pundur, E. A. Slotensietse, and E. B. Sokolov, *Inorganic Materials* **25** (9), 1250 (1989).
7. J. N. Kuznia, M. A. Kahn, D. T. Olson, R. Haplan, and J. Freitas, *J. Appl. Phys.* **73** (9), 4700 (1993).
8. H. Murakami, T. Asahi, H. Amano, K. Hiramatsu, N. Sawaki, and I. Akasaki, *J. Crystal Growth* **115**, 648 (1991).
9. K. Maier, J. Schneider, I. Akasaki, and H. Amano, *Jpn. J. Appl. Phys.*, **32** (6), 846 (1993).
10. I. Akasaki, and H. Amano, *J. Crystal Growth*, **99**, 375 (1990).
11. S. Yoshida, H. Okumura, S. Misawa, and E. Sakuma, *Surf. Sci.* **267** (7), 50 (1992).
12. S. Nakamura, T. Mukai, and M. Senoh, *Jpn. J. Appl. Phys.*, **31** (9), 2883 (1992).
13. S. Nakamura, N. Iwasa, T. Mukai, and M. Senoh, *Jpn. J. Appl. Phys.*, **31** (5), 107 (1992).
14. S. Nakamura, T. Mukai, and M. Senoh, *Jpn. J. Appl. Phys.*, **30** (12A), 1998 (1991).
15. S. Strite, J. Ruan, Z. Li, N. Manning, A. Salvador, H. Chen, D. J. Smith, W. J. Choyke, and H. Morkoç, *J. Va. Sci. Technol. B* **9** (4), 1924 (1991).
16. W. J. Choyke and I. Linkov, *Inst. Phys. Conf. Ser.* **137**, 141 (1993).
17. S. Pacesova and L. Jastrabik, *1979 Phys. Stat. Sol. B* **93**, K111.
18. S. Yoshida, S. Misawa, Y. Fujii, S. Takada, H. Hayakawa, S. Gonda, A. and Itoh, *J. Vac. Sci. Technol.* **16** (4), 990-3 (1979).

19. E. R. Glaser, T. A. Kennedy, H. C. Crookham, J. A. Freitas, Jr., M. Asif Khan, D. T. Olson, and J. N. Kuznia, *Appl. Phys. Lett.* **63** (19), 2673 (1993).
20. E. R. Glaser, T. A. Kennedy, J. A. Freitas, Jr., M. Asif Khan, D. T. Olson, and J. N. Kuznia, from the Fifth International Conference on Silicon Carbide and Related Materials in Washington, D.C., Nov. 1993, to be published in the "International Institute of Physics Conferences" Series.
21. T. Sasaki, T. Matsuoka, A. Katsui, *Appl. Surf. Sci.* **41/42**, 504 (1989).
22. S. Nakamura, N. Iwasa, T. Mukai, and M. Senoh, *Jpn. J. Appl. Phys.* **31** (5A), 1258 (1992).
23. I. Akasaki, and H. Amano, *J. Electrochem. Soc.* **141** (8), 2266 (1994).
24. M. S. Brandt, N. M. Johnson, R. J. Molnar, R. Singh, and T. D. Moustakas, *Appl. Phys. Lett.* **64** (17), 2264 (1994).
25. R. Dingle and M. Ilegems, *Solid State Commun.* **9**, 175 (1971).
26. W. Götz, N. M. Johnson, R. A. Street, H. Amano, and I. Akasaki, *Appl. Phys. Lett.*, **66**, 1340 (1995).
27. R. Dingle, D. D. Sell, S. E. Stokowski, and M. Ilegems, *Phys. Rev. B*, **4**, 1211 (1971).
28. E. F. Schubert, E.O. Gobel, Y. Horikoshi, K. Ploog, and H.J. Queisser, *Phys. Rev. B*, **30** (2), 813 (1984).
29. J. I. Pankove, *Optical Processes in Semiconductors*, Dover Publications, New York (1971).
30. M. A. Khan, D. T. Olson, and J. N. Juznia, *Appl. Phys. Lett.* **65** (1), 64 (1994).
31. K. Itoh, H. Amano, K. Hiramatsu and I. Akasaki, *Jpn. J. Appl. Phys.* **30** (8), 1604 (1991).
32. M. A. Khan, R. A. Skogman, R. G. Schulze, and M. Gershenson, *Appl. Phys. Lett.* **43** (5), 492 (1983).
33. J. Hagen, R. D. Metcalf, D. Wickenden, and W. Clark, *J. Phys. C* **11**, 1143 (1978).
34. P. Perlin, T. Suski, H. Teisseyre, M. Leszczynski, I. Grzegory, J. Jun, S. Porowski, P. Boguslawski, J. Bernholc, J. C. Chervin, A. Polian, and T. D. Moustakas, to be published.

### **XXIII. UV Photoemission Study of Heteroepitaxial AlGaN Films Grown on 6H-SiC**

#### **A. Introduction**

There is increasing interest in electronic devices composed of III-nitride materials for optoelectronic applications in the blue and UV region [1]. An alternative application of these semiconductors is in electron emission devices. Recent studies have demonstrated that diamond surfaces can exhibit a negative electron affinity (NEA). NEA surfaces may prove to be critical elements for cold cathode devices, vacuum microelectronics and photodetectors [2,3]. In addition to diamond, thin films of AlN grown on 6H SiC have been shown to exhibit a negative electron affinity (NEA) [4,5]. The AlN NEA surfaces were obtained from air exposed surfaces, and do not appear to be readily poisoned. In contrast to diamond, AlGaN materials exhibit the wurtzite crystal structure. One of the most significant limitations in the application of diamond is that reliable n-type doping has not been achieved. In contrast, n-type doping has been obtained for GaN and some AlGaN alloys. This study explores further the electron affinity of epitaxial AlGaN films on 6H-SiC.

The wurtzite AlN and GaN form a continuous solid solution of  $\text{Al}_x\text{Ga}_{1-x}\text{N}$  for  $0 \leq x \leq 1$  with bandgaps that range from 3.4 eV (GaN) to 6.2 eV (AlN). Figure 1 displays the bandgap of several materials as a function of the equivalent hexagonal lattice constant. The alloys also are also miscible with inn, hence the inclusion of InN could extend the range to 1.9 eV. The electron affinity of a semiconductor is related to the surface dipole and to the fundamental energy levels of the materials. Because the valence and conduction bands of the semiconductors have origin in the  $\text{sp}^3$  bonding and antibonding levels, it may be suggested that the larger bandgap materials will exhibit a smaller or negative electron affinity. In comparison with diamond, it might be assumed that AlGaN alloys with a bandgap greater than 5.4 eV could exhibit a NEA. In this paper, we report studies of AlGaN with x values of 0.75 and 0.13, as well as preliminary studies of GaN.

The AlGaN and GaN films used in this study were are grown on vicinal 6H-SiC substrates. The n-type SiC substrates used have a small lattice mismatch with AlN ( $3.08 \text{ \AA}$  vs.  $3.11 \text{ \AA}$ ) and GaN ( $a = 3.19 \text{ \AA}$ ). The small lattice mismatch enables heteroepitaxial growth of the wurtzite (2H) structure. Furthermore, the fact that the substrates are conducting avoids charging problems associated with photoemission from large bandgap and insulating materials.

The electron affinity of a semiconductor or the presence of a NEA can be determined by ultraviolet photoemission spectroscopy (UPS) [6-8]. The experiments described here involve directing 21.2 eV light (the He I resonance line) to the surface of the sample and detecting the spectrum of the emitted photo excited electrons as a function of electron kinetic energy.

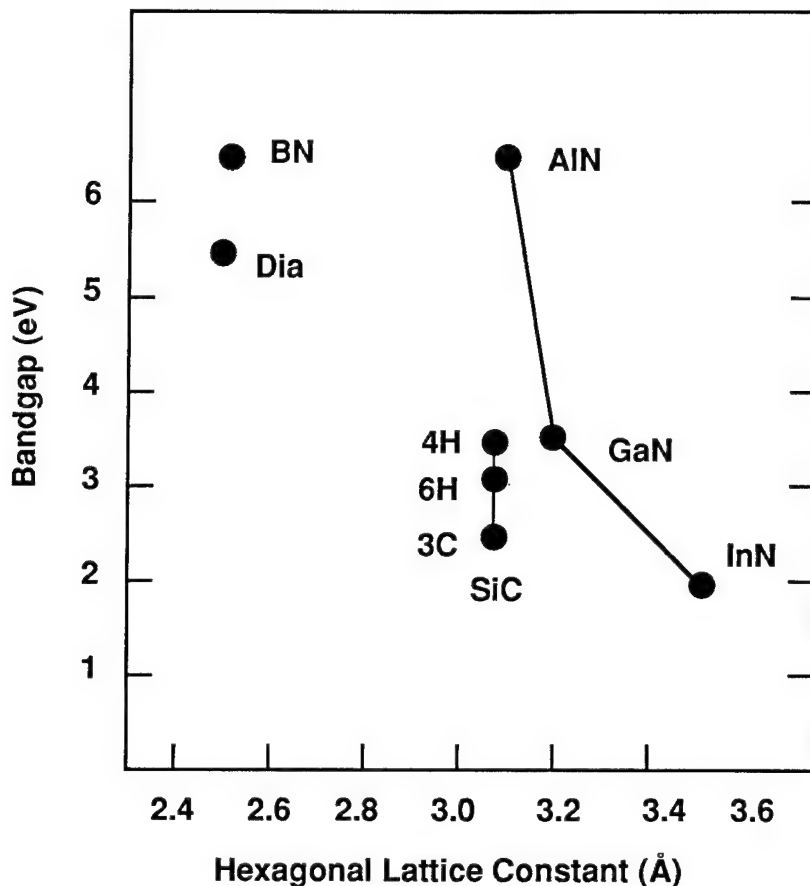


Figure 1. The bandgap vs. hexagonal lattice constant ( $a$ ) for a variety of wide bandgap semiconductors. The lattice constant for the cubic materials has been determined from the (111) plane.

Typically, UPS is used to obtain a profile of the valence band (VB) electronic states. As such, most studies of UPS of semiconductors present data of the most energetic electrons emitted from the surface. Electrons scattered to lower energy and secondary electrons will be displayed in the spectrum at lower kinetic energies. In addition, for a semiconductor which exhibits a NEA surface, a distinctive peak may be observed at the low kinetic energy (highest binding energy) end of the photoemission spectra. Figure 2 depicts a schematic representation of the photoemission spectra from a semiconductor with a negative or positive electron affinity. The low kinetic energy feature is due to secondary electrons which (quasi) thermalize to the conduction band minimum. Note that the solid line indicates a material with a positive electron affinity while the dashed line is a feature indicative of a NEA. In this paper we discuss samples with both positive and negative affinity surfaces.

The sharp features typical of a NEA have been observed from spectra of (111) and (100) diamond surfaces [6-10]. In the studies of diamond, a correlation was made between the

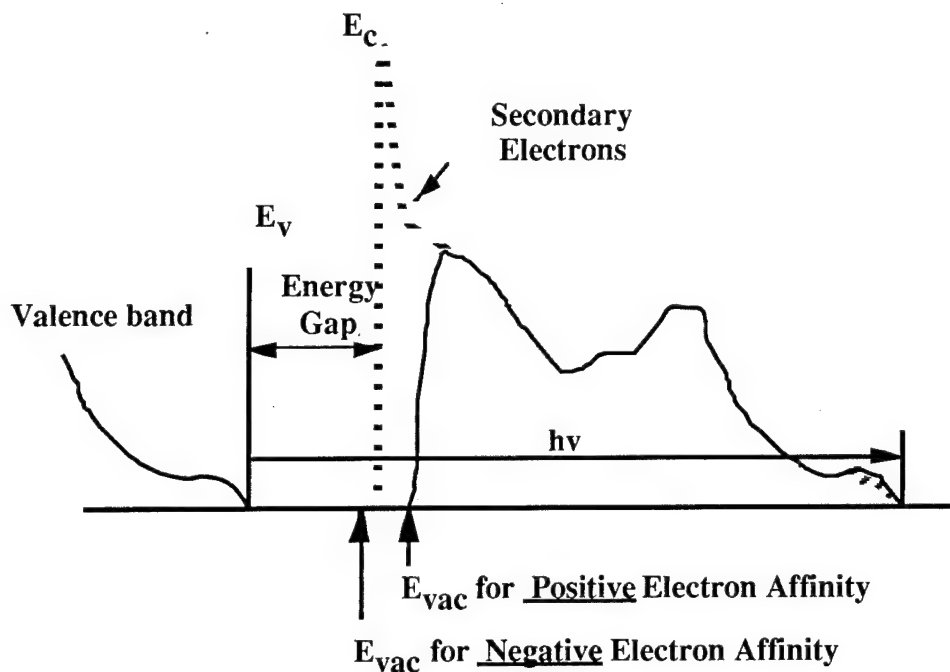


Figure 2. A schematic of the difference in the photoemission spectra of a semiconductor with a positive or negative electron affinity.

presence of hydrogen and the NEA peak [9,10]. In addition, it was also shown that thin metal layers such as Ti or other moderate work function metals could induce a NEA on the diamond surface [10,11]. These measurements verify that the surface dipole can be influenced by surface processing and that the effects contribute to the observation of a NEA.

#### B. Experimental Procedure

The 6H-SiC substrates used in this study were supplied by Cree Research, Inc. The samples were n-type with doping concentrations of  $10^{16}$  to  $10^{18}/\text{cm}^3$ . The AlGaN samples were grown by CVD in a remote location and transported in ambient to the analysis system. To avoid surface contamination, AlN and GaN samples were also grown in the integrated UHV transfer system by gas source molecular beam epitaxy (GSMBE). This system includes the UPS system, LEED, Auger, hydrogen and argon plasma processing chamber, and XPS as well as the GSMBE. The system is described elsewhere [9,11]. The capability of gas source MBE (GSMBE) to grow undoped AlN and GaN films has recently been added.

The AlGaN thin films were grown on vicinal n-type, Si-face  $\alpha$ (6H)-SiC(0001) substrates at  $1100^\circ\text{C}$ . Vicinal wafers were SiC(0001)  $3^\circ$ - $4^\circ$  off-axis toward the  $<11\bar{2}0>$ . The as-received SiC wafers were cut into 7.1 mm squares. The SiC pieces were degreased, dipped into a 10% HF solution for 10 minutes to remove the thermally grown oxide layer and blown dry with  $\text{N}_2$  before being loaded onto the SiC-coated graphite susceptor. The reactor was evacuated to less than  $3 \times 10^{-5}$  Torr prior to initiating growth. The continuously rotating susceptor was RF

inductively heated to the AlGaN deposition temperature of 1100°C in 3 SLM of flowing H<sub>2</sub> diluent. Hydrogen was also used as the carrier gas for the various metalorganic precursors. Once this growth temperature was reached and stabilized, AlGaN deposition was started by flowing triethylaluminum (TEA), triethylgallium (TEG) and ammonia (NH<sub>3</sub>) into the reactor at 23.6 μmol/min, 10.5 μmol/min and 1.5 SLM, respectively. The approximate solid solution alloy concentration using these growth parameters was Al<sub>0.75</sub>Ga<sub>0.25</sub>N. The AlGaN films were doped with Si from a SiH<sub>4</sub> source (8.2 ppm in N<sub>2</sub> balance) at flow rates between 2.89 and 5 nmol/min to minimize charging problems. The system pressure during AlGaN growth was 45 Torr. The AlGaN layer was grown for 90 minutes resulting in an approximate thickness of 1.5 μm. AlGaN samples were transported in air to the analysis system.

The GaN growth took place in a GSMBE. The cleaning procedure is similar to the above described process but differs in that once in vacuum the substrate is annealed in a silane flux [12]. The GaN samples were not intentionally doped, but since very thin films were employed, charging problems were avoided.

The UPS measurements were excited with 21.21 eV radiation (He I resonance line), and emitted electrons are collected with a hemispherical energy analyzer. The base pressure of the UPS system is  $2 \times 10^{-10}$  Torr, and operating conditions involve pressures up to  $1 \times 10^{-9}$  Torr, but the higher pressure is due to the helium inflow and does not contaminate the sample. The 50 mm mean radius hemispherical electron analyzer was operated at a 0.15 eV energy resolution and a 2° angular resolution. The analyzer (VSW HA50) is mounted on a double goniometer and can be tilted with respect to the sample in two independent directions. The samples were fastened with tantalum wire to a molybdenum sample holder. The sample holder is biased by up to 3 V to allow low energy electrons to overcome the work function of the analyzer. The Fermi level of the system (sample and analyzer) is determined by UPS measurement of the sample holder with no sample bias (i.e., grounded). The sample holder can be heated to 1150 °C, and the temperature is measured by a thermocouple.

### C. Results and Discussion

The UV photoemission spectra of all four samples studied here are shown in Fig. 3. The AlN and GaN films were prepared in by gas source MBE and transferred under UHV to the photoemission system. The two alloy samples were prepared by CVD and suffered ambient exposure. Samples were biased with 2-3 V to overcome the work function of the analyzer, and all spectra were shifted to be aligned at the valence band maximum. The spectra were scaled such that the strongest emission was the same for all curves.

The first aspect to be noted is that the spectra of the Al rich alloy and AlN exhibit sharp strong features at the highest binding energy, which corresponds to the lowest kinetic energy.

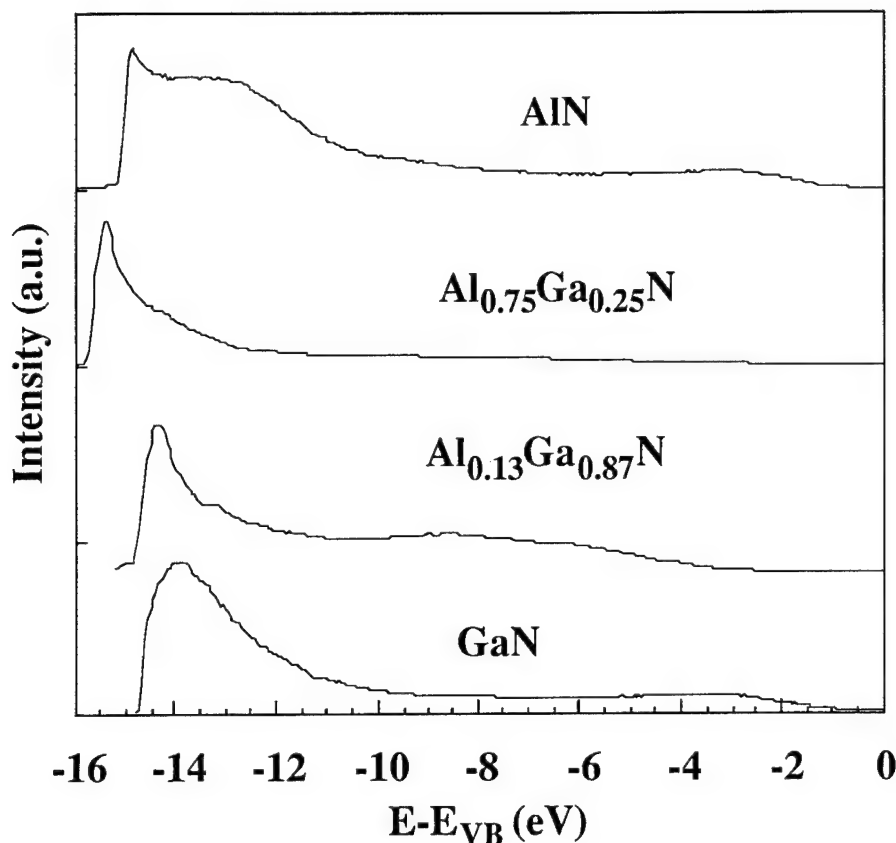


Figure 3. The UV photoemission spectra of  $\text{Al}_x\text{Ga}_{1-x}\text{N}$  for  $x=0, 0.13, 0.75, 1$ . Spectra were aligned at the valence band maximum.

These features are indicative of a negative electron affinity. As noted in the introduction, the feature is attributed to emission from electrons quasi-thermalized to the conduction band minimum. The emission from the  $\text{Al}_{0.13}\text{Ga}_{0.87}\text{N}$  sample is significantly weaker, and the GaN emission does not show the sharp peak at all.

A second indication of the change in electron affinity with alloy concentration is the extension of the  $\text{Al}_x\text{Ga}_{1-x}\text{N}$  spectra to lower energy as  $x$  is decreased. A more precise description of the relation of the NEA is obtained from the spectral width. The spectral width is obtained from a linear extrapolation of the emission onset edge to zero intensity at both the low kinetic energy cutoff and at the high kinetic energy end (reflecting the valence band maximum). For a material with a positive electron affinity, Figure 2 shows that  $\chi = h\nu - E_g - W$ , and for a material with a negative electron affinity Fig. 2 indicates that  $0 = h\nu - E_g - W$ , or rewriting,  $h\nu = E_g + W$ . We note here that the photoemission measurements cannot be used to determine the energy position of the electron affinity for the NEA case.

To determine the energy position of the valence band maximum, the spectral gain was increased, and the intensity was extrapolated to 0 emission. The spectra are aligned in Fig. 3 at the deduced valence band maximum. The spectral widths obtained from the  $\text{Al}_x\text{Ga}_{1-x}\text{N}$  samples were 14.5, 14.5, 15.5, and 15 eV for  $x=0$ , 0.13, 0.75, and 1.0, respectively. To apply the relations noted above, the bandgap of each sample must also be known. The literature values of the AlN and GaN bandgaps are 6.2 and 3.4 eV respectively. Assuming a linear extrapolation for the bandgap of the alloys, we deduce  $E_g = 5.50$  eV for  $x=0.75$  and  $E_g = 3.76$  eV for  $x=0.13$ . Using the relations described above, the AlN and the  $\text{Al}_{0.75}\text{Ga}_{0.25}\text{N}$  surfaces satisfy the relations for a NEA within  $\pm 0.2$  eV, and the GaN and  $\text{Al}_{0.13}\text{Ga}_{0.87}\text{N}$  surfaces, do not satisfy the relations for a NEA. We can, however, determine the value of the electron affinity of these materials and find that  $\chi = 3.3$  eV and 2.9 eV for  $x = 0$  and 0.13 respectively.

Another aspect that is evident from the photoemission spectra is the position of the surface Fermi level relative to the valence band maximum. It was found that  $E_F$  ranges from 2 to 3.5 eV above the valence band maximum for each sample. For the GaN and  $\text{Al}_{0.13}\text{Ga}_{0.87}\text{N}$  surfaces, these values position  $E_F$  in the upper part of the gap while for the Al rich samples, the values indicate that the surface Fermi level is pinned near midgap. The pinning at midgap may be an indication of increased impurity incorporation. In particular, the strong affinity of Al with oxygen often results in increased oxygen incorporation for these films.

To further explore the surface NEA effects, the effect of annealing in vacuum was explored for the  $x=0.75$  sample. The results are shown in Fig. 4. After annealing to 475 °C and 580 °C for 10 minutes the photoemission spectra showed a decrease in the relative intensity of the NEA related peak. Furthermore the width of the spectra also decreases. As these temperatures are much less than the temperatures involved in growth, it is doubtful that we removed some component which is responsible for the NEA. It is more likely that we introduced some type of contamination which attenuated the emission. No LEED pattern was visible for the  $\text{Al}_{0.75}\text{Ga}_{0.25}\text{N}$  sample, and the lack of a LEED pattern for the as-loaded samples is possibly related to carbon and oxygen on the surface (attributed to the transport in air). The annealing may result in more complete bonding of the surface adsorbed hydrocarbon layer which results in a change in the surface dipole.

The deduced electron affinities versus alloy concentration are shown in Fig. 5. Again we note that the photoemission measurements cannot be used to determine the position of the vacuum level for a NEA surface so these points are indicated at  $\chi = 0$  with arrows to larger negative values. The results suggest that the electron affinity depends on the alloy concentration as originally suggested. Unfortunately, we do not have sufficient data at this time to more completely describe the effect. Additionally, we have made no effort to control the

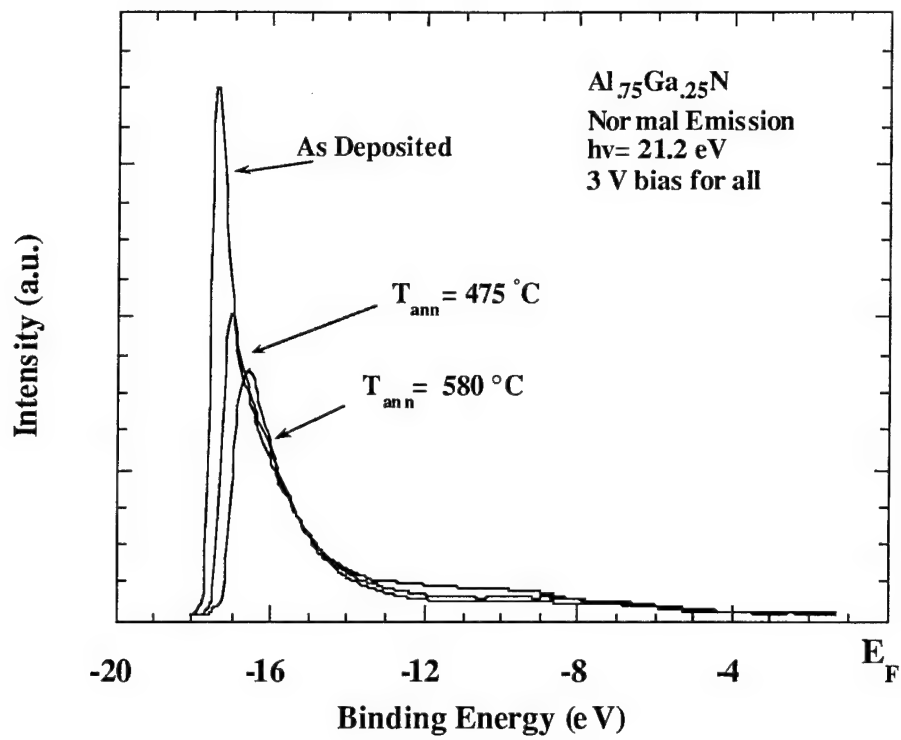


Figure 4. The UV-photoemission from  $\text{Al}_{0.75}\text{Ga}_{0.25}\text{N}$  on 6H-SiC versus annealing temperature.

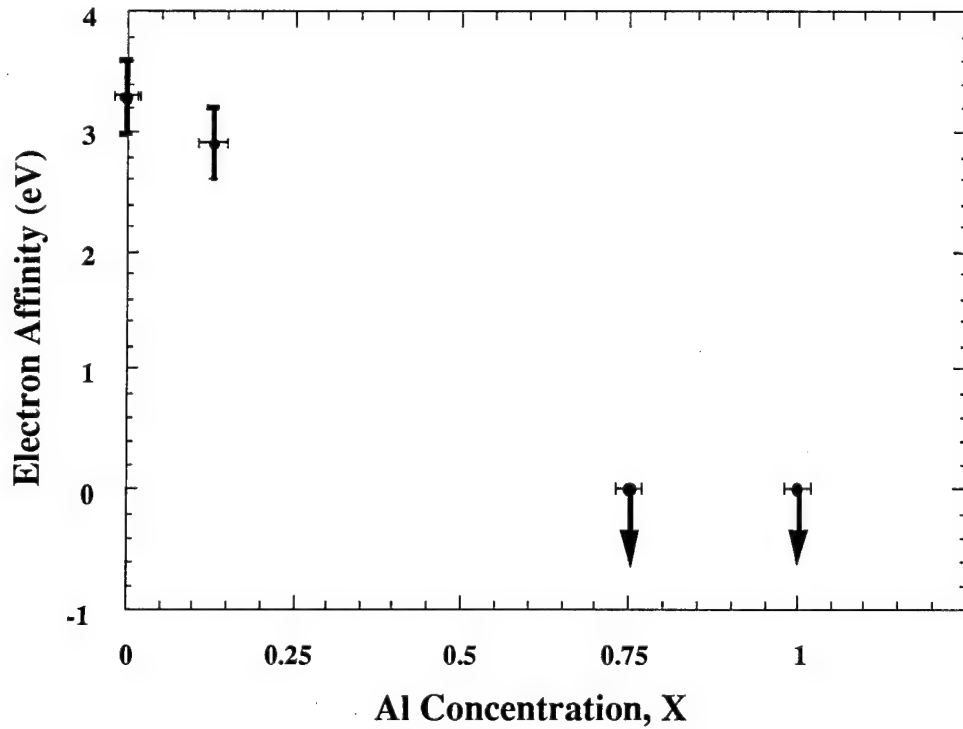


Figure 5. Electron affinities of  $\text{Al}_x\text{Ga}_{1-x}\text{N}$  alloys vs. Al concentration. The arrows indicate that the electron affinity is less than (or equal) 0, but the value cannot be determined from the UV photoemission measurements.

surface termination for these samples. For diamond, it was found that the observation of a NEA is critically dependent on the surface termination. Future studies will explore whether the electron affinity of AlGaN materials is also affected by different surface preparations.

#### D. Conclusions

In summary, we have observed features in the UPS spectra indicative of a NEA surface on AlN and Al<sub>1.75</sub>Ga<sub>.25</sub>N. The spectra exhibited both the sharp features at low kinetic energy that have been found to be characteristic of a NEA, and the width of the spectra was also consistent with the observed effect. The UPS spectra of Ga rich alloys did not show an NEA, but the measurements have been used to determined the electron affinity of GaN and Al<sub>1.13</sub>Ga<sub>.87</sub>N yielding values of 3.3 and 2.9 eV, respectively.

The surface Fermi level was found to shift towards the middle of the band gap for the Al rich samples, and this may indicate an increase in oxygen impurities.

The NEA surfaces were robust showing the effect even after transfer through ambient. Vacuum annealing, though, resulted in a change of the electron affinity from a NEA to a positive electron affinity. This effect was attributed to a change in the surface layer probably related to increased carbon contaminant.

Future work will involve examining samples to fill in the gaps in the solid solution of AlGaN alloys. Furthermore, we will explore whether surface treatments can be employed on the AlGaN alloys to form stable NEA surfaces.

#### E. Acknowledgment

This work was supported in part by the Office of Naval Research through grants N0014-92-J-1477 and N0014-92-J-1604. The SiC substrates used were supplied by Cree Research.

#### F. References

1. S. Strite and H. Morkoç, J. Vac. Sci. Technol. B **10**, 1237 (1992).
2. J. H. Edgar, J. Mater. Res. **7**, 235 (1992).
3. M. D. Williams, M. D. Feuer, S. C. Shunk, N. J. Sauer, and T. Y. Chang, J. Appl. Phys. **71**, 3042 (1992).
4. M. C. Benjamin, C. Wang, R. F. Davis, R. J. Nemanich, Appl. Phys. Lett. **64**, (1994).
5. M. C. Benjamin, C. Wang, R. S. Kern, R. F. Davis, R. J. Nemanich, Mat. Res. Soc. Symp. **339**, 81 (1994).
6. F. J. Himpsel, J. A. Knapp, J. A. van Vechten and D. E. Eastman, Phys. Rev. B **20**, 624 (1979).
7. B. B. Pate, Surf. Sci. **165**, 83 (1986).
8. B. B. Pate, M. H. Hecht, C. Binns, I. Lindau and W. E. Spicer, J. Vac. Sci. Technol. **21**, 364 (1982).
9. J. van der Weide and R. J. Nemanich, J. Vac. Sci. Technol. B **10**, 1940 (1992).
10. J. van der Weide and R. J. Nemanich, Appl. Phys. Lett. **62**, 1878 (1993).
11. J. van der Weide and R. J. Nemanich, Phys. Rev. B **51**, 13629 (1994).
12. R. Kaplan, Surface Science **215**, 111 (1989).

## XXIV. Reactive Ion Etching of GaN and AlN

### A. Introduction

Semiconductor devices are the principle components of electronic and telecommunications systems[1]. In order to densely pack these microscopic components, unidirectional, or anisotropic, etching techniques are required to produce a fine network of uniformly thick lines. Wet etching processes found in many semiconductor manufacturing steps produce multi-directional, or isotropically, etched features with variable thickness through its depth. This is undesirable for microcircuitry since the goal is to produce the smallest devices possible. Therefore, plasma-assisted processes, such as reactive ion etching (RIE), combine the physical characteristics of sputtering with the chemical activity of reactive species to produce a highly directional feature. RIE has the added advantage of providing a more uniform etch and a higher degree of material etch selectivity.

RIE has been employed to etch a wide variety of semiconductor materials including silicon-based materials[2-11], metals, like aluminum[7, 12-18] and III-V compounds, such as GaAs and InP[19-21]. Plasma-assisted etching of newer III-V compounds, such as GaN, AlN and InN, has also been investigated in depth by Pearton *et al.*[22-27] and other investigators[20, 21, 28-31]. There has been widespread interest in using these nitrides for semiconductor device applications requiring visible light emission, high temperature operation and high electron velocities. Since these materials possess wide bandgaps and optical emissions spectra in the blue to near ultraviolet range, they are prime candidates for ultraviolet detection devices.

The objectives of this report are to discuss recent progress made in the field of reactive ion etching of gallium, aluminum and indium nitride. In the following sections, a brief review of pertinent literature on plasma-assisted etching of III-V nitride compounds is provided along with a description of the reactive ion etching system, choice of process gases and results to date.

### B. Literature Review

*Etching of GaN.* Since GaN is a direct transition material with a bandgap ranging from 3.4-6.2 eV at room temperature, it is an ideal candidate for the fabrication of shortwave length light emitters[20, 32]. High quality GaN films have been successfully grown by MOVPE[32], ECR-MBE[33, 34], MOCVD[35] and a layer-by-layer process[36] on a number of substrates. In order to fabricate complete device structures, reliable etching processes need to be developed. Though wet etchants for GaN have been employed, including NaOH/H<sub>2</sub>O[23, 37] and hot H<sub>3</sub>PO<sub>4</sub>[37-40], patterning for device fabrication with wet etchants has not been studied or characterized. Thus, RIE is an effective method for the production of fine line patterning in GaN and does not involve direct exposure to heated, concentrated acid and base solutions.

There have been many reports of etching GaN by plasma-assisted processes in the past two years[20-23, 25, 27-31]. The more conventional technique of plasma etching of III-V nitrides, i.e. reactive ion etching, has been employed by several research groups[21-23, 25, 28, 31]. Fairly high etch rates have been attained with chlorine-based plasmas, as shown in Table I. In the chlorine-based plasmas, the higher etch rates are the result of more active Cl species diffusing to the nitride surface. Thus, as the pressure increases more Cl species are available for reaction and the etch rates increase (as shown in the case for  $\text{BCl}_3/\text{Ar}$  plasma). The addition of  $\text{H}_2$  to a  $\text{Cl}_2$  plasma is believed to tie up nitrogen atoms on the surface as volatile  $\text{NH}_x$ , resulting in increased etch rates with increasing  $\text{H}_2$  flow rates[23]. In addition, there is evidence from Auger electron spectroscopy (AES)[25, 28, 31] that GaN remains stoichiometric after etching and that Cl species are completely reacted and removed from the nitride surface. The AES results concurrently showed that the concentration of oxygen had increased after etching, probably the result of oxygen diffusion to the damaged surface. The source of oxygen was not elucidated, however, water vapor present in the vacuum system may account for a reaction with the GaN surface. Lastly, Adesida *et al.*[28] have demonstrated that fluorine plasmas are impractical to use as etchant gases due to the formation of involatile fluorides with

Table I. Etch Rate Parameters for RIE of GaN

Maximum Etch Rate ( $\text{\AA}/\text{min}$ )	Plasma Gases	Pressure (mtorr)	Power* (watts)	DC Bias (-V)	Ref.
175	$\text{BCl}_3/\text{Ar}$	1	200 (MW)	250	[23]
510	$\text{BCl}_3/\text{Ar}$	50	200 (RF)	NM#	[31]
750	$\text{Cl}_2/\text{H}_2$	1	1000 (MW)	150	[25]
200	$\text{Cl}_2/\text{H}_2$	1	200 (MW)	150	[25]
200	$\text{CCl}_2\text{F}_2/\text{Ar}$	1	200 (MW)	250	[23]
139	$\text{CCl}_2\text{F}_2/\text{Ar}$	20	40 (RF)	NM	[21]
80	$\text{CH}_4/\text{H}_2/\text{Ar}$	1	200 (MW)	300	[23]
350	$\text{CH}_4/\text{H}_2/\text{Ar}$	1	1000 (MW)	250	[25]
500	$\text{SiCl}_4/\text{Ar}$	20	NM	400	[28]
330	$\text{SiCl}_4/\text{Ar}$	50	200 (RF)	NM	[31]

\* MW designates a microwave power supply, whereas RF designates a radio frequency power supply.

# NM designates a parameter that was not mentioned in the reference.

Ga, Al and In at the surfaces. Addition of a fluorine-containing gas ( $\text{SiF}_4$ ) was added to their  $\text{SiCl}_4$  plasma to facilitate removal of atomic nitrogen from the surface. As expected, this addition had no effect on the etch rate probably due to the competitive formation of  $\text{GaF}_x$  and volatile  $\text{GaCl}_x$  at the surface.

Methane-based plasmas have been employed because of the speculation that methyl species and group III metal atoms, in this case Ga, will form a volatile metalorganic compound, such as trimethylgallium. Unfortunately, there is no mass spectrometer data to support this hypothesis. In general, etch rates of GaN are slow, as compared to chlorine-based plasmas, and a DC bias of about -175 V is required for initiation of the surface reaction.

More novel approaches to etching GaN have also been employed. Reactive fast atom beam etching was employed early on by Tanaka *et al.*[20] to etch GaN on sapphire in a  $\text{Cl}_2$  plasma at substrate temperatures ranging between 80-150°C during etching. Etch rates of up to 1000-1200 Å/min produced relatively smooth surfaces and a well defined pattern of elongated rectangular bars. More recently, Adesida *et al.*[30] have employed chemically assisted ion beam etching to etch GaN with an Ar beam in a  $\text{Cl}_2$  gas ambient. Results of their work should be available in the near future. Lastly, Pearton *et al.*[27] have employed a novel processing technique, called sidewall-etchback processing, to fabricate nanostructures of GaN as small as 300Å wide. This technique involves the following steps: photolithography of defined photoresist features, deposition of a thin (300-1000Å) layer of mask material (dielectric or metal) over the photoresist features, anisotropic etching of the mask leaving the vertical sidewalls intact, removal of the photoresist and anisotropic etching of the underlying GaN film. Dry etching in a  $\text{CH}_4/\text{H}_2/\text{Ar}$  plasma (1 mtorr, -200 Vdc, 350 W microwave power) was employed to etch the GaN film slowly to preserve the integrity of the circular nanostructures. The etch-back technique is an important tool allowing one to produce sub-micron features without requiring advanced photolithography processing.

*Etching of AlN.* Aluminum nitride is a candidate material for optoelectronic devices because it possesses a high electrical resistivity, high thermal conductivity, low dielectric constant and has a direct transition bandgap of 6.3 eV[41]. AlN films have been grown by several techniques including CVD, MBE and ALE, and on a variety of substrate materials including sapphire, silicon, spinel, silicon carbide and quartz[42]. Etching fine features in the AlN films is an important step in the fabrication of such devices. AlN has been wet etched for various applications including synthesis of AlN powders from nitrided steels etched in  $\text{FeCl}_3$ [43] and development of piezolayer field effect transistors employing phosphoric acid[44]. In addition, mention of wet etchants, including  $\text{NH}_4\text{F}$ -based solutions[45, 46]  $\text{NaOH}$  solutions[47] hot  $\text{H}_3\text{PO}_4$ [48] and several other strong acids and bases[49], can be found in several Japanese patents regarding device fabrication. Our own research in the laboratory has shown that

significant weight loss of bulk AlN occurs when samples are immersed in high temperature solutions ( $T > 100^\circ\text{C}$ ) of  $\text{H}_3\text{PO}_4$ ,  $\text{NaOH}$ ,  $\text{KOH}$  and  $\text{LiOH}$  solutions.

There have been a few reports of etching AlN in chlorine-based and methane-based plasmas by Pearton *et al.*[22, 23, 25]. High etch rates have been attained, as shown in Table II, especially for  $\text{Cl}_2/\text{H}_2$  plasmas. As the case is for GaN, an increase in pressure produces an increase in the etch rate as a result of a high concentration of Cl at the nitride surface. In addition, the morphology of the etched surfaces becomes more smooth as the flow of  $\text{H}_2$  is increased. This effect is thought to be the result of more efficient removal of the nitrogen etch product from the surface[25]. However, a threshold bias of about -100 V is required for removal of the native oxide and initiation of a surface reaction[23]. Examination of the AlN surfaces before and after etching, using AES, revealed no change in the stoichiometry, but a 2% atomic concentration of Cl was found on the surface. This would seem to indicate that slightly higher surface temperatures are necessary for complete removal of the  $\text{AlCl}_x$  species.

Table II. Etch Rate Parameters for RIE of AlN

Maximum Etch Rate ( $\text{\AA}/\text{min}$ )	Plasma Gases	Pressure (mtorr)	Microwave Power (watts)	DC Bias (-V)	Ref.
110	$\text{BCl}_3/\text{Ar}$	1	200	250	[23]
200	$\text{CCl}_2\text{F}_2/\text{Ar}$	1	200	300	[23]
25	$\text{CH}_4/\text{H}_2/\text{Ar}$	1	200	300	[25]
300	$\text{CH}_4/\text{H}_2/\text{Ar}$	1	1000	250	[25]
550	$\text{Cl}_2/\text{H}_2$	1	200	150	[25]
1100	$\text{Cl}_2/\text{H}_2$	1	1000	150	[25]

*Etching of InN.* Indium nitride also has a direct bandgap of 1.9 eV making it a promising candidate for visible light optoelectronic devices and high efficiency, low cost solar cells. Since the InN growth system is coming on line in our labs, it is desirable to be able to etch InN and fabricate patterned device structures. At the current time, wet etching has been accomplished by exposing (0001) InN samples to  $\text{NaOH}/\text{H}_2\text{O}$  and  $\text{KOH}/\text{H}_2\text{O}$  solutions at temperatures between 20-60°C[50]. Etch rates of up to 600  $\text{\AA}/\text{min}$  and 300  $\text{\AA}/\text{min}$  at 60°C in KOH and NaOH, respectively, were achieved. Smooth surfaces free of etch pits were obtained, but no patterning was demonstrated.

Reactive ion etching has recently been employed to etch InN. Pearton *et al.*[22, 23, 25] have been conducting reactive ion etching on InN at low pressures (1-30 mtorr) in ECR discharges of chlorine- and methane based plasmas. Fairly high etch rates were attained at low pressure and high DC bias, as shown in Table III. With regard to chlorine-based plasmas, InN has a lower etch rate than GaN or AlN which can be attributed mainly to the low volatility of the  $\text{InCl}_x$  species at normal cathode temperatures (around 25°C). Though significant heating of the samples can occur during etching by ion bombardment, the temperature of the samples surface is not high enough for the  $\text{InCl}_x$  species to become volatile. The result is a rough, In-rich surface. AES results from Pearton's work[25] showed a nitrogen deficiency on the etched surface in addition to 6% atomic concentration of chlorine probably due to uncompleted reaction of Cl radicals with In atoms on the nitride surface. Interestingly enough, since the chlorine-based plasma produces fairly slow etch rates, relative to GaN and AlN, layers of InN could be used as etch stops for etching AlGaN/GaN heterostructures. Methane-based plasmas, on the other hand, require significant DC bias to obtain comparable etch rates (as compared to etch rates attained in Cl-based plasmas), i.e. a threshold bias of -175V was required before etch rate of 300 Å/min was attained[25]. High biases may induce significant damage to the surface, a characteristic that is undesirable for optimal device performance.

---

Table III. Etch Rate Parameters for RIE of InN

---

Maximum Etch Rate (Å/min)	Plasma Gases	Pressure (mtorr)	Power* (watts)	DC Bias (-V)	Ref.
175	$\text{BCl}_3/\text{Ar}$	1	200	300	[23]
300	$\text{Cl}_2/\text{H}_2$	1	200	300	[24]
190	$\text{CCl}_2\text{F}_2/\text{Ar}$	1	200	300	[24]
100	$\text{CH}_4/\text{H}_2/\text{Ar}$	1	200	300	[24]
350	$\text{CH}_4/\text{H}_2/\text{Ar}$	1	1000	250	[24]

---

*Etching of Ternary Compounds.* A low pressure (1 mtorr) ECR plasma discharge was employed by Pearton *et al.*[26] for reactive ion etching on  $\text{In}_x\text{Ga}_{1-x}\text{N}$  and  $\text{In}_x\text{Al}_{1-x}\text{N}$  compounds. Etch rates were fairly high ( $\approx 200$ -350 Å/min) over the entire composition range even at high microwave power (1000 W) and DC bias (-250 V) when using a  $\text{CH}_4/\text{H}_2/\text{Ar}$  plasma, but a slight increase in the etch rate (up to  $\approx 400$  Å/min) was observed with increasing In mole fraction. This behavior, Pearton believes, is a result of the In-methyl etch product

being more volatile than its Ga- and Al-methyl counterparts. Smooth surfaces and anisotropically etched features were observed over the whole range of composition. Higher etch rates were obtained for  $\text{Cl}_2/\text{H}_2$  and  $\text{Cl}_2/\text{SF}_6$  plasmas for low In mole fraction. As the In mole fraction decreased from 0% (all GaN and all AlN) to 100% (all InN), the corresponding etch rates dropped from 1000 Å/min and 700 Å/min, for  $\text{In}_x\text{Al}_{1-x}\text{N}$  and  $\text{In}_x\text{Ga}_{1-x}\text{N}$  respectively, to 200 Å/min. Again, this result is expected since at high In mole fraction the  $\text{InCl}_x$  species are more difficult to remove from the surface at normal cathode temperatures. More recently, Adesida *et al.*[30] have reported on reactive ion etching and chemically assisted ion beam etching of GaAlN. Details of their work have not yet been published.

### C. Experimental Procedure

*Experimental Apparatus.* A schematic of the reactive ion etching system is shown in Fig. 1. The main components of the system include gas handling/storage, etcher, gas scrubber and mass spectrometer. Since toxic gases, such as  $\text{BCl}_3$  and  $\text{Cl}_2$ , may be used to etch GaN and AlN, the system is designed for safe shutdown in the event of a power or water failure and/or inadvertent shutdown of the exhaust systems in the building.

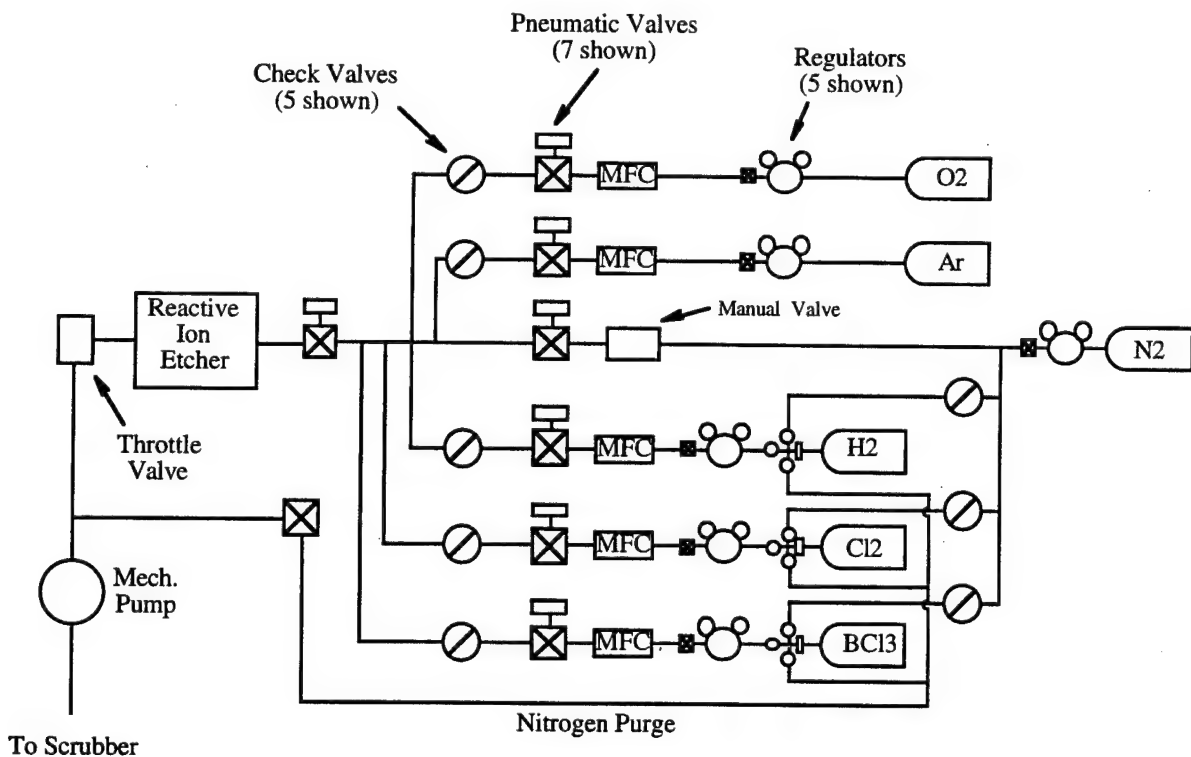


Figure 1. Schematic diagram of the reactive ion etching system.

The gas handling/storage sub-system consists of the gas storage cabinets, gas bottles, bottle regulators and necessary valves and tubing. Dry nitrogen is used to purge the gas lines before and after every run to remove moisture and chlorine from the lines, thus reducing the probability of corrosion of the gas lines. Mass flow controllers are employed for accurate control of the process gases. In the event of a power failure, interruption of the water supply or shutdown of the exhaust system, the solenoid actuated pneumatic valves will isolate the gas lines from the etch chamber.

The design of the etcher is based on that of the standard parallel-plate diode configuration, Fig. 2, in which the bottom electrode is powered by a RF power supply. The etcher, a Technics 85 series RIE, consists of an anodized aluminum chamber with an anodized aluminum water-cooled, driven lower electrode. A 350 Watt, 13.56 MHz RF generator with auto impedance matching network produces the power required to maintain a glow discharge in the chamber. The electrical potential applied across the parallel plate configuration results in ionization of the gas molecules, creating a plasma of neutrals, ions and electrons. Safety interlocks are supplied by Technics to disable the power when the system is vented or a panel is removed. The chamber pressure is measured by a capacitance manometer (absolute pressure) which is mounted to the underside of the chamber. The six channels of process gas (made from stainless steel tubing) are isolated from the injection manifold by means of air-operated electrically actuated isolation valves. In addition, an 19 CFM two-stage corrosive-series direct drive rotary vane pump provides the vacuum on the etch chamber.

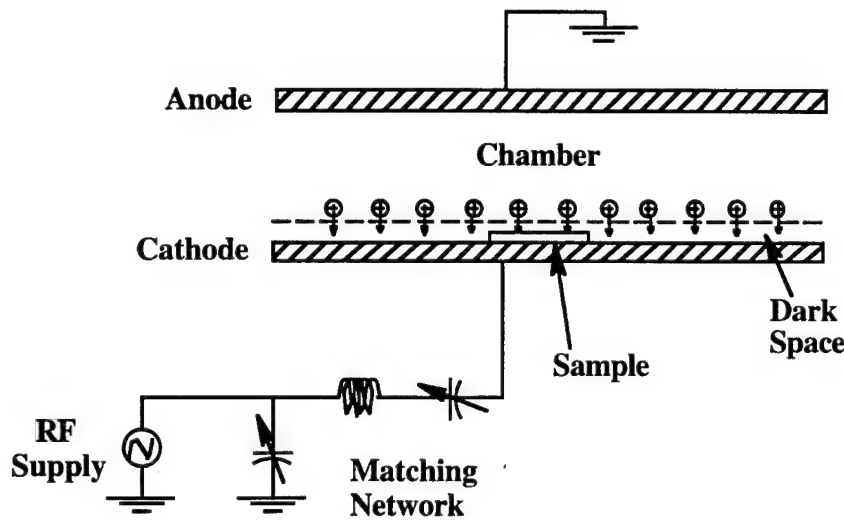


Figure 2. Schematic diagram of the parallel plate configuration.

Residual process gases and reaction by-products from the etcher will pass through a wet scrubber, which is equipped with a water recirculation line. These lines are monitored for water

flow and exhaust ventilation and are an integral part of the control system. Interruption of the water flow or inadequate ventilation will trip the pneumatic valves and close the gas lines. In addition, the pH level of the scrubber water is tested and monitored prior to each days etching runs.

*Choice of Process Gases.* There are a number of process gases that can be used to produce anisotropically etched features. For GaN, AlN and InN, fluorine plasmas are impractical because involatile fluorides are formed with Ga, Al and In at the surfaces, see Table IV, therefore limiting desorption of reaction species from the surface. Chlorine plasmas, on the other hand, have been used extensively for etching these compounds, see Section B above.

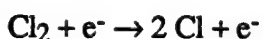
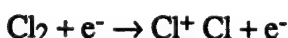
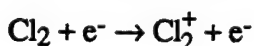
Table IV. Thermodynamic Data for Various Etchant Species

Species	$\Delta G_f^0$ (kJ/mole) at RT#	$T_m(^{\circ}\text{C})^*$	$T_b(^{\circ}\text{C})^*$
GaF <sub>3</sub> (g)	-1203	sublim. 800	-
GaCl <sub>3</sub> (g)	-565	78	201
AlF <sub>3</sub> (g)	-1530	sublim. 1291	-
AlCl <sub>3</sub> (g)	-738	sublim. 177	-
InF <sub>3</sub> (g)	-950	1170	> 1200
InCl <sub>3</sub> (g)	-475	sublim. 300	-

\* From Reference [37].

# From Reference [51].

Based on the success of Pearton *et al.* [22, 23] and others [20, 21, 28] Cl<sub>2</sub> and BCl<sub>3</sub> are currently being used as the main process gases in addition to Ar and N<sub>2</sub> as diluent and purge gases. The chlorine-based gases provide the following ionic and chemically reactive components via reaction of Cl<sub>2</sub> with electrons generated by the plasma:



Experimentation with other gases, such as iodine- and/or bromine-containing gas mixtures and other chlorinated gases, is possible in order to obtain smooth, anisotropic features with reasonably high etch rates.

*Etching Procedure.* Prior to etching, low temperature processes are used to deposit thin layers of silicon dioxide (CVD) and nickel (thermal evaporation) to be used as a mask for patterning the nitride samples. Photolithography is then used to pattern the mask material. This involves spinning photoresist onto the masking layer, exposing unmasked areas of the resist to UV light and developing the resultant hardened resist. Exposed masking layer areas are etched away using wet chemical etchants and the resist is removed by acetone in an ultrasonic cleaner.

The RIE system is checked for proper water, air and exhaust supply. Samples are loaded into the etching chamber and process gas lines are pumped down to  $\approx 5 \times 10^{-4}$  torr. A typical etch run includes the following steps:

1. Argon plasma to remove water vapor and hydrocarbon contamination from the sample and etch chamber,
2. Nitrogen purge to remove argon from etcher,
3.  $\text{Cl}_2/\text{Ar}$  or  $\text{BCl}_3/\text{Ar}$  plasma for processing,
4. Nitrogen purge to remove chlorinated process gases from the chamber,
5. Vent chamber to atmosphere with nitrogen.

After the samples are removed from the etcher, the mask is removed via wet chemical solutions and the step heights of the etched features are measured with a Detach stylus profilometer. In addition, SEM is used to observe the surface roughness and etched steps, and XPS and AES are used to observe the residual gas species on the sample surface.

#### D. Results

A reactive ion etching system has been installed and tested and is now operational. GaN has been etched in  $\text{Cl}_2/\text{H}_2$ ,  $\text{Cl}_2/\text{Ar}$  and  $\text{BCl}_3/\text{Ar}$  plasmas with varying flow rates, pressures, power and DC bias. Typical etching parameters are: 1-10 sccm total gas flow, 35-75 mtorr, 125-200 W power and -(200-300)V bias. Etch rates of up to 200 Å/min and 150 Å/min have been achieved with  $\text{Cl}_2/\text{Ar}$  and  $\text{BCl}_3/\text{Ar}$  plasmas, respectively. Parametric studies are currently underway to optimize etching parameters employing  $\text{Cl}_2/\text{Ar}$  gas plasma. Etch rates of GaN thin films in  $\text{Cl}_2/\text{H}_2$  plasmas vary with power, bias and pressure, as shown in Table V. Repeatability of the etch rate for a given set of etch parameters is also being studied.

#### E. Future Research

In the future, parametric studies will be continued to determine how the power, pressure, gas load and flow rates affect the etching rate of III-V nitrides in various chlorine-based

plasmas. Alternative Cl-containing gases such as methyl and nitrosyl chloride may be used in the future in order to establish etch rates of the nitrides and to study the underlying etch mechanisms. Surface analysis techniques such as AES and XPS will be employed to determine the contamination levels and surface condition of the nitrides before and after etching. In the future, scanning tunneling microscopy and atomic force microscopy may be employed to observe the surface morphology and to correlate etching parameters with surface damage. In addition, experimentation with different cathode materials (such as graphite and quartz) is possible if there is any micromasking from the cathode material. The ultimate goal of this research is to etch features necessary for optoelectronic and semiconductor devices fabrication.

Table V. Etch Parameters for Cl<sub>2</sub>/H<sub>2</sub> Plasmas

Sample	sccm Cl <sub>2</sub>	sccm H <sub>2</sub>	pressure (mtorr)	power (W)	bias (-Vdc)	etch rate (Å/min)
1	1	3	50	100	236	-
2	5	3.3	75	150	205	60
3	2	2	50	100	214	11
4	3	1	50	100	231	13
5	1	1	25	250	370	70
6	5	3.3	75	200	218	30
7	2	1	25	200	285	40

## F. References

1. *Plasma Processing of Materials: Scientific Opportunities and Technological Challenges*, National Research Council—Panel on Plasma Processing of Materials, Eds. (National Academy Press, Washington, D.C., 1991).
2. D. L. Smith, R. H. Bruce, J. Electrochem. Soc. **129**, 2045 (1978).
3. C. J. Mogab, A. C. Adams, D. L. Flamm, J. Appl. Phys. **49**, 3796 (1978).
4. L. M. Ephrath, J. Electrochem. Soc., (August 1979), 1419.
5. S. Matsuo, J. Vac. Sci. Technol. **17**, 587 (1980).
6. L. M. Ephrath, Solid State Technol., (July 1982), 87.
7. D. L. Smith, P. G. Saviano, J. Vac. Sci. Technol. **21**, 768 (1982).
8. Y. H. Lee, M. M. Chen, J. Appl. Phys. **54**, 5966 (1983).
9. M. Zhang, J. Z. Li, I. Adesida, E. D. Wolf, J. Vac. Sci. Technol. B **1**, 1037 (1983).
10. A. J. van Roosmalen, Vacuum **34**, 429 (1984).
11. J. W. Palmour, R. F. Davis, T. M. Wallett, K. B. Bhasin, J. Vac. Sci. Technol. A **4**, 590 (1986).
12. R. H. Bruce and G. P. Malafsky, J. Electrochem. Soc. **136**, 1369 (1983).
13. S. Park, L. C. Rathburn, T. N. Rhodin, J. Vac. Sci. Technol. A **3**, 791 (1985).

14. H. F. Winters, J. Vac. Sci. Technol. B **3**, 9 (1985).
15. D. A. Danner, D. W. Hess, J. Appl. Phys. **59**, 940 (1986).
16. N. N. Efremow, M. W. Geis, R. W. Mountain, G. A. Lincoln, J.N. Randall, N.P. Economou, J. Vac. Sci. Technol. B **4**, 337 (1986).
17. Y. Ochiai, K. Shihoyama, T. Shiokawa, K. Toyoda, A. Masuyama, K. Gama, J. Appl. Phys. **25**, L527 (1986).
18. R. J. A. A. Janssen, A. W. Kolfschoten, G. N. A. van Veen, Appl. Phys. Lett. **52**, 98 (1988).
19. G. Smolinski, R. P. Chang, T. M. Mayer, J. Vac. Sci. Technol. **18**, 12 (1981).
20. H. Tanaka, F. Shimokawa, T. Sasaki, T. Matsuoka, Optoelect. Dev. Technol. **6**, 150 (1991).
21. J. S. Foresi, M.S. Thesis, Boston University, Boston, MA, 1992.
22. S. J. Pearton, C. R. Abernathy, F. Ren, J.R. Lothian, P.W. Wisk, A. Katz, C. Constantine, Semicond. Sci. Technol. **8**, 310 (1993).
23. S. J. Pearton, C. R. Abernathy, F. Ren, J. R. Lothian, P. W. Wisk, A. Katz, J. Vac. Sci. Technol. A **11**, 1772 (1993).
24. C. R. Abernathy, F. Ren, S.J. Pearton, in *IEEE 6th International Conference on Indium Phosphide and Related Materials*, Eds. (IEEE, Piscataway, NJ, 1994), p. 387.
25. S. J. Pearton, C. R. Abernathy, F. Ren, Appl. Phys. Lett. **64**, 2294 (1994).
26. S. J. Pearton, C. R. Abernathy, F. Ren, Appl. Phys. Lett. **64**, 3643 (1994).
27. S. J. Pearton, F. Ren, C. R. Abernathy, J.R. Lothian, Semicond. Sci. Technol. **9**, 338 (1994).
28. I. Adesida, A. Mahajan, E. Andideh, Appl. Phys. Lett. **63**, 2777 (1993).
29. I. Adesida, A. T. Ping, C. Youtsey, T. Dow, M. Asif Khan, D. T. Olsen, J. N. Kuznia, Appl. Phys. Lett. **65**, 889 (1994).
30. I. Adesida, A. T. Ping, in Eds. St. Louis, MO, 17-18 October 1994).
31. M. E. Lin, Z. F. Fan, Z. Ma, L. H. Allen, H. Morkoc, Appl. Phys. Lett. **64**, 887 (1994).
32. I. Akasaki, H. Amano, Physica B **185**, 428 (1992).
33. C. Eddy, Ph.D. Thesis, Boston University, Boston, MA, 1990.
34. T. Lei, T. D. Moustakis, J. Appl. Phys. **71**, 4933 (1992).
35. Z. J. Yu, B. S. Sywe, A. U. Ahmed, J. Electr. Mater. **21**, 782 (1992).
36. J. Sumakeris, Z. Sitar, K. S. Ailey-Trent, Thin Solid Films **225**, 244 (1993).
37. *CRC Handbook of Metal Etchants*, P. Walker, Eds. (CRC Press, Boca Raton, LA, 1991).
38. Y. Morimoto, J. Electrochem. Soc. **121**, 1383 (1974).
39. A. Shintani, S. Minagawa, J. Electrochem. Soc. **123**, 706 (1976).
40. V. V. Malinovskii, L. A. Marasina, N. V. Mitusova, I.G. Pichugin, Izv. Leningr. Elektrotekh. Inst. im. V. I. Ul'yanova **281**, 76 (1981).
41. E. S. Dettmer, B. M. Romenesko, H. K. Charles, B.G. Charkuff, D.J. Merrill, IEEE Trans. Comp. Hybrids Manuf. Technol. **12**, 543 (1989).
42. L. R. Rowland, Ph.D. Thesis, North Carolina State University, Raleigh, NC, 1992.
43. A. V. Omel'Chenko, M. A. Shelagarov, A. N. Frolov, M.E. Getmanova, G.S. Belousov, "Manufacture of Nitrides by Alloy Nitridation Followed by Selective Leaching," Small Enterprise Jilpa Ltd., Russia, PCT Int. Appl., 1992.
44. B. Matthes, E. Broszeit, O. Zucker, P. Gauer, Thin Solid Films **226**, 178 (1993).
45. M. Nagaoka, "Annealing Method for Compound Semiconductor Device Fabrication," Toshiba Corp., Japan, Jpn. Kokai Tokkyo Koho, 1987.
46. H. Kato, M. Sugata, T. Ikeda, "Manufacture of Silicon-Supported X-Ray Mask having Aluminum Nitride-Based Film," Canon K.K., Japan, Jpn. Kokai Tokkyo Koho, 1989.
47. A. Sasame, K. Shibata, H. Sakagami, "Aluminum Nitride Sintered Body with a Metalized Layer and Its Manufacture," Sumitomo Electric Industries, Ltd., Japan, Jpn. Kokai Tokkyo Koho, 1986.
48. "Group IIIA Pnictide Semiconductor Device," Fujitsu Ltd., Japan, Jpn. Kokai Tokkyo Koho, 1982.

49. N. Yamaguchi, S. Ogawa, I. Yoshizawa, S. Kajita, K. Waki, "A Method for Manufacturing a Nitride-Type Ceramic Circuit Board," Matsushita Electric Works, Ltd., Japan, Jpn. Kokai Tokkyo Koho, 1986.
50. Q. X. Guo, O. Kato, A. Yoshida, J. Electrochem. Soc. **139**, 2008 (1992).
51. *HSC Chemistry Program*, Version 2.0, Outokumpu Research Oy, Inc., Pori, Finland, 1993.

## XXV. Surface Cleaning and Contact Formation on GaN

### A. Introduction

The formation of ohmic contacts with semiconductor materials and devices is a fundamental component of solid state device architecture. As device size has diminished and the scale of integration has increased, the quality of these interfaces has become an increasingly important concern. In addition, the presence of parasitic resistances and capacitances, such as those existing at contact interfaces, becomes more detrimental at higher operating powers and higher oscillation frequencies. For many devices, the losses that occur at the contact interfaces account for a large fraction of the total losses, and as such are responsible for significant impact on device performance.

The development of adequate and reliable ohmic contacts to the compound semiconductors, particularly those with wider band gaps, has met a number of challenges. The subject of ohmic contacts to p- and n-type III-V compounds, mostly GaAs, AlGaAs, and InP, has received a great deal of attention over the past decade, and significant advances have been made [1-12]. By comparison, the III-V nitrides have received little attention in this regard. However, interest in these materials has been renewed in recent years as thin film growth techniques have improved, p-type doping in GaN and AlGaN solid solutions has been achieved, and p-n junctions have been fabricated.

*GaN Surface Cleaning.* Over the course of the development of semiconductor device technology, surface cleaning procedures have been devised to 1) degrease and remove gross contamination, 2) remove particulates and metal atom contamination, and 3) remove surface oxides to provide surfaces as atomically clean as possible. In practice, surface cleaning is as much of an art form or craft as it is a science; understanding of the surface composition and structure often lags well behind the successful application of processing steps. Procedures are frequently derived empirically with little detailed understanding of the chemistry or physics involved. Often, the meaning of the word "clean" varies depending on the surface conditions required for success with different processing steps, though surface impurity concentrations may vary by orders of magnitude. Given that the sensitivity of surface analytical techniques for detection of submonolayer coverage is limited, there are inherent limits on the ability to show conclusively that a surface is truly atomically clean [20].

As stated above, there are indications in the literature that cleanliness and preparation of the semiconductor surface prior to contact deposition play significant role in the performance of the interface. The goal of the surface cleaning studies described in this report is to determine the most effective choices of wet chemical cleaning and thermal desorption cleaning to use prior to metallization.

*Metallization Strategies.* The majority of successful ohmic contact systems that have so far been implemented with the more conventional compound semiconductors have relied upon alloying (liquid-phase reaction) or sintering (solid-phase reaction) via post-deposition annealing treatments, and/or the presence of high carrier concentrations near the interface [1,2,6,12]. However, many otherwise successful ohmic contact systems have only limited thermal stability and are subject to degradation, usually in the form of extensive interdiffusion, interfacial reaction, and interphase growth, accompanied by increase in contact resistivity, under subsequent thermal processing steps. It is reasonable to suppose that the cleanliness and preparation of the semiconductor surface prior to contact deposition plays a significant role in the behavior of the interface, and there are indications in the recent literature that support this [2,11-13]. Thorough oxide removal is especially important, though it may well prove to be a persistent challenge with Al-containing compounds in particular.

In this study, two main approaches are being taken in the development of ohmic contacts to GaN and AlN. The first approach is similar to that which has resulted in the majority of successful ohmic contacts to the more conventional compound semiconductors such as GaAs: the creation of high carrier concentrations in the semiconductor at the metal interface by means of alloying, sintering, or implantation of dopant species. The so-called pinning of the Fermi level at this surface, particularly with GaAs, results in a more or less fixed potential barrier at the metal interface. In the case of the pinned Fermi level of GaAs, the approach has generally been to shrink the width of the depletion layer by means of increasing the carrier concentration to the point where carrier tunneling through the barrier occurs readily. Even with optimization of contact composition and annealing times and temperatures, the lowest contact resistivities ( $\rho_c$ ) have been obtained only on the most heavily doped materials. Though there are indications that high doping levels and extensive interfacial reactions through alloying and sintering are not essential for ohmic contact formation in all cases, these processes have proven useful for minimizing  $\rho_c$  [2,11-13].

The other approach toward ohmic contact formation to be taken in this study involves the Schottky-Mott-Bardeen (SMB) model of semiconductor interfaces [14,15]. In this model the relative values of work function of the materials involved determine the band structure of the interface and thus the nature of any potential barriers present. The presence of interfacial states at the semiconductor surface can interfere with the alignment of the Fermi level across the interface and overshadow the effect of the inherent difference in work function between the two materials. The III-V nitride compounds are more ionically bonded than their phosphide and arsenide counterparts, as a result of larger electronegativity differences between the component elements. According to the observations of Kurtin *et al.* [16], this fact indicates that the nitrides should experience less Fermi level stabilization or “pinning” at the surface than do the more covalent compounds. Thus, the barrier heights of contacts to the nitrides should be more

dependent on the contact material than is the case with the more conventional and more covalent semiconductors such as Si, GaAs, InP, SiC, etc. With the work of Foresi and Moustakas [17,18], and more recently M. E. Lin *et al.* [19], this concept is beginning to be investigated. The SMB model also indicates that the cleanliness of the interface plays an important role in its electrical behavior - particularly in the minimization or elimination of any insulating layers at the interface.

## B. Experimental Procedure

*GaN Film Deposition.* The substrates used for III-nitride film growth were 6H-SiC wafers supplied by Cree Research, Inc. Two growth methods have been used for the deposition of III-N films for these contacts studies: ECR plasma-enhanced molecular beam epitaxy (MBE) and metalorganic vapor phase epitaxy (MOVPE). The growth reactors used for the nitride film deposition are described in other sections of this report. Magnesium incorporated into the films during growth as the p-type dopant; Ge was used to grow n-type material via MBE and Si was used as the more effective donor impurity for the MOVPE-grown films.

*Surface Analysis.* Auger electron spectroscopy (AES) was used to characterize the presence of chemical impurities on the cleaned GaN surfaces. This technique involves the energy analysis of characteristic electron emission from the surface of a sample in response to an incident electron beam. Like the related technique x-ray photoelectron spectroscopy (XPS), which uses incident x-ray radiation as the primary energy source, AES allows the detection of atoms in the first few atomic layers of a surface (1-5 nm), to a sensitivity of approximately 0.5-1%. This sensitivity corresponds under most conditions to submonolayer coverage, and thus is usefully applied to studying the contamination of surfaces by oxide and hydrocarbon deposition. Auger electron spectroscopy was performed at the NCSU Surface Science Laboratory, using an AES analysis system manufactured by VG Instruments Ltd. Incident beam energy was 3 kV with a spot size of 1 m. Spectra were acquired over the energy range 30-1230 eV, with an energy resolution of 1 eV/step.

*Contact Deposition.* Prior to metals deposition, the GaN/SiC films were cleaned with a 1:1 HCl:DI H<sub>2</sub>O dip and carefully pulled dry from the solution. Any remaining cleaning solution was blown dry with N<sub>2</sub>. Titanium and TiN were grown on Si-doped GaN (MOVPE-grown,  $n=1.2\times10^{18}$  cm<sup>-3</sup>) using e-beam evaporation of Ti; for TiN deposition, purified N<sub>2</sub> activated by a Kaufman-type ion gun was added. Because this deposition equipment also included the ability to heat samples, a thermal desorption step at 500°C was performed prior to deposition to achieve a cleaner surface. Both the Ti and TiN growth were performed at a substrate temperature of 350°C and a deposition rate of 10-15 Å/min. Total thickness for both metal films was 1000 Å. Auger depth-profiling analysis of TiN films grown under these conditions have revealed them to be stoichiometric TiN and uniform through the thickness even

when variations in pressure and deposition rate occurred during growth. In addition, the metallic gold-like appearance of the TiN compound is a reliable indicator of stoichiometry. Film thicknesses were monitored using a quartz crystal oscillator. The TLM patterns for the Ti and TiN films were defined using photolithography, producing a TLM test pattern identical to that of the shadow mask described in earlier reports, but on a smaller scale.

The Pt films were deposited by means of Ar ion DC sputtering. A shadow mask was used during deposition to create rectangular-bar TLM (transmission line model) patterns for contact resistivity ( $\rho_c$ ) measurements, as described in the earlier semiannual report of June 1993. This sputtering system has no thickness monitor, but the thickness of the Pt deposition was estimated from calibrated values for deposition rate.

*Contact Characterization.* After deposition, I-V measurements were taken between separate pads of the TLM patterns, using tungsten probe tips and an HP 4145C Semiconductor Parameter Analyzer. Annealing treatments were performed in a flowing Ar atmosphere (ultra-pure carrier grade from Air Products, Inc.) at a series of temperatures - 600, 700, 800 and 900°C for 30 s each step - using a Heatpulse 410 rapid thermal annealing (RTA) furnace. TLM measurements were taken by measuring the total resistance between identical contact pads as a function of separation distance  $l$ . The contact resistivity was obtained from the plot of  $R(l)$  vs.  $l$ , as described by Reeves and Harrison [23]. The mathematical assumptions and pattern geometry inherent in this model yield values for  $\rho_c$  that represent an upper limit; thus, the measured values are conservative assessments of performance. In addition, for every test pattern geometry there is a lower limit of  $\rho_c$  below which it is not possible to obtain precise  $\rho_c$  calculations. This is due to the fact that the linear  $R(l)$  plot becomes very steep and too close to the origin with decreasing  $\rho_c$ . For the shadow-mask test geometry used in this study to date, and for many of the TLM results reported by other researchers in the field, the practical lower limit for precise  $\rho_c$  calculation is about  $10^{-6} \Omega \text{ cm}^2$ .

In addition to electrical characterization, the contact samples in this study were also prepared for cross-sectional TEM analysis by Dr. Moon Kim and Dr. Yi Huang at the Center for Solid State Science at Arizona State University. At the time of the writing of this report, microstructural and crystallographic characterization of these contact systems and compositional analysis by means of energy-dispersive x-ray analysis (EDS) and electron energy loss spectroscopy (EELS) is expected in the near future.

## C. Results

*GaN Surface Cleaning.* Acquired AES spectra from surfaces cleaned in a variety of wet chemical solutions are shown in Fig. 1. The label "DI" refers to deionized water; the term "solvent cleaning" refers to the conventional sequence trichloroethylene (TCE), acetone, and

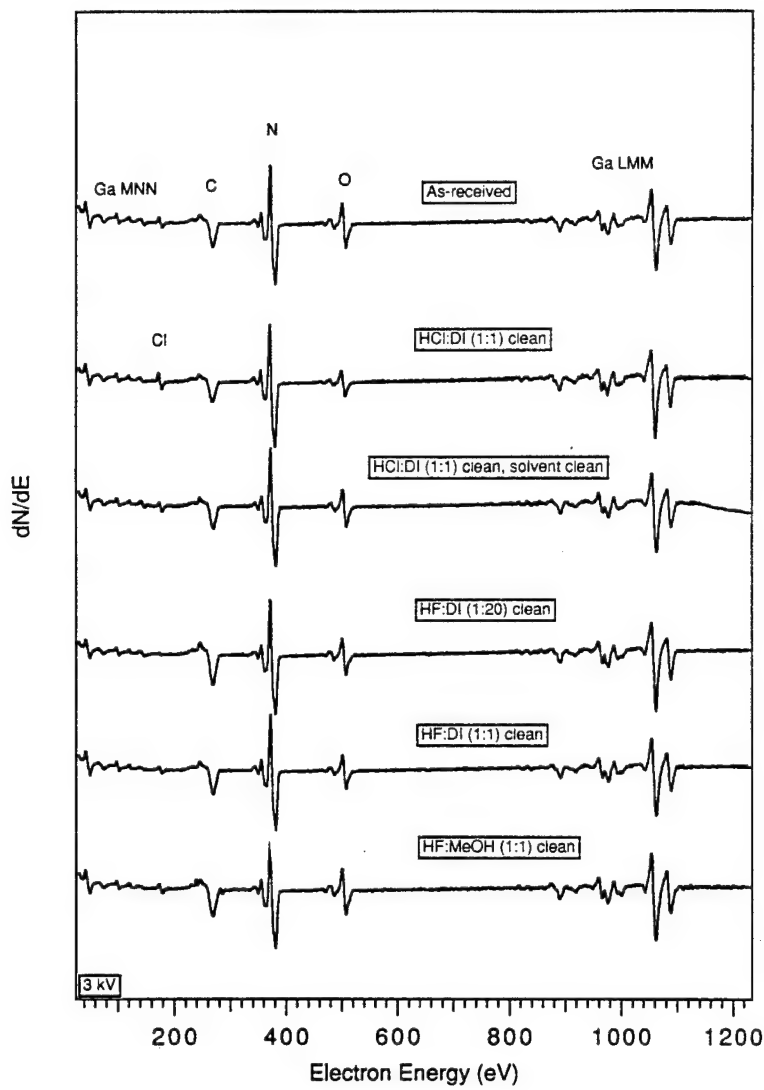


Figure 1. AES survey spectra of GaN surfaces cleaned with different chemical treatments.

methanol (MeOH). With the exception of the as-received sample and the sample which received the solvent cleaning after the HCl:DI (1:1) dip, all of the samples were solvent-cleaned prior to the acid dip step. The last cleaning step for each sample was followed by blowing dry with  $N_2$ , without water rinse. The as-received sample was exposed to air for at least a week prior to characterization; all of the cleaned samples were loaded into the vacuum system (base pressure  $5 \times 10^{-9}$  T and below) as soon as possible. Each received an unavoidable exposure to air for approximately 10 minutes during the time required to secure each sample to the sample holder.

For the purpose of graphing these data, the nitrogen peak-to-peak heights were all set to the same value so that the relative concentrations of O and C may be compared. The associated data of peak height ratios are listed in Table I. The peak-to-peak heights of the oxygen and carbon signals are related to the peak-to-peak height of the nitrogen signal and indicate the relative abundance of oxygen-based and carbon-based surface coverages. The ratios of peak heights

have been used because, though the total number of counts in a given peak may vary from run to run, the *relative* peak intensities remain the same for a given surface.

---

---

Table I. Relative Auger Peak Intensities from GaN Surfaces Cleaned with Different Wet Chemical Treatments.\*

Treatment	O/N	C/N
As-received	0.39	0.28
HCl:DI (1:1)	0.21	0.24
HCl:DI (1:1), solvent clean	0.32	0.28
HF:DI (1:20)	0.33	0.38
HF:DI (1:1)	0.30	0.28
HF:MeOH (1:1)	0.33	0.41

\*Prior to acid cleaning, GaN samples were “solvent cleaned,” using the sequence TCE, acetone, methanol. After the last treatment step, each sample was blown dry with N<sub>2</sub>.

Of all the wet chemical cleaning methods compared here, the HCl:DI (1:1) solution yielded the lowest relative concentrations of O and C on the air-exposed surfaces. A very small Cl peak was observed as well. The placement of the solvent cleaning step after the HCl acid cleaning resulted in an increase of both O and C. All of the remaining cleaning treatments examined showed larger relative concentrations of both O and C. Of all the HF cleaning treatments examined, the HF:DI (1:1) treatment gave the lowest O and C concentrations, with values similar to those seen on the HCl:DI, solvent cleaned surface. The highest concentrations of O and C observed were found on the HF:MeOH-treated surface, slightly higher than those on the as-received surface.

The effects of heating GaN surfaces on the presence of O and C are shown in Fig. 2. Two different wet chemical cleaning methods were compared: HCl:DI (1:1) and HF:MeOH (1:1), both of which included solvent cleaning before and N<sub>2</sub> blow dry after the acid cleaning step. Both desorption series show a gradual decrease in the presence of O and C through 625°C. It was expected that a further reduction of the O and C signals would be observed after the 800°C heating step, but these results were complicated by a possible light contamination of the AES

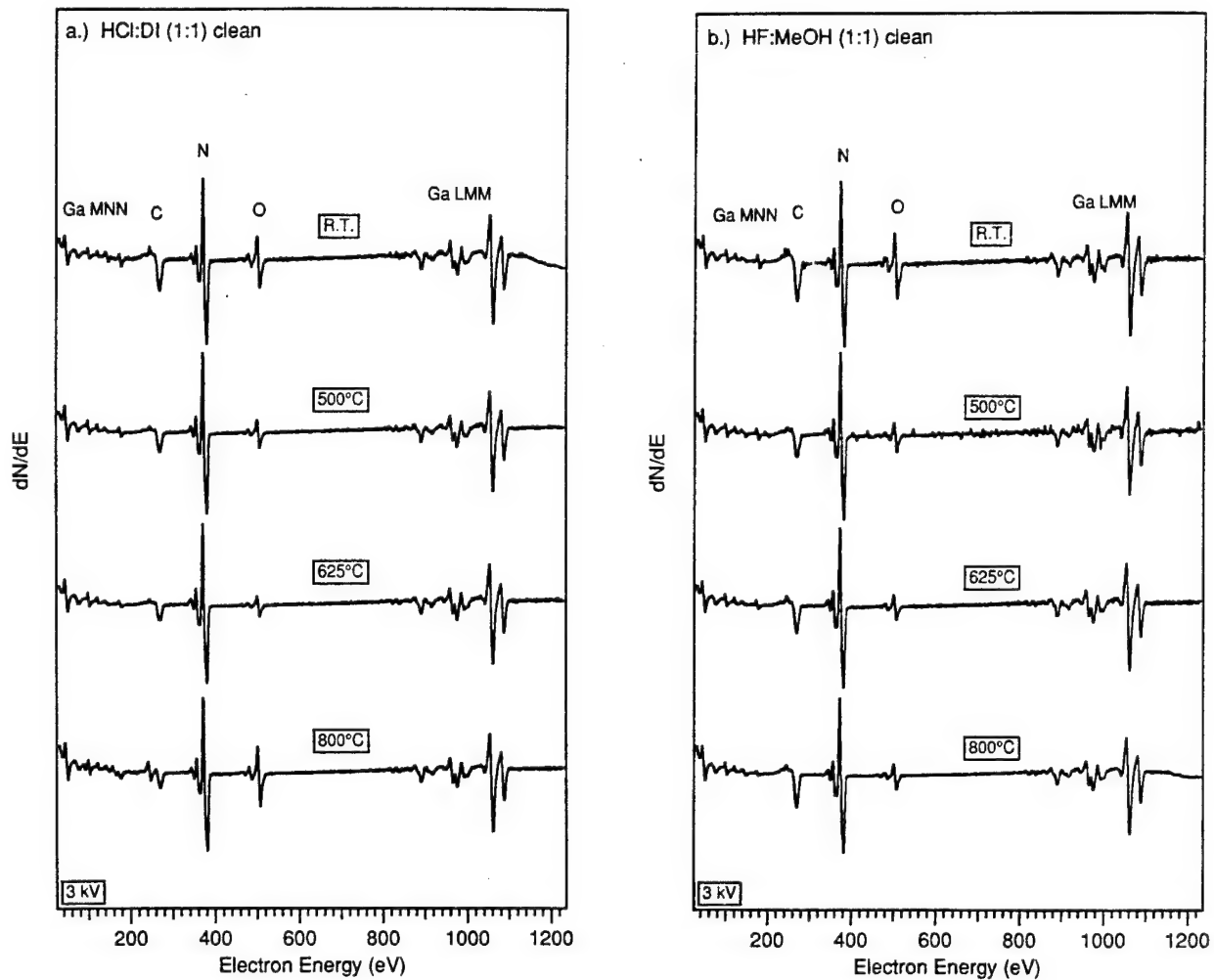


Figure 2. AES survey spectra of GaN surfaces as a function of temperature.

analysis chamber that occurred before acquiring the 800°C spectra. This possibility arises from the unexpected outgassing of a different and unrelated sample in the AES chamber prior to analysis of these samples. However, the results of other recent thermal desorption experiments performed in vacuum on similar GaN films have so far shown that O and C do not completely disappear, even up to temperatures where GaN decomposition occurs (>800-900°C), unless an active species is present to assist in surface removal—i.e., hydrogen plasma, ion bombardment, etc.

The HCl:DI (1:1) cleaning yielded lower O and C concentrations (relative peak-to-peak heights) both at room temperature and as a function of thermal desorption. Both O and C were still present on both samples after the 800°C desorption step, but the complication introduced by the possible contamination from a different experiment is described above. Interestingly, the relative increases of O and C before the 800°C analysis are different for the two cleaning treatments: while the C concentration on the HCl:DI surface remained approximately the same,

Table II. Relative AES Peak Intensities for GaN Surfaces as a Function of Temperature and Surface Treatment.\*

Temperature	HCl:DI (1:1)		HF:MeOH (1:1)	
	O/N	C/N	O/N	C/N
RT	0.21	0.24	0.41	0.33
500°C	0.18	0.17	0.18	0.32
625°C	0.14	0.14	0.16	0.24
800°C	0.39**	0.17**	0.17**	0.29**

\* Prior to acid cleaning, GaN samples were "solvent cleaned," using the sequence TCE, acetone, methanol. After the last treatment step, each sample was blown dry with N<sub>2</sub>.

\*\* Some contamination of GaN surfaces may have occurred upon introduction to the AES analysis chamber after the 800°C heating step, due to the unexpected outgassing of a different and unrelated sample in the AES chamber prior to analysis of these samples.

the relative O signal more than doubled; whereas on the HF:MeOH surface, the C signal increased while the O signal remained the same. In addition, there is some evidence that the C on the HCl:DI surface changed state prior to the 800°C analysis: it shows a different peak shape in that spectrum, while all the other spectra in this study exhibit the typical "aliphatic" C contamination peak shape.

*Ti and TiN Contacts on n-GaN.* In the as-deposited condition, neither the Ti contacts nor the TiN contacts exhibited low specific contact resistivity. Current-voltage measurements revealed their behavior as being quasi-ohmic and having high resistance. The TiN contacts deposited on these GaN:Si films ( $n=1.2\times 10^{18} \text{ cm}^{-3}$ ) did not show the low-resistance behavior exhibited by the as-deposited TiN contacts on more highly doped GaN:Si ( $n=9.4\times 10^{18} \text{ cm}^{-3}$ ) described in the preceding Annual Report (December 1994). The current-carrying capacity of both contact systems increased substantially as a function of annealing, however, and became ohmic and linear. The evolution of the I-V behavior with annealing temperature for both Ti and TiN contacts is shown in Fig. 3 (a) and (b).

Room-temperature TLM measurements showed that the  $\rho_c$  for both the Ti and TiN contacts decreased with increasing temperature, from  $10^2$  to the  $10^{-2} \Omega \text{ cm}^2$  range. These results are plotted in Fig. 4, showing  $\rho_c$  as a function of annealing temperature. Neither the Ti nor the TiN contacts changed substantially with respect to contact resistivity until the 700°C anneal. A large

drop in  $\rho_c$ , of over two orders of magnitude, occurred after 700°C, followed by smaller drops in  $\rho_c$  at higher temperatures.

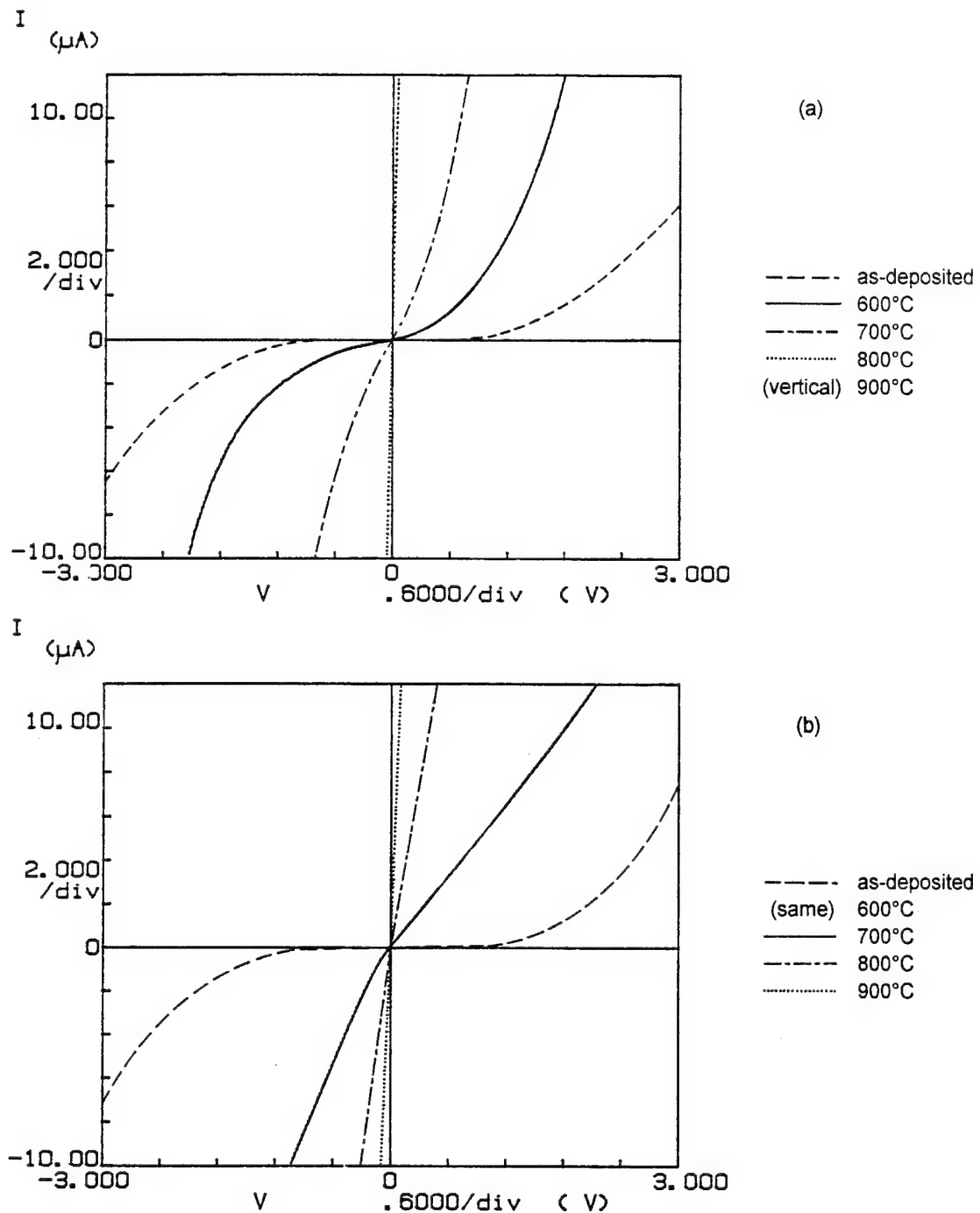


Figure 3. Evolution of I-V behavior for (a) Ti and (b) TiN metal contacts on n-GaN as a function of annealing temperature.

*Pt contacts on p-GaN.* Pt contacts were deposited on Mg-doped GaN by means of Ar-ion sputtering. There was no deposition thickness monitor in the sputtering system, but from

reported deposition rates the Pt film thickness is estimated to be 500-600 Å. These contacts were found to be quasi-ohmic and highly resistive in the as-deposited condition, as shown in Fig. 5 below. Upon annealing at temperatures up through 800°C, the I-V behavior of the Pt contacts became more linear and ohmic and resistances dropped. After the 900°C step, however, the contacts began to turn more resistive again. Associated with this increase in resistance was an increasingly dull appearance of the Pt metal surface, indicative of possible interfacial reaction. Microstructural characterization is upcoming in the near future and hopefully will add to the picture and our understanding of the behavior of this contact system.

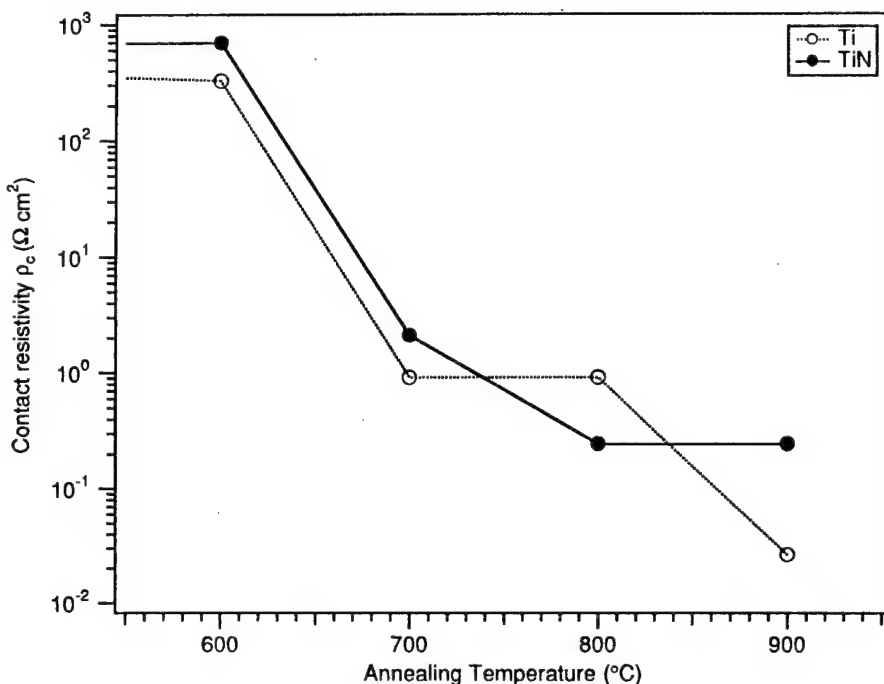


Figure 4. Specific contact resistivity  $\rho_c$  for Ti and TiN contacts on n-GaN as a function of annealing temperature.

#### D. Discussion

*GaN Surface Cleaning.* The presence of measurable amounts of O and C on all of the air-exposed surfaces is not surprising, given the fact that at atmospheric pressure, the time required to adsorb 1 monolayer is less than  $10^{-9}$  s. Of all the wet chemical cleaning methods compared here, the HCl:DI (1:1) solution yielded the lowest relative concentrations of O and C on the air-exposed surfaces. A very small Cl peak was observed as well. Trace amounts of possible Cl appear in the spectra from other samples as well, due perhaps to earlier cleaning treatments (>1 month prior to this study), from HCl or TCE, and/or chloride present as the predominant impurity in even high-purity HF solutions.

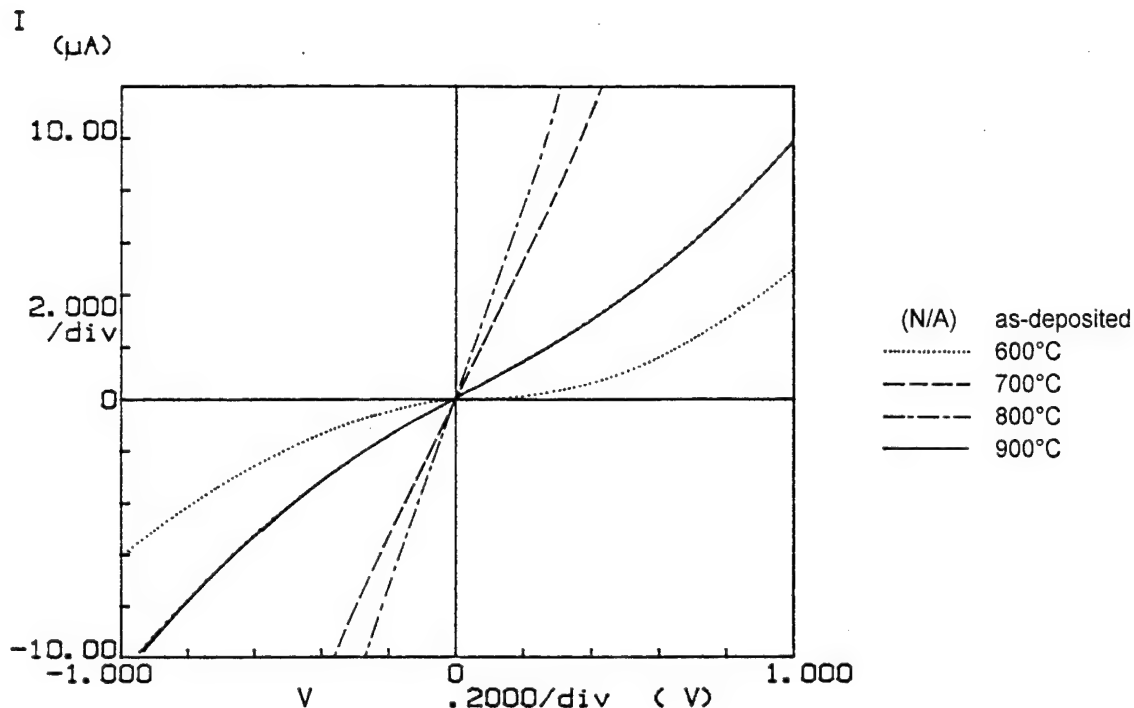


Figure 5. Evolution of I-V behavior for Pt contacts on Mg-doped GaN as a function of annealing temperature.

The placement of the solvent cleaning step after the HCl acid cleaning resulted in an increase of both O and C, possibly due to adsorption of acetone and/or methanol. All of the remaining cleaning treatments examined showed larger relative concentrations of both O and C. Of all the HF cleaning treatments examined, the HF:DI (1:1) treatment gave the lowest O and C concentrations, with values similar to those seen on the HCl:DI, solvent cleaned surface. The highest concentrations of O and C observed were found on the HF:MeOH-treated surface, slightly higher than those on the as-received surface. Again, here the adsorption of methanol is likely to be contributing to the higher peak intensities for O and C.

In the thermal desorption study, the HCl:DI (1:1) cleaning yielded lower O and C concentrations (relative peak-to-peak heights) both at room temperature and as a function of temperature. After the 625°C step, the HCl:DI-treated surface had lost 56% of its initial oxygen coverage and 48% of its carbon coverage, while the HF:MeOH-treated surface had lost 60% of its O and 27% of its C. Both O and C were still present on both samples after the 800°C desorption step; complication introduced by the possible contamination from a different experiment is described above. As stated above, the results of other recent thermal desorption experiments performed in vacuum on similar GaN films have so far shown that O and C do not completely disappear, even up to temperatures where GaN decomposition occurs (>800-900°C), unless an active species is present to assist in surface removal - i.e., hydrogen plasma, ion bombardment, etc. Ingrey *et al.* reported the same phenomenon for InGaAs [21].

An important consideration in this regard is the current concern with the role of H and its compensation of acceptor impurities. The search for a method of obtaining surfaces as atomically "pristine" as possible must necessarily include the characterization of any surface damage or other property degradation that may occur in connection with surface cleaning procedures. The use of ionized, accelerated gas-phase species in cleaning methods is likely to cause some surface damage, depending on the kinetic energy and mass of the ionized species. In addition, there are indications that even short-term exposure to aqueous acid cleaning solutions can cause microroughening of GaAs surfaces, which increases with time of exposure [22].

The relative increases of O and C before the 800°C analysis were different for the two cleaning treatments. While the C concentration on the HCl:DI surface remained approximately the same, the relative O signal more than doubled. On the HF:MeOH surface, the C signal increased while the O signal remained the same. In addition, there is some evidence that the C on the HCl:DI surface changed state prior to the 800°C analysis: it shows a different peak shape in that spectrum, while all the other spectra in this study exhibit the typical "aliphatic" C contamination peak shape. Assuming that the suspected contamination of the samples involved both O and C, the differences between the samples may reflect different types of surface passivation or protection against further surface coverage. The larger amount of C-containing surface coverage on the HF:MeOH-treated GaN may have served to protect against subsequent oxidation, as described in Ingrey's work on III-V surface cleaning [20], while the essentially cleaner HCl:DI-treated surface lacked such protection. Overall, the HCl:DI treatment produces the cleanest surfaces observed to date, both with and without subsequent thermal desorption. The possible additional protection offered by the HF:MeOH treatment may be useful for longer-term storage of GaN films, depending on the methods used for further cleaning.

*Ti and TiN Contacts on n-GaN.* Both Ti and TiN are low work function metals, with TiN having the lower value ( $\phi_{Ti}=4.1$  eV,  $\phi_{TiN}=3.74$  eV), and thus according to the Schottky-Mott-Bardeen model should be more likely to form ohmic contacts to n-type semiconductors. In addition, there are reasons to expect that both Ti and TiN might deposit epitaxially on GaN and AlN, as they both do on 6H-SiC [24, 25]. Titanium has a hexagonal structure and a basal-plane lattice parameter ( $a_{Ti}=2.951$  Å) similar to that of SiC, GaN and AlN ( $a_{SiC}=3.08$  Å;  $a_{GaN}=3.189$  Å;  $a_{AlN}=3.112$  Å). TiN has the NaCl structure and has a reasonably close lattice match to hexagonal GaN (-5.9 %) and AlN (-3.6 %) in the close-packed (111) planes. TiN is thermally very stable and highly resistant to oxidation, forming only a thin passive oxide film on the surface. Though Ti oxidizes readily, it too forms only a thin passive film on the surface under normal conditions, and has a fairly high melting point.

The Ti and TiN were deposited at the same temperature to the same thickness (1000 Å) on similar GaN:Si films. The primary difference between the two metal depositions is the presence

of extra available N during TiN growth to fully bond with the Ti. In TiN the Ti becomes stoichiometrically nitrided and strongly bound to N, whereas in the case of Ti alone, any Ti nitride formation that takes place must derive its nitrogen from the GaN. The nitridation of Ti is thermodynamically favored with respect to GaN: the Gibbs free energy of formation  $\Delta G_f^0$  for TiN at 298 K is -6309.2 kJ/mol, while  $\Delta G_f^0$  for GaN is only -77.8 kJ/mol. The difference in  $\Delta G_f^0$  between the two does not change appreciably through 1000 K. The removal of Ti from the GaN would result in N vacancies, which are widely believed to function as shallow donors in GaN. M.E. Lin and H. Morkoç *et al.* have estimated that 2 monolayers of TiN formation at a contact interface is sufficient to form a 10 nm surface layer of GaN having an electron density of  $10^{20} \text{ cm}^{-3}$  through which electrons could efficiently tunnel, thus greatly increasing the current-carrying capacity of the contact interface [19, 26].

The TiN contacts deposited on these GaN:Si films ( $n=1.2 \times 10^{18} \text{ cm}^{-3}$ ) did not show the low-resistance behavior exhibited by the as-deposited TiN contacts on more highly doped GaN:Si ( $n=9.4 \times 10^{18} \text{ cm}^{-3}$ ) described in the preceding Annual Report (December 1994). This large difference in GaN carrier concentration may account for much of the difference in  $\rho_c$  behavior. Overall, the Ti and TiN contacts in this experiment behaved similarly with respect to annealing treatment - possibly for different reasons. The TiN has a lower work function and thus may produce a lower barrier than Ti on GaN, but the un-nitrided Ti is able to create N vacancies in the GaN interfacial region, which would also result in improved contact behavior. More detailed study of this contact system, especially high-resolution microstructural characterization via X-TEM to look for epitaxial relationships and any compositional changes that take place, is planned to help understand the current transport mechanisms and establish the utility of this contact system for high-temperature device applications.

*Pt contacts on Mg:GaN.* Platinum is a very high work function metal ( $\phi_{Pt}=5.65 \text{ eV}$ ) and thus provides a favorable band offset for ohmic contact formation to a p-type semiconductor. In addition, Pt is thermally very stable and highly resistant to oxidation. In the preceding annual report for this project (December 1994), linear ohmic behavior and very low  $\rho_c$  was observed for as-deposited Pt contacts to Mg-doped GaN. Investigation of Pt as an ohmic contact candidate for p-type GaN was conducted earlier in this study, as described in the semi-annual report for June 1993, but the results were not as promising at that time. Substantial improvements in GaN film quality and electrical properties have been made since then. The newer Mg:GaN described here were grown by MOVPE instead of MBE, as was the case when the earlier study was conducted. However, it should be pointed out that Mg doping procedures in the MOVPE system at NCSU, as well as annealing procedures for improvement of acceptor activation, are still undergoing improvement and optimization. Further work is necessary to confirm the type and carrier concentrations in the Mg:GaN films being grown currently, and to optimize the activation of acceptor impurities. The measurement of carrier concentration and

mobility via Hall measurements has been difficult for p-type GaN so far, due to inconsistent ohmic contact behavior.

The work of Sands *et al.* [31,32] has shown that extensive interfacial reaction can occur between Pt and GaAs, due to metallurgical reactions involving both Ga and As. Though lacking the mobile and reactive As species, GaN nevertheless has shown the ability to react with noble metals when annealed at high temperature, as described in the preceding annual report in connection with Au contacts on p-GaN. Thus, changing behavior of the Pt contacts as a function of annealing temperature is not surprising. The increasing resistance seen for the 900°C anneal is likely due to a progression of interfacial phase formation. Upcoming high-resolution microstructural characterization will provide additional information and aid in the understanding of the behavior of this contact system.

#### E. Conclusions

The results of surface cleaning experiments conducted in this study so far has shown that HCL:DI (1:1) solution cleaning produces the cleanest surfaces of all the wet chemical cleaning methods yet examined on GaN films, particularly if the wet cleaning is followed by a thermal desorption to at least 625°C. All of the cleaning methods examined that involved HF were found to leave more O and C on the surface in general, though there was some evidence that the HF:MeOH treatment might protect a GaN surface from further oxygen coverage. As yet, complete removal of O and C from air-exposed GaN surfaces has not been seen, even up to temperatures where GaN decomposition occurs (>800-900°C), unless an active species is present to assist in surface removal - i.e., hydrogen plasma, ion bombardment, etc.

The comparison of Ti and TiN contacts on similarly-doped n-GaN has shown them to behave similarly with respect to the effects of annealing on the specific contact resistivity. In both cases, the  $\rho_c$  dropped significantly as a result of annealing through 900°C. It is likely that the improvement in the behavior of the Ti contact system is due to the formation of TiN at the GaN interface. More detailed study of this contact system, especially high-resolution microstructural characterization via X-TEM to look for epitaxial relationships and any compositional changes that take place, is planned to help understand the current transport mechanisms and establish the utility of this contact system for high-temperature device applications.

Annealing studies of sputtered Pt contacts on Mg-doped GaN have shown an improvement in current-carrying behavior as a result of annealing, though a deterioration in performance was observed for the highest annealing temperature (900°C). The achievement of low-resistivity ohmic contacts to p-GaN is a necessary component for the development and application of many types of GaN-based devices. Further characterization of contact candidates for p-type material, including microstructural information obtained from X-TEM analysis, will yield

greater understanding of the chemical and structural contributions to contact behavior and will allow more rapid and knowledgeable development of improved contact schemes and their capabilities.

#### F. Future Plans and Goals

In addition to further chemical and structural characterization of the contact systems described in this report, other schemes for improving contact performance will be investigated. Combined with the search for improved contacts to the III-nitrides is the ongoing investigation of Fermi-level pinning and defect states, and the role played by work function and electron affinity differences in contact properties. The evidence examined to date indicates that GaN does indeed experience much less Fermi-level pinning than its more covalently bonded relatives such as GaAs; further work will help to clarify this issue and assist the development of advanced microelectronic and optoelectronic devices.

The issues of surface cleaning and sample preparation will continue to be important in the areas of device fabrication. The role of oxygen and other contaminants at the contact interface is important to understand, and will become even more critical for AlGaN and AlN-based devices due to the strong affinity of Al for oxygen. For such cases the cleanliness of the contact deposition environment will probably be of greater importance as well.

The results of preliminary TLM measurements, reported in the last semi-annual report for this project (December 1994) show that Cu<sub>3</sub>Ge, as well as Cu contacts in the as-deposited state, form ohmic contacts on both Ge:GaN and Mg:GaN. To date, the properties of Cu<sub>3</sub>Ge films have been documented by Aboelfotoh *et al.* [27-30], but the interfacial properties of CuGe contacts to semiconductor surfaces are only beginning to be investigated. The results of I-V measurements of UHV-deposited, alloyed-*in situ* Cu<sub>3</sub>Ge contacts indicate low-resistivity ohmic behavior. At the present time the work function and electron affinity properties of CuGe compounds have not yet been studied, so it is not known how this contact system compares with the Schottky-Mott-Bardeen model. It is possible that even if a contact metal does not have a favorable work function relationship to a semiconductor for ohmic contact formation according to the Schottky model, the role of a barrier at the surface can be bypassed by means of other current transport mechanisms. The time intervals and temperatures of the alloying and/or contact annealing steps, along with the cleanliness of the deposition environment, have significant effects on the resulting current-carrying abilities of the contacts. The details of the alloying and annealing procedures would influence the rate and amount of any interfacial diffusion that take place and the reactions that occur at the interface. Film composition is also evidently of critical importance in the behavior of this contact system, given the difference between the UHV and non-UHV-deposited contacts. All of these factors have an effect on the

behavior of the contacts. Given the success of this contact system with GaAs materials and its promise for the nitrides, investigations will continue.

#### G. References

1. T. C. Shen, G. B. Gao, H. Morkoç, J. Vac. Sci. Technol. B **10** (5), 2113 (1992).
2. R. Williams, *Modern GaAs Processing Techniques* (Artech House, Norwood, MA, 1990)
3. M. Murakami, Materials Science Reports (5), 273 (1990).
4. A. Piotrowska and E. Kaminska, Thin Solid Films **193/194**, 511 (1990).
5. A. Piotrowska, A. Guivarc'h and G. Pelous, Solid-St. Electron. **26** (3), 179 (1983).
6. V. L. Rideout, Solid-St. Electron. **18**, 541 (1975).
7. K. Tanahashi, H. J. Takata, A. Otsuki and M. Murakami, J. Appl. Phys. **72** (9), 4183 (1992).
8. H. J. Takata, K. Tanahashi, A. Otsuki, H. Inui and M. Murakami, J. Appl. Phys. **72** (9), 4191 (1992).
9. M. C. Hugon, B. Agius, F. Varniere, M. Froment and F. Pillier, J. Appl. Phys. **72** (8), 3570 (1992).
10. W. O. Barnard, G. Myburg and F. D. Auret, Appl. Phys. Lett. **61** (16), 1933 (1992).
11. G. Stareev, Appl. Phys. Lett. **62** (22), 2801 (1993).
12. E. D. Marshall and M. Murakami, in *Contacts to Semiconductors*, edited by L.J. Brillson (Noyes, Park Ridge NJ, 1993).
13. F. W. Ragay, M. R. Leys and J. H. Wolter, Appl. Phys. Lett. **63** (9), 1234 (1993).
14. H. K. Henisch, *Semiconductor Contacts*. (Clarendon Press, Oxford, 1984).
15. E. H. Rhoderick, *Metal-Semiconductor Contacts* (Oxford University Press, New York, 1988).
16. S. Kurtin, T. C. McGill and C. A. Mead, Phys. Rev. Lett. **22** (26), 1433 (1969).
17. J. S. Foresi, *Ohmic Contacts and Schottky Barriers on GaN*, M.S. Thesis, Boston University (1992).
18. J. S. Foresi and T. D. Moustakas, Appl. Phys. Lett. **62** (22), 2859 (1993).
19. M. E. Lin, Z. Ma, F. Y. Huang, Z. F. Fan, L. H. Allen, and H. Morkoç, Appl. Phys. Lett. **64** (8), 1003 (1994).
20. S. Ingrey, J. Vac. Sci. Technol. A **10** (4), 829 (1992).
21. S. Ingrey, W. Lau, and R. Sodhi, J. Vac. Sci. Technol. A **7**, 1554 (1989).
22. D. E. Aspnes and A.A. Studna, Appl. Phys. Lett. **46** (11), 1071 (1985).
23. G. K. Reeves and H. B. Harrison, IEEE Electron Device Lett. **EDL-3** 111 (1982).
24. L. M. Porter, R. F. Davis, J. S. Bow, M. J. Kim, R. W. Carpenter, and R. C. Glass, J. Mater. Res., **10** (3), 668 (1995).
25. R. C. Glass, Ph.D. thesis, North Carolina State University, June 1993.
26. H. Morkoç, S. Strite, G. B. Gao, M. E. Lin, B. Sverdlov, and M. Burns, J. Appl. Phys. **76** (3), 1363 (1994).
27. L. Krusin-Elbaum and M. O. Aboelfotoh, Appl. Phys. Lett. **58** (12), 1341 (1991).
28. M. O. Aboelfotoh, H. M. Tawancy, and L. Krusin-Elbaum, Appl. Phys. Lett. **63** (12), 1622.
29. M. O. Aboelfotoh, K. N. Tu, F. Nava, and M. Michelini, J. Appl. Phys. **75** (1), (1994).
30. M. O. Aboelfotoh, H. M. Tawancy, J. Appl. Phys. **75** (4), (1994).
31. T. Sands, V. G. Keramidas, A. J. Yu, K-M. Yu, R. Gronsky, and J. Washburn, J. Mater. Res. **2** (2), 262 (1987).
32. T. Sands, V. G. Keramidas, K-M. Yu, J. Washburn, and K. Krishnan, J. Appl. Phys. **62** (5), 2070 (1987).

## **XXVI. Distribution List**

Mr. Max Yoder Office of Naval Research Electronics Division, Code: 312 Ballston Tower One 800 N. Quincy Street Arlington, VA 22217-5660	3
Administrative Contracting Officer Office of Naval Research Regional Office Atlanta 101 Marietta Tower, Suite 2805 101 Marietta Street Atlanta, GA 30323-0008	1
Director, Naval Research Laboratory ATTN: Code 2627 Washington, DC 20375	1
Defense Technical Information Center Bldg. 5, Cameron Station Alexandria, VA 22304-6145	2